Gone with the Wind:

Dust Entrainment in Photoevaporative Winds

Raphael Franz

München 2022

Vom Winde verweht:

Staubmitnahme in photoevaporativen Winden

Raphael Franz

Dissertation
an der Fakultät für Physik
der Ludwig–Maximilians–Universität
München

vorgelegt von
Raphael Franz
aus Kempten (Allgäu)

München, den 21. März 2022

Erstgutachter: Prof. Dr. Barbara Ercolano
Zweitgutachter: Prof. Dr. Til Birnstiel
Tag der mündlichen Prüfung: 10. Mai 2022

Zusammenfassung

Planetensysteme wie das Sonnensystem entstehen aus protoplanetaren Scheiben. Diese zirkumstellaren Scheiben enthalten große Mengen an Gas und Staub; insbesondere letzterer stellt das Material für das Wachstum von Planetesimalen und schließlich Planeten zur Verfügung. Der zeitliche Rahmen für die Planetenentstehung ist allerdings durch die Auflösung der Scheibe begrenzt. Photoevaporative Winde, angetrieben von vom Stern emittierter Röntgen- und extrem ultravioletter (zusammen: XEUV-) Strahlung, sind eventuell die hauptsächlichen Antriebskräfte hinter dieser Auflösung; ein eindeutiger Nachweis solcher Winde mittels Emissionslinienspektroskopie ist jedoch weiterhin schwierig.

Das Ziel dieser Arbeit ist eine quantitative Abschätzung der Mitnahme μm-großer Staubteilchen im von XEUV-Winden angetriebenen Gasausfluss, um so eine alternative Nachweismethode zu schaffen. Mit den ermittelten Staubdichten können Vorhersagen für bildgebende Beobachtungen – zum Abgleich mit tatsächlichen Daten – sowie für astrochemische Modelle notwendige Opazitätsverteilungen erstellt werden.

Hierfür wurde die Bewegung von Staubteilchen in der Windregion von im Fließgleichgewicht befindlichen, XEUV-bestrahlten Gasmodellen von Primordial- und Übergangsscheiben simuliert. Zur Berechnung der Staubdichten wurden die daraus abgeleiteten Staubverteilungen mit zwei verschiedenen Modellen für die Staubdichte zwischen Mittelebene und Oberfläche der Scheiben kombiniert – im ersten wurde eine vollständige Kopplung der Gas- und Staubdichten angenommen, im zweiten eine vertikale Sedimentierung des Staubs. Mit den ermittelten Dichten für den Staubausfluss wurden per Strahlungstransportsberechnungen Bilder erstellt und hieraus Beobachtungen in Streu- und polarisiertem Licht synthetisiert.

Im von einem T-Tauri-Stern mit relativ hoher Röntgen-Intensität angetriebenen Wind werden Staubkörner von bis zu zirka zehn μm weggetragen. Da größere Teilchen in der Scheibe verbleiben und außerdem die kleinsten Partikelarten am meisten zum Staubausfluss beitragen, ergeben sich Masseverlustraten, die deutlich kleiner sind, als was von den zugehörigen Gas-Ausflussraten in Verbindung mit einem normalen Staub-zu-Gas-Masseverhältnis zu erwarten wäre. Besonders bei größeren Neigungswinkeln weisen die Modelle alle eine trichter- bzw. kaminförmige Ausflusssignatur auf; für die Übergangsscheiben ist diese ausgeprägter. In Streulich ist sie im Vergleich zur Scheibe nicht sehr hell; aber mit modernsten Geräten wie zum Beispiel JWST könnte sie mittels koronographischer Aufnahmen entdeckt werden. In polarisiertem Licht ist der Staub im Wind besser zu erkennen; er dürfte mit modernen Teleskopen wie VLT SPHERE unter optimalen Bedingungen oder mittels einer Analyse der Spektralindizes nachweisbar sein.

Zusammenfassend sollte der Staubeinschluss von von XEUV-Strahlung angetriebenen Winden besonders bei Übergangsscheiben beobachtbar sein. Die in dieser Arbeit erstellten künstlichen Aufnahmen können zum Vergleich mit entsprechenden Beobachungsreihen und zur Weiterentwicklung von Windmodellen verwendet werden.

Abstract

Planetary systems such as the solar system form from protoplanetary disks. These circumstellar disks contain large masses of gas and dust; especially the latter supplies material for the growth of planetesimals and ultimately planets. However, the timeframe for planet formation is limited by the dispersal of the disk. Photoevaporative winds driven by X-ray and extreme ultraviolet (together: XEUV) radiation from the host star may be the main driver behind this dispersal; yet this remains difficult to observationally prove via emission line spectroscopy.

This work aims to quantify the entrainment of small μm-sized dust grains by the gas in XEUV-driven winds, in order to provide an alternative observational tracer. The determination of dust densities allows for imaging predictions to be benchmarked by actual data, as well as the computation of opacity maps needed to refine astrochemical models.

To this end, dust trajectories were simulated in the wind regions of steady-state gas models of XEUV-irradiated primordial and transitional disks. They were subsequently converted into dust population maps, and combined with two different density prescriptions for the region from the disk midplane up to the disk-wind interface – one assuming the dust to be fully coupled to the gas, and one imposing vertical settling on the dust – in order to retrieve the dust densities in the wind. With those, radiative-transfer images of the dusty outflow were computed, and synthesised into observational responses in scattered and polarised light.

For a T-Tauri star with a relatively high X-ray luminosity, grains of up to about ten μm are picked up by the wind. Because larger grains remain in the disk and moreover, the smallest grain sizes contribute the most to the overall dust outflow, dust mass-loss rates are significantly lower than what would be expected from the corresponding gas mass-loss rates in combination with standard dust-to-gas ratios. All models exhibit a cone- or chimney-shaped outflow pattern especially at higher inclinations; it is more prominent for the transitional disks. The scattered-light features of the dusty wind are rather dim relative to the disk; but they may be picked up via coronagraphic imaging using state-of-the art instruments like JWST. In polarised light, the dusty wind is slightly brighter; it may be observable with modern instruments such as VLT SPHERE under optimal conditions, or noticeable from the analysis of spectral indices.

In conclusion, dusty outflows driven by XEUV winds should be detectable especially for transition disks; the synthetic images produced in this work may be employed as benchmarks for according observational campaigns, and as a basis for refined models of dusty disk winds.

Contents

Chapter 1

Introduction

There are many pieces to the puzzle of human existence. While the concept of self-awareness necessitates the question 'Who am I?', the exploration of the present in turn leads to questions about the past and the future – 'Where do I come from?' and 'Where am I going?'. Both of these are intrinsically related to 'Why am I?'.

Since ancient times, philosophers as well as religions have attempted to find and provide answers to these deceptively simple questions. However, as the saying goes, *quot homines tot sententiae* – there are as many opinions as there are people. Fundamentally, every person may have their own mental construct for a given topic, and even assuming that said construct is the same for two individuals, they may still arrive at different interpretations. Throughout the history of human civilization, these differing world views – held by different individuals, or groups of individuals – have led to countless conflicts and wars. From a purely pragmatic point of view, these may even have been reasonable; when (usually not if) one side wins, its world view prevails, while the one of the opposing side perishes. The justification for the (from a humanitarian or moral point of view) inhumane nature of war is the promise that it shall prevent any and all future conflict. Whether it achieves its goal is a very different story; from a historian's perspective, the answer may well be 'No'.

Enter the natural sciences. Their promise is to provide answers based solely on verifiable facts; and since facts are facts, this should quell any possibility for a conflict to arise. For instance, there simply is no philosophical argument that can make Newton's famous apple not fall onto the ground, but instead towards the sky; so there cannot be any disagreement as to its motion, and any dispute is futile. While in principle, this may seem like the best, perhaps even only, way to prevent disagreements, it is not entirely flawless either.

Firstly, all parties must agree to respect the scientific process and its results; Archimedes's *noli turbare circulos meos* (do not disturb my circles), as well as the still ongoing debate on climate change showcase just two examples that this is not always a given. Nonetheless, this was the motivation behind Kant proclaiming (Horace's) *sapere aude!* ('dare to know!', Kant, 1784), which became one of the guiding principles of Enlightenment. Likewise, Goethe's Faust is driven by a very like-minded motivation (Goethe, 1808; Goethe & Taylor, 1872):

> *Daß ich erkenne, was die Welt // Im Innersten zusammenhält*
>
> That I may detect the inmost force // Which binds the world, and guides its course

Secondly, it raises the question of how something is proven. Evaluating the case of the apple in terms of a more rigorous approach, one single apple falling downwards certainly demonstrates the *possibility* that an apple *can* fall downwards; but it is not necessarily *proof* that all apples *must* fall downwards. However, observing every single apple is impossible.(1) So how does one proceed? – The established answer is provided by the *scientific method*, one version of which is sketched in Fig. 1.1.(2)

The real world leads to observations (or ideas), which can be formulated in terms of a hypothesis (e.g. 'If I let go of an apple, it will fall downwards.'). After doing experiments to verify this hypothesis (e.g. 'I've dropped a hundred apples, and all of them have fallen downwards.'), one can then formulate a theory or model (e.g. 'Apples fall downwards.', or rather $\vec{F} = m\,\vec{a}$, see Newton, 1687). This theory can then lead to new ideas (and thus hypotheses) for experiments (e.g. 'Oranges behave like apples.'), which will have to be tested for further refinement.

(1) Unobserved apples *might* even stick to their branches forever, if Schroedinger's cat has any say in this.

(2) Note, however, that even for this 'established answer', an internet search yields far more than one version (although the underlying concepts are similar).

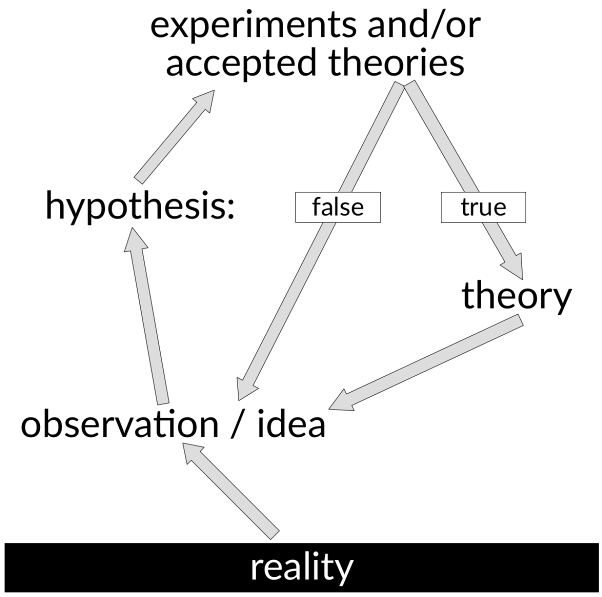

Figure 1.1: The scientific method (adapted from Demtröder, 2006). The objective reality informs subjective views, which can then be converted into testable hypotheses. The outcome of the testing determines whether the hypothesis is upheld as a theory (or integrated into one), or refined. Thus, a circular process evolves (but the derived model of reality has no back-reaction on reality).

In this process, Popper (1935) states, it is important to choose experimental setups that are actually able to falsify the current model, and to treat the results in an unbiased manner, because it is the process of objective verification as well as falsification and refinement that drives the development of the theory, and thus scientific progress. After all, the theory is shaped by reality, but it does not shape reality; Fig. 1.1 does not contain any arrow from any stage of the scientific process to reality (see also Heng, 2014). So while, in astronomical terms, there are for instance data indicating a mean filament width of 0.1 pc, this may well just be a measurement bias (see e.g. Panopoulou et al., 2017, 2022), in which case the observed filaments will not change their actual widths to comply. Alternatively, highly accurate measurements of the Hubble constant indicate that it is likely constant (see e.g. Planck Collaboration et al., 2020), but these measurements do not make it a (global) constant, even if theorists like the author would prefer it to be (see e.g. Riess et al., 2019; Dainotti et al., 2021). Similarly, while it would be a very reasonable first hypothesis to assume that a parallel universe – if existent – follows the same laws as this one, this is not a necessity (Carroll, 2019).

Returning to the question at hand, that is how something is proven, the answer may seem unwelcome: All we we can do is find models that work for all test cases tested; so their primary value is heuristic (see e.g. Oreskes et al., 1994). However, this could also be considered an incredibly exciting finding – the next phenomenal discovery might be just around the corner, in a place where nobody has cared to look yet.

A topic that should also be discussed in this regard is what exactly we actually consider to be *proof*. In relation to climate change (or in other words, a change in the atmospheric composition of the simplest-to-observe planetary atmosphere, on a comparatively short timescale), a possible heating effect from CO_2 was reported already by Foote (1856); subsequent investigations by, for example, Arrhenius (1897) and Callendar (1938) pointed in the same direction, but were often considered not scientifically rigorous enough to be taken seriously. The development of the Keeling curve (Keeling, 1960) commenced a gradual change of that perspective, but it took until 2021 to establish a (still almost) unanimous (scientific) consensus that climate change is indeed happening, and is caused by humans (Lynas et al., 2021). This showcases an interesting example of when a theory is generally accepted. While a purely scientific approach might prefer to let climate change play out so that it can be studied and evaluated a posteriori, taking early results more seriously – even if not entirely believing them – may have helped to significantly speed up the development of new models (and, in this case, countermeasures). This course of action may of course be met with resistance, considering that a falsification of the original claim of global warming would have meant the efforts spent would have been wasted; yet nonetheless, they may have yielded interesting ideas that could have been transferrable to other areas of research, and thus been worthwhile regardless.

Likewise, while already Bruno (1584) speculated on the existence of planets around stars other than the Sun, it took the work of Mayor & Queloz (1995) to fully convince the community that other Sun-like systems can indeed host planets; earlier observational campaigns had resulted in either more tentative statements (Campbell et al., 1988), or a confirmation of planets around non-solar objects (Wolszczan & Frail, 1992). The theoretical modelling for the formation of such planets (or at the very least the solar system), which had been going on already for some time, could successively be used as the basis for a vast new field of research.

Thirdly, a topic that may appear entirely unscientific, but is nonetheless necessitated by the human nature of the researchers, is the concept of ethics. Does Faust's intent to understand the world justify all of his actions? Moreover, does a scientist have the responsibility to ascertain that the knowledge they attain and share will not be used for evil purposes? And in this context, what is 'evil', and what is 'good'? Are the societal thought experiments of *Brave New World* (Huxley, 1932) and *1984* (Orwell, 1949) desirable, considering that they, on average, improve living conditions, and prevent conflict and thus lots of premature deaths? – The author is neither literate nor fatuous enough to claim to have answers to these questions; yet they should at least be asked.[(1)]

In the end, one may conclude, as Plato alleges Socrates once did, that *I know that I know nothing* – or rather, as several authors claim, *I think that I know nothing*, because else the 'I' would indeed know something. Of course, this approach has its own flaws – just like an emergency doctor has a much better chance of saving a patient when starting the treatment without first questioning it, an astrophysicist would not make much progress if they started each day by re-deriving Kepler's laws. So this short discussion is not in the least meant to discourage from the participation in the scientific process and the discovery of the countless mysteries of the Universe; it is intended merely as a word of caution to thoroughly investigate an area or subject of research before making a strong statement about it, and to continue to be open to new data and ideas even after that.

1.1 The research question

Returning to the very beginning of this introduction, one of the questions relating to 'Where do I come from?' is that of the origin of life, and in that context, the formation of the solar system and of planet Earth. This entails the question of how planets – and before that, planetesimals – are formed in general, an area of research that has been active for quite some time (see e.g. Goldreich & Ward, 1973; Raymond & Morbidelli, 2020, and sources therein). Due to the scale of the problem and the rather long time frames needed for planet formation (see e.g. Drążkowska & Dullemond, 2018), laboratory experiments seem impractical; thus, in the spirit of the scientific method discussed above, theoretical models are developed in order to run simulations which in turn are benchmarked by, and reworked in accordance with, observational data (see e.g. Ercolano & Pascucci, 2017).

While having just a few processes which dominate the process of planet formation – or at least certain phases thereof –, would considerably simplify matters, it is questionable – and has repeatedly been questioned (see e.g. Avenhaus et al., 2018; Bate, 2018; Stamatellos & Inutsuka, 2018; van der Marel et al., 2021) – whether all planetary systems have been created equal, rendering the modelling quite intricate. Planets, on the other hand, are formed from, and shaped by, their host disks; so in order to better understand their creation and early evolution, a thorough understanding of their host system(s) is required (see e.g. Morbidelli & Raymond, 2016).

From a naive point of view, planets are big clumps of gravitationally bound material that have not reached the mass and hence internal pressure needed for initiating nuclear fusion, and therefore are not stars (see e.g. Prialnik, 2010). The material for their formation must be supplied from the parent molecular cloud and/or the circumstellar disk; so once the disk is gone, planet formation will necessarily stall (see e.g. Alexander et al., 2014). Hence it is fundamentally important to understand the processes behind disk dispersal.

One of these processes is mass loss due to gas and dust outflows caused by protostellar winds; these can (for instance) be driven by highly energetic radiation from the accreting host star (see e.g. Hollenbach et al., 1994; Clarke et al., 2001). While models for these so-called photoevaporative winds are already quite developed from a theoretical perspective (see e.g. Clarke & Alexander, 2016; Picogna et al., 2019; Ercolano et al., 2021; Sellek et al., 2021), verifying them observationally is an ongoing challenge. Typically, shifts and broadening of various molecular lines are used to benchmark simulations (see e.g. Ercolano &

[(1)]Admittedly, moral considerations are more relevant for the fields of, for instance, genetic modification or artificial intelligence than for astronomy.

Pascucci, 2017); however, they have not yet resolved the question of which process is the main force behind the wind-driven, gaseous outflow.[1] A different approach was tried by Owen et al. (2011a), who used a simplified model of dust entrainment in photoevaporative winds to produce observational predictions that could be tested via imaging campaigns; this could then be used for an observational verification (or falsification) of the model (in accordance with Fig. 1.1). The goal of this work is to produce a slightly more intricate model for the entrainment of small dust grains in X-ray-enhanced photoevaporative winds, which should allow for more detailed synthetic images. Furthermore, estimating the dust densities in the wind region of the disk allows for the computation of opacity maps to be used in astrochemical models (such as Grassi et al., 2017), which would further help to refine our understanding of the process of planet formation (see e.g. Testi et al., 2014; Ercolano & Pascucci, 2017).

1.2 Outline of this thesis

This thesis is organised as follows:

Chap. 2: A brief overview over the various processes involved in the formation of a new stellar system is provided. In addition, current models of disk evolution and dispersal are summarised.[2][3]

Chap. 3: A model of a steady-state primordial gas disk irradiated by high-energy photons emitted from its central T-Tauri star is used to model the trajectories of small Lagrangian dust grains in the gaseous outflow; the X-ray luminosity of the star is chosen to be quite high, in order to provide a scenario with a strong photoevaporative wind. This yields a first understanding of what grain sizes can be entrained (depending on their internal density) – especially in comparison to wind models without an X-ray component, and MHD winds –, and how they behave in the wind. This allows us to compile a list of potentially identifying characteristics of dusty photoevaporative outflows, which will be tested in Chaps. 4 and 5.[4]

Chap. 4: With the dust grain trajectories modelled in Chap. 3, the dust content in the wind is computed for a set of grain sizes. To this end, the dust motions in the wind are converted into density maps, and combined with two different prescriptions for the dust densities at the disk-wind interface. The resulting dust densities are then used to create radiative-transfer images in scattered and polarised light, as well as synthesised observations for two current instruments.[5]

Chap. 5: The methods developed in Chaps. 3 and 4 are refined to work with models of transition disks; they are then employed to compute dust trajectories and densities for two steady-state gas models of disks with inner holes of 20 and 30 AU in order to offer a direct comparison between dusty winds from primordial and transition disks. As in Chap. 4, radiative-transfer images and synthetic observations for two current instruments are produced, and analysed with respect to the observability of the dust entrained in the outflows.[6]

Chap. 6: The results of Chaps. 3, 4, and 5 are summarised. Furthermore, an outlook towards possible future projects on the basis of this work is provided, regarding both simulations and observations.

[1] The review of Ercolano & Pascucci (2017) may be seen as the motivation behind the DFG-funded research unit 'Transition Disks', a sub-project of which funded this research.

[2] Due to the colossal amount of literature on these topics, this overview is necessarily incomplete, but should suffice as a basis for the investigations to follow. The topic of winds in particular is addressed in Sect. 2.3, with Sect. 2.3.3 dedicated to photoevaporative winds, the main focus of this work.

[3] The interested reader is furthermore referred to the soon-to-be published proceedings of *Protostars and Planets VII*, which will convey a much broader and much more in-depth (re)view of the status of current research.

[4] A dedicated summary of the results is given at the beginning of Chap. 3 itself.

[5] A dedicated summary of the results is given at the beginning of Chap. 4 itself.

[6] A dedicated summary of the results is given at the beginning of Chap. 5 itself.

Chapter 2

Stars, disks, and winds

2.1 The birth of stars

Stars are born in regions of enhanced gas density in the interstellar medium (ISM) of galaxies, which themselves are regions of enhanced matter density compared to their surroundings. These density variations can be driven by supernovae (SNe), the collisions of clouds, or by differential motion in magnetic fields, but are most likely due to gravitational instabilities (see e.g. McKee & Ostriker, 2007; Prialnik, 2010, and references therein), giving way to a top-down formation of objects (as theorised by Hoyle, 1953). The resulting regions of enhanced density are commonly referred to as giant molecular clouds (GMCs); this expression already hints at their usual extent of several to several hundred parsec (see e.g. Larson, 1981). Once a part of a GMC – typically a filament (see e.g. André et al., 2014) – becomes massive enough that locally, gravity outweighs its internal pressure, it collapses (Jeans, 1902).

Hydrostatic equilibrium, that is a balance between the force from the internal pressure P of a system and the gravitational force counteracting it, demands (see e.g. Prialnik, 2010)[(1)]

$$P(r + \mathrm{d}r)\,\mathrm{d}S - P(r)\,\mathrm{d}S \stackrel{!}{=} -\frac{G\,M}{r^2}\,\varrho\,\mathrm{d}S\,\mathrm{d}r \tag{2.1}$$

for $\mathrm{d}V = \mathrm{d}S \cdot \mathrm{d}r$ a volume element, G the gravitational constant, ϱ the mass density, and

$$M = \int_0^r \varrho \cdot 4\,\pi\,r'^2\,\mathrm{d}r' \tag{2.2}$$

the mass enclosed within r. Eq. (2.1) can be rearranged to

$$\frac{\mathrm{d}P}{\mathrm{d}r} = -\varrho \cdot \frac{G\,M}{r^2}\ ; \tag{2.3}$$

multiplication by V and integration leads to the virial theorem,[(2)]

$$2\,E_\mathrm{kin} = -E_\mathrm{grav}\ , \tag{2.4}$$

where E_kin stands for the internal or kinetic energy of the (stable) system, and E_grav for its potential energy. The kinetic energy for an ideal gas (with three degrees of freedom) is (see e.g. Demtröder, 2006)

$$E_\mathrm{kin} = \frac{3}{2}\,N\,k_\mathrm{B}\,T\ , \tag{2.5}$$

with N the amount of gas particles, k_B the Boltzmann constant, and T its temperature. The gravitational energy of a sphere can be computed by bringing a series of particles of infinitesimal mass $\mathrm{d}M$ from infinity to r,

$$E_\mathrm{grav} = \int_0^M \left(\int_\infty^r -\frac{G\,M'\,\mathrm{d}M'}{r'^2}\,\mathrm{d}r' \right) = \tag{2.6}$$

$$= \int_0^M \frac{G\,M'}{r}\,\mathrm{d}M'\ . \tag{2.7}$$

[(1)]The notation used in this thesis is (r, ϑ, φ) for spherical coordinates, and (R, φ, z) for cylindrical coordinates; this is noted in App. A alongside a list of the constants, abbreviations, and symbols used.

[(2)]For a detailed derivation, see for instance Prialnik (2010), or Landau & Lifschitz (2007) for a more general approach.

In the remaining integral, M depends on r; assuming ϱ to be uniform allows us to integrate Eq. (2.2) to

$$M = \frac{4\,\pi}{3}\,\varrho\,r^3\;; \tag{2.8}$$

hence, with $\mathrm{d}M/\mathrm{d}r = 4\,\pi\,r^2$ from Eq. (2.2),

$$E_{\mathrm{grav}} = -\int_0^r \frac{G}{r'}\cdot\frac{4\,\pi}{3}\,\varrho\,r'^{\,3}\cdot 4\,\pi\,\varrho\,r'^{\,2}\,\mathrm{d}r' = \tag{2.9}$$

$$= -\frac{16\,\pi^2}{15}\,G\,\varrho^2\,r^5\;. \tag{2.10}$$

Inserting Eqs. (2.5) and (2.10) into Eq. (2.4) yields

$$3\,N\,k_{\mathrm{B}}\,T = \frac{16\,\pi^2}{15}\,G\,\varrho^2\,r^5\;, \tag{2.11}$$

with

$$N = \frac{M}{\mu\,m_{\mathrm{H}}} \tag{2.12}$$

the number of particles, and $\mu\,m_{\mathrm{H}}$ the mean mass of one gas particle. Using Eq. (2.8), we can solve Eq. (2.11) for r:

$$r_{\mathrm{Jeans}} = \sqrt{\frac{15}{4\,\pi}\cdot\frac{k_{\mathrm{B}}}{G\,m_{\mathrm{H}}}\cdot\frac{T}{\mu\,\varrho}}\;, \tag{2.13}$$

$$\propto \sqrt{\frac{T}{\mu\,\varrho}} \tag{2.14}$$

Eq. (2.13) specifies the commonly found formula for the Jeans length, a more intricate definition for which was originally derived by Jeans (1902). It characterises the minimum volume that can contain material of mean density ϱ and temperature T without collapsing; so if T becomes too small or

$$\varrho = n\,\mu\,m_{\mathrm{H}} \tag{2.15}$$

too big, the region is no longer stable and collapses. For $T = 10\,\mathrm{K}$, $n = 10/\mathrm{cm}^3$ (typical values for a GMC environment, see Blitz, 1993),[(1)] and $\mu = 2.3$, Eq. (2.13) gives $r \approx 4\,\mathrm{pc} \simeq 8\cdot 10^5\,\mathrm{AU}$.[(2)]

Similarly, solving Eq. (2.11) for M (again using Eqs. 2.8 and 2.12) yields the Jeans mass (see e.g. Karttunen et al., 2007)

$$M_{\mathrm{Jeans}} = \sqrt{\left(\frac{5\,k_{\mathrm{B}}\,T}{G\,m_{\mathrm{H}}\,\mu}\right)^3\cdot\left(\frac{3}{4\,\pi\,\varrho}\right)}\;, \tag{2.16}$$

$$\propto \sqrt{\frac{T^3}{\mu^3\,\varrho}}\;, \tag{2.17}$$

that is the maximum (cloud) mass stable against collapse. With the same values as above, we obtain $M \approx 1.7\cdot 10^2\,\mathrm{M}_\odot$ ($M \approx 5.5\cdot 10^3\,\mathrm{M}_\odot$ for $T = 100\,\mathrm{K}$). Hence the gravitational collapse of (or within) a GMC impacts a large region, leading to the formation of many stars relatively close to each other (a stellar cluster, see e.g. Lada & Lada, 2003; Getman et al., 2006); this process is likely hierarchical (Hoyle, 1953), but not necessarily fully coeval (Herbig, 1962). Furthermore, winds emitted from the newly formed objects may change ϱ and thus limit star formation (see e.g. Shu et al., 1987, and references therein).

The stellar masses in these clusters can be described by the initial mass function (IMF), first formulated by Salpeter (1955) for $0.4 \le M_*\,[\mathrm{M}_\odot] \le 1.0$:

$$\xi(M_*) \propto M_*^{-1.35} \tag{2.18}$$

[(1)] Lada & Lada (2003) give larger values of $n = 10^4 ... 10^5/\mathrm{cm}^3$ for the core regions of a GMC, but for a basic order-of-magnitude estimate, the value used above should be sufficient. Alternatively, Karttunen et al. (2007) give values of $T = 100\,\mathrm{K}$ and $n = 1/\mathrm{cm}^3$, yet also specify a rough length scale of 10 pc for a collapsing cloud.

[(2)] Both 'AU' and 'au' as abbreviations for 'astronomical unit' are encountered in literature; in this thesis, we use the former merely because it corresponds to the standard setting of `astropy` (thus simplifying automated unit specifications in plots).

Many studies have since worked to refine this IMF and extend it to a larger range of M_* (see e.g. Kroupa, 2001; Villaume et al., 2017); there is however an undisputed trend of low-mass stars being more frequent than high-mass ones, as indicated by the negative exponent in Eq. (2.18) (see also e.g. Offner et al., 2014).

While stellar clusters may disperse after star formation, the initial material composition within one cluster is supposedly quite similar, and the initial evolution of the individual stellar systems happens in close vicinity to each other (see e.g. Parker et al., 2021b); yet it is not necessarily the same even within one and the same cluster (see e.g. Armitage, 2010). Furthermore, the individual systems may (often) consist of more than one star (see e.g. Duchêne & Kraus, 2013; Parker, 2020), but for this work, we will limit ourselves to investigating single-star systems.

On a per-system level, the gravitational collapse of material leads to the formation of a protostar (see e.g. Larson, 1969; Penston, 1969; Shu, 1977): The (gravitational) energy released from the dynamical infall of material is radiated away until the accreting core grows dense and hot enough to be opaque to its own radiation (see e.g. Prialnik, 2010). Once this core reaches hydrostatic equilibrium (see Eq. 2.3), it has become a protostar (see e.g. Karttunen et al., 2007; Prialnik, 2010). In this stage, there are two main groups of objects: Firstly, (low-mass) T-Tauri stars with $M_* < 2\,\mathrm{M}_\odot$, and secondly, (intermediate-mass) Herbig Ae/Be stars with $2 \lesssim M_*\,[\mathrm{M}_\odot] < 8$ (see e.g. Perez & Grady, 1997; Montesinos et al., 2009). This thesis will focus on T-Tauri stars because they are both more common (see Eq. 2.18) and more comparable to the solar system.

The protostar then contracts further during its pre-main-sequence phase; finally, when the core reaches a pressure high enough to start hydrogen fusion, the star enters the main sequence (MS) on the Hertzsprung-Russell (HR) diagram (Hertzsprung, 1911; Russell, 1914a,b).

2.2 Protoplanetary disks

During the formation of a protostar, the overall angular momentum

$$\mathcal{L} = R^2\, M\, \Omega \tag{2.19}$$

of its parent cloud (or rather filament, see André et al., 2014) must be conserved, with Ω the angular velocity of the material of mass M. So as the material is gravitationally pulled towards the star, its rotation becomes faster or angular momentum must be redistributed outwards. Furthermore, there is one dominating direction $\langle\hat{\mathcal{L}}\rangle$ for the angular momentum, which results from uniform rotation being the motion of least energy (Lynden-Bell & Pringle, 1974). Consequently, infall towards the star along $\langle\hat{\mathcal{L}}\rangle$ is less hindered. This leads to an initially spherical cloud flattening perpendicular to $\langle\hat{\mathcal{L}}\rangle$ (see e.g. Terebey et al., 1984; Armitage, 2010; Owen, 2016; Andrews, 2020), with most of the angular momentum being stored in the less massive far-out regions of the disk (see Lynden-Bell & Pringle, 1974, and Sect. 2.2.2.3). Thus, a protoplanetary disk is formed (also multiple systems may form, see e.g. Matsumoto & Hanawa, 2003), at least in the traditional picture; as summarised by Li et al. (2014), a magnetised (and not merely viscous) environment may significantly complicate this process (see also e.g. Li et al., 2011; Zhao et al., 2016).

2.2.1 Observations

Since reality should inform any modelling efforts (see Chap. 1), it is instructive to first consider the observationally determined properties of circumstellar disks. The first direct images, taken with the Hubble Space Telescope (HST), were presented by O'Dell et al. (1993) and O'Dell & Wen (1994).[(1)] At least since then, the community has been highly interested in gathering data about circumstellar disks; new instruments such as the Atacama Large Millimeter/submillimeter Array (ALMA) and the Very Large Telescope (VLT) have considerably facilitated that, for instance by providing first high-resolution images of disks (e.g. HL Tauri, see ALMA Partnership et al., 2015, reproduced in Fig. 2.1) or even a disk within a disk (e.g. the circumplanetary disk of PDS 70c, see Isella et al., 2019; Benisty et al., 2021). Before the arrival of these instruments, spectral energy distributions (SEDs), showing the wavelength-dependent flux $\lambda\, F_\lambda$, had been the main tracer for the presence of disks; a circumstellar disk and the resulting extinction change the shape of the curve for $\lambda\, F_\lambda$ (see e.g. the review by Andrews, 2015). Furthermore, studies had inferred disks from molecular lines (see e.g. Edwards et al., 1987; Basri & Bertout, 1993).

[(1)] Earlier data had already suggested the presence of a circumstellar mass distribution, but suffered from low resolution (see e.g. Beckwith et al., 1984; Beckwith & Sargent, 1993).

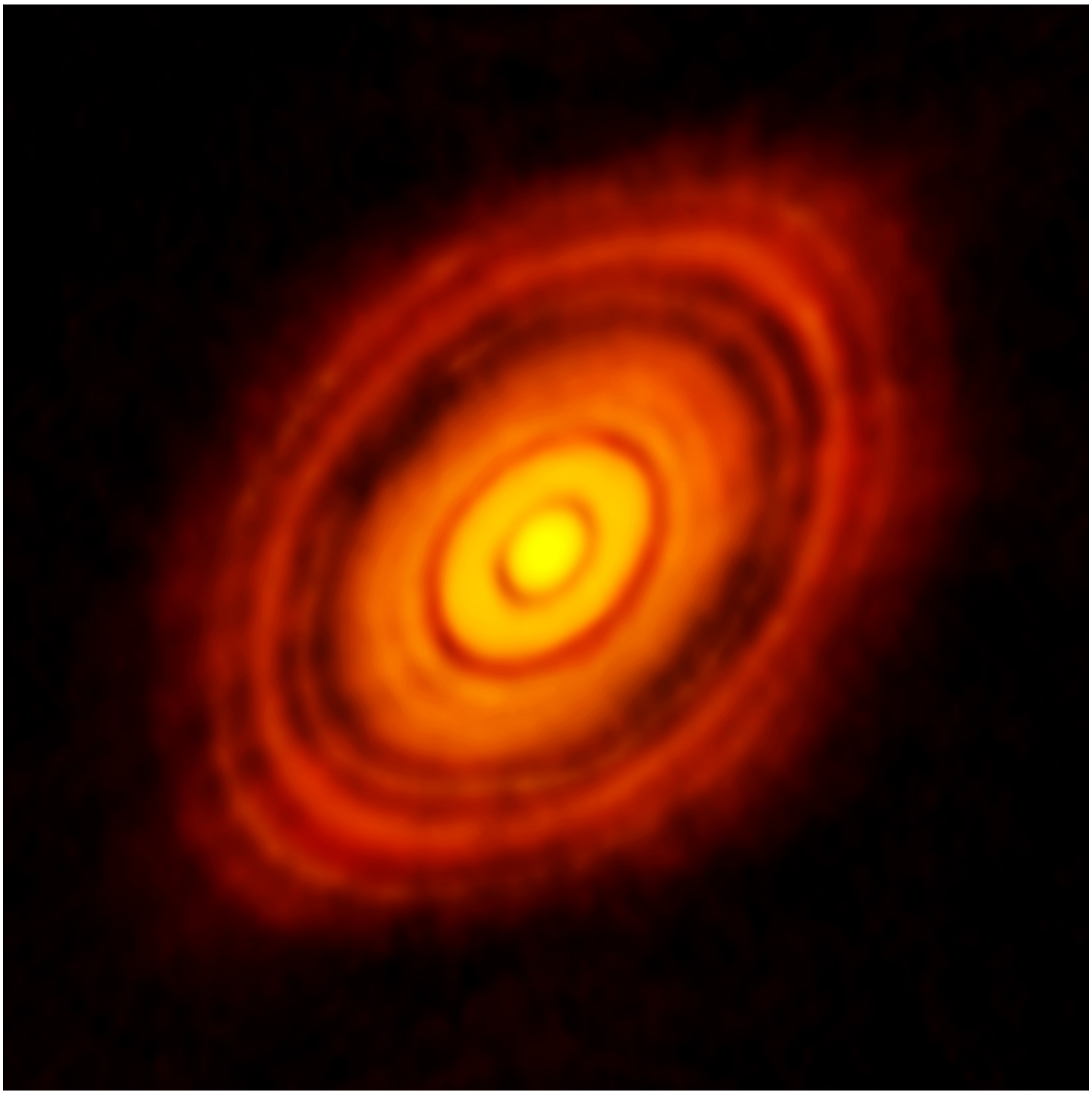

Figure 2.1: ALMA image of HL Tauri (HL Tau) at 1.28 mm (ALMA Partnership et al., 2015). The high resolution reveals a tremendous amount of substructure within the circumstellar disk, especially in comparison to previous HST images (see e.g. O'Dell et al., 1993).
Image credit: ALMA (ESO/NAOJ/NRAO)

2.2.1.1 Classification

While observations cannot track the evolution of individual systems due to the time frames involved, they allow for their classification; this can then be used to inform modelling efforts. A common classification scheme is based on the infrared (IR) luminosities of young stellar objects (see e.g. Greene et al., 1994); since temperatures vary along the radial extent of the disk, their structures can already be investigated via unresolved spectra (see e.g. Williams & Cieza, 2011).

Historically, a first classification of low-mass (T-Tauri) stars was proposed by Lada (1987), based on the spectral index α of an object,

$$\alpha := \frac{\mathrm{d}\log(\lambda\, F_\lambda)}{\mathrm{d}\log(\lambda)}\,, \tag{2.20}$$

with F_λ the flux density at wavelength λ. Three categories were then defined according to IR α (α_{IR}) values as (I) $0 < \alpha_{\mathrm{IR}} \lesssim +3$, (II) $-2 \lesssim \alpha_{\mathrm{IR}} \leq 0$, and (III) $-3 < \alpha_{\mathrm{IR}} \lesssim -2$ (Lada, 1987).[(1)] This initially purely data-driven model has since been refined by various works (see e.g. Williams & Cieza, 2011, and references therein); and based on observations of a young protostar, an additional class (0) was suggested by Andre et al. (1993). Kenyon & Hartmann (1995) confirmed the hypothesis of an underlying evolution

[(1)] Lada (1987) give the λ-range as $1 \leq \lambda\,[\mu\mathrm{m}] \leq 20$. Armitage (2010) and Williams & Cieza (2011) refine that to $2 \leq \lambda\,[\mu\mathrm{m}] \lesssim 25$.

of protostars through these classes. Furthermore, theoretical models of how the individual stages are interlinked were soon developed (see e.g. Adams et al., 1987).[(1)] Armitage (2010) and Williams & Cieza (2011) summarise the current understanding as follows:

Class 0: no features in α_{IR}
The protostar is deeply embedded in its surrounding local cloud, which is more massive than the star, which in turn is more massive than the forming disk ($M_{\text{cloud}} > M_* > M_{\text{disk}}$). This corresponds to the phase of gravitational collapse, which Evans et al. (2009a) estimate a lifetime of 0.1...0.16 Myr for.

Class I: $\alpha_{\text{IR}} > -0.3$
The star is still obscured by its enveloping cloud, but the mass ratio has shifted to $M_* > M_{\text{cloud}} \approx M_{\text{disk}}$, that is the star has gained a significant amount of mass. High-velocity outflows may be present, and the disk may start to be detectable.

Greene et al. (1994) introduced an additional (sub-)category of flat-spectrum sources; these cover $-0.3 < \alpha_{\text{IR}} < 0.3$, with $\alpha_{\text{IR}} > 0.3$ then indicating 'true' class-I objects. The flat-spectrum sources mark the transition from class-I to class-II objects. Evans et al. (2009a) estimated a median timeframe of about 0.44...0.54 Myr for the 'original' class-I stage, and an additional 0.35...0.40 Myr for the flat-spectrum phase.

Class II: $-1.6 < \alpha_{\text{IR}} < -0.3$
The envelope has been mostly accreted ($M_{\text{cloud}} \approx 0$), while the circumstellar disk still remains (and causes an IR excess), with M_{disk} a fraction of M_* (see Sect. 2.2.1.3). The star is clearly visible. Accretion from the disk onto the star induces an excess in Hα and ultraviolet (UV) emission.[(2)]

Class III: $\alpha_{\text{IR}} < -1.6$
The circumstellar disk has mostly disappeared ($M_{\text{disk}} \lll M_*$), and accretion has (mostly) ceased. Hence the IR excess is minuscule; the object can still be differentiated from 'normal' (MS) stars by stronger X-ray emission. Furthermore, a debris disk may still be present.

Williams & Cieza (2011) do however point out that on its own, this classification may produce misleading results; for instance, when seen edge-on, the disk of a class-II object would obscure the protostar, hence giving the impression of a class-I object. And indeed, it seems that fewer disks appear edge-on (i.e. highly inclined) than expected from purely geometrical considerations (Wolff et al., 2017).

Concurrently, there is the notion of classical T-Tauri stars (CTTS) and weak-lined T-Tauri stars (WTTS); for instance, according to Telleschi et al. (2007) and Williams & Cieza (2011), the former have strong Hα and UV emission, indicating ongoing accretion from the disk onto the star, while the latter do not. Accordingly, although they do not necessarily fully overlap, the terms 'CTTS' and 'class II' are often used interchangably, as well as 'WTTS' and 'class III' (see e.g. Alexander et al., 2014).

2.2.1.2 Sizes

A recent review by Andrews (2020) gives (dust) disk sizes of $10 \lesssim R_{\text{disk, dust}}\,[\text{AU}] \lesssim 500$ from mm-observations of Tripathi et al. (2017), Andrews et al. (2018a), and Hendler et al. (2020); these values represent the radius encircling 90% of the observed luminosity (an approach which may be slightly skewed, see Rosotti et al., 2019; Tazzari et al., 2021). Different birth environments have different mean values for $R_{\text{disk, dust}}$ (see e.g. Hendler et al., 2020), underlining that no two GMC environments are identical. Furthermore, μm observations suggest potentially larger disk sizes at smaller wavelengths (i.e. dust sizes, see Andrews, 2020).

From (gas-tracing) CO line emissions, Ansdell et al. (2018) extracted $70 \lesssim R_{\text{disk, gas}}\,[\text{AU}] \lesssim 500$ (similar to the values of Dutrey et al., 2007, for instance); their data may be limited by the instrumentation available (Andrews, 2020). Yet in all their cases, $R_{\text{disk, dust}} < R_{\text{disk, gas}}$, with Andrews (2020) and Sanchis et al. (2021) finding a (tentative) linear relation between $R_{\text{disk, dust}}$ and $R_{\text{disk, gas}}$. While Andrews et al.

(1) The terminology seems to have caused some confusion due to various interpretations, resulting in the release of a 'diskionary' (Evans et al., 2009b).

(2) Hα emission, corresponding to $\lambda \simeq 656.3$ nm, is the Balmer-α line, that is the transition of a hydrogen atom's electron from its third- to second-lowest energy level ($3 \to 2$); it is used to trace (hot) hydrogen (i.e. gas) distributions (see e.g. Karttunen et al., 2007).

(2018a) have furthermore reported a positive correlation between $R_{\rm disk,\,dust}$ and M_*, the results of Hendler et al. (2020) indicate that this may be limited to some select star-forming regions.

In terms of vertical extent, typical gas disk scale heights (for the definition, see Sect. 2.2.2.2) are estimated at $5 \lesssim H_{\rm gas}\,[\rm AU] \lesssim 17$ at $R = 100\,\rm AU$ (see e.g. Burrows et al., 1996; Stapelfeldt et al., 1998, 2003; Glauser et al., 2008; Wolff et al., 2017, 2021; Zhang et al., 2021, and Sect. 2.2.1.7).

2.2.1.3 Masses

The gas and dust masses of a disk ($M_{\rm disk,\,gas}$ and $M_{\rm disk,\,dust}$, respectively) can be taken as a first indication of its potential to form planets. Yet these quantities cannot be measured directly; research into how to most reliably determine them from observational data is still ongoing (see e.g. Franceschi et al., 2022). Dust disk masses are computed from F_λ in the millimeter region via (see e.g. Bergin & Williams, 2018)

$$M_{\rm disk,\,dust} = \frac{F_\lambda\, d^2}{\kappa_\lambda\, B_\lambda(T_{\rm dust})}\ , \tag{2.21}$$

with d the distance of the object from the observer, κ_λ the opacity at wavelength λ, and $B_\lambda(T_{\rm dust})$ the Planck spectral radiance, (see e.g. Karttunen et al., 2007)

$$B_\lambda(T) = \frac{2\,h\,c^2}{\lambda^5} \cdot \frac{1}{\exp\left(\frac{h\,c}{\lambda\,k_{\rm B}\,T}\right) - 1}\ , \tag{2.22}$$

with h the Planck constant, and c the speed of light.(1) Despite the various uncertainties in the quantities in Eq. (2.21), $M_{\rm disk,\,dust}$ is simpler to derive than its gas counterpart (see e.g. Bergin & Williams, 2018; Veronesi et al., 2019). But the gas dominates the total disk mass budget (see e.g. Ansdell et al., 2016), so an additional conversion factor from $M_{\rm disk,\,dust}$ to $M_{\rm disk,\,gas} \approx M_{\rm disk}$ is needed, suitably labelled the dust-to-gas ratio

$$\varepsilon_{\rm dtg} := \frac{M_{\rm disk,\,dust}}{M_{\rm disk,\,gas}}\ . \tag{2.23}$$

Commonly, $\varepsilon_{\rm dtg}$ is estimated at 0.01 (see e.g. Wyatt, 2008; Andrews et al., 2009; Bergin et al., 2013; Manara et al., 2016; Owen, 2016; Miotello et al., 2017; Zhang et al., 2021), the value for the ISM (Bohlin et al., 1978). It may however be higher than that for some disks (see e.g. Ansdell et al., 2016; Miotello et al., 2017), especially if they have had time to evolve (see e.g. Soon et al., 2019, and references therein); and it most likely evolves over time (see e.g. Birnstiel & Andrews, 2014; Franceschi et al., 2022). This matches reports that disk masses inferred from $M_{\rm disk,\,dust}$ significantly differ from ones inferred from $M_{\rm disk,\,gas}$ (see e.g. Manara et al., 2016; Bergin & Williams, 2018; Sellek et al., 2020b), which could for instance be caused by a depletion of gas tracers (see e.g. Bergin & Williams, 2018; Zhang et al., 2021; Trapman et al., 2022).

Observations for a certain dust size (i.e. radius) a assume an underlying distribution of sizes $n(a)$ to compute $M_{\rm disk,\,dust}$. Usually, the Mathis et al. (1977, MRN) distribution is employed (see also Mathis, 1990),

$$n(a) \propto a^{-\eta_{\rm MRN}}\ , \tag{2.24}$$

with $\eta_{\rm MRN} = 3.5$, such that the number of grains within a size interval $[a_1; a_2]$ is

$$N(a_1, a_2) \propto \int_{a_1}^{a_2} n(a)\, {\rm d}a \propto a^{-2.5}\Big|_{a_1}^{a_2}\ . \tag{2.25}$$

The exponent in Eq. (2.24) may vary depending on what physical processes are going on in the disk (see e.g. Birnstiel et al., 2011); for instance, Ricci et al. (2010a,b) deduce a tentative $2.5 \lesssim \eta \lesssim 3$ from observational data. In addition, we know from Eq. (2.8) that the mass of a (spherical) dust grain scales as $m \propto a^3$, so as long as $\eta_{\rm MRN} < 4$, the choice of the upper limit will strongly impact the overall mass budget $M_{\rm dust} = \int_{a_1}^{a_2} n(a)\, m(a)\, {\rm d}a$. With these caveats, Andrews (2020) combines several recent surveys to find $0.1 \lesssim M_{\rm disk,\,dust}\,[\rm M_\oplus] \lesssim 550$, with smaller values from this range being much more frequent (see also e.g. van Terwisga et al., 2020). As $\rm M_\odot \simeq 3.3 \cdot 10^5\, M_\oplus$, this indicates that $M_{\rm disk} = M_{\rm disk,\,gas} + M_{\rm disk,\,dust} \ll M_*$ as would be expected.(2)

(1) For replacing λ with $\nu = c/\lambda$ in Eq. (2.22), use $\int_{\lambda_1}^{\lambda_2} B_\lambda\, {\rm d}\lambda \overset{!}{=} \int_{\nu_2}^{\nu_1} B_\nu\, {\rm d}\nu = -\int_{\lambda_1}^{\lambda_2} B_\nu\, \frac{{\rm d}\nu}{{\rm d}\lambda}\, {\rm d}\lambda$, as for $\lambda_1 < \lambda_2$, $\nu_1 = c/\lambda_1 > \nu_2 = c/\lambda_2$ (see e.g. Karttunen et al., 2007).

(2) Commonly, $M_{\rm disk,\,gas} \gg M_{\rm disk,\,dust}$ and thus $M_{\rm disk} \simeq M_{\rm disk,\,dust}/\varepsilon_{\rm dtg}$ is assumed (see e.g. Andrews, 2015; Manara et al., 2016).

$M_{\rm disk}$ may, and is often thought to, correlate with M_*. For the dust mass, $M_{\rm disk,\,dust} \propto M_*^{1\ldots1.9}$ is commonly found (see e.g. Ansdell et al., 2016; Pascucci et al., 2016; Bergin & Williams, 2018); concerning the overall $M_{\rm disk}$, an estimate of $M_{\rm disk} \simeq 10^{-2}\, M_*$ has been reported by various studies (see e.g. Andrews & Williams, 2005, 2007b), and is often employed in modelling (see e.g. Alexander et al., 2014).[(1)]

2.2.1.4 Mass-accretion rates

T-Tauri stars continue to accrete mass from their disks after the gravitational collapse of the protostellar core; this process is thought to be driven by angular momentum exchange along magnetic fieldlines, but is still not fully understood (for a review, see e.g. Hartmann et al., 2016). Observationally, the corresponding mass-accretion rate $\dot{M}_{\rm acc}$ is estimated via (see e.g. Calvet et al., 2004; Clarke & Pringle, 2006; Natta et al., 2006; Gatti et al., 2008)

$$\dot{M}_{\rm acc} \simeq \frac{L_{\rm acc}\, R_*}{G\, M_*} \,, \tag{2.26}$$

where the accretion luminosity $L_{\rm acc}$, derived from line emissions (see e.g. Hartmann et al., 1998; Natta et al., 2006), carries various uncertainties (see e.g. Gatti et al., 2008).[(2)] The general range of values reported is $10^{-12} \lesssim \dot{M}_{\rm acc}\,[{\rm M}_\odot/{\rm yr}] \lesssim 10^{-6}$ (see e.g. Basri & Bertout, 1993; Blum & Wurm, 2008; Hartmann et al., 2016; Flaischlen et al., 2021, and references therein). Values not too close to the upper end of this range appear to be more frequent (see also Muzerolle et al., 2003a; Gatti et al., 2008; Alexander et al., 2014); Hartmann et al. (2016) give a rough estimate of $\dot{M}_{\rm acc} \approx 10^{-8}\,{\rm M}_\odot/{\rm yr}$ for low-mass T-Tauri stars.

For intermediate stellar masses ($1.5 \lesssim M_*\,[{\rm M}_\odot] \lesssim 4$), Calvet et al. (2004) reported a somewhat higher $\dot{M}_{\rm acc} \approx 3 \cdot 10^{-8}\,{\rm M}_\odot/{\rm yr}$. This matches the general consensus that $\dot{M}_{\rm acc}$ correlates with M_*; early works quantified the relation as $\dot{M}_{\rm acc} \propto M_*^2$, whereas more recent observational analyses tend towards $\dot{M}_{\rm acc} \propto M_*^{1.5\ldots1.9}$ at least for $M_* \lesssim 1\,{\rm M}_\odot$ (see Li & Xiao, 2016, and references therein).[(3)] Furthermore, data suggests a anti-correlation between $\dot{M}_{\rm acc}$ and stellar age (see e.g. Hartmann et al., 1998; Gatti et al., 2008).

Low-mass objects such as FU Orionis and EX Lupi furthermore undergo accretion (and thus luminosity) bursts (see e.g. Herbig, 1966, 1977, 1989), with $\dot{M}_{\rm acc}$ as high as $10^{-4}\,{\rm M}_\odot/{\rm yr}$ (see also e.g. Königl & Pudritz, 2000, and references therein). The reasons for these outbursts are still under investigation (see e.g. Audard et al., 2014; MacFarlane et al., 2019; Vorobyov et al., 2020); they may be related to mass accretion in the earliest phases of stellar evolution (Zakri et al., 2022), or the dust disk in general (see e.g. Bozhinova et al., 2016; Dodin et al., 2019; Gárate et al., 2019).

2.2.1.5 X-ray luminosities

Before nuclear fusion starts inside the star, one might assume that accretion shocks produce the main part of the stellar high-energy (X-ray) radiation (see e.g. Calvet & Gullbring, 1998). However, from studying a nearly complete sample of young stars in the Orion Nebula Cluster taken from the Chandra Orion Ultradeep Project (COUP, Getman et al., 2005), Preibisch et al. (2005) found that the mean accretion luminosities $L_{\rm acc}$ are notably smaller than the observed X-ray luminosities $L_{\rm X}$ (see also Güdel et al., 2007, and references therein). So while accretion flows – in combination with magnetic effects – may be responsible for a part of the soft X-ray spectrum (see e.g. Güdel et al., 2007; Güdel & Telleschi, 2007; Telleschi et al., 2007), they cannot provide enough X-ray emission on their own; alternative sources may be solar-like coronal structures and magnetic energy released from the field lines (Preibisch et al., 2005).

In addition, accreting protostars are less bright than non-accreting ones (Preibisch et al., 2005; Feigelson et al., 2007, and references therein); Preibisch et al. (2005) speculate that this may be due to the former having higher surface densities which lead to lower temperature spikes from reconnections of magnetic field lines, or due to structural changes because of the accretion flows. Indeed, simulations have shown that coronal X-ray emissions can modulate the accretion process by means of photoevaporative winds (see Sect. 2.3.3), which starve the accretion flow (Drake et al., 2009); thus, the absence of accretion would mandate higher X-ray fluxes as observed (see also Owen et al., 2011b). Further data analysis by Flaischlen et al. (2021), yielding a slight anti-correlation between $\dot{M}_{\rm acc}$ and $L_{\rm X}$, has corroborated this view.

[(1)] Bate (2018) suggest a higher value of $0.1 \lesssim M_{\rm disk}\,[M_*] \lesssim 1$ based on numerical models.

[(2)] Due to these uncertainties, a pre-factor of order unity, which is sometimes found in literature (often $1/0.8 = 1.25$; see e.g. Hartmann et al., 1998; Font et al., 2004; Manara et al., 2013; Hartmann et al., 2016), has been disregarded in Eq. (2.26).

[(3)] In addition, Manara et al. (2016) have suggested a correlation between $M_{\rm disk,\,dust}$ and $\dot{M}_{\rm acc}$.

Numbers-wise, measurements indicate $10^{27.5} \lesssim L_\mathrm{X}\,[\mathrm{erg/s}] \lesssim 10^{32}$ for young stars (see Feigelson & Montmerle, 1999; Preibisch et al., 2005; Feigelson et al., 2007; Bhatt et al., 2013; Preibisch et al., 2014; Flaischlen et al., 2021; Getman et al., 2022). Flares of up to $L_\mathrm{X} \lesssim 10^{34}$ erg/s have been detected (see e.g. the analysis of Chandra surveys by Getman & Feigelson, 2021); these are most likely not due to star-disk interactions (see e.g. Getman et al., 2021), but could indicate variations in the structure of the inner disk (see e.g. Feigelson et al., 2007; Espaillat et al., 2014; Gárate et al., 2019; Petrov et al., 2019), and additionally may well impact disk evolution.

In relative terms, L_X can be compared to the bolometric luminosity L_bol; the upper limit is given by the saturation limit of $L_\mathrm{X}/L_\mathrm{bol} \lesssim 10^{-3}$ (see e.g. Fleming et al., 1989). For pre-main-sequence objects, commonly $L_\mathrm{X}/L_\mathrm{bol} \approx 10^{-3.6}$ is found (see e.g. Flaccomio et al., 2003; Preibisch et al., 2005; Bhatt et al., 2013); the exact value may vary between classical and weak T-Tauri stars (Telleschi et al., 2007), that is depending on the state of the circumstellar disk. Furthermore, since $L_\mathrm{X}/L_\mathrm{bol} > 10^{-5}$, T-Tauri stars have an X-ray luminosity which is significantly higher than the solar value of $(L_\mathrm{X}/L_\mathrm{bol})_\odot \simeq 10^{-6.5}$ (Preibisch et al., 2005). This can be used to observationally distinguish between MS and pre-MS objects (see also e.g. Getman et al., 2022).

In relation to the stellar mass, L_X and $L_\mathrm{X}/L_\mathrm{bol}$ both increase with M_* (see e.g. Preibisch et al., 2005). Concerning time evolution, Preibisch & Feigelson (2005) retrieved $L_\mathrm{X} \propto t_*^{-1/3}$ for the first $\approx 10\,\mathrm{Myr}$ of (proto)stellar age t_*, indicating only little decrease during this period (see also Getman et al., 2022).

2.2.1.6 Lifetimes

As already alluded to in Sect. 2.2.1.1, there is an evolutionary process going on from the initial collapse of the parent cloud to the eventual dispersal of the circumstellar disk. This also becomes obvious when considering a simplistic system with $M_* = 1\,\mathrm{M}_\odot$, $M_\mathrm{disk} \approx 0.01\,\mathrm{M}_\odot$ (see Sect. 2.2.1.3), and $\dot{M}_\mathrm{acc} \approx 10^{-8}\,\mathrm{M}_\odot/\mathrm{yr}$ (see Sect. 2.2.1.4) – it would dissipate within 1 Myr, just a tiny fraction of the overall lifetime of the (disk-less) solar system. While we will take a closer look at models for the physical processes involved in Sect. 2.2.2, observational data can be used to establish constraints on the time frame for disk evolution and dispersal.

A first systematic study of disk lifetimes by Haisch et al. (2001), based on data from several young clusters with ages $0.3 \lesssim t_\mathrm{cluster}\,[\mathrm{Myr}] \lesssim 30$, yielded a mean disk lifetime of $t_\mathrm{disk} \approx 6\,\mathrm{Myr}$ independent of M_*.(1) Since then, this value has been refined in various works; for instance, Mamajek (2009) parametrised the disk fraction for stars with $M_* < 2\,\mathrm{M}_\odot$ within a cluster as

$$f_\mathrm{disk} = f_0 \cdot \exp\left(-\frac{t}{\tau_\mathrm{disk}}\right) , \tag{2.27}$$

with an e-folding time of $\tau_\mathrm{disk} \simeq 2.5\,\mathrm{Myr}$, and assuming that every star is born with a disk ($f_0 = 1$).

Amongst many others, Ribas et al. (2014) performed an extensive analysis of multi-wavelength data from 22 clusters with $1 \lesssim t_\mathrm{cluster}\,[\mathrm{Myr}] < 100$. They found that disks persist longer at longer wavelengths, with $\tau_\mathrm{disk} \approx 2.3\,\mathrm{Myr}$ for $\lambda \approx 4\,\mu\mathrm{m}$, and $\tau_\mathrm{disk} \approx 5\,\mathrm{Myr}$ at $\lambda \approx 23\,\mu\mathrm{m}$; furthermore, they suggested different evolutionary timescales for the (faster) inner and (slower) outer disk regions. Richert et al. (2018) extended and refined the data analysis even more, evaluating 69 clusters with $t_\mathrm{cluster} \lesssim 5\,\mathrm{Myr}$, retrieving $\tau_\mathrm{disk} \approx 2.4...5.0\,\mathrm{Myr}$ depending on the evolutionary model subsumed; this highlights the importance of the underlying assumptions. So while the exact values differ between individual investigations (of which many more have been performed), the general trend of disk lifetimes on the order of $t_\mathrm{disk} \lesssim 10\,\mathrm{Myr}$ persists throughout the literature (see also e.g. Ercolano & Pascucci, 2017, and references therein).

A particular phenomenon is presented by the so-called 'Peter Pan disks', a term coined by Silverberg et al. (2020) to describe old systems ($t_\mathrm{disk} \gtrsim 20\,\mathrm{Myr}$) around low-mass stars which still have a gas accretion signature. It is still unclear whether their long lifetime merely appears as an oddity due to earlier observational constraints, or whether there are particular physical properties – like stellar mass (Nakatani et al., 2021) – or processes – like a low-radiation environment (Wilhelm & Portegies Zwart, 2022), or giant planets carving a gap which conserves the outer disk even throughout the MS phase (Kluska et al., 2022) – that render these protoplanetary disks long-lived (Silverberg et al., 2020).

2.2.1.7 Substructure

ALMA has enabled high-resolution mm-imaging of protoplanetary disks such as HL Tauri (ALMA Partnership et al., 2015, see Fig. 2.1) and TW Hydrae (Andrews et al., 2016, see Fig. 2.2). Both of those disks

(1) Earlier studies of individual clusters do exist; they yielded comparable, yet usually less confined results (see e.g. Strom et al., 1989; Skrutskie et al., 1990).

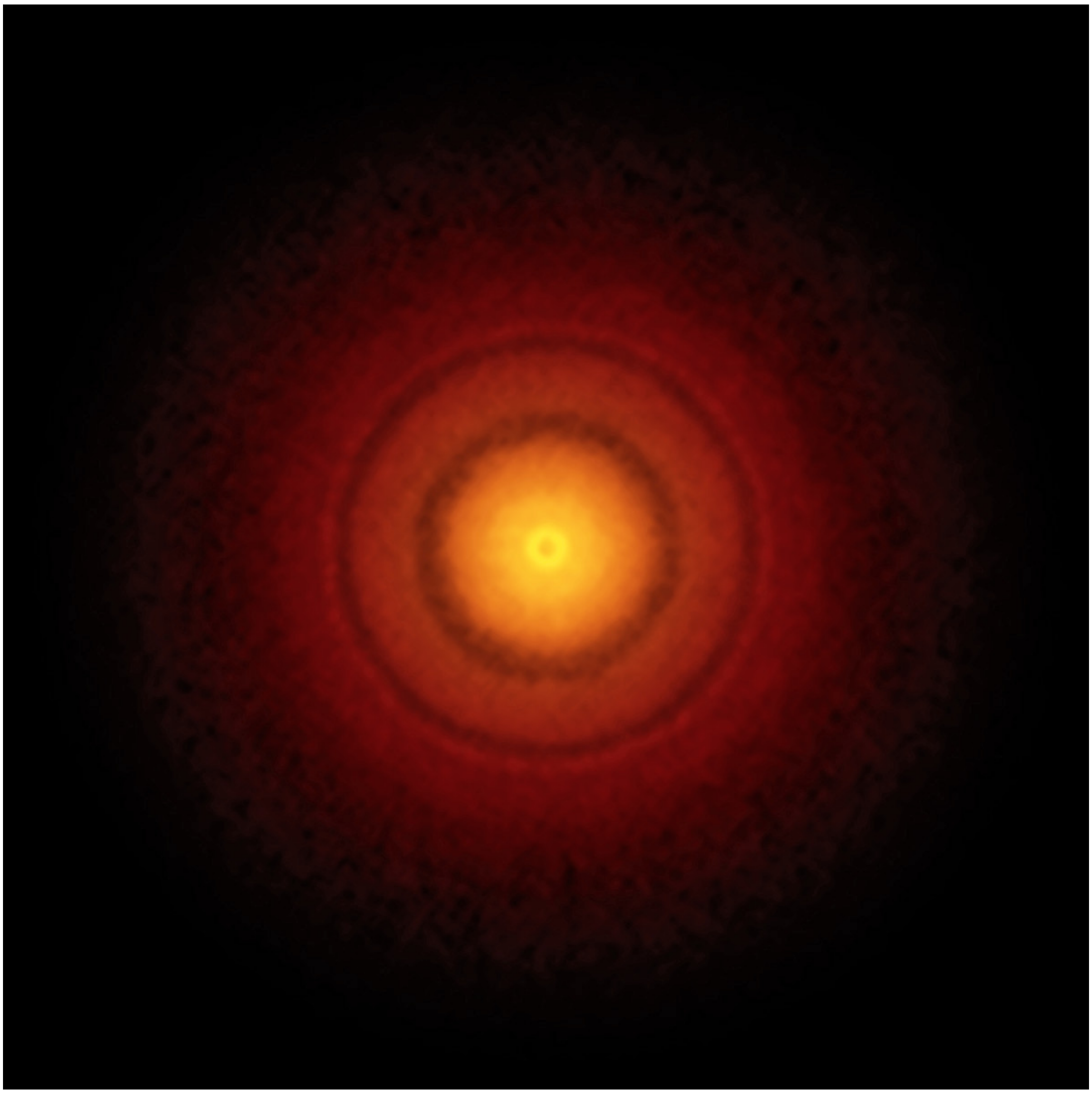

Figure 2.2: ALMA image of TW Hydrae (TW Hya) at $\lambda = 870\,\mu\text{m}$ (Andrews et al., 2016). Its face-on inclination as well as comparatively small distance to Earth ($\approx 54\,\text{pc}$, see van Leeuwen, 2007; Weinberger et al., 2013) make it a very suitable candidate for observations. As it is not depleted of gas (see e.g. Bergin et al., 2013) despite its age of about 10 Myr (Weinberger et al., 2013), an in-depth study of this system may also give implications as to the physics impacting the disk evolution. This high-resolution image shows axisymmetric and concentric rings at several and several ten AU.
Image credit: S. Andrews (Harvard-Smithsonian CfA); B. Saxton (NRAO/AUI/NSF); ALMA (ESO/NAOJ/NRAO)

exhibit clear structures such as rings and gaps (which may be asymmetrical, see e.g. Casassus, 2016, and references therein) –, in other words, a wealth of intricate substructures; these appear to be common (see e.g. Jennings et al., 2022). Substructures clearly differ between individual disks; they are highly likely to be impacted by, and in turn impact, the evolution of the disk (see e.g. Andrews, 2020).

Disks with higher masses are more likely to exhibit substructure (van der Marel et al., 2016b). Furthermore, this substructure can vary between different tracers for one and the same disk (see e.g. Cleeves et al., 2016; Öberg et al., 2021), which may be interpreted as a sign of ongoing evolutionary processes (see e.g. Facchini et al., 2017; Villenave et al., 2019). A non-exclusive list of radial substructures from many different observations has recently been compiled by Andrews (2020); they divide them into four categories:

Cavity and ring: Fully transitional disks (TDs) with a depleted cavity between the star and the disk (see e.g. the reviews by Espaillat et al., 2014; Casassus, 2016), indicating inside-out dispersal of the disk (see e.g. Ercolano et al., 2011; Koepferl et al., 2013; Ercolano et al., 2015). This gap is mostly cleared of gas, and (almost) entirely devoid of dust (see e.g. Pérez et al., 2015; van der Marel et al., 2016a, 2018).[(1)] It is usually thought to be a sign of disk age (see e.g. Ercolano & Pascucci, 2017; van der Marel et al., 2019a); based on IR data (see Sect. 2.2.1.1), already Strom et al. (1989) brought up the idea that an inner cavity may mark a transitional phase in the evolution of the circumstellar disk (from a massive to a low-mass structure, as they put it; see also e.g. Skrutskie et al., 1990).

The strongly reduced densities within the inner cavity entail a pressure maximum at the gap edge which traps dust grains, resulting in a bright and narrow ring at said gap edge. The cavity itself usually covers some tens of AU in radius, but this may very well be due to instrument limitations and hence an incomplete sample of systems. Depending on the exact nature of the hole, $\dot{M}_{\rm acc}$ can either stay similar to pre-transitional values (see e.g. Manara et al., 2014; Alcalá et al., 2017), or decrease by at least an order of magnitude (see e.g. Espaillat et al., 2012; Kim et al., 2013; Najita et al., 2015). Since several disks with $\dot{M}_{\rm acc} \gg 0$ have been encountered, the observed cavities may not be fully devoid of material (see e.g. Pinilla et al., 2012b, and references therein).[(2)]

Roughly 10% of all observed circumstellar disks exhibit an inner cavity, with this fraction increasing with cluster age (see e.g. Currie & Sicilia-Aguilar, 2011; Espaillat et al., 2014; van der Marel et al., 2018, and references therein); this indicates that this evolutionary stage is relatively short-lived (see e.g. Luhman et al., 2010).

Rings and gaps: A concentric, azimuthally symmetric pattern of brightness peaks (rings) and dips (gaps) in comparison to a hypothetical primordial profile, as for instance seen in Fig. 2.2. One example of a disk with many rings is AS 209 (Guzmán et al., 2018); conversely, for instance, V883 Orionis is an object with just one brightness dip separating the inner and outer regions of the disk (Cieza et al., 2016). Huang et al. (2018) showcase many more examples from the Disk Substructures at High Angular Resolution Project (DSHARP, Andrews et al., 2018b); there is a wide variety of ring-and-gap patterns, which can emerge at any r, and also already quite early on (Segura-Cox et al., 2020). In terms of dust concentration, Pinte et al. (2016) have estimated a significantly enhanced $\varepsilon_{\rm dtg} \approx 0.2$ for the rings of HL Tauri (instead of the usual base value of 0.01, see Sect. 2.2.1.3).

Arcs: In contrast to rings, arcs only cover parts of the azimuth (φ), introducing brightness asymmetries. For example, HL Tauri exhibits a few partially ring-like structures, that is arcs (see Fig. 2.1). Furthermore, Garufi et al. (2018) lists the shadows produced by rings, arcs, or planets as an explicit feature.

Spirals: Just like spiral galaxies, circumstellar disks may have spiral arms; they appear to be more frequent around multiple-star systems. The spiral structure itself can take on a variety of shapes (see e.g. Muto et al., 2012; Akiyama et al., 2016; Pérez et al., 2016; Benisty et al., 2017; Monnier et al., 2019; Andrews, 2020; Muro-Arena et al., 2020; Casassus et al., 2021; Wölfer et al., 2021).

Another feature are snowlines, that is the condensation fronts of specific materials at which these transition between a gaseous and an icy composition (see e.g. Lewis, 1974; Cieza et al., 2016; Öberg et al., 2021); they may intricately affect disk evolution (see e.g. Cieza et al., 2016; Drążkowska & Alibert, 2017). Additionally, as already noted to in Sect. 2.2.1.2, the radial distributions of the gas and the various dust species are not necessarily the same (see also e.g. Akiyama et al., 2016; Pinte et al., 2016; Villenave et al., 2019, 2020).

Moving on from their radial layout, disks can differ in their vertical structure, too (see e.g. Andrews, 2020); this includes misalignments of an inner and outer disk as well as warps and consequential disk shadowing (see e.g. Marino et al., 2015; Casassus et al., 2018; Sai et al., 2020). The vertical temperature (or velocity) structure is not constant; for the gas, this has been shown for instance by CO observations (see e.g. Dartois et al., 2003; Rosenfeld et al., 2013; Pinte et al., 2018). By using different wavelengths, different gas (and dust) regions or layers of a disk (such as the cold midplane, i.e. $z \simeq 0$, and heated surfaces) can be traced, also in terms of densities (see e.g. Dullemond et al., 2007; Rigliaco et al., 2013;

[(1)] Dust remnants close to the star have been found, however (see e.g. Benisty et al., 2010; Espaillat et al., 2010; Pinilla et al., 2019, 2021); it is still unclear whether the corresponding disks present special cases (such as a distinct population of long-lived disks proposed by Owen & Clarke, 2012).

[(2)] Michel et al. (2021) suggest the existence of two distinct types of disk dispersal, depending on the amount of substructure.

Dutrey et al., 2017; Rab et al., 2017; Pinte et al., 2018; Podio et al., 2020; Doi & Kataoka, 2021; Flores et al., 2021; Law et al., 2021). A vertical variation of gas properties, which may be partially caused by radial substructures such as rings, has been corroborated by data from the recent Molecules with ALMA at Planet-forming scales (MAPS, Öberg et al., 2021) survey (Law et al., 2021). Dust has been measured to be settled towards the disk midplane, more so at larger grain sizes (see e.g. Pinte et al., 2016; Villenave et al., 2019, 2020; Wolff et al., 2021), although exceptions to the rule exist (Rich et al., 2021).

2.2.1.8 Planets

A star is an object that is (or rather was) massive enough to start nuclear fusion processes in its core (see e.g. Prialnik, 2010); however, not all objects in space will attain masses high enough to supply this kind of internal pressure. Thus, planets can be seen as failed stars. More accurately, according to Resolution 5A of the IAU General Assembly (2006), a planet is a celestial body that is in orbit around the Sun, has sufficient mass for its self-gravity to overcome rigid body forces so that it assumes a hydrostatic equilibrium (nearly round) shape, and has cleared the neighbourhood around its orbit. While this definition is intended for the solar system, there is no formal definition of the term 'exoplanet', which is used to describe planet-like objects not orbiting the Sun; but since the host star is the only difference between the two, we will be using the terms 'planet' and 'exoplanet' interchangeably.

As mentioned in Chap. 1, Mayor & Queloz (1995) have presented the first unambiguous detection of a planet orbiting a Sun-like star. Since then, well over 4000 exoplanet detections have been confirmed (see e.g. Gaudi et al., 2021; Exoplanet Team, 2022), the number steadily increasing (see also Thompson et al., 2018).[(1)] In terms of observational techniques, radial velocity, transits, microlensing, and direct imaging are commonly employed (see e.g. Armitage, 2010; Gaudi et al., 2021).[(2)]

It has been established that most stellar systems host at least one planet (see e.g. Cassan et al., 2012; Winn & Fabrycky, 2015), with less massive (rocky) planets being more common than (giant) ones (with a gaseous envelope) because the planetary mass distribution appears to be linked to the stellar mass distribution (see e.g. Howard et al., 2012; Suzuki et al., 2016a; Zhu & Dong, 2021, and Sect. 2.1). Furthermore, the initial mass budget of a disk determines whether giant planets can be formed at all (see e.g. van der Marel & Mulders, 2021). The properties of the planets have opened up a whole new field of research (see e.g. Helled et al., 2014; Madhusudhan et al., 2014; Laughlin & Lissauer, 2015; Heng & Marley, 2018; Madhusudhan, 2019, 2021), and their habitability is yet another topic of research (see e.g. Güdel et al., 2014; Madhusudhan et al., 2016; Dehant et al., 2019); nonetheless, Earth-like planets in the 'habitable zone' around other stars have already been detected, for instance by Quintana et al. (2014).[(3)]

While nowadays, it is commonly assumed that planets form from – or rather within – protoplanetary disks (see e.g. the reviews by Ercolano & Pascucci, 2017; Armitage, 2018; Bergin & Williams, 2018), free-floating planets, that is planets not currently gravitationally bound to a host star, have also been detected (see e.g.the recent discovery by Miret-Roig et al., 2022, and references within). Yet they seem to be comparatively rare (see e.g. Scholz et al., 2012); as summarised by Miret-Roig et al. (2022), their formation mechanism is still not entirely constrained, but dynamical ejection from a circumstellar disk is a definite option (see also Zhu & Dong, 2021).

2.2.2 Modelling

The question of how circumstellar disks evolve is intricately linked to that of how the solar system came to be the way it is today; various theoretical hypotheses have been formulated already in the 18th century (see Woolfson, 1993, and references therein), and been reworked and refined ever since (see e.g. Whipple, 1964; Parker, 2020; Lichtenberg et al., 2021). The more observational data are available (see Sect. 2.2.1), the more informed these modelling attempts can be. In general, there are two main approaches:

Detailed simulations: These may well represent the standard idea of an 'astrophysical simulation'. They are set up to intricately simulate the evolution of one particular system; many physical processes are accounted for at high resolution, resulting in large computational costs per simulation. This gives a detailed impression of one particular scenario (see e.g. Rodenkirch et al., 2021), but renders parameter

[(1)] As stated by Hinkel et al. (2021), the establishment of a comprehensive and continuously updated database on exoplanets and their host systems, while possibly tedious, would benefit a large community, and considerably simplify future work.

[(2)] The Kepler space telescope, via transit dimming detections, has contributed sizably to the current number of detections (see e.g. Borucki et al., 2010; Koch et al., 2010; Thompson et al., 2018).

[(3)] For a rather humorous take on the subject, see Pedbost et al. (2020).

investigations rather costly (see e.g. Mordasini et al., 2009). Nonetheless, these studies can be used to derive fundamental system properties (see e.g. Alexander et al., 2006a,b; Bai, 2016; Tamfal et al., 2018; Picogna et al., 2019; Gressel et al., 2020).

Population syntheses: Using a simplified – often one-dimensional – model, parameter space studies are performed with a large sample of simulated systems (see e.g. Benz et al., 2014). This avoids the main negative aspect of in-detail simulations, which is their high individual computational cost; of course, the model still needs to be physically valid despite the simplifications, so comparisons to 'full' simulations are important (see e.g. Monsch et al., 2021a). The resulting statistics of the generated systems can then be compared to observational data to better constrain the parameters investigated, and (probable) key processes can be deduced (see e.g. Ida & Lin, 2004; Mordasini et al., 2009; Ercolano & Rosotti, 2015; Bate, 2018; Monsch et al., 2019; Emsenhuber et al., 2021a,b; Zormpas et al., 2022).

2.2.2.1 Steady-state radial gas distribution

The main disk mass component is the gas (see Sect. 2.2.1.3). Assuming azimuthal symmetry, its radial distribution can be specified in terms of the surface density (see e.g. Birnstiel et al., 2010)

$$\Sigma_{\mathrm{gas}}(R) = \int_{-\infty}^{+\infty} \varrho_{\mathrm{gas}}(R, z)\,\mathrm{d}z\ . \tag{2.28}$$

Hayashi (1981) described the gas density distribution of the minimum-mass solar nebula (MMSN) as[(1)]

$$\Sigma_{\mathrm{gas}} = \Sigma_{\mathrm{gas},0}\, R^{-\gamma}\ , \tag{2.29}$$

with the free parameter γ, which they set to $\gamma = 1.5$. This (truncated) power law is often found in the literature due to its simplicity (see e.g. Dutrey et al., 2007; Dullemond et al., 2007; Fromang & Nelson, 2009; Drążkowska & Alibert, 2017; Tamfal et al., 2018), usually with $\gamma \approx 1$ as well as $\gamma \lesssim 1.5$ (see e.g. Andrews & Williams, 2007a; Birnstiel et al., 2016).

The similarity solutions of Lynden-Bell & Pringle (1974) are better suited to describe observational data because they have no sharp outer edge, but instead an exponential falloff towards large R (see e.g. Hughes et al., 2008). The time-independent formulation is (see e.g. Andrews et al., 2009, and Sect. 2.2.2.3)

$$\Sigma_{\mathrm{gas}} = \Sigma_{\mathrm{gas},0} \cdot \left(\frac{R}{R_c}\right)^{-\gamma} \cdot \exp\left[-\left(\frac{R}{R_c}\right)^{2-\gamma}\right]\ , \tag{2.30}$$

with

$$\Sigma_{\mathrm{gas},0} = (2-\gamma) \cdot \frac{M_{\mathrm{gas}}}{2\,\pi\, R_c^2} \tag{2.31}$$

a normalization factor, $M_{\mathrm{gas}} \equiv M_{\mathrm{disk,\,gas}}$, and R_c the characteristic (scaling) radius indicating the transition from power-law (for $R \lesssim R_c$) to exponential (for $R \gtrsim R_c$) falloff (see e.g. Birnstiel et al., 2016). This form of Σ_{gas} can only be employed if the (kinematic) viscosity of the system is time-independent and can be written as (see e.g. Hughes et al., 2008; Lodato et al., 2017)

$$\nu = \nu_0 \cdot \left(\frac{R}{R_c}\right)^{\gamma}\ , \tag{2.32}$$

with $\nu_0 = \mathrm{const.}$

Equating the gravitational pull of the star on a particle of mass m,

$$F_{\mathrm{grav}} = \frac{G\,M_*\,m}{r^2}\ , \tag{2.33}$$

with its centripetal force,

$$F_{\mathrm{cp}} = m\,\Omega^2\,r\ , \tag{2.34}$$

yields, for $m \ll M_*$, its orbital velocity at the midplane (where $r = R$):

$$\Omega_K = \sqrt{\frac{G\,M_*}{R^3}} \tag{2.35}$$

[(1)]The MMSN is the minimum disk mass required to form the planets, asteroids, and comets of the solar system (see e.g. Kuiper, 1956); Hayashi (1981) estimated it at $M_{\mathrm{MMSN}} \simeq 0.013\,\mathrm{M}_\odot$ (see also e.g. Desch, 2007).

Ω_K is the Keplerian angular velocity. For a steady-state disk, Pringle (1981) give the radial momentum equation

$$\frac{v_\varphi^2}{R} = v_R \cdot \frac{\partial\, v_R}{\partial\, R} + \frac{1}{\varrho_{\mathrm{gas}}} \cdot \frac{\partial\, P_{\mathrm{gas}}}{\partial\, R} + \frac{G\, M_*}{R^2} \; ; \tag{2.36}$$

assuming radial equilibrium, that is $\partial v_R / \partial R = 0$, this can be rewritten for the disk midplane as

$$\Omega_\varphi^2\, R = \frac{v_\varphi^2}{R} = \Omega_K^2\, R + \frac{1}{\varrho_{\mathrm{gas}}} \cdot \frac{\partial\, P_{\mathrm{gas}}}{\partial\, R} \; . \tag{2.37}$$

Since the gas pressure is highest close to the star, $\partial P_{\mathrm{gas}} / \partial R < 0$, which leads to $\Omega_\varphi < \Omega_K$. So the orbital speed of the gas is usually sub-Keplerian due to pressure support from the inside, but may become locally super-Keplerian in the case of pressure bumps (see also e.g. Armitage, 2010, 2015).

2.2.2.2 Steady-state vertical gas distribution

In a steady-state model, the disk is in vertical hydrostatic equilibrium. Neglecting the self-gravity of the disk (because $M_{\mathrm{disk}} \ll M_*$, see Sect. 2.2.1.3), Eq. (2.3) can be applied in vertical direction:

$$\frac{\mathrm{d}P_{\mathrm{gas}}}{\mathrm{d}z} = -\varrho_{\mathrm{gas}} \cdot \frac{G\, M_*}{R^2 + z^2} \cdot \cos(\vartheta) \tag{2.38}$$

For a thin disk, or at the disk midplane, $z \ll R$, $R \approx r$, and thus $\cos(\vartheta) = z/r \approx z/R$ (see e.g. Armitage, 2015).(1) Together with the isothermal sound speed

$$c_s = \sqrt{\frac{P_{\mathrm{gas}}}{\varrho_{\mathrm{gas}}}} \; , \tag{2.39}$$

this leads to

$$\frac{\mathrm{d}}{\mathrm{d}z} (c_s^2\, \varrho_{\mathrm{gas}}) = -\varrho_{\mathrm{gas}} \cdot \frac{G\, M_*}{R^3} \cdot z \; , \tag{2.40}$$

and in conjunction with Eq. (2.35) and the aforementioned assumption of isothermality to

$$c_s^2 \cdot \frac{\mathrm{d}}{\mathrm{d}z}\, \varrho_{\mathrm{gas}} = -\varrho_{\mathrm{gas}}\, \Omega_K^2\, z \; . \tag{2.41}$$

This, in turn, can be integrated to

$$\varrho_{\mathrm{gas}} = \varrho_{\mathrm{gas},0} \cdot \exp\left(-\frac{z^2}{2\, H_{\mathrm{gas}}^2} \right) \; , \tag{2.42}$$

using the vertical gas scale height (see e.g. Birnstiel et al., 2010)

$$H_{\mathrm{gas}} := \frac{c_s}{\Omega_K} \; , \tag{2.43}$$

which can also be expressed as a dimensionless quantity,

$$h_{\mathrm{gas}} := \frac{H_{\mathrm{gas}}}{R} \; . \tag{2.44}$$

The disk surface, that is the interface between the (relatively) high-density disk and the low-density regions above it, is typically located at several H_{gas} (see e.g. Ercolano & Pascucci, 2017; Wang et al., 2019; Booth & Clarke, 2021, and Sect. 2.3).

Eq. (2.42) indicates a Gaussian profile for the vertical distribution of the dust, centered around the midplane ($z = 0$). Integration of Eq. (2.42) according to Eq. (2.28) yields (see e.g. Armitage, 2015)

$$\varrho_{\mathrm{gas},0} = \frac{\Sigma_{\mathrm{gas}}}{\sqrt{2\,\pi}\, H_{\mathrm{gas}}} \tag{2.45}$$

for the scaling factor.

H_{gas} is likely not constant with radius. The simplest assumption would be a linear relation (i.e. $h_{\mathrm{gas}} = \mathrm{const}$). Yet already Kenyon & Hartmann (1987) argued that a (slightly) flared disk, that is a disk with $\partial h_{\mathrm{gas}} / \partial R > 0$, better matches observational data; disk flaring can also be motivated from theoretical considerations of the thermal structure of the disk (see e.g. Armitage, 2015).

(1) With gas scale heights of $\lesssim 20\,\mathrm{AU}$, the assumption of a thin disk may be an oversimplification, see Sect. 2.2.1.2. However, this is unlikely to significantly impact the solution for ϱ_{gas} (Armitage, 2015).

2.2.2.3 Viscous evolution of the radial gas distribution

In the model of Pringle (1981), a disk is a succession of interlinked, azimuthally symmetric annuli. For one annulus, its $\dot{\Sigma}_{\rm gas}$ is equal to the net influx from the neighbouring annuli; furthermore, the angular momentum of the system must be conserved (i.e. exchanged between the annuli via viscous coupling), and the central star can be considered as a point mass exerting the gravitational potential. The according ansatz reads (Pringle, 1981)

$$\frac{\partial\,\Sigma_{\rm gas}}{\partial\,t} = \frac{3}{R}\cdot\frac{\partial}{\partial R}\left[R^{1/2}\cdot\frac{\partial}{\partial R}\left(R^{1/2}\cdot\nu\cdot\Sigma_{\rm gas}\right)\right] \ . \tag{2.46}$$

Hartmann et al. (1998) give the corresponding similarity solution (from Lynden-Bell & Pringle, 1974); its common notation reads (see e.g. Lodato et al., 2017)

$$\Sigma_{\rm gas} = (2-\gamma)\cdot\frac{M_{\rm disk,gas,0}}{2\,\pi\,R_c^2}\cdot\left(\frac{R}{R_c}\right)^{-\gamma}\cdot\left(\frac{1}{\tau}\right)^{\frac{2.5-\gamma}{2-\gamma}}\cdot\exp\left[-\frac{1}{\tau}\cdot\left(\frac{R}{R_c}\right)^{2-\gamma}\right] \ , \tag{2.47}$$

with $M_{\rm disk,gas,0} \equiv M_{\rm disk,gas}(t=0)$,

$$\tau = 1 + \frac{t}{t_\nu} \tag{2.48}$$

a dimensionless time, and

$$t_\nu = \frac{R_c^2}{3\,(2-\gamma)^2\,\nu_0} \tag{2.49}$$

the viscous time. For $t = 0$, Eq. (2.47) is reduced to the steady-state solution of Eq. (2.30).

On a timescale much smaller than the viscous time, that is $t \ll t_\nu$, little evolution occurs as $\tau \approx 1$ (Hartmann et al., 1998). So in order for the total disk mass (Hartmann et al., 1998)

$$M_{\rm disk,gas} = \int_0^\infty \Sigma_{\rm gas}(R,t)\,\mathrm{d}R \tag{2.50}$$

$$= M_{\rm disk,gas,0}\cdot\tau^{-\frac{1}{2(2-\gamma)}} \ , \tag{2.51}$$

to decrease with time, $\gamma < 2$ is required (see e.g. Lodato et al., 2017); likewise, Eq. (2.47) would give (a non-physical) $\Sigma_{\rm gas} \leq 0$ for $\gamma \geq 2$.

This viscous spreading of the disk accounts for mass loss, or rather transport, only according to Eq. (2.47); other processes such as explicit accretion onto the host star are not accounted for (see e.g. Lodato et al., 2017). Nonetheless, the gas distribution following Eq. (2.47) will carry most of the mass towards $R = 0$, and most of the angular momentum towards $R \to \infty$ (see Lynden-Bell & Pringle, 1974; Pringle, 1981), with the boundary between the regions of inwards and outwards motion moving to larger R at later times (Hartmann et al., 1998). This scenario is dominated by the viscosity ν (Eq. 2.32, necessary for Eq. 2.49). ν can be expressed in terms of the dimensionless α-viscosity of Shakura & Sunyaev (1973) via (Pringle, 1981)

$$\nu = \alpha\,c_s\,H_{\rm gas} \ , \tag{2.52}$$

with $0 < \alpha \leq 1$.[(1)] For simulations, α is commonly chosen as a fixed value within $10^{-4} \lesssim \alpha \lesssim 10^{-2}$ (see e.g. Nakamoto & Nakagawa, 1994; Dullemond et al., 2007; Rafikov, 2017; Drążkowska & Dullemond, 2018; Booth & Ilee, 2019); recent results suggest values towards the lower end of this range (see e.g. Pinte et al., 2016; Flaherty et al., 2018, 2020; Sellek et al., 2020b; Zormpas et al., 2022). Moreover, α probably is constant neither in time, nor over R, nor for different disk components (see e.g. Shi & Chiang, 2014; Bai, 2016; Béthune et al., 2017; Flaherty et al., 2017; Flock et al., 2017; Shadmehri et al., 2018; Zhu & Stone, 2018; Flock et al., 2020).

Inserting observationally motivated values into Eq. (2.49) leads to a viscous timescale of $t_\nu \approx 10^{13}$ yr for molecular hydrogen (Armitage, 2010); this is considerably longer than the $10^6 \ldots 10^7$ yr typically presumed for disk dispersal (see Sect. 2.2.1.6), and thus unrealistic. So for viscous disk evolution to match observational data, non-microscopic turbulent effects need to be included in ν; their exact nature is however still unclear. Some candidates are as follows (see e.g. Gammie & Johnson, 2005; Dullemond et al., 2007; Li et al., 2014):

[(1)] Despite being commonly, and hence also in this work, referred to by the same symbol, the spectral index (see e.g. Sect. 2.2.1.1) and the α-viscosity are entirely unrelated.

Magneto-rotational instability (MRI)**:** Balbus & Hawley (1991) and Hawley & Balbus (1991) showed that a weak magnetic field can act to couple inner and outer parts of the disk if they are sufficiently ionised, thus introducing turbulence and allowing for angular momentum transport. Conversely, low temperatures as well as low levels of cosmic rays or high-energy photons from the central star can create areas with insufficient ionisation levels for the MRI, leading to its suppression (see e.g. Chiang & Murray-Clay, 2007; Dullemond et al., 2007, and references therein). The resulting MRI-inactive regions are often referred to as 'dead zones' (Gammie, 1996; Turner & Drake, 2009); they are thought to be located around the disk midplane at $R \lesssim 10\,\mathrm{AU}$ (see e.g. Bai & Stone, 2011; Bai, 2011a,b), where the least amount of stellar irradiation can penetrate to. In these regions, non-ideal magneto-hydrodynamical effects affect the magnetic field (see e.g. Wardle & Ng, 1999; Nakano et al., 2002; Gammie & Johnson, 2005; Armitage, 2010; Li et al., 2014; Lesur, 2020, and references therein):

Firstly, Ohmic resistivity; charge carriers collide with other particles, which reduces the magnetic flux, and converts magnetic energy into thermal energy. To be efficient, this process requires high ϱ_{gas}.[(1)][(2)]

Secondly, the Hall effect; the trajectories of charge carriers in a magnetic field are affected by Lorentz forces, and their deflection changes the morphology of the magnetic field. This process impacts mainly intermediate ϱ_{gas}.

Thirdly, ambipolar diffusion; the magnetic field is coupled to the charge carriers and moves with them, drifting in relation to the neutral particles. Collisions between the charge carriers and neutral particles transform magnetic energy into thermal energy. This process is thought to be most important at low ϱ_{gas}.

Gravitational instability: If the disk is massive, its self-gravity becomes non-negligible; this can be quantified in terms of the Toomre parameter (Toomre, 1964),

$$Q_{\mathrm{Toomre}} := \frac{c_s\,\Omega}{\pi\,G\,\Sigma_{\mathrm{gas}}} \,, \tag{2.53}$$

with $Q_{\mathrm{Toomre}} \gtrsim 2$ required for the system to be stable; $1 \lesssim Q_{\mathrm{Toomre}} \lesssim 2$ indicates marginal stability, and systems with $Q_{\mathrm{Toomre}} < 1$ are unstable (see e.g. Birnstiel et al., 2010). Thus, changes in the density (Σ_{gas}) or the temperature (and hence c_s) distributions may trigger local instabilities, which will introduce turbulence; they may as well act to quell it, which can create a feedback loop.

Vertical shear instability: In analogy to the concept of differentially rotating stars (Goldreich & Schubert, 1967), the vertical shear instability stems from gas parcels moving from (R_0, z_0) to $(R_0 + \delta R, z_0 + \delta z)$, while initially keeping their angular momentum from (R_0, z_0) (Urpin & Brandenburg, 1998). It is thought to drive turbulence especially where the MRI does not have an effect, that is in the MRI-dead zones (see also e.g. Nelson et al., 2013).

Further effects: Other processes, such as convection, baroclinic instability, and global magnetic fields may also create macroscopic viscosity.

2.2.2.4 Radial dust motion

While the gas is the main mass carrier at least in primordial circumstellar disks (PDs; see Sect. 2.2.1.3), the rocky cores of planetesimals and planets are formed from dust, which also impacts disk chemistry (see e.g. Booth & Ilee, 2019), and thus is a non-negligible constituent of disks. The motion of the dust in relation to the gas is often parametrised in terms of the dimensionless Stokes number (see e.g. Birnstiel et al., 2016),

$$St := \Omega_K\, t_{\mathrm{stop}} \,, \tag{2.54}$$

where t_{stop} is the stopping time, defined as the ratio of the momentum of a dust grain to the drag force it is experiencing from the gas around it (see e.g. Birnstiel et al., 2010).[(3)] So St gives a measure of how well (in terms of orbital times) the dust flow is coupled to the gas; for low $St \ll 1$, gas and dust are

[(1)] For order-of-magnitude estimates for the ϱ_{gas} at which the non-ideal effects operate best, see for instance Nakano et al. (2002), Armitage (2011, their Fig. 5) or Lesur (2020, their Fig. 9).

[(2)] The dominance of one non-ideal effect at a certain particle density does not necessarily imply that the others can safely be ignored (see e.g. Lesur, 2020).

[(3)] The usage of t_{stop} for dust transport across significant density drops (such as the disk-wind interface) may potentially cause issues, see Hutchison & Clarke (2021).

well-coupled, whereas they are decoupled for high $St > 1$. Rudimentarily, grains with smaller sizes (i.e. radii) a are more coupled to the gas.(1) More rigorously, there are different regimes for $t_{\rm stop}$:

In the Epstein regime (Epstein, 1924), that is for $a \lesssim \frac{9}{4}\,\ell_{\rm fp}$, with

$$\ell_{\rm fp} = \frac{1}{n_{\rm gas}\,\sigma_{\rm gas}} \tag{2.55}$$

the mean free path length, where $n_{\rm gas}$ is the gas number density (see Eq. 2.15) and $\sigma_{\rm gas}$ is the collisional cross section of a gas molecule, it can be written as (Whipple, 1972; Weidenschilling, 1977)

$$t_{\rm stop} = \frac{\varrho_{\rm grain}\,a}{\varrho_{\rm gas}\,v_{\rm therm}}\ . \tag{2.56}$$

Here, $\varrho_{\rm grain}$ is the internal material density of a dust grain such that Eq. (2.8) applies for a spherical particle,(2) and

$$v_{\rm therm} = \sqrt{\frac{8}{\pi}\cdot\frac{k_{\rm B}\,T}{\mu\,m_{\rm H}}} = \tag{2.57}$$

$$= \sqrt{\frac{8}{\pi}}\cdot c_s \tag{2.58}$$

is the mean thermal velocity (see e.g. Armitage, 2015), where we have used Eq. (2.39) in conjunction with Eq. (2.15) and the ideal gas law

$$P\,V = N\,k_{\rm B}\,T\ . \tag{2.59}$$

In the Stokes regime (i.e. for $a > \frac{9}{4}\,\ell_{\rm fp}$; Stokes, 1851; Whipple, 1972; Weidenschilling, 1977),

$$t_{\rm stop} = \begin{cases} \dfrac{2\,\varrho_{\rm grain}\,a^2}{9\,\nu_{\rm mol}\,\varrho_{\rm gas}} & \text{for} \quad Re < 1\ , \\ \dfrac{2^{0.6}\,\varrho_{\rm grain}\,a^{1.6}}{9\,\nu_{\rm mol}^{0.6}\,\varrho_{\rm gas}^{1.4}\,\Delta v_{\rm gas,\,dust}^{0.4}} & \text{for} \quad 1 < Re < 800\ , \\ \dfrac{6\,\varrho_{\rm grain}\,a}{\varrho_{\rm gas}\,\Delta v_{\rm gas,\,dust}} & \text{for} \quad Re > 800\ . \end{cases} \tag{2.60}$$

Here, Re is the (dimensionless) Reynolds number,

$$Re := \frac{2\,a\,\Delta v_{\rm gas,\,dust}}{\nu_{\rm mol}}\ , \tag{2.61}$$

$\Delta v_{\rm gas,\,dust}$ is the relative velocity of the gas and the dust particle, and

$$\nu_{\rm mol} = \frac{\ell_{\rm fp}\,v_{\rm therm}}{2} \tag{2.62}$$

is the (kinematic) molecular viscosity of the gas.

As Eqs. (2.56) and (2.60) indicate, $t_{\rm stop}$ and thus via Eq. (2.54) also St are positively correlated with a throughout the Epstein and Stokes regimes; so smaller grains have lower St and follow the gas flow more closely (see also the review by Birnstiel et al., 2016).(3)(4)

In Sect. 2.2.2.1 we have seen that the gas is pressure-supported and thus mostly orbits the star at sub-Keplerian $\Omega < \Omega_K$. By contrast, (large enough) dust grains must rotate with Ω_K to maintain their orbit; they hence feel a headwind from the gas, which causes them to lose momentum and drift further inward (see also e.g. Weidenschilling, 1977; Birnstiel et al., 2010; Testi et al., 2014). From Eq. (2.37), Takeuchi & Lin (2002) deduced the factor

$$\eta := -\frac{1}{R\,\varrho_{\rm gas}\,\Omega_K^2}\cdot\frac{\partial P_{\rm gas}}{\partial R} \tag{2.63}$$

(1) For the time being, we shall assume dust grains to be spherical to simplify theoretical considerations; this may be an oversimplifaction, however (see e.g. Kirchschlager & Bertrang, 2020).

(2) $\varrho_{\rm grain}$ is typically of the order of $1\,{\rm g/cm^3}$, (see e.g. Love et al., 1994; Joswiak et al., 2007).

(3) These considerations all assume $\varrho_{\rm dust} < \varrho_{\rm gas}$, and hence a negligible back reaction of the dust on the gas. This is not necessarily the case (see e.g. Dipierro et al., 2018; Gárate et al., 2020); for a generalisation of the formalism, see Nakagawa et al. (1986).

(4) To give a rough impression, the Epstein regime is probably more relevant than the Stokes regime at least for grains with $a < 1\,{\rm cm}$ in the disk midplane (see e.g. Cuzzi et al., 1993; Dullemond & Dominik, 2004).

to quantify the deviation from Keplerian motion, such that

$$\Omega_\varphi \equiv \Omega = \Omega_K \sqrt{1-\eta} \,. \tag{2.64}$$

For $\partial P_{\mathrm{gas}}/\partial R < 0$, this yields $\eta > 0$ (and thus $\Omega < \Omega_K$, see Sect. 2.2.2.1). They then formulated the radial drift speed of the dust as

$$v_{r,\,\mathrm{dust}} = \frac{v_{r,\,\mathrm{gas}} - St\,\eta\,R\,\Omega_K}{1+St^2} \,, \tag{2.65}$$

which shows that $v_{r,\,\mathrm{dust}} \to v_{r,\,\mathrm{gas}}$ for $St \to 0$, $v_{r,\,\mathrm{dust}} \to 0$ for $St \to \infty$, and $v_{r,\,\mathrm{dust}} < v_{r,\,\mathrm{gas}}$ (i.e. enhanced inwards drift) for intermediate St. For the latter case, Testi et al. (2014) estimated drift speeds of up to $50\,\mathrm{m/s} \simeq 0.01\,\mathrm{AU/yr}$ (see also e.g. Birnstiel et al., 2010; Kanagawa et al., 2017).

This then raises the issue that unmitigated radial drift would clear out disks far too fast to match observed lifetimes (see e.g. Takeuchi & Lin, 2005). However, locally, $\partial P_{\mathrm{gas}}/\partial R \geq 0$ is possible (see e.g. Klahr & Henning, 1997; Takeuchi & Lin, 2002; Pinilla et al., 2012a, and Sect. 2.2.2.6).(1)

2.2.2.5 Vertical dust distribution

As we have seen in Sect. 2.2.2.2, the gas disk is pressure-supported, allowing it to reach several H_{gas} in vertical extent. The dust, by contrast, is not (see e.g. Armitage, 2015). So while small grains may still be well-coupled to the gas (this is not necessarily the case, see Krijt & Ciesla, 2016; Lebreuilly et al., 2020), and hence be present far above the disk midplane, large grains are not.

The contribution from the gravitational force in Eq. (2.38) is

$$|F_{\mathrm{grav}}| = \frac{G\,M_*\,m_{\mathrm{grain}}}{R^3+z^3} \cdot z \,; \tag{2.66}$$

for a thin disk with $R > z$, $R^3 \gg z^3$, this can be rewritten as (see e.g. Armitage, 2015)

$$|F_{\mathrm{grav}}| = \Omega_K^2\, m_{\mathrm{grain}}\, z \tag{2.67}$$

using Eq. (2.35). The frictional force onto a dust grain in the gas is (Dullemond & Dominik, 2004)

$$|F_{\mathrm{fric}}| = \frac{4\,\pi}{3}\, a^2\, \varrho_{\mathrm{gas}}\, v_{\mathrm{sett}}\, c_s \tag{2.68}$$

for a (vertical) settling speed $v_{\mathrm{sett}} < c_s$. Via $|F_{\mathrm{grav}}| \overset{!}{=} |F_{\mathrm{fric}}|$, the vertical drift timescale can be derived as (Dullemond & Dominik, 2004)

$$t_{\mathrm{sett}} = \frac{z}{v_{\mathrm{sett}}} = \frac{4\,\pi}{3} \cdot \frac{a^2\, \varrho_{\mathrm{gas}}\, c_s}{m_{\mathrm{grain}}\, \Omega_K^2} \,. \tag{2.69}$$

Typically, t_{sett} is on the order of $10^5\,\mathrm{yr}$ (see e.g. Armitage, 2015), clearly shorter than usual disk lifetimes (see Sect. 2.2.1.6); so dust settling can significantly impact disk evolution.

Turbulent stirring counteracts the settling (see Dullemond & Dominik, 2004, and references therein). The ratio of gas diffusivity D_{gas} to dust diffusivity D_{dust} is the Schmidt number (Youdin & Lithwick, 2007)(2)

$$Sc := \frac{D_{\mathrm{gas}}}{D_{\mathrm{dust}}} \tag{2.70}$$

$$\approx 1 + St^2 \,. \tag{2.71}$$

Schräpler & Henning (2004) described the time-dependent vertical diffusive process via

$$\frac{\partial\, \varrho_{\mathrm{dust}}}{\partial\, t} - \frac{\partial}{\partial\, z}\left(z\, \Omega_K^2\, t_{\mathrm{stop}}\, \varrho_{\mathrm{dust}}\right) = \frac{\partial}{\partial\, z}\left[\varrho_{\mathrm{gas}}\, D_{\mathrm{dust}} \cdot \frac{\partial}{\partial\, z}\left(\frac{\varrho_{\mathrm{dust}}}{\varrho_{\mathrm{gas}}}\right)\right] \,; \tag{2.72}$$

a time-independent solution was given by Fromang & Nelson (2009):

$$\varrho_{\mathrm{dust}} = \varrho_{\mathrm{dust,0}} \cdot \exp\left[-\frac{St|_{z=0}\; Sc}{\alpha}\left(\exp\left[\frac{z^2}{2\,H_{\mathrm{gas}}^2}\right] - 1\right) - \frac{z^2}{2\,H_{\mathrm{gas}}^2}\right] \tag{2.73}$$

(1) For a dive into the processes possibly involved, see for instance the review by Andrews (2020).

(2) Youdin & Lithwick (2007) have demonstrated that $Sc \approx 1 + St$, as had been proposed and employed before, is incorrect.

Furthermore, Birnstiel et al. (2010) parametrised the dust scale height H_{dust} as

$$H_{\mathrm{dust}} = H_{\mathrm{gas}} \cdot \min\left(1; \sqrt{\frac{\alpha}{\min(St; 1/2) \cdot (1 + St^2)}}\right) , \tag{2.74}$$

which guarantees $H_{\mathrm{dust}} \leq H_{\mathrm{gas}}$ for all St and hence a, as expected from the considerations above.[(1)]

2.2.2.6 Dust growth

Planets are thought to grow from the material present in the circumstellar disk (see e.g. Blum & Wurm, 2008, and references therein); this growth spans many orders of magnitude, from $a \lesssim 10^{-6}$ m (see e.g. Draine, 2003a) to $a \gtrsim 10^6$ m (the radius of planet Earth being $\mathrm{R}_\oplus \simeq 6.4 \cdot 10^6$ m).

Starting at the lower end of the scale, small dust grains collide, and these collisions can lead to fragmentation, bouncing, partial mass transfers, or the two particles fully sticking together; as Blum & Wurm (2008) summarise, the collisions are caused by non-zero relative velocities due to Brownian motion, the sub-Keplerian motion of the gas and resulting radial drift (see Sects. 2.2.2.1 and 2.2.2.4), bulk motion such as vertical settling (see Sect. 2.2.2.5), or gas turbulence (see Sect. 2.2.2.3).[(2)]

The time evolution of how many grains of which sizes exist is parametrised by the coagulation equation (Smoluchowski, 1916), which can be written as (see e.g. Armitage, 2010)

$$\frac{\partial}{\partial t} n(m) = \frac{1}{2} \int_0^m K(m', m - m') \cdot n(m') \cdot n(m - m') \, \mathrm{d}m' - \int_0^\infty K(m', m) \cdot n(m') \, \mathrm{d}m' \, . \tag{2.75}$$

Here, the number of particles of mass m, $n(m)$, is expressed as all particles growing to mass m during a time step (first right-hand term of Eq. 2.75; the factor of 0.5 counteracts the duplicate counting of collisions between $m_1 = m'$ and $m_2 = m - m'$ to $m_1 + m_2 = m$) minus all particles of mass m growing or fragmenting to mass $m' \neq m$ (second right-hand term of Eq. 2.75). $K(m_1, m_2)$ stands for the collision kernel between particles with masses m_1 and m_2, which can be expressed for instance via the probability of a sticking encounter, the collisional cross section, and the relative velocities (see also e.g. Birnstiel et al., 2010; Testi et al., 2014).

Numerical solutions are necessary for non-trivial K. They have shown fast growth of small particles to about (centi)meter size (see e.g. Blum & Wurm, 2008; Testi et al., 2014, and references therein); this process is known as 'dust coagulation'. Fragmentation must occur to replenish smaller sizes as these are commonly observed in circumstellar disks (Dullemond & Dominik, 2005); it happens at relative speeds $\gtrsim 1...10$ m/s (see e.g. Güttler et al., 2010; Wada et al., 2013; Johansen et al., 2014; Gundlach & Blum, 2015; Birnstiel et al., 2016), with the exact value often thought to depend on the presence or absence of ices (see e.g. Pinilla et al., 2016). Furthermore, radial drift can impede growth if the growth timescale is larger than the drift timescale (Birnstiel et al., 2010, 2012a).

Bouncing and fragmentation limit the maximum grain size attainable from coagulation models to around (milli)meter size (see e.g. Brauer et al., 2008a; Zsom et al., 2010; Raymond & Morbidelli, 2020), the famous 'meter-size barrier'. At this size, the material clumps are not yet massive enough to gravitationally accrete (for this, $a \gtrsim 10^5$ m would be required, see e.g. Ida et al., 2008), so further growth needs to be driven by alternate processes. It also must be fast as else, the newly formed (m)m agglomerates would quickly radially drift into the star (on a timescale of about 100 yr, see e.g. Blum & Wurm, 2008); this necessitates the formation of local overdensities where particles can grow rapidly (see e.g. the review by Johansen et al., 2014).

In Sect. 2.2.2.4, we have assumed $\partial P_{\mathrm{gas}}/\partial R < 0$. However, locally, pressure maxima with a corresponding region of $\partial P_{\mathrm{gas}}/\partial R \gtrsim 0$ are possible; they can concentrate the dust as well as slow its inward drift (see e.g. Klahr & Henning, 1997; Fromang & Nelson, 2005; Johansen et al., 2007, 2009, and Sect. 2.2.2.4). Corresponding concentrations of up to cm-sized grains have been observed (see e.g. Casassus et al., 2015; Dullemond et al., 2018).[(3)] Enhanced particle densities around snowlines (whose location need not be fixed, see Owen, 2020) can act similarly (see e.g. Brauer et al., 2008b; Ros & Johansen, 2013; Drążkowska & Alibert, 2017; Stammler et al., 2017); furthermore, magnetised stars can induce density waves (see e.g. Romanova et al., 2013). In addition, once the first planet has formed, it will carve its

[(1)] Youdin & Lithwick (2007) had deduced $H_{\mathrm{dust}} \approx \sqrt{D_{\mathrm{gas}}/(\Omega_K \, St)}$ (see also Shadmehri et al., 2018).

[(2)] Most current simulations employ one or few different dust species; while this can definitely work (see e.g. Birnstiel et al., 2012a), too simplistic prescriptions may detrimentally affect the results (see e.g. Schaffer et al., 2018; Tamfal et al., 2018; Savvidou et al., 2020).

[(3)] However, some apparent dust pile-ups can be explained by simple dust growth instead (Stammler, 2018).

path through the circumstellar disk, creating a pressure bump in the process (see e.g. Paardekooper & Mellema, 2004; Lyra et al., 2009; Zhu et al., 2014; Dipierro & Laibe, 2017; Tamfal et al., 2018).(1)

From considerations of full coupling between gas and dust via drag forces, Youdin & Goodman (2005) found that enhanced dust-to-gas ratios may entail local perturbations (and hence, enhancements) of the dust distribution via back-reactions of the dust onto the gas, entailing a self-reinforcing accumulation of dust via the so-called streaming instability (see e.g. Youdin & Johansen, 2007; Johansen & Youdin, 2007; Carrera et al., 2017; Schaffer et al., 2018). The latter is considered one of the main mechanisms to overcome the meter-size barrier (see e.g. Armitage, 2018), although it may be less efficient than initially assumed (Krapp et al., 2019). It concentrates the dust together with processes like midplane settling and general turbulences (which can counteract the concentration, too) (see e.g. Johansen et al., 2014). Thinking back of the Toomre parameter (Eq. 2.53) which quantified the gravitational (in)stability of the gas, a high enough particle concentration will entail a local gravitational collapse of the dust grains; this can be parametrised in terms of the Roche density (see e.g. Johansen et al., 2014). This gravitational collapse of the overdensities then allows for (rapid) planetesimal formation.

2.2.2.7 Planets

Once a planetesimal ($a \gtrsim 10^3\,\mathrm{m}$, see e.g. Birnstiel et al., 2016) has formed, it can grow further via runaway growth, oligarchic growth, and pebble accretion (see e.g. Bitsch et al., 2015; Armitage, 2018; Raymond & Morbidelli, 2020, and references therein); it needs to do so before the disk has dispersed (see Sect. 2.2.1.6), and may start as early as star formation itself (Alves et al., 2020). In the case of runaway growth, the mass accretion scales with the mass of the planetesimal; thus, one or few massive bodies soak up all the smaller bodies in the system. During oligarchic growth, the accretion rate decreases with the mass of the accretor; so the most massive protoplanets will end up with similar masses. Furthermore, Ormel & Klahr (2010) and Lambrechts & Johansen (2012, 2014) proposed the (fast) sweep-up of small particles (pebbles) by growing planetesimals until those have carved a gap into the circumstellar disk (see also Chatterjee & Tan, 2014; Morishima, 2018; Picogna et al., 2018; Drążkowska et al., 2021); once the accretors have reached the pebble isolation mass, the pressure bump at the gap edge is too high to allow for further material influx onto and past the protoplanet. In addition, the planet may accrete a gaseous envelope from the protoplanetary disk.

During and after its formation, the protoplanet is moving through the circumstellar disk (see e.g. Baruteau et al., 2014). Depending on the gas density profile, the headwind from the gas usually slows it down, which leads to a decaying orbit (see e.g. Raymond & Morbidelli, 2020). This may even lead to more massive planets being swallowed up by their host star unless the gas disk dissipates during their migration (see e.g. Armitage & Bonnell, 2002; Monsch et al., 2019, 2021a,b). However, changes in the underlying ϱ_{gas} or interactions with other planets may lead to halted (or even outward) migration (see e.g. Lin & Papaloizou, 2012; Rometsch et al., 2020).(2) In addition, if massive enough, the planet affects the gas distribution itself (see e.g. Binkert et al., 2021), and carves a gap – or several ones, as it may excite spiral density waves (see e.g. Kanagawa et al., 2016; Zormpas et al., 2020; Rodenkirch et al., 2021; Rometsch et al., 2021).(3)(4)

Dust is thought to make up about 1% of the initial disk mass (see Sect. 2.2.1.3). Since planets, even gas giants, form mainly from dust, this limits their potential impact on the overall mass budget of the disk (see e.g. Alexander et al., 2014, and references therein); in addition, recent observations have shown clearly non-zero amounts of ‘free’ dust in protoplanetary systems (see e.g. ALMA Partnership et al., 2015; Ansdell et al., 2016, and Figs. 2.1 and 2.2), although these are already quite evolved (see e.g. Keppler et al., 2018; Benisty et al., 2021). So while planets may clear gaps, they are unlikely to dominate disk dispersal (at least in most systems).

(1) Photoevaporation (see Sect. 2.3.3) may also create a dust overdensity, but its success is still debated (see e.g. Carrera et al., 2017; Ercolano et al., 2017b).

(2) Radiative heating from the star can also lead to outward migration for small-ish planets (see e.g. Kley & Crida, 2008; Kley et al., 2009).

(3) Furthermore, Wu & Lithwick (2021) have shown that passive disks can undergo irradiation instabilities, which may drive thermal waves.

(4) (This) Sect. 2.2.2.7 gives only a very superficial overview over the topic of planet formation and topics related to it; the actual evolution is far more intricate (see e.g. Armitage, 2010; Helled et al., 2014; Baruteau et al., 2014; Birnstiel et al., 2016; Disk Dynamics Collaboration et al., 2020; Parker, 2020; Lichtenberg et al., 2021).

2.2.2.8 Transition disks

Observations have shown that a subset of circumstellar disks exhibits a depleted inner cavity (between the star and the remainder of the circumstellar disk; see Sect. 2.2.1.7), and literature mostly agrees that these transition disks mark a transitional phase between full, primordial disks and gas-depleted debris disks (see e.g. Wyatt, 2008; Alexander et al., 2014; Ercolano & Pascucci, 2017).[(1)] Modelling efforts have thus tried to find explanations for the depletion in gas and especially in small dust grains that has been evidenced by IR observations (see Sects. 2.2.1.1 and 2.2.1.7). As summarised by Espaillat et al. (2014) and Owen (2016), some of the mechanisms proposed are simple viscous evolution (see Sect. 2.2.2.3), dust grain growth (see e.g. Dullemond & Dominik, 2005; Birnstiel et al., 2012b), MRI-driven dust flows or winds (see e.g. Chiang & Murray-Clay, 2007; Suzuki & Inutsuka, 2009), and tidal effects due to stellar companions (see e.g. Marsh & Mahoney, 1992; Artymowicz & Lubow, 1994). The dominant mechanism may also depend on the how massive the disk is (see e.g. van der Marel et al., 2018), and is not necessarily exclusive (see e.g. Rosotti et al., 2015).

Related to the hole formation by a companion, planet-disk interactions, that is (massive) planets clearing the disk along their orbits, may also create transition disks (see e.g. van der Marel et al., 2018, 2019a).[(2)] The gap-clearing capacity of one planet is limited to about its Hill sphere radius (Hill, 1878),

$$r_{\mathrm{Hill}} := r_{\mathrm{planet}} \cdot \left(\frac{M_{\mathrm{planet}}}{3\, M_*} \right)^{1/3} , \tag{2.76}$$

with r_{planet} the orbital radius of the planet around the star of mass M_*, and M_{planet} its mass (see e.g. Armitage, 2018); r_{Hill} describes the region (from the center of mass of the planet) within which its gravitational attraction dominates over that of the central star.[(3)] Thus, a single planet has only a limited capability to carve a substantial gap (see e.g. Paardekooper & Mellema, 2004), even in combination with radial migration (see e.g. Clarke & Owen, 2013); and if it does, the hole may still not be readily detectable from SED data (see e.g. Pinilla et al., 2016). Alternatively, scenarios with multiple planets have been proposed (see e.g. Zhu et al., 2011; van der Marel et al., 2015); they, as well as single-planet systems, manage to keep up mass flow from the outer disk to the star, resulting in continuedly high $\dot{M}_{\mathrm{acc}}$ (see e.g. Lubow & D'Angelo, 2006; Zhu et al., 2011, 2012; Casassus et al., 2013, and Sect. 2.2.1.7).

Another option for the clearing of an inner hole are disk winds, and in particular photoevaporation; this topic will be explored below.

2.3 Disk winds

A disk wind can be defined as outflowing material from a few scale heights above the midplane (see e.g. Pascucci et al., 2020). To this date, the material in this wind often remains unresolved in direct images (see e.g. Cabrit et al., 1990; Ray et al., 2007; Pascucci et al., 2018; Ricci et al., 2021); thus, the Doppler shift in (sufficiently resolved) observed (forbidden) emission line spectra such as [O I] ($\lambda = 6300\,\text{Å} = 0.63\,\mu$m) and [Ne II] ($\lambda = 12.81\,\mu$m)[(4)] is used to determine the outflow characteristics (see e.g. Ercolano & Pascucci, 2017).[(5)]

T-Tauri stars exhibit both a high-velocity and a low-velocity wind component (HVC and LVC, respectively), which can be linked to the existence of a circumstellar disk (see e.g. Königl & Ruden, 1993; Hamann, 1994; Hartigan et al., 1995); outflow directed away from the observer may be obscured by said disk (Appenzeller et al., 1984; Edwards et al., 1987). In terms of outflow velocity, the differentiation is generally $v_{r,\,\mathrm{LVC}} \lesssim 30\,\mathrm{km/s} \lesssim v_{r,\,\mathrm{HVC}}$ (see e.g. Simon et al., 2016; Banzatti et al., 2019; Gangi et al., 2020; Pascucci et al., 2020).[(6)] However, the HVC jets attain speeds $v_{r,\,\mathrm{HVC}} > 100\,\mathrm{km/s}$ (see e.g. Cabrit, 2007; Ray et al., 2007; Xu et al., 2021).

The HVC is well-collimated and originates close to the star ($R \ll 1\,\mathrm{AU}$, see e.g. Anderson et al., 2003) in the form of (micro-)jets (see e.g. Kwan & Tademaru, 1988). The micro-jets are typically supplanting

(1) A cleared gap does however not necessarily present a clear indication for the age of the disk (see e.g. D'Alessio et al., 2005).

(2) The idea that planets are the sole, or at least main, cause of disk dispersal (see e.g. Armitage & Hansen, 1999) has been rebutted by newer literature (see e.g. Owen, 2016, and references therein).

(3) For an extension of Eq. (2.76) to a system with multiple planets, see Hill (1913).

(4) The ionisation energy needed for [Ne I] to become [Ne II] is about 21.56 eV (see e.g. Kaufman & Minnhagen, 1972).

(5) The rotation of the disk causes a different double-peaking of the lines (see e.g. Pontoppidan et al., 2011; Banzatti et al., 2022).

(6) The boundary of 30 km/s was revised from an earlier value of 50 km/s (compare e.g. Ray et al., 2007); Nisini et al. (2018) used 40 km/s.

actual jets when the objects transition from class 0/I to class II (see e.g. Simon et al., 2016; Banzatti et al., 2019);[1] in addition, their size and shape may be related to the alignment of the magnetic fields of the parent GMC and the disk itself (Ménard & Duchêne, 2004). Jets drive mass-loss rates of $10^{-9} \lesssim \dot{M}_{\mathrm{HVC}}\,[\mathrm{M}_\odot/\mathrm{yr}] \lesssim 10^{-7}$ (see e.g. Frank et al., 2014); however, at least for class-II objects, $\dot{M}_{\mathrm{HVC}}$ is lower than $\dot{M}_{\mathrm{acc}}$ by at least an order of magnitude (see e.g. Cabrit et al., 1990; Cabrit, 2007; Fang et al., 2018; Nisini et al., 2018). Class-III objects often lack the HVC (Fang et al., 2018).

The LVC is launched farther from the star than the HVC (see e.g. Kwan & Tademaru, 1988; Anderson et al., 2003). It also accounts for an associated mass loss $\dot{M}_{\mathrm{LVC}} \lesssim 10^{-8}\,\mathrm{M}_\odot/\mathrm{yr}$, with the notion that for any one object, $\dot{M}_{\mathrm{LVC}} < \dot{M}_{\mathrm{HVC}}$ (see e.g. Kwan & Tademaru, 1995; Natta et al., 2014). At $T_{\mathrm{LVC}} \approx 10^4\,\mathrm{K}$, it is rather warm (Natta et al., 2014; Fang et al., 2018), which further complicates attempts to accurately determine $\dot{M}_{\mathrm{LVC}}$ (see e.g. Ercolano & Owen, 2016). The LVC can be subdivided into a narrow and a broad component (LVC-NC and LVC-BC, respectively; Rigliaco et al., 2013), with the LVC-BC being more common and associated with the inner disk, and sources with mainly LVC-NC (emitted from further out) probably being transition disks (Simon et al., 2016; Fang et al., 2018). In general, low-velocity winds are thought to cover a wide outflow angle (see e.g. Pontoppidan et al., 2011).

Concurrently, as noted in Sect. 2.2.1.4, outflows may lead to stellar variability. The opacity of these winds is likely driven by dust particles entrained in it (see e.g. Bozhinova et al., 2016; Dodin et al., 2019; Petrov et al., 2019). Miotello et al. (2012) presented evidence for a dusty outflow from Orion 114-426 from HST images; targeted modelling of interferometric data for SU Aurigae also suggests entrainment of $0.4\,\mu$m-sized dust grains in a wind, although that would require a very high $\dot{M}_{\mathrm{acc}} \approx 10^{-6}\,\mathrm{M}_\odot/\mathrm{yr}$ (Labdon et al., 2019).

In particular the emission-line observations outlined above – quantitatively still the main source of actual information available (see e.g. Ray et al., 2007; Frank et al., 2014) – have spurred various efforts to attribute them to underlying physical processes, in particular driving by magnetohydrodynamics (MHD) or photoevaporation (see e.g. Anderson et al., 2003; Ferreira et al., 2006; Pascucci & Sterzik, 2009; Rigliaco et al., 2013; Simon et al., 2016; Ercolano et al., 2017a; Nisini et al., 2018; Banzatti et al., 2019; Weber et al., 2020);[2] understanding which mechanism dominates during which epochs would allow for more concise modelling of disk evolution and also dispersal. In the following, we will take a closer look at the proposed processes.

2.3.1 Magnetically-driven winds

The allure of MHD effects as main wind drivers lies in the self-collimation of the fast jets, which were the first outflow feature to be observed (see e.g. Königl & Pudritz, 2000; Ferreira et al., 2006; Frank et al., 2014, and references therein); furthermore, nascent stars are likely to be embedded in a magnetic field (see e.g. Königl & Ruden, 1993).

One of the main problems concerning the evolution of protoplanetary disks is the transport of angular momentum; apart from viscous evolution, which on its own cannot provide the timescales needed for dispersal (see Sect. 2.2.2.3), MHD winds are thought to be the main mechanism accountable for it (see e.g. Frank et al., 2014; Li et al., 2014; Turner et al., 2014; Najita & Bergin, 2018). Already Blandford & Payne (1982) posited that angular momentum may be removed from protoplanetary disks via outflows (particularly jets) driven along magnetic field lines threading the surface of the (thin) disk;[3] thermal effects were thought to play a minor role. MHD jets can be launched from the stellar surface itself,[4] from close to the star ('X-winds', see e.g. Shu et al., 2000; Mohanty & Shu, 2008, and references therein), or extended warm surfaces ($0.1 \lesssim R\,[\mathrm{AU}] \lesssim 3$), with the latter scenario deemed the most likely (see e.g. Ferreira et al., 2006). However, the launching from the (warm) disk surfaces does not make the wind thermal as long as its energy is supplied by the magnetic field (see e.g. Turner et al., 2014).

The magnetic field strength is often expressed in terms of the (dimensionless) plasma parameter (see e.g. Suzuki, 2007, and assuming a vertically isothermal setup, i.e. Eq. 2.39)

$$\beta := 8\,\pi \cdot \frac{\varrho_{\mathrm{gas}}\, c_s^2}{B_z^2}\ , \tag{2.77}$$

[1] For an example for a 'full' jet, see for instance HH 212 (Lee et al., 2018).

[2] It may be a topic for discussion whether new observational analyses should be published in direct conjunction with a physical interpretation, or alongside them, possibly in separate manuscripts; the latter alternative would serve to not 'stain' the data regarding their interpretation.

[3] While the magneto-centrifugal wind model of Blandford & Payne (1982) was targeted at black holes, they remarked that it should also apply to lower-mass objects.

[4] For a description of solar winds, see for instance Parker (1958, 1965).

with B_z the (net) vertical magnetic field strength (i.e. the background field); thus, lower β correspond to higher B_z.[(1)] Nowadays, the midplane value is typically assumed to be $10^4 \lesssim \beta \lesssim 10^7$ (see e.g. Suzuki & Inutsuka, 2009; Gressel et al., 2015; Bai, 2016; Béthune et al., 2017; Rodenkirch et al., 2020); at the disk-wind interface, $\beta \lesssim 1$ (see e.g. Turner et al., 2014). Using a non-zero vertical field B_z in ideal MHD simulations, Suzuki & Inutsuka (2009) stated that the MRI (see Sect. 2.2.2.3) can enhance magnetic fields and thus drive an outflow (see also Simon et al., 2013a,b); earlier models had questioned whether a disk could be formed at all, as magnetic braking (due to the accumulation of more and more magnetic flux in the central star, see e.g. Li et al., 2014) would be too efficient to allow for disk formation (Allen et al., 2003; Galli et al., 2006; Li et al., 2011).

Subsequently, simulations including non-ideal MHD effects (see Sect. 2.2.2.3) – in particular, Ohmic resistivity and ambipolar diffusion – showed the MRI and the corresponding magneto-turbulent wind to be suppressed; instead, a magneto-centrifugal wind is launched (Bai & Stone, 2013). The outflows emanate from $|z| \approx 4.5\,H_{\mathrm{gas}}$ and $R \lesssim 10\,\mathrm{AU}$ (see e.g. Gressel et al., 2015; Hartmann et al., 2016; Bai, 2017; Mori et al., 2019; Rodenkirch & Dullemond, 2022), and are not necessarily symmetric (see e.g. Bai, 2017; Béthune et al., 2017). A detailed dive into the current status of research is provided by dedicated reviews (e.g. Hartmann et al., 2016; Lesur, 2020); however, the accurate determination of ionisation levels due to high-energy radiation from the star and its neighbourhood has been shown to be important for both non-ideal and even ideal MHD calculations (Igea & Glassgold, 1999; Shang et al., 2002; Perez-Becker & Chiang, 2011; Mohanty et al., 2013). This has given rise to combined magneto-thermal wind models (see Sect. 2.3.4), because while recent studies have reported that magnetic winds can drive mass loss as well as accretion (see e.g. Suzuki et al., 2016b; Lesur, 2021; Tabone et al., 2021) – even for transition disks (Wang & Goodman, 2017a) –, it remains questionable to which degree (Armitage et al., 2013; Zhu & Stone, 2018), and the quantitative strength of the non-ideal MHD effects is still debated (see e.g. Lesur, 2020), and may well depend on the magnetic background field.

Suzuki & Inutsuka (2009) speculated that MRI-driven waves could concentrate small dust grains towards the midplane. This vertical motion was further explored by Miyake et al. (2016), who found that dust with sufficiently small St could float at $|z| \approx 4\,H_{\mathrm{gas}}$ and possibly be picked up by a wind, while large grains would be left in the disk. Quantitatively, they reported grains with $a \lesssim \{20, 0.5\}\,\mu\mathrm{m}$ to be blown out from $R \lesssim \{1, 10\}\,\mathrm{AU}$. Giacalone et al. (2019) investigated the radial transport of dust grains in MRI-driven winds, and found small μm-sized grains to be picked up close to the star, and deposited back into the disk further out (at $R \lesssim 10...20\,\mathrm{AU}$); even smaller grains could be fully entrained in the wind (see also Safier, 1993).[(2)] Material returning to the disk drifts back inwards; it is still debated whether grain growth will limit the amount of small particles being picked up by the wind (Misener et al., 2019; Okamoto & Ida, 2022).

2.3.2 Radiation pressure

Although radiation pressure is not assumed to drive the observed large-scale outflows of protoplanetary disks (see e.g. Königl & Ruden, 1993; Booth & Clarke, 2021), it may still account for the removal of small dust grains. Takeuchi & Lin (2003) modelled the outwards motion of such particles from the surface layer of protoplanetary disks, and concluded that the mass outflow is insignificant unless the stellar luminosity is very high, but will remove grains of $a \approx 0.1\,\mu\mathrm{m}$. Vinković (2009) added that grains with $a \gtrsim 1\,\mu\mathrm{m}$ can be transported some distance outwards from the inner disk region along the disk surface (but not out of the system) due to vertical radiation pressure (see also Jaros et al., 2020; Vinković & Čemeljić, 2021). As shown by Tazaki & Nomura (2015), the size limit strongly depends on the shape, composition, and porosity of the grains. In addition, azimuthal asymmetries in the dust distribution may lead to an outward recession of the gap edge (Bi & Fung, 2022), even though radiation pressure cannot prevent dust from entering the gap (Dominik & Dullemond, 2011).

Owen & Kollmeier (2019) argued that radiation pressure can disperse small dust grains ($a \lesssim 1\,\mu\mathrm{m}$) in particular from the gap edge of a transition disk created by photoevaporation (see Sect. 2.3.3), and that fragmentation of larger grains accumulated there may consecutively entail a rapid loss of dust mass. The model was expanded to disks without a pressure bump by Krumholz et al. (2020), who also found a relatively fast removal of small grains from transition disks; this is in line with the earlier works of Takeuchi & Artymowicz (2001), and of Klahr & Lin (2001) who had estimated that radiation pressure can remove dust grains of around μm-size from the debris disk of HR 4796A (for recent images, see

[(1)]Fundamentally, $\beta \propto P_{\mathrm{gas}}/B_z^2$ is a pressure ratio, with P_{gas} the thermal pressure, and $P_{\mathrm{mag}} \propto B^2$ the magnetic pressure (see e.g. Suzuki, 2007; Bai & Stone, 2011).

[(2)]If the corresponding $\dot{M}_{\mathrm{dust}}$ were high enough, this could impact disk evolution, as Zhao et al. (2016) found the removal of grains with $a \lesssim 0.1\,\mu\mathrm{m}$ to be beneficial for disk survival.

e.g. Schneider et al., 2018). These results suggest that outflows driven by radiation pressure gain in importance when the circumstellar disk has already evolved.

2.3.3 Photoevaporative winds

Protoplanetary disks disperse within a few Myr (see Sect. 2.2.1.6); about one tenth of that time is spent in a transitional stage (see Sect. 2.2.1.7). This suggests a two-timescale evolutionary track, where at some point, rapid disk dispersal (from the inside out) is triggered (see e.g. Kenyon & Hartmann, 1995; Alexander et al., 2014; Ercolano & Pascucci, 2017). Based on an the work of Hollenbach et al. (1994, see also the references therein), Clarke et al. (2001) proposed photoevaporation (PE) due to ultraviolet (UV) stellar radiation – which can heat the gas enough to allow for material to escape – as a mechanism that could reproduce exactly this two-timescale behaviour.

Put simplistically, the gas within the gravitational radius (Hollenbach et al., 1994),(1)

$$R_{\mathrm{grav}} := \frac{G\,M_*}{c_s^2}\ , \tag{2.78}$$

remains (gravitationally) bound to the central star even at high temperatures ($T_{\mathrm{gas}} \approx 10^4\,\mathrm{K}$);(2) for example, an isothermal scenario with $c_s = 10\,\mathrm{km/s}$ and $M_* = 1\,\mathrm{M}_\odot$ yields $R_{\mathrm{grav}} \simeq 9\,\mathrm{AU}$. Outside of R_{grav}, the thermal energy allows for the escape of the gas (see also e.g. Alexander et al., 2014).(3) Over time, the UV irradiation leads to a density drop around R_{grav}, and subsequently, the gas at $R < R_{\mathrm{grav}}$ is quickly viscously accreted onto the star – in about $10^5\,\mathrm{yr}$, yielding the fast transition between CTTS and WTTS –, while the disk at $R \gtrsim R_{\mathrm{grav}}$ is photoevaporated, and thus cannot resupply the inner disk (Clarke et al., 2001). As found by Adams & Shu (1986), Adams et al. (1987), and Alexander et al. (2004a), radiation directly from the host star (and not from accretion shocks) dominates the photon budget (see also Andrews, 2015); so the stellar emission would be sustained even at $\dot{M}_{\mathrm{acc}} \simeq 0$.(4)

Clarke & Alexander (2016) presented self-similar solutions for the gas streamlines of a thermal wind; the disk was assumed to be geometrically thin (with the winds being launched from the midplane) and isothermal, and have a density $\varrho_{\mathrm{gas}} \propto R^{-\gamma}$ (see Sect. 2.2.2.1). The analytic solutions agreed quite well with according hydrodynamic simulations for $R \gtrsim 0.5\,R_{\mathrm{grav}}$, providing a means of modelling the gaseous outflow at considerably lower computational cost. Sellek et al. (2021) extended this model to include an angled launch surface (i.e. a disk-wind interface with $h_{\mathrm{gas}} = \mathrm{const}$) as well as to allow for temperature variations along the base of the outflow. For the gas streamlines, they found almost vertical launching from the disk surface (also at $z/R = \tan(36°) \simeq 0.7$, in addition to the $(z/R = 0)$-case investigated by Clarke & Alexander, 2016), and confirmed launch velocities of $v_{\mathrm{launch,\,gas}} \simeq 0.3\,c_s$ for $\gamma = 1.5$.

When considering highly energetic photons emitted by the host star, there are three main energy regimes to consider: far ultraviolet (FUV), extreme ultraviolet (EUV), and X-ray; Table 2.1 gives an overview over their respective energy domains and penetration depths into the disk. These three components are thought to drive mass loss from different (radial) regions of the disk (see e.g. Armitage, 2011; Alexander et al., 2014).

2.3.3.1 Extreme-ultraviolet radiation

A first dedicated hydrodynamical model of EUV-driven disk winds around T-Tauri stars, based on the prescriptions of Hollenbach et al. (1994), was presented by Font et al. (2004). It was built around a star with $M_* = 1\,\mathrm{M}_\odot$, emitting photons at a rate of $\Phi_* = 10^{41}/\mathrm{s}$, and thus heating the disk surface. The EUV penetration depth (see Table 2.1) is comparatively low; absorption and re-emission of photons indirectly heats (and ionises) the wind region to around $T_{\mathrm{gas}} \simeq 10^4\,\mathrm{K}$ (see also Hollenbach et al., 2000), in agreement with observational data (see e.g. Johns-Krull et al., 2000). From their simulations, Font et al. (2004) reported an outflow velocity of $v_{\mathrm{wind,\,gas}} \approx 10\,\mathrm{km/s}$, launched at $v_{\mathrm{launch,\,gas}} \approx 0.3\,c_s$, and a peak in the mass-loss rate rather close to the star (at $R \simeq 0.14\,R_{\mathrm{grav}}$, see Alexander et al., 2014). Successively,

(1) R_{grav} is derived from $c_s = \Omega_K\,R$, and indicates the maximum region within which the heated gas can remain bound to the star (see e.g. Clarke et al., 2001).

(2) The corresponding dust temperature T_{dust} is most likely smaller than T_{gas}, in particular in low-density regions (see e.g. Alexander et al., 2014).

(3) Photoevaporative winds being launched mainly from $R > R_{\mathrm{grav}} \gg 1\,\mathrm{AU}$ associates them with the LVC of the wind (see above).

(4) Nonetheless, Clarke et al. (2001) noted that the energy source for the sustained stellar emission after the clearing of the gap is unclear; they speculated that magnetic activity could play a role, which suggests that MHD effects and photoevaporation may well be intertwined processes (see also Sect. 2.3.4).

Table 2.1: Energy ranges and approximate penetration depths (in terms of number column densities, i.e. gas particles per area) for the different types of high-energy radiation considered.

Type	Energy [eV]			Wavelength [Å]			Optical depth [1/cm^2]		
FUV	6	...	13.6	912	...	2066	10^{21}	...	10^{22}
EUV	13.6	...	100	124	...	912		10^{20}	
X-ray (soft)	100	...	$2 \cdot 10^3$	6.20	...	124	10^{21}	...	10^{22}
X-ray (hard)	$2 \cdot 10^3$	...	10^5	1.24	...	6.20		10^{22}	

The values listed have been taken from the review by Ercolano & Pascucci (2017) (compare Hollenbach & Gorti, 2009; Alexander et al., 2014; Gorti, 2016, and references therein); they should be regarded as order-of-magnitude estimates, as the actual penetration depths depend on the exact material compositions (and hence opacities) in the irradiated regions. In broad terms, EUV photons penetrate less into the disk than X-ray and FUV ones; hard X-ray radiation penetrates deeply, but scarcely heats the gas.

the models of Alexander et al. (2006a,b) yielded similar $v_{\mathrm{wind,\,gas}}$, and showed that once an inner cavity has opened, direct irradiation becomes non-negligible at its edge, speeding up the timescale for final disk dispersal to about 10^5 yr – that is, roundabout the observationally derived value (see Sect. 2.2.1.7), and comparable to the timescale of viscous accretion of the inner disk.

Yet the low penetration depth of the photons means that they may already be absorbed in the jet (Shang et al., 2002), or the material accreting from the disk onto the star (Alexander et al., 2004a) or the wind region close to it (Gorti & Hollenbach, 2009; Owen et al., 2012). This leads to a rather long timescale of about 10^7 yr for the photoevaporative formation of a cleared gap (see e.g. Hollenbach et al., 2000; Clarke et al., 2001), longer than usual disk lifetimes (see Sect. 2.2.1.6). Mass-loss rates are accordingly low, with $\dot{M}_{\mathrm{EUV}} \approx 10^{-10}\,\mathrm{M}_\odot/\mathrm{yr}$ for primordial disks (Clarke et al., 2001; Font et al., 2004) and $\dot{M}_{\mathrm{EUV}} \approx 10^{-9}\,\mathrm{M}_\odot/\mathrm{yr}$ for transition disks accounting for direct irradiation (Alexander et al., 2006a, 2014).(1)(2) In all cases, the models yielded (Hollenbach et al., 1994; Clarke et al., 2001; Alexander et al., 2006a)

$$\dot{M}_{\mathrm{EUV}} \propto \sqrt{\Phi_* \cdot M_*}\;; \tag{2.79}$$

so uncertainties in Φ_*, which is estimated at $10^{41} \lesssim \Phi_*\,[1/\mathrm{s}] \lesssim 10^{42}$ (Alexander et al., 2005; Herczeg et al., 2007; Alexander, 2008; Hollenbach & Gorti, 2009), do not strongly impact $\dot{M}_{\mathrm{EUV}}$.(3)

Owen et al. (2011a) simulated the motion of small dust grains in an EUV-driven outflow around a Herbig Ae/Be star ($M_* = 2.5\,\mathrm{M}_\odot$, $\Phi_* = 10^{43}/\mathrm{s}$), assuming that the dust motion was governed by gas drag. In their edge-on, wind-only model, grains with $a \lesssim 2.2\,\mu\mathrm{m}$ were entrained, and radiative-transfer (RT) modelling with `Mocassin` (Ercolano et al., 2003, 2005, 2008a) revealed a 'wingnut' morphology for their wind-only dust distributions. Using the EUV wind model of Hutchison & Laibe (2016), Hutchison et al. (2016a) simulated vertical dust distributions via smoothed-particle hydrodynamics (SPH; Gingold & Monaghan, 1977); the largest particles were entrained from $R_{\mathrm{grav}} \lesssim R \lesssim 2\,R_{\mathrm{grav}}$. In a follow-up study, Hutchison et al. (2016b) reported dust of internal density $\varrho_{\mathrm{grain}} = 3\,\mathrm{g/cm}^3$ and sizes $a \lesssim \{3, 4\}\,\mu\mathrm{m}$ to be entrained in the EUV outflow from a $M_* = \{1, 0.7\}\,\mathrm{M}_\odot$ star; they noted that dust settling (see Sect. 2.2.2.5) may decrease this size limit to $a < 1\,\mu\mathrm{m}$. However, their model was not set up to retrieve dust densities in the wind region (Hutchison, priv. comm.). Recently, Hutchison & Clarke (2021) have presented a semi-analytical model of dust entrainment based on the work of Clarke & Alexander (2016) and the EUV flux parametrisation of Hollenbach et al. (1994), aimed at predicting dust trajectories in the wind region as well as vertical advection or diffusion of dust to the disk-wind interface; they verified their results by means of the enhanced gas-and-dust SPH code of Hutchison et al. (2018). As suggested by Hutchison et al. (2016b), Hutchison & Clarke (2021) found the delivery of material to the disk-wind interface to be the main constraint on the grain sizes picked up by the photoevaporative outflow, limiting them to $a < 1\,\mu\mathrm{m}$ for $\Phi_* = 10^{41}/\mathrm{s}$.

(1) As $\varrho_{\mathrm{gas}} \gg \varrho_{\mathrm{dust}}$ (see Sect. 2.2.1.3), and because dust also undergoes vertical settling especially at the larger a (see Sect. 2.2.2.5) which carry most of the mass (see Sect. 2.2.1.3), we have $\dot{M}_{\mathrm{wind}} \approx \dot{M}_{\mathrm{wind,\,gas}} \gg \dot{M}_{\mathrm{wind,\,dust}}$.

(2) In the case of a dust-free disk around a high-mass ($M_* \geq 10\,\mathrm{M}_\odot$) star, direct irradiation would also matter for the primordial phase, and drive somewhat higher $\dot{M}_{\mathrm{EUV}}$ especially from $R \gg R_{\mathrm{grav}}$ (Tanaka et al., 2013).

(3) The values reported for $\dot{M}_{\mathrm{EUV}}$ above were computed for $\Phi_* = 10^{41}/\mathrm{s}$.

2.3.3.2 X-ray radiation

EUV-driven winds cause rather low mass-loss rates, which (on their own) would not succeed in dispersing protoplanetary disks within the observationally determined timeframe of a few Myr (see Sect. 2.2.1.6). However, observations have shown that pre-MS stars have comparatively high L_{X} (see Sect. 2.2.1.5); these may act to enhance the photoevaporative outflows.[(1)]

A first study by Alexander et al. (2004b) estimated an X-ray-driven mass loss of $\dot{M}_{\mathrm{X}} < \dot{M}_{\mathrm{EUV}}$. Gorti & Hollenbach (2009) found that X-rays could not drive a high mass-loss on their own, but significantly enhanced EUV (and FUV; see Sect. 2.3.3.3) photoevaporation. Ercolano et al. (2008b) claimed $\dot{M}_{\mathrm{X}} \approx 10^{-8}\,\mathrm{M}_{\odot}/\mathrm{yr}$, a value which Ercolano et al. (2009) revised to $\dot{M}_{\mathrm{X}} \approx 10^{-9}\,\mathrm{M}_{\odot}/\mathrm{yr}$ accounting for vertical hydrostatic equilibrium; both works noted that in comparison to EUV-only irradiation, the disk-wind interface is less well defined for X-ray photoevaporation (which can penetrate deeper, see Table 2.1), rendering the retrieved $\dot{M}_{\mathrm{X}}$ highly dependent on where exactly the boundary is located (see also Gorti & Hollenbach, 2008).[(2)] This led to the fully hydrodynamical modelling of an X-ray-enhanced EUV (XEUV) wind by Owen et al. (2010), who found $\dot{M}_{\mathrm{XEUV}} \simeq 10^{-8}\,\mathrm{M}_{\odot}/\mathrm{yr} \gg \dot{M}_{\mathrm{EUV}}$ (similar to Ercolano et al., 2008b), coming from a larger range in R (i.e. $1 \lesssim R\,[\mathrm{AU}] \lesssim 70$) than in the R_{grav}-centric EUV cases, and showing that indeed, X-rays do have a non-negligible impact on photoevaporation. This was underlined by their result that the ionisation parameter (Tarter et al., 1969)

$$\xi_{\mathrm{ion}} := \frac{L_{\mathrm{X}}}{n_{\mathrm{gas}}\, r^2}\,, \tag{2.80}$$

which is evidently X-ray-driven, is very closely correlated to the gas temperature T_{gas}. The latter was found to be somewhat lower than the EUV-induced value of $10^4\,\mathrm{K}$ especially at larger R, so X-ray photoevaporation is more effective at larger R than its EUV counterpart (see also Alexander et al., 2014). In addition, Owen et al. (2010) could also reproduce the two-timescale behaviour of Clarke et al. (2001), but on timescales matching observational data.[(3)]

While Owen et al. (2010) had used a single $L_{\mathrm{X}} = 2 \cdot 10^{30}\,\mathrm{erg/s}$,[(4)] Owen et al. (2011b) extended their model to $10^{28} \leq L_{\mathrm{X}}\,[\mathrm{erg/s}] \leq 10^{31}$ (yet stayed with $M_* = 0.7\,\mathrm{M}_{\odot}$). This yielded mass-loss rates of $4 \cdot 10^{-10} \lesssim \dot{M}_{\mathrm{XEUV}}\,[\mathrm{M}_{\odot}/\mathrm{yr}] \lesssim 8 \cdot 10^{-8}$, and an empirical relation (Owen et al., 2011b)

$$\dot{M}_{\mathrm{XEUV}} \propto L_{\mathrm{X}}^{1.14}\,, \tag{2.81}$$

slightly steeper than their analytical prediction of $\dot{M}_{\mathrm{XEUV}} \propto L_{\mathrm{X}}$; a comparison to Eq. (2.79) suggests a clearly stronger dependence of the wind mass-loss rate ($\dot{M}_{\mathrm{wind}}$) on L_{X} than on Φ_*. However, they noted that their model cannot account for transition disks with large inner holes and high $\dot{M}_{\mathrm{acc}}$ (which have been observed, see Sects. 2.2.1.4 and 2.2.1.7); this can be resolved by invoking a dead zone (Morishima, 2012; Gárate et al., 2021, see Sect. 2.2.2.3). Owen et al. (2012) found a negligible impact of stellar mass (independent of L_{X}; see Sect. 2.2.1.5) on the model, that is roughly $\dot{M}_{\mathrm{XEUV}} \propto M_*^{-0.1}$ for both primordial and transitional disks, retrieved from simulations for $M_* \in \{0.1, 0.7\}\,\mathrm{M}_{\odot}$. In addition, they encountered a photoevaporative dispersal of the remainder of their transition disk on dynamical timescales once the inner hole had grown to 20...40 AU, a process they dubbed 'thermal sweeping' (see also Owen et al., 2013).[(5)]

Eq. (2.81) shows a strong dependence of $\dot{M}_{\mathrm{XEUV}}$ on L_{X}; however, as observations have shown, the latter is unconstrained by several orders of magnitude (see Sect. 2.2.1.5 as well as the low inferred estimates of Sellek et al., 2020b). In addition, microphysics and dust distributions may heavily impact the amount of X-ray and EUV irradiation actually heating the disk (see e.g. Ercolano et al., 2009; Ercolano & Clarke, 2010; Ercolano & Glassgold, 2013; Alexander et al., 2014; Ercolano & Owen, 2016; Nakatani et al.,

---

(1) While EUV photons can effectively ionise hydrogen atoms (see Table 2.1), the higher energy of X-ray photons renders the latter more likely to interact with heavier elements. Re-emission of photons due to recombinations can then act to not only heat, but also ionise the surrounding hydrogen gas (see e.g. Tarter et al., 1969; Tarter & Salpeter, 1969; Alexander et al., 2014).

(2) This can additionally be seen from the wind parametrisation of Clarke & Alexander (2016): The mass outflow can be approximated via $\dot{\Sigma}_{\mathrm{gas}} \propto \varrho_{\mathrm{base,\,gas}} \cdot c_s$, using the base density $\varrho_{\mathrm{base,\,gas}}$ and a launch velocity of order c_s. The (simplifying) assumption of an ideal gas in an isothermal environment yields $c_s^2 = P_{\mathrm{gas}}/\varrho_{\mathrm{gas}} \propto n_{\mathrm{gas}}\, k_{\mathrm{B}}\, T_{\mathrm{gas}}/\varrho_{\mathrm{gas}} \propto T_{\mathrm{gas}}$ via Eqs. (2.39) and (2.59); so very roughly, $\dot{\Sigma}_{\mathrm{gas}} \propto \varrho_{\mathrm{base,\,gas}} \cdot \sqrt{T_{\mathrm{gas}}}$ (see also Gorti, 2016; Ercolano & Pascucci, 2017).

(3) Gorti et al. (2009) stated that over time, the hardness of the X-ray spectrum emitted by the star changes; this may help to establish a two-phased disk dispersal. Furthermore, Flaischlen et al. (2021) found the observed anti-correlation between $\dot{M}_{\mathrm{acc}}$ and L_{acc} (see Sect. 2.2.1.5) to be stronger for softer X-rays.

(4) Actual stellar L_{X} can vary over time (see Sect. 2.2.1.5), which may impact the results both directly and indirectly (via altering the subsequent gas evolution; see also Owen et al., 2012).

(5) The efficiency of thermal sweeping is still debated, see Haworth et al. (2016a), but also Picogna et al. (2019).

2018a,b; Wölfer et al., 2019). Recent modelling efforts have thus concentrated on finding observational tracers to benchmark the validity of the underlying XEUV simulations (based on Owen et al., 2010). For instance, Ercolano et al. (2014) showed that they could reproduce the observed correlation between M_* and $\dot{M}_{\rm acc}$ (see Sect. 2.2.1.4) quite well. Ercolano et al. (2018) showcased a synthesised population of transition disks whose gap sizes and $\dot{M}_{\rm acc}$ matched actual data, derived for disks depleted of carbon and oxygen; this depletion decreases cooling and thus extends the region affected by photoevaporation (see also Gorti et al., 2009). Their model was refined by Wölfer et al. (2019), who found carbon and oxygen depletion to indeed significantly enhance $\dot{M}_{\rm XEUV}$.

To allow for more exact studies, Picogna et al. (2019) presented a new generation of XEUV photoevaporation models, using coupled RT and HD computations; starting from similar parameters as Owen et al. (2010) for $10^{28.3} \leq L_{\rm X}\,[{\rm erg/s}] \leq 10^{31.3}$, they found $\dot{M}_{\rm XEUV}$ to be slightly higher (by a factor of about 2) for $R > 10\,{\rm AU}$ (see also Rodenkirch & Dullemond, 2022).(1) In addition, they improved upon the emission-line predictions of Ercolano & Owen (2016), provided the basis for follow-up studies (such as Wölfer et al., 2019; Weber et al., 2020), and retrieved a more intricate relation between $L_{\rm X}$ and $\dot{M}_{\rm XEUV}$ than Eq. (2.81), levelling off at high $L_{\rm X}$.(2) Nonetheless, qualitatively, they stated that the X-ray component of the stellar radiation provides a vital ingredient to photoevaporation just like in the models of Owen et al. (2010, 2011b, 2012). Subsequently, Picogna et al. (2021) extended these simulations to a wide range of stellar masses ($0.1 \leq M_*\,[{\rm M}_\odot] \leq 1$); in contrast to the (less detailed) work of Owen et al. (2012), they found an approximately linear relation (Picogna et al., 2021)

$$\dot{M}_{\rm XEUV} \propto M_* \tag{2.82}$$

even for fixed $L_{\rm X}$, giving much more weight to M_* than the EUV case (Eq. 2.79). This was caused by lower $h_{\rm gas}$ in disks around higher-mass stars, allowing further-out regions to be photoevaporated. Furthermore, their model predicted inner-disk lifetimes matching observational data from λ Orionis (Bayo et al., 2012).

The shape of the X-ray profile (in other words, its hardness) can significantly impact results; Ercolano et al. (2009) found a harder spectrum to decrease $\dot{M}_{\rm X}$ by one dex, and Gorti et al. (2009) found a softer spectrum to halve disk lifetimes.(3) This was verified by Ercolano et al. (2021), who refined the input spectra of Picogna et al. (2019) (who had been using the spectra of Ercolano et al., 2008a) with data from the COUP survey (Getman et al., 2005, see Sect. 2.2.1.5). Yet their (1D) population synthesis still produced less transition disks with large inner holes as well as high $\dot{M}_{\rm acc}$ than observed (see also Monsch et al., 2021b); this may well be due to model oversimplifications (Ercolano et al., 2021).

A different approach to wind tracing could be to consider small dust grains entrained in the outflow; any notable patterns (such as the EUV-driven wingnut morphology predicted by Owen et al., 2011a) could be directly checked against observational images, presenting yet another way to benchmark XEUV photoevaporation. In addition, accurate dust population maps would yield the added benefit of allowing for improved thermal and chemical modelling (see e.g. Gorti & Hollenbach, 2009; Bai, 2016; Wang et al., 2019, and Sect. 1.1). Until recently, this approach had not been explored, rendering the dust density computations presented in Chaps. 3, 4, and 5 the first of their kind. Concurrently, Booth & Clarke (2021) stated that much like for an EUV wind (see Hutchison & Clarke, 2021), dust delivery to the disk-wind interface is the limiting factor in dust entrainment, resulting in the entrainment of grains with $a \lesssim 2.5\,\mu{\rm m}$ for the gas models of Picogna et al. (2019) (see also Sects. 4.4.1.1 and 5.3.2).

2.3.3.3 Far-ultraviolet radiation

FUV photons cannot ionise hydrogen (see Table 2.1). However, as summarised by Hollenbach & Tielens (1997), they still raise $T_{\rm gas}$ via photo-electric heating of small dust grains, in particular polycyclic aromatic hydrocarbons (PAHs), effectively launching electrons into the gas. Additionally, FUV photons can excite or even photo-dissociate simple molecules such as (primarily) H_2, leading to the emission of IR photons. Therefore, disk microphysics cannot be neglected when investigating FUV photoevaporation (see also

(1) As illustrated by Picogna et al. (2019, their Fig. C1), differences in $\dot{M}_{\rm XEUV}$ can be at least partially due to the choice of the outer computational boundary (see also Rodenkirch et al., 2020, and Sect. 4.2.1).

(2) The numerical fit provided by Picogna et al. (2019) reads:

$$\log_{10}\left(\frac{\dot{M}_{\rm XEUV}}{{\rm M}_\odot/{\rm yr}}\right) = -7.2580 - 2.7326 \cdot \exp\left[-\left(\ln\left(\log_{10}\left(\frac{L_{\rm X}}{{\rm erg/s}}\right)\right) - 3.3307\right)^2 / \left(2.9868 \cdot 10^{-3}\right)\right]$$

It was further refined by Ercolano et al. (2021).

(3) The degree of sampling of the spectrum is also likely to have an impact (see e.g. Picogna et al., 2019).

Tielens & Hollenbach, 1985), rendering dedicated simulations quite computationally costly.[(1)]

Building on the X-ray, EUV, and FUV photoevaporation model of Gorti & Hollenbach (2004, 2008), Gorti & Hollenbach (2009) reported FUV to mainly account for the erosion of the outer disk regions, with $\dot{M}_{\rm FUV}$ peaking locally at $R \simeq 20\,$AU and globally at $R \gtrsim 100\,$AU. For $M_* = 1\,{\rm M}_\odot$, they retrieved $\dot{M}_{\rm FUV} > 10^{-8}\,{\rm M}_\odot/{\rm yr}$ from $R \gtrsim 100\,$AU, yielding $\dot{M}_{\rm acc} \approx \dot{M}_{\rm FUV}$; Wang & Goodman (2017b) revised that value to $\dot{M}_{\rm wind} \approx 2.5 \cdot 10^{-9}\,{\rm M}_\odot/{\rm yr}$, but did so using a computational domain limited to $R \leq 100\,$AU.

While Gorti & Hollenbach (2009) had incorporated X-ray irradiation, they found it to play mainly a supporting role compared to FUV (see Sect. 2.3.3.2).[(2)] In a follow-up study, Gorti et al. (2009) simulated disk evolution until dispersal. They stated that the stellar $L_{\rm FUV}$ is driven by $\dot{M}_{\rm acc}$, leading to FUV-driven winds especially in high-viscosity disks with no or just small gaps. Their disks showed gap formation around $R \approx 3\,$AU after a few Myr ($R \approx 10\,$AU in the updated models of Gorti et al., 2015), largely due to FUV irradiation.

By contrast, in the hydrodynamical, but chemistry-less models of Owen et al. (2012), X-ray photoevaporation drove disk evolution at $R \lesssim 100\,$AU, whereas FUV dominated $\dot{M}_{\rm wind}$ only for $L_{\rm FUV} > 100\,L_{\rm X}$. So while FUV irradiation most likely determines the fate of the outer disk regions, its role at $R \lesssim 20\,$AU is less well-constrained, and may also depend on individual system properties such as dust distribution and composition (which impact its penetration depth, see also Alexander et al., 2014; Gorti, 2016);[(3)] Gorti et al. (2015) estimated that dust evolution only plays a minor role.

Small dust particles efficiently absorb FUV photons. Nakatani et al. (2018a) reported that this holds for heavy atoms, too, whose abundance can be parametrised in terms of the metallicity Z, with $Z_\odot$ the solar value.[(4)] While for $Z \lesssim 10^{-2}\,Z_\odot$, ionisable material is too sparse to allow for efficient FUV heating, they found mass-loss rates as high as $\dot{M}_{\rm FUV} \lesssim 10^{-7}\,{\rm M}_\odot/{\rm yr}$ for $0.1 \lesssim Z\,[Z_\odot] \lesssim 10$, with $\dot{M}_{\rm FUV} \propto Z^{-0.85}$ within the latter range, indicating an increasing shielding of further-out disk regions at high Z.[(5)] Like the earlier study of Gorti & Hollenbach (2009), Nakatani et al. (2018a) reported a very substantial fraction of $\dot{M}_{\rm FUV}$ emerging from $R \gtrsim 100\,$AU. Nakatani et al. (2018b) extended the model of Nakatani et al. (2018a) by an X-ray component, and found FUV irradiation to drive the main $\dot{M}_{\rm wind}$ except for metallicities $Z < 10^{-1.5}\,Z_\odot$, where the X-ray component dominated. Subsequently, Komaki et al. (2021) investigated the dependence of $\dot{M}_{\rm FUV}$ in that model on M_*, $L_{\rm FUV}$, and $L_{\rm X}$; they deduced (Komaki et al., 2021)

$$\dot{M}_{\rm FUV} \propto M_*^2 \cdot \sqrt{L_{\rm FUV}}\,. \tag{2.83}$$

Furthermore, they found $\dot{M}_{\rm wind} \propto L_{\rm X}^{0.25}$ for an FUV-dominated scenario, and $\dot{M}_{\rm wind} \propto L_{\rm X}^{0.6}$ for an X-ray-dominated one. The latter relation is still shallower than Eq. (2.81), although somewhat in line with the results of Picogna et al. (2019) for $L_{\rm X} \gtrsim 10^{30}\,$erg/s; as pointed out by Gorti et al. (2009) and Ercolano et al. (2021), the simulations of Gorti & Hollenbach (2009), Gorti et al. (2009), Wang & Goodman (2017b), and Nakatani et al. (2018b) used a rather hard X-ray spectrum (see also Sect. 2.3.3.2), which may well explain the differences.

2.3.3.4 External photoevaporation

Stars are born in clusters (see Sect. 2.1), so protoplanetary disks are unlikely to evolve in isolation. Based on HST images of the Orion Nebula Cluster, already O'Dell et al. (1993) proposed that protoplanetary disks may be dispersed by radiation from nearby massive stars (see also O'Dell & Wen, 1994). This was formalised by Johnstone et al. (1998), who argued that EUV and FUV photons from sources external to the disk could drive a mass outflow from $R \gtrsim 0.5\,R_{\rm grav}$ (or even $R \gtrsim 0.2\,R_{\rm grav}$, see also Adams et al., 2004), emptying them within a timeframe of around $10^6\,$yr (see also e.g. Clarke, 2007; Alexander et al., 2014). In contrast to external FUV irradiation, neither common EUV (see e.g. Scally & Clarke, 2001) nor X-ray (see e.g. Rab et al., 2018) radiation fields drive significant (external) mass losses $\dot{M}_{\rm ext}$; close encounters have an even smaller impact on disk evolution (see e.g. Adams et al., 2006; Winter et al.,

(1) Observational data as to the abundance of PAHs in protoplanetary disks are still sparse, further complicating simulations; new observational campaigns are being designed to resolve this issue (see e.g. Ercolano et al., 2022).

(2) A direct comparison of their results to XEUV models is difficult because they only provide an X-ray-only scenario alongside their combined model of EUV, FUV, and X-ray photoevaporation; furthermore, their (1+1D) models do not evolve hydrodynamically (see also Ercolano & Pascucci, 2017), which Owen et al. (2010) found to be important at least for XEUV irradiation.

(3) By contrast, X-ray penetration depth is mainly dependent on the gas (see e.g. Rab et al., 2018).

(4) In the astrophysical sense, 'metals' are atoms heavier than hydrogen or helium. The metallicity Z describes the mass fraction of these metals, such that in combination with the mass fraction of hydrogen, X, and helium, Y, the total is $X + Y + Z = 1$ (see e.g. Wallerstein & Carlson, 1960; Asplund et al., 2009).

(5) Ercolano & Clarke (2010) investigated the Z-dependence of X-ray irradiation; they found a comparable $\dot{M}_{\rm X} \propto Z^{-0.77}$.

2018). So as $R_{\mathrm{grav}} \approx 100\,\mathrm{AU}$ for FUV heating (see e.g. Adams et al., 2004), disks can be cleared down to their inner 10...30 AU in case of a strong external FUV field (see e.g. Adams et al., 2004, 2006; Haworth et al., 2018; Parker et al., 2021a).[1]

The actual impact external irradiation has on a specific disk strongly depends on its position in and motion through its host cluster, and the stellar density therein (see e.g. Scally & Clarke, 2001). The importance of the initial position is debated. Mann & Williams (2010); Mann et al. (2014) reported truncated masses for the protoplanetary disks closest to a high-luminosity source in Orion,[2] and similar trends have also been observed in other regions (see e.g. Ansdell et al., 2017; van Terwisga et al., 2020); yet this may just be a projection effect (Mann et al., 2015; Parker et al., 2021b).

Building on the work of Haworth et al. (2016b), Haworth et al. (2018) performed an extensive parameter study of disk sizes, disk and stellar masses, and the (external) FUV field; their results show a very clear dependence of $\dot{M}_{\mathrm{ext}}$ on all of these parameters. $\dot{M}_{\mathrm{ext}}$ was found to scale with R_{disk} (see also e.g. Facchini et al., 2016; Haworth et al., 2016b), M_{disk}, and FUV field strength; high stellar masses can reduce mass loss due to their deeper gravitational potential (see also e.g. Adams et al., 2004; Winter et al., 2019). In absolute terms, 'optimal' systems with low M_*, and high M_{disk} and R_{disk}, were computed to reach $\dot{M}_{\mathrm{ext}} > 10^{-6}\,\mathrm{M}_\odot/\mathrm{yr}$ in a high-radiation environment (see also Parker et al., 2021a); this is considerably higher than the (already high) $\dot{M}_{\mathrm{ext}} \gtrsim 10^{-7}\,\mathrm{M}_\odot/\mathrm{yr}$ reported by earlier studies and targeted observations (see e.g. Henney et al., 2002; Facchini et al., 2016). By contrast, disks of smaller size and mass in a weak external FUV field can experience $\dot{M}_{\mathrm{ext}} < 10^{-10}\,\mathrm{M}_\odot/\mathrm{yr}$ (i.e. significantly smaller than $\dot{M}_{\mathrm{XEUV}}$ or $\dot{M}_{\mathrm{FUV}}$, see Sects. 2.3.3.2 and 2.3.3.3). To illustrate their results, Haworth et al. (2018) applied them to the Taurus star-forming region; for the sample of stars modelled, they retrieved $10^{-10} \lesssim \dot{M}_{\mathrm{ext}}\,[\mathrm{M}_\odot/\mathrm{yr}] \lesssim 4 \cdot 10^{-6}$. The effect of external FUV irradiation is hence strongly dependent on the particular birth environment and location of a protostellar system. Parker et al. (2021a) noted that the quantity of nearby high-mass ($M_* \gtrsim 5\,\mathrm{M}_\odot$) stars determines the overall evolution of the neighbourhood (see also van Terwisga et al., 2019); even in low-density clusters, a considerable fraction of disks may be photoevaporated within a few Myr. Viscous spreading of the disks (see Sect. 2.2.2.3) can further reduce disk lifetimes by a factor of a few because it spreads the disk mass and replenishes the outer regions (Parker et al., 2021a).

As suggested by Winter et al. (2019), disk dispersal could be probed observationally by analysing the relation between M_{disk} and M_* (commonly $M_{\mathrm{disk}} \propto M_*^{1\ldots1.9}$, see Sect. 2.2.1.3); they stated that external FUV irradiation should steepen it to over $M_{\mathrm{disk}} \propto M_*^{2.7}$. Furthermore, Winter et al. (2020) proposed $\dot{M}_{\mathrm{wind}} > \dot{M}_{\mathrm{acc}}$ as a tracer for regions with ongoing (strong) external photoevaporation.

Like for internal FUV irradiation, small dust grains can shield disk regions from heating; so Facchini et al. (2016) found that dust growth can results in strongly enhanced $\dot{M}_{\mathrm{ext}}$. Concerning the dust reservoir itself, simulations by Sellek et al. (2020a) saw blow-out of up to half of the entire dust budget of the disk while grains were still small enough to be entrained, that is within around 10^5 yr (see also Adams et al., 2004); larger grains were found to drift inward.[3]

2.3.3.5 Provisional summary

Already on its own, the topic of photoevaporation is rather diverse. While EUV irradiation alone cannot provide sufficient mass-loss rates to drive disk dispersal, X-ray and/or FUV heating can; but the relative magntiudes of $\dot{M}_{\mathrm{XEUV}}$ and $\dot{M}_{\mathrm{FUV}}$ are still debated. Further modelling, for instance by adding FUV photons (as well as the thereby necessitated, full chemical modelling) to the models of Picogna et al. (2019), refined with the updated spectra of Ercolano et al. (2021), should allow for a better understanding of the relative importance of the different energy ranges. Alternatively, a variation of the X-ray spectrum in the (FUV-dominated) simulations of Nakatani et al. (2018b) would provide additional insights.

The current, tentative consensus in the field seems to be that XEUV photoevaporation drives inside-out dispersal, while FUV irradiation, both from the star itself and its environment, drives mass loss at large R, potentially entailing an 'outside-in' dispersal of the disk (Ercolano & Pascucci, 2017). EUV irradiation serves to heat the regions close(st) to the star, and gains in importance after the formation of a gap (see Sect. 2.3.3.1). This matches the comparison of the individual $\dot{M}_{\mathrm{wind}}(R)$ compiled by Armitage (2011, their Fig. 9) and Alexander et al. (2014, their Fig. 3), but neglects the small peak in $\dot{M}_{\mathrm{FUV}}$ at

[1] The strength of the field is usually specified in units of $G_0 = 1.6 \cdot 10^{-3}\,\mathrm{erg}/(\mathrm{cm}^2\,\mathrm{s})$ for $912 < \lambda\,[\mathrm{Å}] < 2400$ (see Habing, 1968, and compare Table 2.1).

[2] The star in question, θ_1 Orionis C, is so bright that in order to explain that there still are disks around it at all, a birth within the last $< 2\,\mathrm{Myr}$ needs to be invoked (Scally & Clarke, 2001; Clarke, 2007).

[3] Conversely, Parker et al. (2021b) claimed that even a strong FUV background does not lead to high mass-loss in terms of dust, but simply assumed a low fraction of small grains. Yet for instance, Ansdell et al. (2017) reported an observed reduction in dust masses (which may however be a projection effect as noted above, see Parker et al., 2021b).

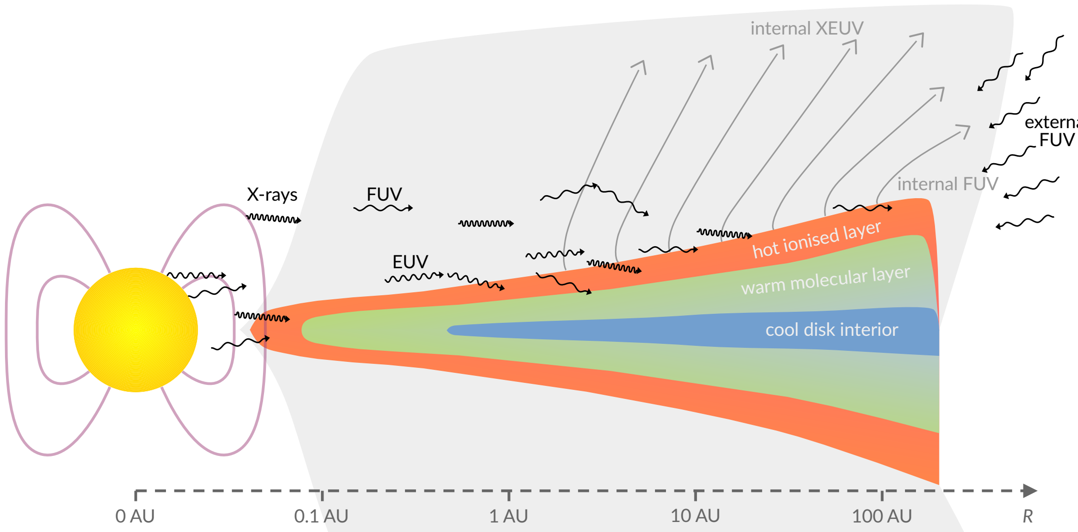

Figure 2.3: Schematics of a disk irradiated by high-energy photons, and the resulting photoevaporative outflow (adatpted from Armitage, 2015; Ercolano & Pascucci, 2017; Armitage, 2018; Picogna et al., 2019; Ercolano et al., 2021), not accounting for MHD effects. EUV heating is most effective close to the star and does not penetrate far into the disk, X-rays heat the upper disk layers in particular at intermediate R, and either internal (sketched below the disk midplane) or both internal and external (sketched above the disk midplane) FUV photons drive the mass-loss from high R. Apart from the rudimentary scaling indicated for R, the plot is not to scale.

$R \simeq 10\,\mathrm{AU}$ found there. The impact of external irradiation is highly variable; Alexander et al. (2014) conclude that it likely matters most for stars born close to the centers of massive clusters. As shown for instance by van Terwisga et al. (2019), some systems may be largely unaffected by it.

In terms of the disk temperature profile, the penetration depths of Table 2.1 provide a first idea of which type of radiation heats which regions. A very rough sketch of the resulting structure for a photoevaporating disk (as discussed above, and without accounting for the MHD winds of Sect. 2.3.1) is provided in Fig. 2.3. However, the lack of full parameter studies for a combined model of winds driven by a combination of EUV, X-ray, and FUV photons means there are still various uncertainties in the model (see e.g. Alexander et al., 2014; Ercolano & Pascucci, 2017).

2.3.4 Magneto-thermal winds

So far, we have treated disk winds as driven by either magnetic effects or photoevaporation. Yet as already noted in Sect. 2.3.1, ionisation levels induced by highly energetic photons can heavily impact (non-)ideal MHD processes, and conversely, strong magneto-centrifugal winds may dominate over photoevaporative ones. Furthermore, MHD winds can be launched from the regions close to the star where photoevaporation is ineffective (see e.g. Bai & Stone, 2013; Ercolano & Pascucci, 2017; Wang & Goodman, 2017b), and from where the HVC of the wind originates (see e.g. Sheikhnezami et al., 2012; Armitage et al., 2013). For a comprehensive model of angular-momentum transport and mass loss (evolution) in protoplanetary disks, combined, self-consistent studies are therefore necessary (see e.g. Bai et al., 2016), even though these are still prohibitively expensive and thus commonly simplified in some way (see e.g. Béthune et al., 2017; Picogna et al., 2019; Wang et al., 2019; Gressel et al., 2020).(1) This gives rise to magneto-thermal wind models, that is magnetically co-driven winds launched from a heated disk surface layer (see e.g. Bai, 2017; Béthune et al., 2017; Wang et al., 2019); mass loading is thought to be primarily due to thermal pressure gradients (Bai et al., 2016; Gressel et al., 2020; Lesur, 2020), but magnetic forces cannot be excluded (Béthune et al., 2017). The underlying disks are found to be laminar (see e.g. Gressel et al., 2015; Bai, 2017), and similarly to photoevaporative outflows, the winds are launched from the (FUV) ionisation front at a few H_{gas} (see e.g. Gressel et al., 2015; Bai et al., 2016, and Sect. 2.3.1); yet also EUV (Wang et al., 2019) and X-ray (Bai, 2017) irradiation affect the outflow. To accurately model the wind structure, the disk-wind interface needs to be modelled self-consistently (see e.g. Gressel et al., 2020).

(1) While semi-analytical models of both MHD (Lesur, 2021) and photoevaporative (Clarke & Alexander, 2016; Sellek et al., 2021) exist, these have not yet been combined into a unified model (which may be rather complex to do).

An additional aspect of combining MHD and PE is that the former can account for angular momentum transport, and hence $\dot{M}_{\rm acc}$ (see e.g. Bai et al., 2016; Bai, 2016, 2017; Ercolano & Pascucci, 2017; Rodenkirch et al., 2020); so even if photoevaporative outflows dominate $\dot{M}_{\rm wind}$ (as used to be hypothesised, see e.g. Bai et al., 2016), magneto-centrifugal ones are non-negligible for overall disk evolution, in particular in low-turbulence disks (see e.g. Béthune & Latter, 2020). $\dot{M}_{\rm acc}$ and $\dot{M}_{\rm wind}$ were shown to depend on the magnetic background field B_z (see e.g. Bai et al., 2016; Bai, 2016); Béthune et al. (2017) retrieved $\dot{M}_{\rm wind} \propto \beta^{-1/2}$ (i.e. $\dot{M}_{\rm wind} \propto B_z$, see Eq. 2.77). This matches the MHD-dominated regime of Rodenkirch et al. (2020, $\beta \lesssim 10^7$), which yielded up to $\dot{M}_{\rm wind} \simeq 6 \cdot 10^{-7} {\rm M}_\odot/{\rm yr}$ at $\beta = 10^5$, and down to $\dot{M}_{\rm wind} \simeq 1 \cdot 10^{-8} {\rm M}_\odot/{\rm yr}$ in the PE-dominated case of $\beta > 10^7$. These wide ranges in mass-loss rates illustrate the importance of better confining B_z, which to date is large unconstrained (see e.g. Bai et al., 2016; Vlemmings et al., 2019; Rodenkirch et al., 2020; Lankhaar et al., 2022); however, as is the case with external photoevaporation (see Sect. 2.3.3.4), it may be highly specific to the environment of the protostellar system (see also Béthune et al., 2017).

Since the field of magneto-thermal winds is still developing rapidly, drawing a conclusion here would be premature; however, the studies conducted thus far have suggested that disk winds likely are the main force behind the evolution of circumstellar disks (see e.g. Bai, 2016), in particular winds launched from the outer disk ($R \gtrsim 1...10\,{\rm AU}$; see e.g. Kunitomo et al., 2020). While the models are still not detailed enough to allow a final verdict on whether magnetic or photoevaporative effects dominate, and at which distances from the star and evolutionary stages (see e.g. Rodenkirch & Dullemond, 2022), MHD-driven and PE-driven winds may well serve different roles (Kunitomo et al., 2020). In this context, taking a closer look at one or more components of these disk winds – as we will do in the following chapters – should allow for model benchmarking and subsequential refinement, which in turn will benefit future simulation efforts.

Chapter 3

Dust entrainment: The impact of X-rays

The contents of this chapter have been published as Franz et al. (2020).[(1)]

Chapter abstract

Context: X-ray- and EUV- (XEUV-) driven photoevaporative winds acting on protoplanetary disks around young T-Tauri stars may crucially impact disk evolution, affecting both gas and dust distributions.

Aims: We investigate the dust entrainment in XEUV-driven photoevaporative winds and compare our results to existing MHD and EUV-only models.

Methods: We used a 2D hydrodynamical gas model of a protoplanetary disk irradiated by both X-ray and EUV spectra from a central T-Tauri star to trace the motion of passive Lagrangian dust grains of various sizes. The trajectories were modelled starting at the disk surface in order to investigate dust entrainment in the wind.

Results: For an X-ray luminosity of $L_{\mathrm{X}} = 2 \cdot 10^{30}$ erg/s emitted by a $M_* = 0.7\,\mathrm{M}_\odot$ star, corresponding to a wind mass-loss rate of $\dot{M}_{\mathrm{wind}} \simeq 2.6 \cdot 10^{-8}\,\mathrm{M}_\odot/\mathrm{yr}$, we find dust entrainment for sizes $a_0 \lesssim 11\,\mu$m ($9\,\mu$m) from the inner 25 AU (120 AU). This is an enhancement over dust entrainment in less vigorous EUV-driven winds with $\dot{M}_{\mathrm{wind}} \simeq 10^{-10}\,\mathrm{M}_\odot/\mathrm{yr}$. Our numerical model also shows deviations of dust grain trajectories from the gas streamlines even for μm-sized particles. In addition, we find a correlation between the size of the entrained grains and the maximum height they reach in the outflow.

Conclusions: X-ray-driven photoevaporative winds are expected to be dust-rich if small grains are present in the disk atmosphere.

[(1)] This work resulted from a collaboration with the coauthors listed in the corresponding bibliography entry, that is G. Picogna (GP), B. Ercolano (BE), and T. Birnstiel (TB). In particular, GP provided the steady-state gas disk model as well as the code for the particle motion and provided guidance for the initial setup. BE and TB helped with the interpretation and discussion of the results. The author (RF) adapted the particle code for the new use case, reworked it to significantly reduce computational times, extracted and evaluated the dust trajectories from the simulations, and drafted the manuscript.

3.1 Introduction

Planets form from the gas and dust surrounding newly born stars, whose physical properties and final dispersal are strongly influenced by the stellar irradiation from their host star. In particular, high-energy radiation may warm up the disk atmosphere, launching a thermal wind (see e.g. Hollenbach et al., 1994; Gorti & Hollenbach, 2009; Alexander et al., 2014). Models predict that this photoevaporative wind can ultimately disperse the disk and may have important consequences for the formation and evolution of planetary systems (Alexander & Pascucci, 2012; Ercolano & Rosotti, 2015; Ercolano & Pascucci, 2017; Carrera et al., 2017; Jennings et al., 2018; Monsch et al., 2019).

Despite the potential influence of this process on the formation of planets, the magnitudes of photoevaporative winds are still largely uncertain, with model predictions diverging by several orders of magnitude (Armitage, 2011; Alexander et al., 2014; Ercolano et al., 2017a). One problem is that to date, the only direct evidence of these winds is blue-shifted forbidden-line emission towards T-Tauri stars, including [Ne II] 12.8μm and [O I] 6300Å(e.g. Hartigan et al., 1995; Pascucci et al., 2008; Rigliaco et al., 2013; Natta et al., 2014; Simon et al., 2016; Banzatti et al., 2019). While the intensity and low-resolution profiles of these lines can be matched very well by X-ray photoevaporation models (Alexander, 2008; Ercolano & Owen, 2010, 2016), it has been demonstrated that these lines do not trace the base of the wind. Furthermore, their extreme temperature dependence makes them a tracer of the heating mechanism of an already unbound wind rather than tracing the wind-driving mechanism itself (Ercolano & Owen, 2016). An additional problem is that high resolution data has revealed very complex line profiles which may include components emitted in a magnetically-driven wind (Banzatti et al., 2019).

Different types of wind diagnostics would be desirable for constraining disk dispersal models; small dust grains – which can be entrained by the wind – may provide an interesting avenue towards this end (Giacalone et al., 2019). A previous work by Owen et al. (2011a) has shown that grains up to about 2 μm in size (i.e. radius) can be lifted up and blown out by an EUV-driven wind around a Herbig Ae/Be star. More recently, Hutchison et al. (2016b) have investigated EUV-driven dust outflow by means of a two-fluid smoothed particle hydrodynamics (SPH) code (Hutchison et al., 2016a); they find entrainment of grains of up to 4 μm around a 0.75 $M_\odot$ T-Tauri star (although they note that this value may drop to about 1 μm due to grains settling towards the disk midplane). Both Owen et al. (2011a) and Hutchison et al. (2016b) show that the wind selectively entrains grains of different sizes from different radii. This results in a dust population which spatially varies in the wind, due to the topology of the gas streamlines which propagate almost radially outwards. At NIR wavelengths, this variable grain population produces a 'wingnut' morphology which may already have been observed in the case of PDS 144N (Perrin et al., 2006). Yet Owen et al. (2011a) could not reproduce the color gradient of the observations, which show redder emission at larger heights above the disk; they suggest that this could be because the synthetic observations might be dominated by emission from the smallest grains entrained in the flow. Grain growth in the underlying disk (see Testi et al., 2014), which they neglected in their calculations for simplicity, could reduce the population of small grains, and may hence provide a solution to this color problem. While it is unclear whether the observations of PDS 144N can be explained by dust entrainment in a photoevaporative wind, Owen et al. (2011a) have demonstrated that a significant amount of small grains – which dominate the opacity in the FUV – do populate disk winds, and hence play an important role in their chemistry.

In this work, we study the entrainment of dust grains in an X-ray driven wind around a T-Tauri star. For this we use a particle approach (Picogna et al., 2018), bootstrapped onto a steady-state hydrodynamical simulation of a photoevaporating disk (Picogna et al., 2019). Our results aim to facilitate more detailed studies of the detectability of winds in scattered light, as well as wind opacity models. The latter should allow for more realistic chemical modelling of the gas in the wind, enabling us to search for new wind diagnostics.

This chapter is organised as follows: We present the numerical setup of the gas disk and photoevaporative disk wind, and the dust grain evolution in Sect. 3.2. In Sect. 3.3, we take a detailed look at what we can extract from the dust grain trajectories we obtain. We discuss our findings in Sect. 3.4 and summarise them in Sect. 3.5.

3.2 Methods

The dynamics of dust grains in protoplanetary disks can be studied either by directly integrating the orbits of a large number of dust 'super-particles', which sample the local properties of the dust population, or by solving the collisionless Boltzmann equation for the particle distribution function. For a population of very small (i.e. tightly coupled to the gas) dust particles, the Boltzmann equation can be reduced to the zero-pressure fluid equation (Cuzzi et al., 1993; Garaud et al., 2004); this 'two-fluid' approach has already been used to study planet-disk interactions (e.g. Paardekooper & Mellema, 2004, 2006; Zhu et al., 2012). However, it is limited to a single population of small particles as it cannot account for the full velocity distribution of the grains at a single location, and it is not able to capture strong density gradients.

In contrast, a particle approach as implemented by Picogna et al. (2018) has the notable advantage of following the evolution of solid particles with different physical properties, recovering the dust dynamics very well also in the limit where the grains are decoupled from the gas (Youdin & Johansen, 2007; Miniati, 2010; Bai & Stone, 2010). This method has been successfully applied to the study of planet-disk interaction with both SPH and grid-based codes (Fouchet et al., 2007; Lyra et al., 2009; Fouchet et al., 2010; Ayliffe et al., 2012; Zhu et al., 2014), and to modelling the draining of dust grains from the inner region of a photoevaporating transition disk (Ercolano & Pascucci, 2017).

3.2.1 Gas disk with XEUV wind

The set-up of the hydrodynamical calculations for the gas disk has been described in detail in Picogna et al. (2019), so here we limit ourselves to summarising the basic parameters of the specific run employed in this work. We studied a protoplanetary disk of $M_{\mathrm{disk}} \simeq 0.01\,M_*$ around a $M_* = 0.7\,M_\odot$ T-Tauri star. This star was set to emit X-ray and EUV radiation according to the emission line spectrum presented by Ercolano et al. (2008b, 2009); the X-ray luminosity of the star was $L_{\mathrm{X}} = 2 \cdot 10^{30}\,\mathrm{erg/s}$, which is close to the median of the X-ray luminosity distribution for this stellar mass (Preibisch et al., 2005).

The hydrodynamics (HD) simulations were performed via a modified version of the `Pluto` code. In this version, at each HD step, temperatures are updated according to the local ionization parameter[(1)] and column density to the central source (for further details, see Picogna et al., 2019). The temperature parametrization was obtained via detailed radiative-transfer calculations using the `Mocassin` code (Ercolano et al., 2003, 2005, 2008a). Within the `Pluto` code used for the gas evolution (Mignone et al., 2007), we employed a 2.5D Eulerian grid in spherical coordinates.[(2)] To avoid any boundary effects, a large radial range of $0.33 \le r\,[\mathrm{AU}] \le 1000$ in 412 logarithmically-spaced steps was modelled, with $0.005 \le \vartheta \le \pi/2$ in 320 uniform steps.

The v_r- and ϱ-profiles of the gas disk employed for the simulations are showcased in Fig. 3.1; we used only the inner $\approx 300\,\mathrm{AU}$ (352 cells) of the hydrodynamical grid in order to follow the dust evolution because the mass loss due to the photoevaporative wind becomes negligible at larger radii (see Picogna et al., 2019).

The (sonic) disk surface is defined as the plane where the gas velocities change from locally sub- to super-sonic. The base of the X-ray and EUV (XEUV) flow, by contrast, is given by the location of the largest temperature gradient (see e.g. Ercolano et al., 2009), and lies slightly below the sonic surface. It coincides with a strong drop in gas density (see Fig. 3.1).

Due to the high grid resolution employed and the disk having settled into a stable (quasi-equilibrium) state, the (numerically computed) base of the wind is quite smooth (as would be expected; see also Bai, 2017); hence, we forgo additional artificial smoothing. In Fig. 3.1, we have added lines indicating one, 3.5, and 5.5 scale heights H, the latter two framing the base of the flow; here we use $H = h \cdot R$, and $H = c_s/\Omega_K$, with c_s the local sound speed and $\Omega_K = \sqrt{G\,M_*/r^3}$ the Keplerian orbital velocity.

The flow base being located at a scale height of $h \simeq 0.08$ (0.14; 0.23) at $R = 10\,\mathrm{AU}$ (100 AU; 300 AU) implies that the disk is still rather hot and puffed up and that the dust grains have to travel rather far above the midplane if they are to enter the wind region (see comparable simulations by Owen et al., 2012; Bai, 2016).

3.2.2 Dust grains

The dust grains were modelled as passive Lagrangian particles inserted in the steady-state gas solution, as originally implemented by Picogna et al. (2018), to whom we refer for the details of the implementation.[(3)] The motion of these particles is driven by their gravitational attraction towards the central star, the drag force from the surrounding gas, and turbulent diffusion below the disk surface as prescribed by Charnoz et al. (2011).

[(1)] The ionization parameter is defined as $\xi = L_*/(n\,r^2)$, with L_* the stellar luminosity, n the gas density, and r the (spherical) radial distance from the star.

[(2)] '2.5D' meaning a 2D coordinate system (r, ϑ) with 3D velocity information $(v_r, v_\vartheta, v_\varphi)$.

[(3)] We are dropping their non-inertial $\vec{F}_{\mathrm{nonin}}$ because we are not including a planet in our simulations.

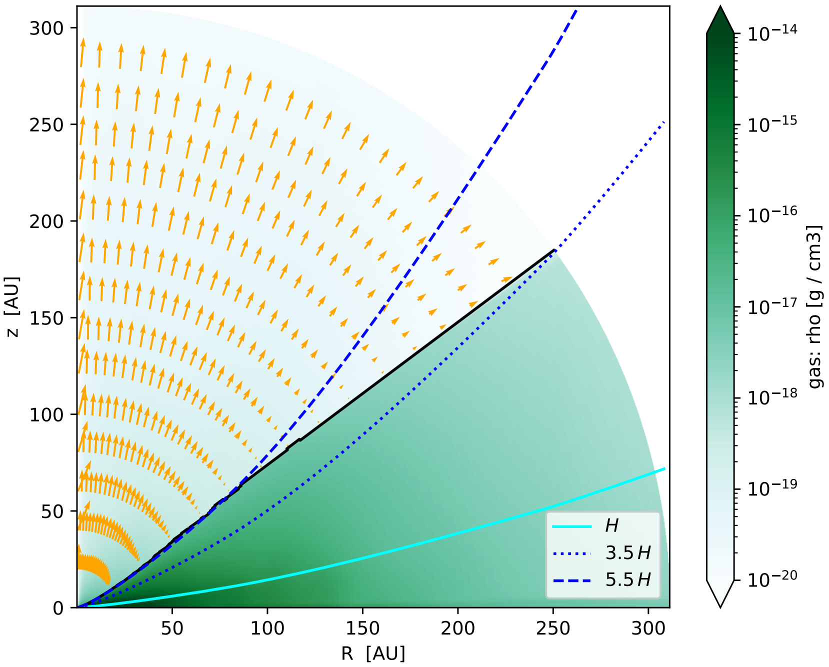

Figure 3.1: Density (green) and velocity map (yellow arrows: $\vec{v}$) of the gas disk model from Picogna et al. (2019). The base of the XEUV flow (i.e. the location of the largest gradient in temperature) is shown in black, and coincides with a strong drop in density. v_r is pointing radially outwards everywhere in the wind but very close to the sonic surface where $\vec{v}$ points outwards, but away from the disk (for $R < 200\,\mathrm{AU}$). The cyan line represents $z(R) = H$; additional lines for $3.5\,H$ (dotted blue) and $5.5\,H$ (dashed blue) show the range of scale heights the disk surface covers.

Ormel & Liu (2018) give a concise comparison of their stochastic equation of motion to the strong-coupling approximation of Charnoz et al. (2011). Although the former may be preferable for modelling grain motion within the disk, we are mainly interested in what happens once a grain enters the wind region where the gas density and thus turbulence are low; hence, just like Giacalone et al. (2019) proceed for their MHD-wind model of dust motion, we do not optimise our model for the disk interior.

Above the disk surface, gas densities are too low to induce kicks (see Fig. 3.1), allowing us to neglect an otherwise necessary (Flock et al., 2017), more intricate distinction between MRI and VSI.[(1)]

3.2.2.1 Grain sizes

In their EUV-only simulations, both Owen et al. (2011a) and Hutchison et al. (2016b) find that grains around μm size are entrained. In the MRI computations of Miyake et al. (2016), the grain distribution considered is $0.1 \leq a_0\,[\mu\mathrm{m}] \leq 100$, and the maximum entrainable grain size is found to decrease very steeply with the (cylindrical) midplane radius $R = \sqrt{x^2 + y^2}$. Furthermore, Giacalone et al. (2019) investigate $5 \cdot 10^{-3} \lesssim a_0\,[\mu\mathrm{m}] \lesssim 5$.

Therefore, we ran an initial set of simulations with grain sizes $10^{-3} \leq a_0\,[\mu\mathrm{m}] \leq 10^2$, which established that for our model, the size barrier for wind blow-out lies between 5 and $15\,\mu$m. On the basis of this initial experiment, we restricted our size range to $0.01 \leq a_0\,[\mu\mathrm{m}] \leq 20$, with steps of $\Delta a_0 = 1\,\mu$m for $1 \leq a_0\,[\mu\mathrm{m}] \leq 15$. We forwent a higher size resolution in favor of increasing spatial resolution, that is tracing more dust grains per each size. All different a_0 modelled are listed in Table 3.1 (and Fig. 3.2); per size, we simulated the trajectories of at least 5,000 dust grains, yielding at least 25 grains per 1 AU of launching radius along the disk surface.

3.2.2.2 Internal grain density

Following Owen et al. (2011a) and in order to facilitate a direct comparison to their results, we assume a uniform internal density of $\varrho_{\mathrm{grain}} = 1\,\mathrm{g/cm}^3$ for the dust particles. This value is on the lower end of

(1) Flock et al. (2017) investigate this difference and conclude that the VSI may be more adept at lifting up grains.

the $0.3 \lesssim \varrho_{\rm grain}\,[{\rm g/cm^3}] \lesssim 6.2$ interval established by Love et al. (1994), and agrees best with the values Joswiak et al. (2007) find for material of cometary origin ($0.6 \lesssim \varrho_{\rm grain}\,[{\rm g/cm^3}] \lesssim 1.7$). Similar values are used in other works, too (e.g. Tamfal et al., 2018; Owen & Kollmeier, 2019).

Other models employ somewhat different values for $\varrho_{\rm grain}$. For instance, Li & Greenberg (1997) and Miyake et al. (2016) use the average value given by Love et al. (1994), $\varrho_{\rm grain} \simeq 2\,{\rm g/cm^3}$; Hutchison et al. (2016b) and Flock et al. (2017) employ $\varrho_{\rm grain} = 3\,{\rm g/cm^3}$, and Weingartner & Draine (2001) and Giacalone et al. (2019) use $\varrho_{\rm grain} = 3.5\,{\rm g/cm^3}$. These values are closer to the ones Joswiak et al. (2007) find for asteroidal material, which may have been heated slightly less than the cometary grains. Future on-site analysis of interplanetary and interstellar dust grains will provide further constraints on these intervals (e.g. Arai et al., 2018, Destiny+).

3.2.2.3 Initial positioning

We position our grains directly on the base of the flow which is located slightly below the disk surface. This allows us to study their trajectories from when they enter the wind-dominated region above the disk. Within $0.33 \leq r\,[{\rm AU}] \leq 200$, we use a random distribution uniform in r for the initial placement.

The left panel of Fig. 3.2 shows the initial grain positioning along the base of the flow (in black), with the dust grains colored according to their size.

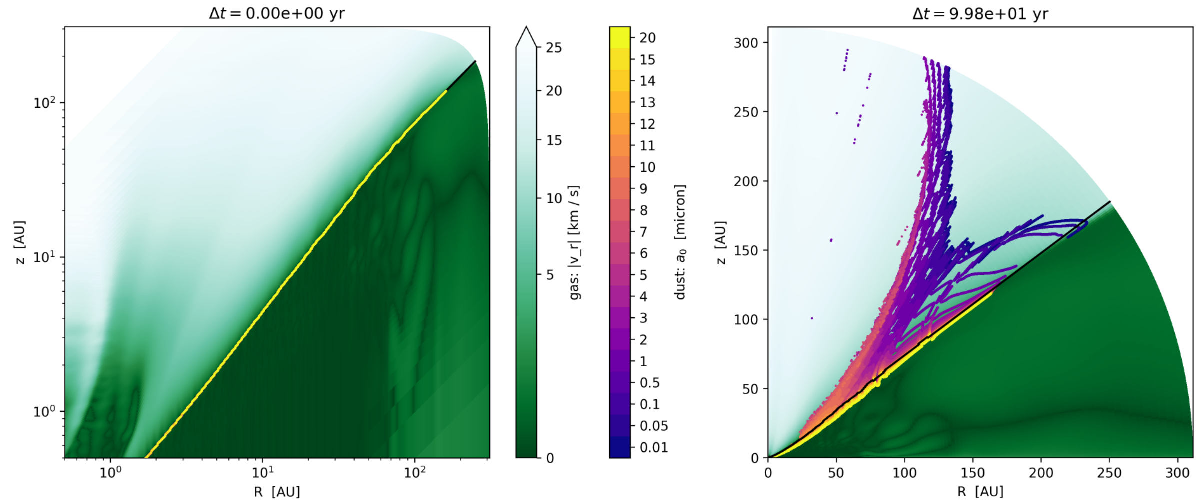

Figure 3.2: *Left*: Initial placement of the dust grains at $\Delta t = 0$ at the base of the photoevaporative flow (black), slightly below the sonic surface. The grains are colored according to their size and the color scale (scaling with $\sqrt{|v_r|}$) of the gas disk represents the extent of its local radial velocity (with $-2 \lesssim v_r\,[{\rm km/s}] \lesssim 30$). The gas map is mostly smooth in the region of interest, that is everywhere but close to the midplane at high R. *Right*: A snapshot of the grain positions at $\Delta t \simeq 100\,{\rm yr}$, all else equal. The very low spread of the lines of individual grain sizes is due to the initial setup, placing particles directly on the disk surface without a spread in their initial velocities. For comments on this, see also Sects. 3.3 and 3.6.2.

Our model is intended to be combined with a vertical mixing prescription later on in order to extract a realistic dust density distribution in the wind. So we may very well, just as Hutchison et al. (2016b) note they did, model grain sizes that will not migrate far enough vertically to actually reach the wind region (see also Youdin & Lithwick, 2007; Krijt & Ciesla, 2016).

The dust grains were placed – and remain – well outside of the sublimation radius applicable for a $M_* = 0.7\,{\rm M_\odot}$ star (Giacalone et al., 2019). However, we note that the intense X-ray radiation from the young stellar object may destroy PAH-size grains in the disk atmosphere before they can be entrained in the wind (Siebenmorgen & Krügel, 2010; Siebenmorgen & Heymann, 2012); we did not include such events in our simulation.

3.2.2.4 Initial velocities

We initialised our dust particles to start from a quasi-equilibrium; so we set both $v_{r,0}$ and $v_{\vartheta,0}$ to 0 because the local gas velocities are quite low anyways and will hence not cause a strong upwards motion

($|v_\vartheta| \lesssim 50\,\mathrm{m/s}$ along the disk surface compared to $|v_r| \lesssim 200\,\mathrm{m/s}$).

For $v_{\varphi,0}$, we assumed a Keplerian velocity of $v_{\varphi,0} = r\,\Omega_K$; since the starting positions are at $z \gtrsim 3.5\,H$ (see Fig. 3.1), we computed the Keplerian speed for the spherical radius r, and not for the midplane radius R.

3.2.2.5 Further limitations

To cut computational costs and allow for a reasonable amount of particles to be modelled, we made a series of simplifying assumptions:

Firstly, we neglected MHD effects.[(1)]

Secondly, we did not include self-gravity from the disk. We show in Sect. 3.6.1 that this simplification should not significantly affect our results.

Thirdly, we did not include dust-gas back reactions. As shown by Dipierro et al. (2018) and Tamfal et al. (2018), these are important in the disk midplane; but we focus our modelling efforts on the wind regions above the disk, where dust-to-gas ratios are not expected to be enhanced (Krijt & Ciesla, 2016).

Fourthly, dust-dust interactions were neglected. The gas drag accelerates the dust grains to at least a few km/s (i.e. $v_{r,\mathrm{esc}} = \sqrt{2\,G\,M/r} \approx 11\,\mathrm{km/s}$ at $r = 10\,\mathrm{AU}$, or $v_{r,\mathrm{esc}} \approx 2\,\mathrm{km/s}$ at $r = 300\,\mathrm{AU}$), but the dust densities in the wind are much lower than around the disk midplane. At the latter, the growth time scale is already around 10^2 to 10^3 yrs (Birnstiel et al., 2016). We shall see below that therefore, assuming no interactions provides a reasonable approximation.

3.3 Results

We traced the trajectories of the dust grains over time until they either leave the computational domain or until the simulation time frame of $\Delta t_{\mathrm{sim}} \simeq 2.2\,\mathrm{kyr}$ ends.

If they left the domain, they were replaced by a new grain of the same size, placed as described in Sect. 3.2; the actual amount of dust particles modelled per a_0 is listed in Table 3.1.[(2)] Merely for visualizing the actual simulation, the right panel of Fig. 3.2 shows a snapshot of the simulation after around 100 yr.

A selection of trajectories obtained from the simulation is shown in Fig. 3.3; for clarity, we limit ourselves to plots for three distinguished grain sizes (0.1, 4, and 10 μm) below. These were chosen because they represent the three major varieties of grains encountered (see Sect. 3.6.3). Panels containing the complete set of 20 different a_0 are included in Sect. 3.6.3.

In general terms, the grains analyzed are either fully entrained (blown out by the XEUV wind, leaving the computational domain above the disk surface), fall back below the base of the flow at $R \gtrsim 160\,\mathrm{AU}$, or are not even picked up by the wind despite the turbulent kicks allowing for upwards motion. Additionally, we find that trajectories for a given grain size do (almost) never intersect, wherefore different starting positions will lead to different paths in the wind. Thus, the initial positioning of a grain of size a_0 along the launching region pre-determines which wind regions it can populate. This matches with – and is a direct result of – the gas wind velocity map seen in Fig. 3.1 pointing radially outwards almost everywhere.

(1) For an in-depth treatment of dust in a magneto-centrifugal disk wind with a setup similar to ours, see Giacalone et al. (2019).

(2) Since some of the large particles may leave the computational domain due to the gas motion below the disk surface dragging them out, more than the minimum of 5,000 (see Sect. 3.2) trajectories are modelled for all grain sizes.

Table 3.1: Number of modelled trajectories per a_0.

$a_0\,[\mu\mathrm{m}]$	N	$a_0\,[\mu\mathrm{m}]$	N	$a_0\,[\mu\mathrm{m}]$	N
0.01	82106	4	27165	11	5126
0.05	82293	5	21606	12	5064
0.1	80834	6	16866	13	5054
0.5	67418	7	12367	14	5072
1	57766	8	8996	15	5063
2	46456	9	7357	20	5056
3	35644	10	6356	(total)	583665

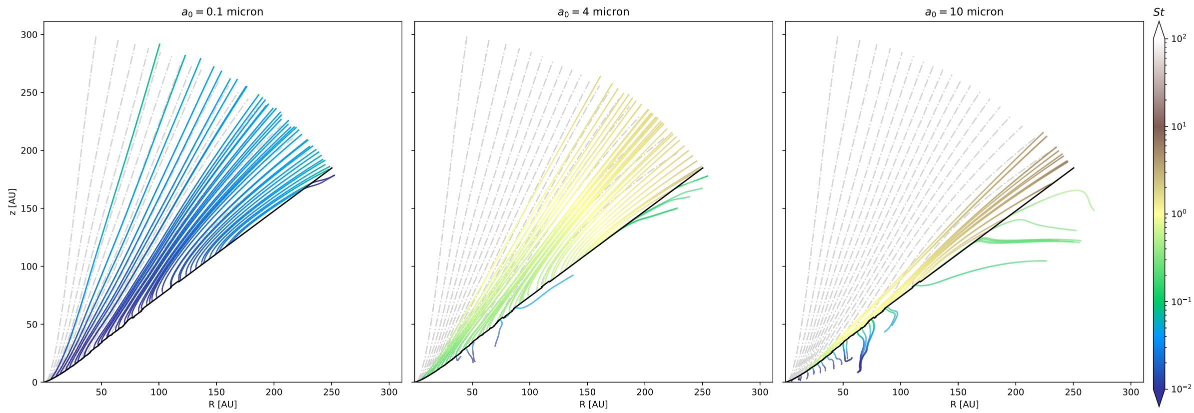

Figure 3.3: Randomly selected dust trajectories for $a_0 = 0.1$, 4, and 10 μm (left, middle, and right panels, respectively). The trajectory color represents the local value of the Stokes number. Entrained dust grains, launching from the launching region (black), migrate upwards on the colorbar the as they move to regions of lower gas density. Gas streamlines are shown in dash-dotted grey. (For all simulated grain sizes, see Fig. 3.17.)

3.3.1 Robustness of the initial velocity setup

In Sect. 3.2, we have described a rather simplistic initial velocity setup, with $\vec{v}_0$ depending only on Ω_K. However, in order for our grains to even reach the 3.5...5.5 H which we launch them from (see Fig. 3.1), the gas must have some degree of turbulence, implying some variety in the initial velocities.

To account for this, we have run a series of tests with a Gaussian spread of $\sigma(v_i) = 100\,\mathrm{m/s}$ in all three directions $i \in \{r; \vartheta; \varphi\}$ of the initial velocity vector $\vec{v}_0$. This value was chosen because it is an overestimate of the fragmentation speeds given by Birnstiel et al. (2009, 10 m/s) and Wada et al. (2013, $\lesssim 8\,\mathrm{m/s}$ for silicates, $\lesssim 80\,\mathrm{m/s}$ for icy aggregates), and because it is slightly higher than the upwards speed of the gas which we find along the base of the flow, $|v_\vartheta| \lesssim 50\,\mathrm{m/s}$. So it should make for a suitable approximation of a velocity spread introduced by turbulent vertical mixing.

The results obtained do not deviate significantly from those retrieved without this spread; therefore we will proceed to show only the latter. For a more extensive elaboration on the similarities and differences identified, see Sect. 3.6.2.

3.3.2 Dust coupling to the gas

In Fig. 3.3, the trajectories are colored by their Stokes number $St = t_{\mathrm{stop}} \cdot \Omega_K$, with $t_{\mathrm{stop}} = m_{\mathrm{dust}}\, v_{\mathrm{dust}} / F_{\mathrm{drag}}$ their local stopping time.[(1)] Besides, gas streamlines spaced by 5% of the total mass-loss rate of the gas in the wind region (i.e. $\dot{M}_{\mathrm{wind}}$) have been added in (dash-dotted) grey for direct comparison.

$St \ll 1$ indicates that the dust motion is well-coupled to the gas flow; hence $St \ll 1$ is needed for a particle to be lifted up by the wind, since it is only affected by gas drag and stellar gravity. Indeed, we find all entrained grains to have $St \lesssim 0.4$ when they are picked up by the wind (i.e. colors from blue to green). While in the wind, they are sped up by the rather fast photoevaporative flow (of up to $v_r \lesssim 30\,\mathrm{km/s}$, see Fig. 3.2), which leads to a steady increase in their speed, and thus also St; the latter may grow by up to an order of magnitude.

At low St, the dust grains follow the gas flow (see especially the left panel of Fig. 3.3); at $St \to 1$ however, they decouple from the gas flow (see the middle and right panels of Fig. 3.3, especially for higher R). For $R \gtrsim 160\,\mathrm{AU}$, the gas streamlines – in particular those close to the disk – start to bend towards it because the stellar irradiation is starting to decline this far out. As a result, the dust grains that have already reached a relatively high radial velocity at this point overshoot the gas streamlines. Further inwards and at higher z, the dust trajectories fall below the gas streamlines if they become decoupled.

For an in-depth analysis of the dust motion, Fig. 3.4 shows two randomly selected dust particles launched from $R \simeq 20\,\mathrm{AU}$. These are representative of the dust grains picked up by the wind from this R, with other grains entrained from around this R showing very similar trajectories; we opted for a launching point rather close to the star in order to showcase fully-entrained grains.[(2)]

(1) For the definition of the drag force F_{drag} employed here, see Picogna et al. (2018).

(2) As we will see further down, this is also the R from which the most massive grains are entrained.

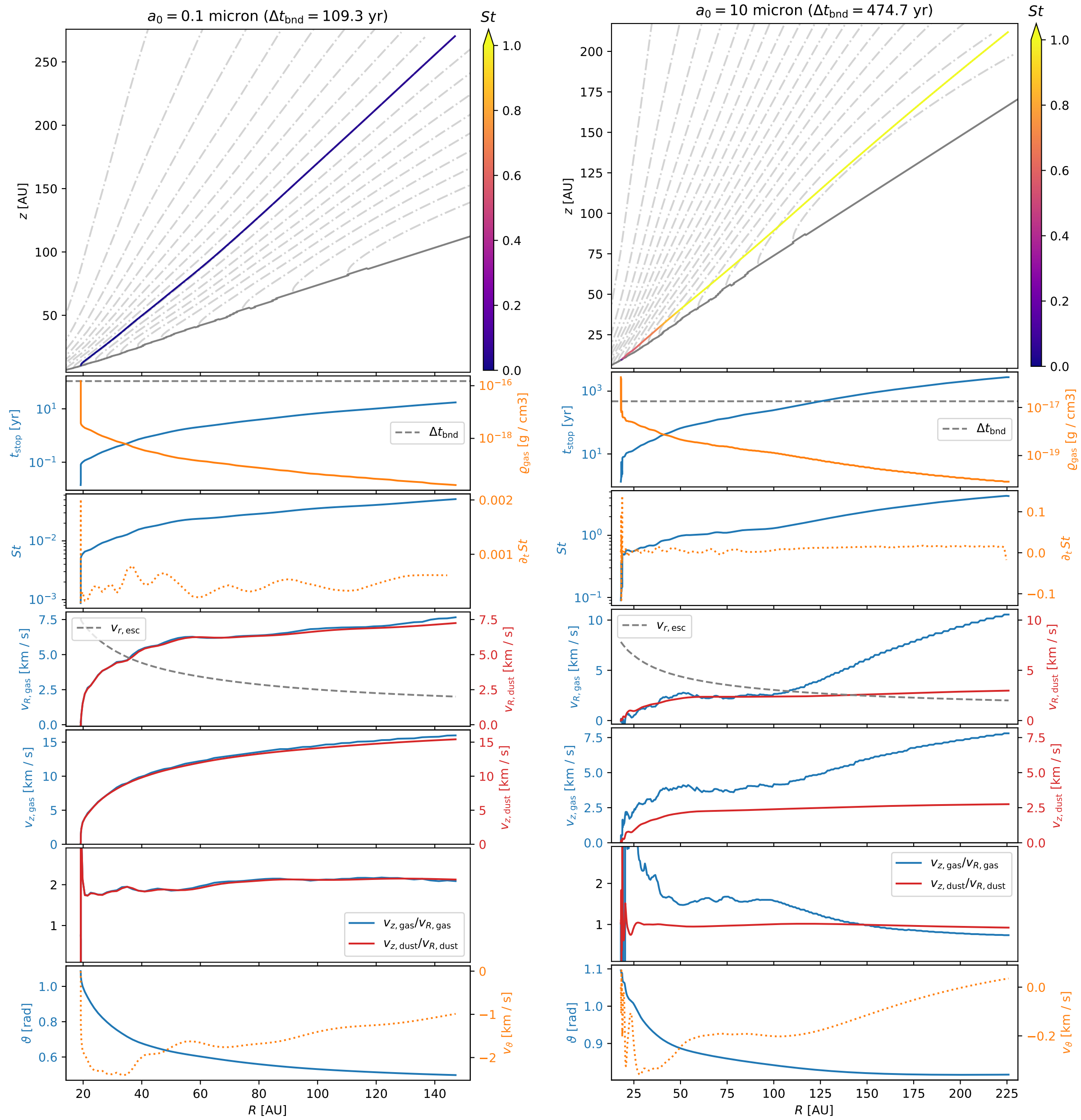

Figure 3.4: Analysis of two dust trajectories (left: $a_0 = 0.1\,\mu$m, right: $a_0 = 10\,\mu$m) entrained in the photoevaporative outflow from $R \simeq 20$ AU. The top panels show the actual motion in the (R, z)-plane colored by St. The lower panels illustrate, from top to bottom, $t_{\rm stop}$ and $\varrho_{\rm gas}$, St and $\partial_t\, St$, the horizontal speed v_R of gas and dust, the vertical speed v_z of gas and dust, a comparison of the direction of the motion v_z/v_x for gas and dust, and ϑ and v_ϑ. See the text for an in-depth commentary.

The $0.1\,\mu$m particle (left column) remains entrained in the photoevaporative flow and follows the gas motion almost perfectly; its Stokes number remains small ($St < 0.1$) throughout its trajectory. Its $t_{\rm stop}$ also stays small, even after the strong increase (of a factor of about 4) it experiences when being picked up by the wind, simultaneous to the strong decrease in the density of the surrounding gas (of a factor of almost 100). While the grain is at $r < 300$ AU, $t_{\rm stop}$ is always smaller than the time needed for blow-out to 300 AU (dashed grey line in the second panel), which may serve as a further indication that the particle stays coupled to the gas. The fourth through sixth panels show a comparison of gas (blue) and dust (red) velocities for v_R and v_z, where we can also observe a strong coupling. It is only at $r \to 300$ AU that a slight deviation of $\vec{v}_{\rm dust}$ from $\vec{v}_{\rm gas}$ occurs; the decoupling does not necessarily coincide with the particles reaching escape velocities (dashed grey lines in the fourth panel). This means that even sub-micron particles start decoupling from the gas flow at high r, that is after picking up enough momentum from the wind. Also, with the curve for ϑ flattening down and v_ϑ being rather small in comparison to v_R, the motion of the showcased particle is almost fully radial at larger R. As $v_\vartheta < 0$, a small additional upwards component remains.

On the other hand, the $10\,\mu$m particle (right column) decouples from the gas flow within the first few AU of entering the wind region; simultaneously, its Stokes number quickly becomes $St > 0.5$. Its $t_{\rm stop}$ grows even larger than the time passing between wind pick-up and leaving the domain (again, dashed blue line). The XEUV wind drags the grain along, increasing its v_R which remains comparable to $v_{R,\rm gas}$ for the first part of its trajectory. By contrast, v_z quickly diverges from the gas flow, which leads to the direction of the dust motion clearly (visually) differing from the gas streamlines, intersecting multiple ones. At $R \gtrsim 160\,$AU, the gas flow starts pointing back down towards the disk, but since the grain is already decoupled, it does not seem to be affected by this; in the sixth panel, we see that its direction of motion remains almost constant after the initial acceleration, as would be expected for high $t_{\rm stop}$.

Despite the gravitational pull acting on the $10\,\mu$m grain, its v_R and v_z are slightly increasing for $R \gtrsim 100\,$AU. This is caused by the relatively high difference in gas and dust velocity $|v_{\rm gas} - v_{\rm dust}|$; even if this additional speed-up were missing, the grain would still reach $v_{r,\rm esc}$ well within $r < 300\,$AU, as the grey dashed line in the fifth panel shows.

3.3.3 Dust timescales in the wind

In Fig. 3.4, we have included a timescale $\Delta t_{\rm bnd}$ for the motion of the dust grains. This timescale was computed as the difference between the time at which the particle is picked up by the wind ($t_{\rm wind,0}$) and the time at which it crosses the domain at $r > 300\,$AU while being entrained ($t_{\rm bnd}$), thus $\Delta t_{\rm bnd} = t_{\rm bnd} - t_{\rm wind,0}$. The full distribution of timescale data points for all trajectories is shown in Fig. 3.5 (cyan and blue).

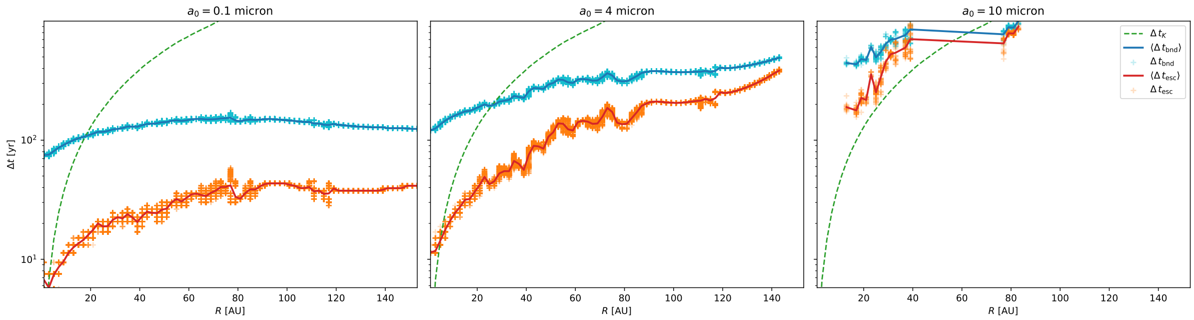

Figure 3.5: Time needed to fully blow out dust particles from when they first enter the wind at $t_{\rm wind,0}$ to the domain boundary, which they reach at $t_{\rm bnd}$ (data points in cyan, mean in blue), and time needed to accelerate dust grains to $v_{\rm r,esc}$ (data points in orange, mean in red); both for a selection of three a_0. Keplerian orbital times ($t_{\rm dyn} \equiv \Delta t_K$) at the disk surface are included as dashed green lines. The rasterization of the data points results from a time-discrete particle tracking and a binning in R-direction; thus, one raster point may represent multiple data points. (For all a_0, see Fig. 3.18.)

In general, wind entrainment timescales appear to span 10^2 to $10^3\,$yr. This is similar to the range given by Birnstiel et al. (2016) for midplane dust growth; since dust densities at $z \gtrsim 3.5\,H$ (see Fig. 3.1) are considerably lower, dust-dust interactions should indeed be negligible, as claimed in Sect. 3.2. More concisely, Kornet et al. (2001) have established that the dust growth timescale goes as $t_{\rm grow} \propto \varrho_{\rm dust} \cdot v_{\rm dust}$, with $\varrho_{\rm dust}$ the local dust density.[1] As Table 3.2 shows, $\varrho_{\rm gas}$ drops off heavily towards the disk surface while $v_{\rm gas} \equiv |\vec{v}_{\rm gas}|$ remains very comparable; Figs. 3.1 and 3.2 illustrate that the wind speed picks up slightly above – and not at – the base of the flow (as would be expected considering the latter is located slightly below the disk surface). Hence the dust-dust interaction timescale is much longer than the wind blowout time, if we assume a constant dust-to-gas ratio. In case of a more realistic relation, dust would be even more scarce than gas for similar z (Krijt & Ciesla, 2016).

The $0.1\,\mu$m grains of Fig. 3.5 have $\Delta t_{\rm bnd}$ as low as $70\,$yrs if they are picked up at small R; this means that the longer distance to the domain boundary is outweighed by the higher acceleration the dust experiences close to the star. For $R \gtrsim 80\,$AU, $\Delta t_{\rm bnd}$ decreases; if we assume the general trend of slower

[1] $\varrho_{\rm dust}$ is not to be confused with the internal grain density $\varrho_{\rm grain}$.

Table 3.2: Comparison of gas densities and velocities at the disk midplane and the base of the XEUV flow.

		10 AU	100 AU
$\varrho_{\rm gas}$ [g/cm^3]	midplane	$8 \cdot 10^{-13}$	$8 \cdot 10^{-16}$
	flow base	$2 \cdot 10^{-17}$	$2 \cdot 10^{-19}$
$\lvert\vec{v}_{\rm gas}\rvert$ [km/s]	midplane	8	2
	flow base	8	2

speed-up from larger R to persist, this would mean that the grains are picked up close enough to the computational boundary (at $R \simeq 300$ AU) to be blown out faster than those from slightly further in. So this drop-off is caused by the numerical setup, not by the actual physics involved.

For $a_0 \geq 0.5\,\mu$m, we do not see this fall-off anymore. Disregarding the various local peaks in $\Delta t_{\rm bnd}$ which are caused by the base of the wind not being perfectly smooth,[(1)] a clear trend of the blow-out time Δt increasing with the launching position R emerges. For $10\,\mu$m grains, we find $\max(\Delta t) \approx 10^3$ yr, which is still well below the simulation time frame $\Delta t_{\rm sim}$, validating the latter a posteriori.

Since the cutoff at $r \simeq 300$ AU is somewhat arbitrary, the orange and red parts of Fig. 3.5 show a different approach to defining a timescale: These represent the time between wind pick-up ($t_{\rm wind,0}$, as above) and reaching $v_{r,\rm esc}$ at $t_{\rm esc}$, that is $\Delta t_{\rm esc} = t_{\rm esc} - t_{\rm wind,0}$. Because the velocity field of the gas flow in the wind is pointing outwards (see Fig. 3.1), it is highly unlikely that a grain will not be fully blown out by the XEUV wind once it has reached $v_{r,\rm esc}$.

The overall appearance of the average values for $\langle\Delta t_{\rm bnd}\rangle$ (blue) and $\langle\Delta t_{\rm esc}\rangle$ (red) is quite similar; both show a rather distinct upwards trend, mitigated only for $R \gtrsim 80$ AU and $a_0 < 0.5\,\mu$m. Interestingly, this feature also holds for $\Delta t_{\rm esc}$, which in contrast to $\Delta t_{\rm bnd}$ does not depend on the choice of the computational boundary.

The values retrieved for $\Delta t_{\rm esc}$ are different – and always smaller. This difference is most pronounced for small grains, which reach $v_{r,\rm esc}$ within 5 to 60 yr (for $a_0 = 0.1\,\mu$m), while needing 70 to 170 yr to leave the simulation domain. Dust particles with $a_0 \leq 8\,\mu$m launched close to the star are accelerated to $v_{r,\rm esc}$ within merely a few years; bigger grains take longer to pick up speed, or are too heavy to be picked up by the wind at all ($a_0 \geq 12\,\mu$m).

The dashed green lines in Fig. 3.5 indicate the steady-state dynamical timescale $t_{\rm dyn} = 2\,\pi/\Omega_K = 2\,\pi/\sqrt{G\,M_*/r^3}$ for a Keplerian orbit at the base of the XEUV-driven flow. For $a_0 = 0.1\,\mu$m, $t_{\rm dyn}$ dominates the dust motion only for starting points $R \lesssim 20$ AU; this increases to $R \lesssim 30$ AU for $a_0 = 4\,\mu$m. By contrast, the photoevaporation of the $10\,\mu$m grains is largely dominated by $t_{\rm dyn}$, which for those is mostly larger than $\Delta t_{\rm bnd}$.

Because $\Delta t_{\rm esc} < \Delta t_{\rm bnd}$, we find $t_{\rm dyn} > \Delta t_{\rm esc}$ for both $0.1\,\mu$m and $4\,\mu$m for $R > 10$ AU, meaning that for almost all grains the blow-out happens (considerably) faster than their 'usual' timescale. It is only for the large particles ($a_0 = 10\,\mu$m) that the time needed for acceleration to the escape velocity becomes comparable to the Keplerian timescale.

3.3.4 Maximum entrained grain size

As has already been suggested in Fig. 3.2, dust grains may be too heavy to be blown out by the XEUV wind. This is investigated further in Fig. 3.6 where the blue line shows the maximum grain size $\max(a_0)|_R$ that can be fully entrained in the wind from a starting position R along the base of the flow. As noted in Sect. 3.2, the latter is not entirely smooth; this, in turn, causes the craggy appearance of the graph for $\max(a_0)$.

To facilitate direct comparisons, we have included the corresponding EUV-only curve of Hutchison et al. (2016b) in orange and the MHD-wind results of Miyake et al. (2016) in green. The figure shows that overall, an X-ray driven wind is able to entrain larger grains over a larger radial range than its EUV-only or MHD-driven counterparts; this may have a noticeable impact on deduced opacity maps, and also on the detectability of the wind in scattered light.

[(1)]This can be seen from a close examination of the black lines in Fig. 3.2, as well as Fig. 3.16.

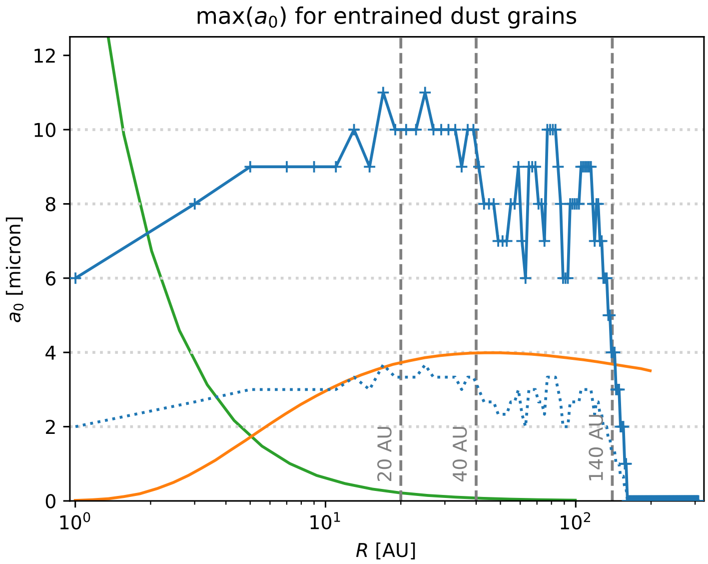

Figure 3.6: Size of the largest grains entrained from a point R along the base of the wind (blue, peak at about 20 AU); the saw-tooth appearance of the curve at larger R is caused by the finite resolution of the underlying gas grid. When comparing to Hutchison et al. (2016b, their Fig. 7 for $M_* = 0.75\,\mathrm{M}_\odot$) (orange, peak at around 40 AU), we can see the size enhancement – especially at smaller R – caused by the inclusion of X-rays in our photoevaporative wind model. The blue dashed line represents our results scaled down by a factor of 3, to compensate for the differing internal grain densities of Hutchison et al. (2016b) and this work; yet, $\dot{M}_\mathrm{wind}$ still differs between the models, making a direct comparison difficult. The MHD wind model investigated by Miyake et al. (2016, their Fig. 4) (green) shows a distinctly different entrainment curve, starting off at very high a_0 in the jet region but dropping towards $\max(a_0) = 0$ very quickly. Around $R \simeq 140$ AU, our $\max(a_0)$ plummets to 0.

The biggest grains that are blown out, that is $a_0 = 11\,\mu$m, are entrained from $15 \lesssim R\,[\mathrm{AU}] \lesssim 30$. Closer to the star, stellar gravity counteracts the gas drag force; but since the gravitational pull drops off with r^2, the drag force dominates particle motion further out.(1) With increasing R, $\max(a_0)$ slowly decreases out to $R_\mathrm{max} \simeq 140$ AU, where it quickly drops to $\max(a_0) = 0$. This coincides with the maximum radius at which XEUV photoevaporation is effective for the gas component of the disk; Picogna et al. (2019) show that the surface mass-loss rate ($\dot{\Sigma}_\mathrm{gas}$) drops to negligible values at $R \approx 140$ AU. So both gas and dust residing at the disk surface at $R \gtrsim 140$ AU are very unlikely to be thermally unbound from there. Thus, for both their and our simulations this marks the outer boundary of the XEUV-wind-dominated region of the protoplanetary disk. Furthermore, it validates a posteriori our choice to limit the computational domain to $r \lesssim 300$ AU and the initial particle placement to $r \leq 200$ AU.(2)

As mentioned in Sect. 3.2, ϱ_grain is not well-constrained. A variation of the dust density is found to directly anti-correlate with $\max(a_0)$, that is $\varrho_\mathrm{grain} \propto 1/\max(a_0)$; this agrees with the analytical findings of Hutchison et al. (2016b, their Eq. 15). Hence, for a threefold internal grain density of $\varrho'_\mathrm{grain} = 3\,\mathrm{g/cm}^3 = 3\,\varrho_\mathrm{grain}$, our global $\max(a_0)$ drops to $\max(a_0)' = \max(a_0)/3 \approx 3.5\,\mu$m. An accordingly scaled version of our results is included in Fig. 3.6 as the blue dashed line in order to allow for simpler comparison to the results of Hutchison et al. (2016a,b); but it should be kept in mind that their and our mass-loss rates are not entirely similar. While they quote a surface mass-loss rate of $\dot{\Sigma}_\mathrm{gas} = 3.6 \cdot 10^{-12}\,\mathrm{g/(cm^2\,s)}$ at $R = 5$ AU, we have $\dot{\Sigma}_\mathrm{gas} \approx 2 \cdot 10^{-13}\,\mathrm{g/(cm^2\,s)}$ (Picogna et al., 2019, their Fig. 5).

A 2D map of the grain sizes that can populate different regions of the wind is shown in Fig. 3.7.(3) The larger grains remain rather close to the disk surface; by contrast, smaller ones are lifted up to larger scale heights. For the same launching position R, smaller grains reach higher z. The abrupt decline of the 20 μm grains at $R \gtrsim 160$ AU results from the initial placement of the particles within $0.33 \leq r\,[\mathrm{AU}] \leq 200$,

(1) This correlates to Clarke & Alexander (2016) limiting the applicability of their scale-free gas motion to $R \gg R_g$, with R_g the gravitational radius.

(2) The base of the flow is at $z \approx 103$ AU at $R = 140$ AU (see Fig. 3.1), yielding $r \approx 174$ AU < 200 AU.

(3) For this, the particle motions were mapped to a 2 AU × 2 AU grid; a much higher resolution would introduce artifacts due to insufficient particle count whereas a lower one would smear out features.

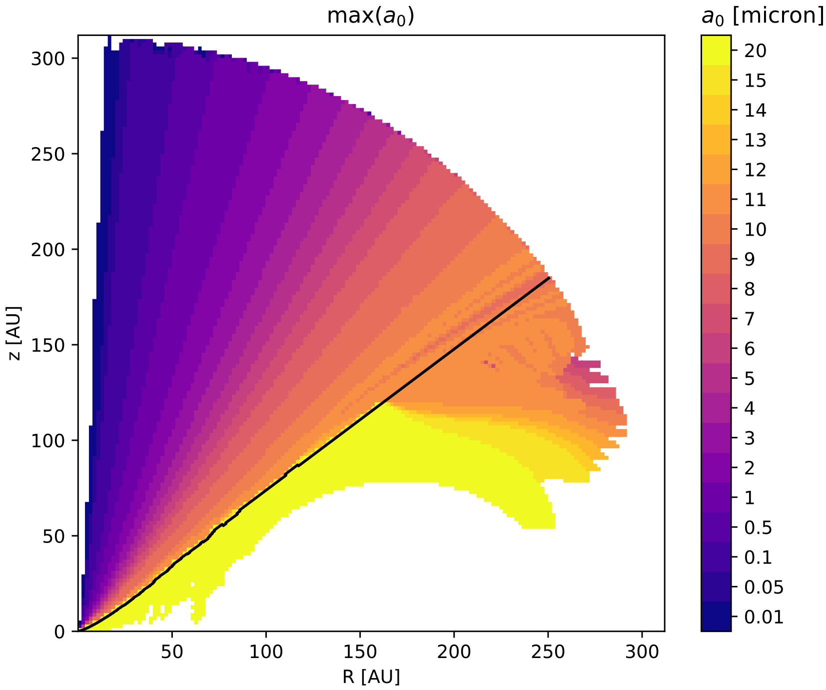

Figure 3.7: Maximum size max(a_0) of the dust grains in the wind in analogy to Owen et al. (2011a, their Fig. 2). The brightest color found above the sonic surface indicates a global maximum of max(a_0) = 11 μm; the region below the base of the wind (black) is included merely for completeness. The visible correlation between grain size and maximum scale height is further investigated in Fig. 3.8.

or equivalently $0.3 \lesssim R\,[\mathrm{AU}] \lesssim 160$.

In Fig. 3.8, we see the regions which are populated by grains of a given a_0 in green. We find that there are no deserts of smaller dust particles in regions populated by larger ones; for instance, wherever we find grains with $a_0 = 10\,\mu$m, we also find grains with $a_0 = 0.1\,\mu$m and $a_0 = 4\,\mu$m. From Fig. 3.7, we have learnt that smaller grains will reach higher scale heights; to quantify this behaviour, we have included the maximum height $\max(z)|_R$ for a certain a_0 at R in orange in Fig. 3.8. Fits with a simple second-order polynomial,

$$\max(z)|_R = c_1\,R + c_2\,R^2\ , \tag{3.1}$$

are shown as blue dotted lines; they match $\max(z)|_R$ quite well except for the very inner region where the dust distribution is slightly more flared.[(1)] Higher-order polynomials fit the inner region better, however they are not included here since these fits are not a physically-derived, but merely a numerical prescription which we intended to keep quite simple.

The fit parameters c_1 and c_2 for all grain sizes are shown in Fig. 3.9 together with merely phenomenological prescriptions for the scaling of c_1 and c_2 with a_0 which are intended for comparisons to observational data from edge-on disks in future work. The fit formulas used are meant solely for a simplified reproduction of the values of c_1 and c_2; they are not based on physical considerations.

As may have been expected, both c_1 and c_2 decrease with increasing a_0, indicating the decline of the slope of $\max(z)|_R$ with a_0 already seen in Fig. 3.8. The higher errors at lower a_0 result from the larger inclination of $\max(z)|_R$ for smaller grains; in addition, the population map shown in Fig. 3.8 has a finite resolution as outlined above, which further contributes to a larger uncertainty especially for very steep lines.

Furthermore, we find $c_1 \gg c_2$ for all a_0 modelled; this corresponds to the mostly linear appearance of $\max(z)|_R$ especially for larger R. Yet c_2 does not drop to zero, so a certain amount of flaring is preserved for all particle sizes.

[(1)]Note that omitting disk gravity should not have a strong effect on the strength of the flaring seen here, see Sect. 3.6.1.

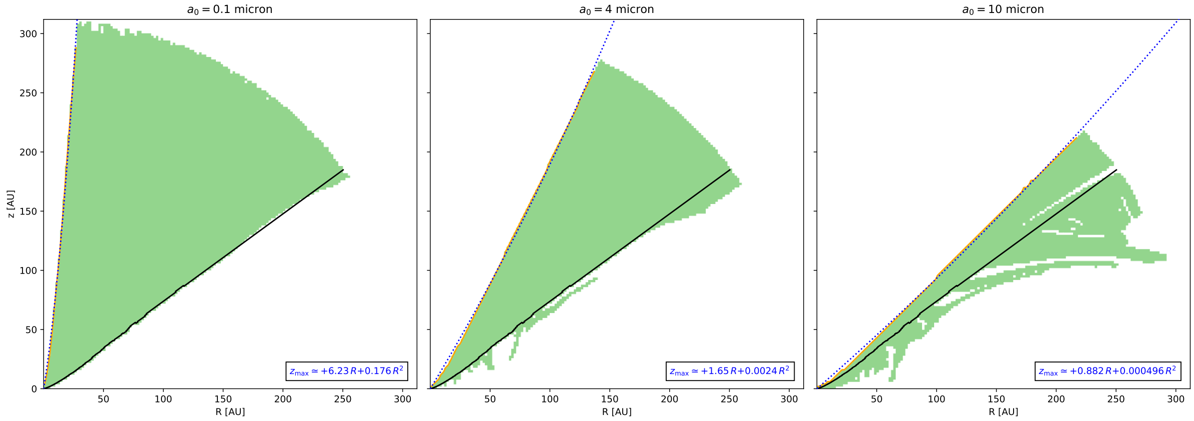

Figure 3.8: Areas populated by the dust grains (green); since we do not start from a realistic distribution along the base of the wind, we do not portray a density map. Smaller grains reach higher z at similar R. Wind base in black, numerical $\max(z)|_R$ in orange, and corresponding fit in (dotted) blue; fits according to Eq. (3.1) annotated. (For all a_0, see Fig. 3.19.)

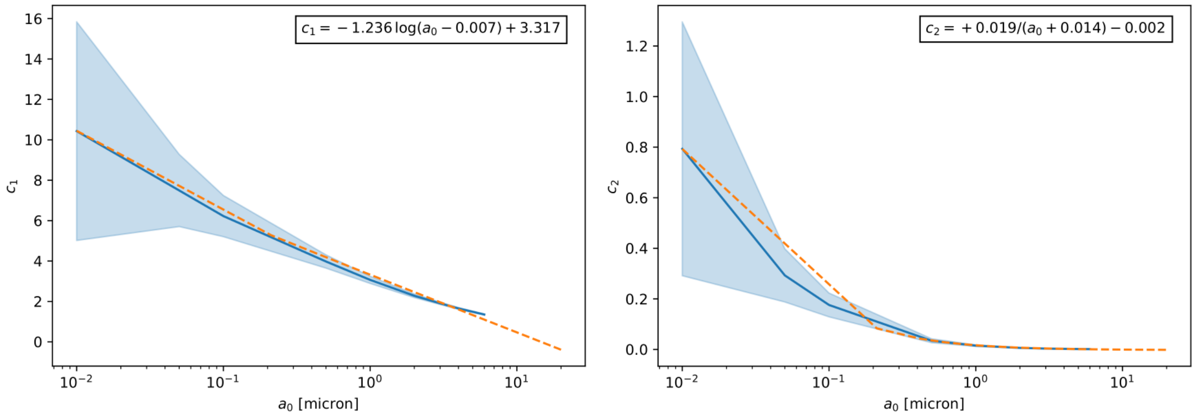

Figure 3.9: Fit parameters for all fits for $\max(a_0)|_R$ as a function of a_0 in blue, with $3\,\sigma$-errors included as shaded regions. Non-physical fits to these fit parameter curves in orange, with the parametrisations given in the text boxes.

3.4 Discussion

We have numerically simulated the trajectories of dust grains in the XEUV-irradiated wind regions of a gaseous protoplanetary disk. As was to be expected (see e.g. Armitage, 2015), we found small dust particles to show very good agreement with the gas streamlines and, in contrast, bigger grains to noticeably deviate from them. Thus, analytical models of gas motion as provided by Clarke & Alexander (2016) cannot be used to accurately model the trajectories of dust grains attaining $St \gtrsim 0.5$ in the wind.

3.4.1 Photoevaporative winds and radiation pressure

Owen & Kollmeier (2019) use the X-ray photoevaporation model of Owen et al. (2011b) to quantify grain blow-out due to direct radiation pressure alone; since their M_*, M_{disk}, and L_X are the same as used in this work and their internal grain density of $1.25\,\text{g/cm}^3$ only slightly differs from our $\varrho_{\text{grain}} = 1\,\text{g/cm}^3$, this allows for an almost perfect comparison of their results to grain entrainment by XEUV winds.[(1)] Using an effective stellar surface temperature of 4500 K, they find $\max_{\text{rad}}(a_0) \simeq 0.6\,\mu$m for the largest grains for which the radiation pressure from an equivalent black body still outweighs stellar gravity. Thus, a photoevaporative XEUV wind enhances the size of dust grains blown out by a factor of almost 20 over radiation pressure alone.

[(1)] Picogna et al. (2019) provide a more in-depth explanation of the differences between their model and that of Owen et al. (2011b).

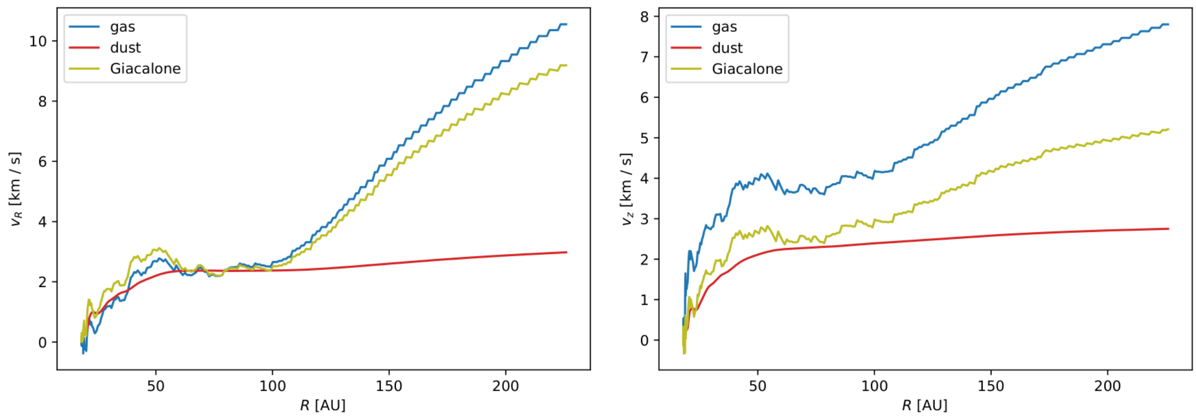

Figure 3.10: Re-plot of v_R and v_z for the same dust grain as in the right column of Fig. 3.4 ($a_0 = 10\,\mu$m). The dust parameters are colored red, the surrounding gas in blue; the motion according to Eqs. (1) and (3) of Giacalone et al. (2019), with $t_{\rm stop}$ as retrieved from our model, is added in green. Especially towards larger R, the semi-analytical prescription does not reproduce the dust motion very well. It should be noted, however, that Giacalone et al. (2019) do not use it for grains this big.

Hence we can conclude that a photoevaporative XEUV-driven wind is much more effective at removing larger dust grains than direct radiation pressure.

3.4.2 Comparison to MHD wind models

Miyake et al. (2016), building on an MHD model established by Suzuki & Inutsuka (2009), performed 1D simulations of dust motion in MHD-driven winds. While they mainly focused on floating grains,[(1)] they also give a maximum entrainable grain size for their model along R; we have included it in Fig. 3.6 in orange. This shows that whereas MHD winds excel at removing large dust grains from regions very close to the star, photoevaporative winds start to dominate – in terms of entrained grain size – at $R \gtrsim 2\,$AU. Thus, MHD winds would seem to be limited to the jet region and its immediate surroundings.

Recently, Giacalone et al. (2019) have investigated dust transport in (cold) magneto-centrifugally-driven disk winds in 2D; they conclude that the region of interest for dust pick-up from and re-deposition on the disk surface covers their full modelled range of R, which they chose to set up as $0.1 \leq R\,[\mathrm{AU}] \leq 100$. For their T-Tauri model, they find entrainment of grains with $a_0 \lesssim 2\,\mu$m (their Fig. 3). This value was obtained for a disk surface temperature of $T_{\rm surf} = 600\,$K, which seems very plausible from an MHD point of view, but somewhat low from a photoevaporative one. They show as well that $\max(a_0)$ clearly depends on said $T_{\rm surf}$, with higher $T_{\rm surf}$ increasing their $\max(a_0)$.

In contrast to our numerical setup, Giacalone et al. (2019) opted for a semi-analytical approach to trajectory modelling (see their Eqs. 1 through 3); Fig. 3.10 compares the grain velocities we extract for the $10\,\mu$m grain of Fig. 3.4 to their prescription. We are only showing a comparison for a large dust particle here because for small a_0, gas and dust velocities are very similar. It should be noted, in this regard, that Giacalone et al. (2019) use their semi-analytical equations just for relatively small dust grains, considering their $\max(a_0)$ as quoted above; we present Fig. 3.10 merely to show that numerical simulations are still necessary for modelling the trajectories of the larger grains whose velocity distinctly decouples from the gas flow. Thus, until more intricate analytical prescriptions are introduced for tracing dust motion in a photoevaporative wind, a numerical approach must be employed for accurate results.

3.4.3 Comparison to EUV wind models

Previous investigations of dust entrainment in photoevaporative winds have limited themselves to EUV-only photoevaporation (Owen et al., 2011a; Hutchison et al., 2016b).

Owen et al. (2011a) base their work on an EUV-luminosity optimised model of a $2.5\,\mathrm{M}_\odot$ Herbig Ae/Be star; while this means that our results are not directly comparable in terms of stellar parameters, both

[(1)] By 'floating grains', Miyake et al. (2016) refer to dust particles of sizes $25 \lesssim a_0\,[\mu\mathrm{m}] \lesssim 45$ which float near the sonic surface of the disk, neither too heavy to fall back down towards the midplane nor light enough to be blown out by their MHD wind.

their and our work test the respective highest-luminosity (i.e. best-case) scenario, and hence aim to provide an upper limit to $\max(a_0)$. Comparing their $\max(a_0) \simeq 2.2\,\mu$m (see their Fig. 2) to our value of $11\,\mu$m, both retrieved for $\varrho_{\rm grain} = 1\,{\rm g/cm^3}$, we find a clear enhancement of particle sizes blown out by the wind. Thus, depending on the mass-loss rates caused by XEUV photoevaporation, the inclusion of X-ray photons in the disk irradiation model may be a crucial component for accurately predicting dust entrainment.

The basic mechanics do not change, though; when comparing our Fig. 3.7 to Owen et al. (2011a, their Fig. 2), we see the same qualitative behaviour. In both cases, the maximum height which a grain of a given a_0 at a given R can be lifted to decreases with increasing a_0. As expected, the largest entrainable grains are not lifted up very high above the disk by the photoevaporative wind.

Hutchison et al. (2016b) explore a wide range of stellar parameters; apart from choosing a penetration depth typical for T-Tauri stars (provided by Woitke et al., 2016), they also ran their models for a stellar mass of $0.75\,{\rm M_\odot}$, very similar to our $M_* = 0.7\,{\rm M_\odot}$. Just like us, they find an anti-correlation $M_* \propto 1/\max(a_0)$ which explains their value of $\max(a_0) \simeq 4\,\mu$m in comparison to Owen et al. (2011a).

This value is still distinctly smaller than the $11\,\mu$m we have found to be picked up; yet as already noted in Sect. 3.3, we get very close to their EUV-only results with our model when using their $\varrho_{\rm grain} = 3\,{\rm g/cm^3}$. However, as pointed out above as well, the entrainable grain sizes are still not comparable since gas mass-loss rates strongly differ between Hutchison et al. (2016a,b) and our model. This is due merely to the different numerical setup of their and our models; Owen et al. (2012) and Owen & Jackson (2012) show that for viable $L_{\rm X}$, X-ray driven winds clearly dominate over EUV-driven ones in terms of $\dot{M}_{\rm wind}$. In addition to this, we have now seen that even at lower $\dot{\Sigma}_{\rm gas}$, XEUV winds may entrain larger grains than EUV-only ones.

Furthermore, Fig. 3.6 shows that independent of the exact grain size, X-ray irradiation shifts the peak in $\max(a_0)$ towards lower R. The T-Tauri star of Hutchison et al. (2016b) entrains its $\max(a_0)$ from $40 \lesssim R\,[{\rm AU}] \lesssim 50$, and the more luminous Herbig Ae/Be star of Owen et al. (2011a) from $30 \lesssim R\,[{\rm AU}] \lesssim 40$. Interestingly, albeit exerting a stronger gravitational pull, the higher-mass star blows out its largest grains from further in; thus it seems that the higher gravity is outweighed by an even stronger wind launched.

In comparison, our XEUV wind picks up its largest grains from $20 \lesssim R\,[{\rm AU}] \lesssim 30$, indicating that dust grains are entrained more efficiently closer to the star. In contrast to Giacalone et al. (2019) and their MHD wind model, we only find grain fallback for $R > 200\,{\rm AU}$ ($a_0 = 0.1\,\mu$m), or $R \gtrsim 150\,{\rm AU}$ ($a_0 = 10\,\mu$m; see Fig. 3.8) for launching positions within a similar range of R – as noted above, the trajectories do not intersect (see Fig. 3.3). Hence, the photoevaporative wind re-deposits only little material on the disk surface. This agrees with the conclusions of Owen et al. (2011a) that once entrained, a dust grain will almost always remain in the wind, and be carried out to large radii. Furthermore, as noted above, all grains leaving the computational domain above the disk surface have $v_r > v_{r,{\rm esc}}$, and are hence very likely to entirely leave the protostellar environment.

3.5 Summary

We have modelled dust trajectories for grain sizes $10^{-3} \leq a_0\,[\mu{\rm m}] \leq 10^2$ in the wind region of a $M_{\rm disk} \simeq 10^{-2}\,M_*$ gas disk around a $M_* = 0.7\,{\rm M_\odot}$ T-Tauri star, irradiating its surroundings with $L_{\rm X} = 2\cdot 10^{30}$ erg/s on top of an EUV spectrum. Our main findings are as follows:

- X-ray driven winds are able to entrain grains up to a size of $a_0 \lesssim 11\,\mu$m; this is larger than the maximum entrained grain size from EUV-only models.
- XEUV winds pick up the largest particles from $R \simeq 20\,{\rm AU}$. By contrast, EUV-only winds entrain their largest dust from further out (i.e. $R \simeq 40\,{\rm AU}$). MHD winds show a very different profile, picking up very large grains from regions very close to the star ($R \ll 3\,{\rm AU}$), but then rapidly loosing momentum farther from the star.
- Dust grains are launched with Stokes numbers $St < 0.4$ (i.e. $St \ll 1$). Once entrained, the large grains decouple from the gas flow; smaller dust particles decouple at later times.
- μm-sized dust grains of are blown out of the inner 300 AU of a protoplanetary disk on a timescale of 10^2 to 10^3 yr.
- For a given grain size, the launching point of a grain determines its further trajectory.

- Smaller dust grains may be lifted up higher by the wind, with the maximum height $\max(z)$ at a given R decreasing with grain size a_0.
- An anti-correlation between $\max(z)|_R$ and a_0 may be a typical signature of dusty photoevaporative winds.

Much like Owen et al. (2011a), we have found a strong dependence of the $\max(a_0)$ in the wind on R (see Figs. 3.7 and 3.8). This signature structure may be detectable in observations of edge-on disks if vertical mixing is strong enough to transport large grains to the disk surface; however, as has been shown by Hutchison et al. (2016b), this may not be the case, or may need additional MHD effects (Miyake et al., 2016).

In a future work we aim to present dust opacity maps and synthetic observations of typical protoplanetary dusty XEUV winds in order to investigate their detectability with current and future instrumentation. As the mass-loss profiles of winds due to the different mechanisms – that is, EUV, X-ray, MHD, etc. – are shown (or expected) to be different, this will reflect in the size distribution and density of dust particles entrained at different locations in the wind. While a quantitative discussion requires a calculation of detailed emission maps via radiative transfer modelling, we can speculate from the wind profiles of the gas that an X-ray-driven wind might produce a more extended launching region for larger grains than an EUV-only wind for which most of the entrainment is expected to occur near the gravitational radius of the disk. The dust emission is expected to be concentrated even closer to the star in the case of an MHD wind. Whether these differences are detectable with current instrumentation remains a matter of future investigation.

Acknowledgements: We would like to thank Cathie Clarke and Mark Hutchison for very helpful discussions, and the (anonymous) referee for a constructive report that improved the manuscript.
This research was supported by the German Research Foundation (DFG, Deutsche Forschungsgemeinschaft), grants FOR 2634/1, ER 685/8-1, and ER 685/9-1, the Munich Institute for Astro- and Particle Physics (MIAPP) of the DFG cluster of excellence *Origin and Structure of the Universe*. T.B. acknowledges funding from the European Research Council (ERC) under the European Union's Horizon 2020 research and innovation programme under grant agreement No 714769. The simulations have been carried out on the computing facilities of the Computational Center for Particle- and Astrophysics (C2PAP).

3.6 Appendix

3.6.1 Omitting disk gravity

As noted in Sect. 3.2, we decided not to include the gravitational pull from the gas disk in our model in order to cut computational costs. We verified a posteriori that this does not strongly impact our results.

To this end we compared, at each recorded position of all of our dust particles, the gas drag force

$$F_{\mathrm{drag,z}} = \frac{\Delta v_{\mathrm{gas,z}}\, m}{t_{\mathrm{stop}}}\ , \tag{3.2}$$

with a grain mass of $m = \frac{4\,\pi}{3}\, a_0^3\, \varrho_{\mathrm{grain}}$, to an overestimate of the gravitational pull the disk would produce,

$$F_{\mathrm{disk,z}} = -\frac{G\, M_{\mathrm{disk}}\, m}{z^2}\ . \tag{3.3}$$

The latter formula leads to a slight overestimate of the z-component of F_{disk} because the disk is not centered exactly below a given particle. If $F_{\mathrm{disk,z}} \ll F_{\mathrm{drag,z}}$, or rather $F_{\mathrm{disk,z}}/F_{\mathrm{drag,z}} \ll 1$, neglecting disk gravity should not noticeably affect our results. To determine whether this is the case, we compute the mean value $\langle|F_{\mathrm{disk,z}}\,/\,F_{\mathrm{drag,z}}|\rangle$ of all grains of size a_0 on a $2\,\mathrm{AU} \times 2\,\mathrm{AU}$ grid. The maximum values (over all a_0) for all these means are shown in Fig. 3.11. As the colors demonstrate, the gas drag clearly dominates over the overestimated gravitational pull from the protoplanetary disk. We find only a few exceptions: Firstly, well within the disk, from where it would be rather unlikely to see wind entrainment (as noted in Sect. 3.2, we have concentrated on realistically modelling the wind region, not the disk interior); secondly, very close to the host star, that is at $R \ll 10\,\mathrm{AU}$, from where we do not see substantial entrainment (see Fig. 3.6); and thirdly, around the base of the flow for $R \gtrsim 180\,\mathrm{AU}$, which lies beyond the region from which wind pick-up happens in the first place, as noted in Sect. 3.3.

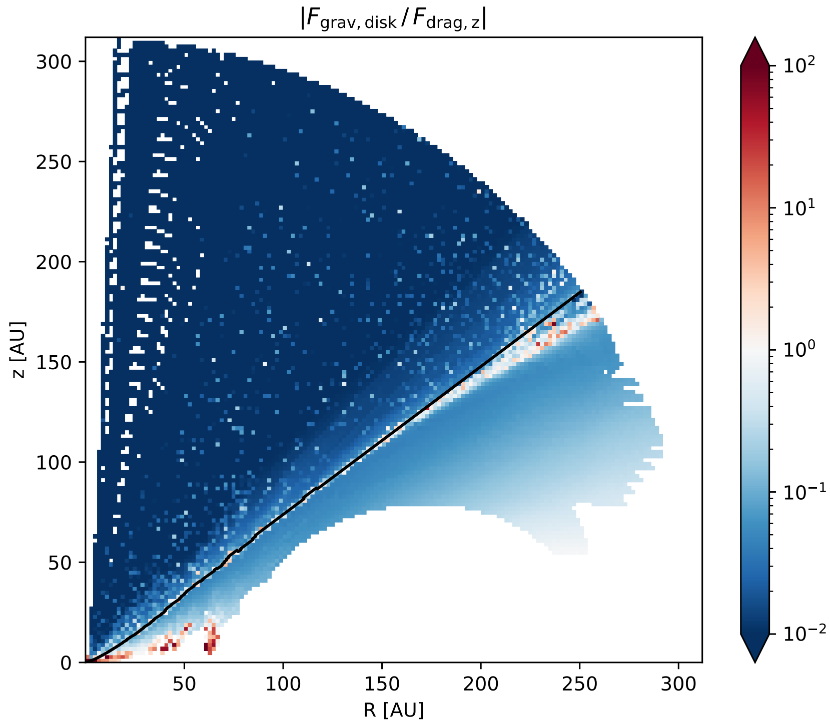

Figure 3.11: Maximum of the per-a_0 mean values for $|F_{\mathrm{disk,z}}/F_{\mathrm{drag,z}}|$ (see colorbar), mapped to a $2\,\mathrm{AU} \times 2\,\mathrm{AU}$ grid. The gas drag clearly dominates over the (overestimated) disk gravity, especially in the wind region (base of the wind in black). Empty (white) regions above the sonic surface indicate that no particle has been recorded while in this cell, owing to the high grain speeds there (in contrast to Sect. 3.3, we did not interpolate between recorded particle positions).

In other words, we find that the photoevaporative wind is – at low r – strong enough to compensate for both the closeness of the grain launching area to the disk midplane (and hence the center of mass) and also the concentration of the disk mass within $r \lesssim 100\,\mathrm{AU}$ (see Fig. 3.1).

At high r, the wind will not lose momentum (see the green velocity maps in Fig. 3.2), but the center of mass of the disk will have moved farther away from the base of the photoevaporative flow, meaning that gravity is even less likely to play a major role for wind entrainment.

3.6.2 Including a spread in the initial velocities

As outlined in Sects. 3.2 and 3.3, our model was set up with no initial velocity spread, that is for all our grains, we set $\vec{v}_0 = r\,\Omega_K\,\hat{\vec{v}}_\varphi$. Fig. 3.12 shows that even large entrained grains reach $v_{r,\mathrm{esc}}$ well inside the computational domain (i.e. at $r \ll 300\,\mathrm{AU}$); so we may assume that a variation of the starting velocities will not strongly affect $\max(a_0)$.

However, some turbulence is needed to vertically transport the dust particles to base of the wind; hence, we would realistically assume some spread in $\vec{v}_0$. The main contribution to vertical mixing stems from v_ϑ which we found to be rather low in the vicinity of the base of the wind ($|v_\vartheta| \lesssim 50\,\mathrm{m/s}$). So in order to check the effects of varying starting velocities, we introduced a Gaussian spread of $\sigma(v_i) = 100\,\mathrm{m/s}$ in all three coordinate directions $i \in \{r, \vartheta, \varphi\}$.

As a first step, we compared entrainment ratios from along the base of the flow. We expect them to differ due to grains with a reduced (enhanced) upwards velocity being less (more) likely to be picked up by the photoevaporative wind. In Fig. 3.13, we see a comparison of said entrainment ratios for $\sigma(v) = 0$ (labelled η_0) and $\sigma(v) = 100\,\mathrm{m/s}$ (labelled $\eta_{\sigma(v)}$).

While we encounter some statistical variation between the two, there is no clear systematic distinction. Grains with $a_0 \lesssim 5\,\mu\mathrm{m}$ show little variation, with $0.95 \lesssim \eta_0/\eta_{\sigma(v)} \lesssim 1.2$; so overall, they are slightly less likely to be picked up if $\sigma(v) > 0$. This may seem counterintuitive at first; it is probably a consequence of the combination of three individual directional, randomly positive or negative offsets to $\vec{v}_0$. A reduced speed in either of the three coordinate directions thus may be difficult to compensate via possibly positive changes along the other two axes of motion.

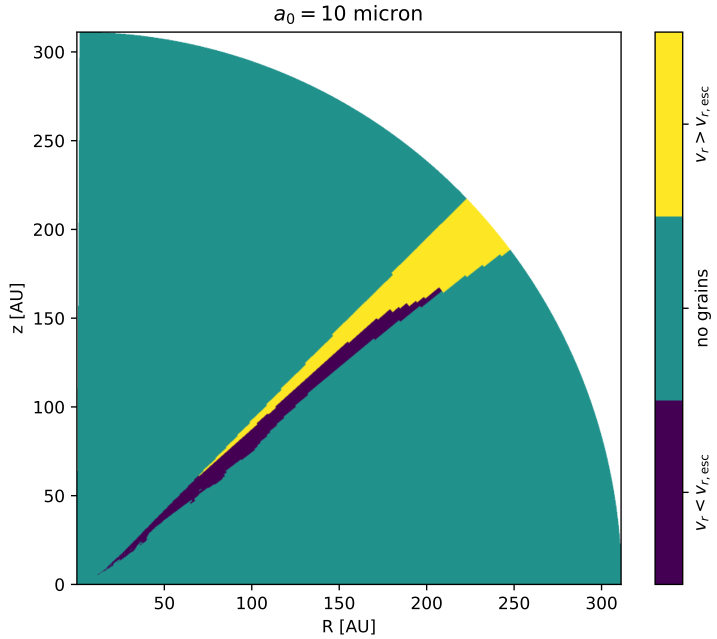

Figure 3.12: Acceleration of entrained grains of $a_0 = 10\,\mu$m: wherever there is at least one particle with $v_r < v_{r,\mathrm{esc}}$, the area is colored in dark blue; if all grains have reached $v_r > v_{r,\mathrm{esc}}$, it is yellow; cyan areas are not traversed by any grains of this size. Even for these comparatively large grains, $v_{r,\mathrm{esc}}$ is reached well within the computational domain (if at all).

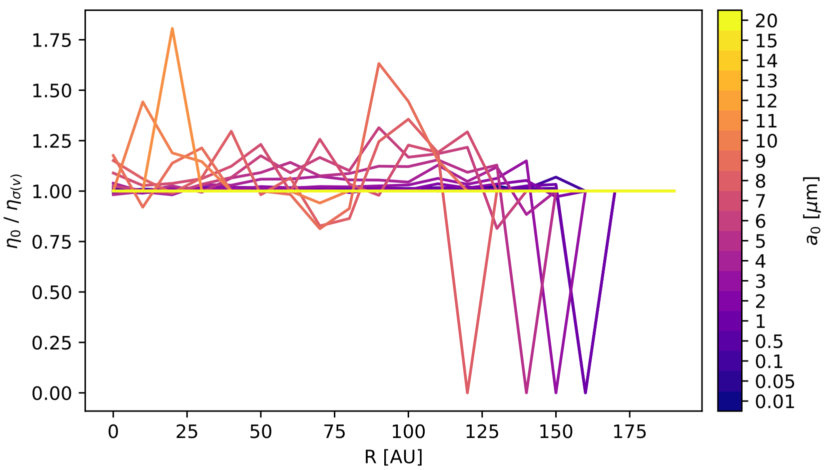

Figure 3.13: Ratio of the fraction of grains entrained for $\sigma(v) = 0$ (i.e. η_0) and the fraction of grains entrained for $\sigma(v) = 100\,\mathrm{m/s}$ (i.e. $\eta_{\sigma(v)}$) for bins of 10 AU along the launching area. For clarity, we required at least 20 grains to be entrained for either $\eta > 0$. While there are distinct deviations between η_0 and $\eta_{\sigma(v)}$, they do not exhibit a clear pattern. Dips to 0 indicate regions where $\sigma(v) > 0$ allows for additional wind pick-up of some dust particles that could not have been entrained with $\sigma(v) = 0$.

Dips to 0 indicate R-bins where $\eta_0 = 0$ and $\eta_{\sigma(v)} > 0$; in order to avoid a series of minima produced by only very few stray grains, we have introduced a threshold of at least twenty grains to be entrained for either $\eta > 0$.

For $6 \lesssim a_0\,[\mu\mathrm{m}] \leq 11$, entrainment fractions may vary by a factor of up to 2; in addition, the peaks are more pronounced due to the lower-number statistics for larger grains (see Table 3.1).

So while we may expect the dust content of the wind to vary according to the strength of the turbulent mixing, this should not be detrimental to the rest of our findings.

Furthermore, the maximum entrained grain size is affected merely marginally; this can be checked

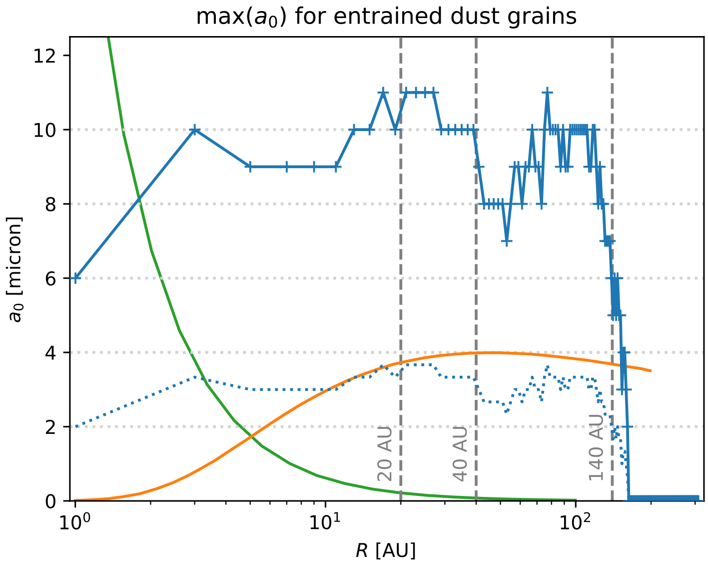

Figure 3.14: Maximum entrained grain size $\max(a_0)$ along the disk surface when $\sigma(v_i) = 100\,\mathrm{m/s}$ is included in the grain setup. The differences to Fig. 3.6, which forgoes the velocity spread, are minor, and mostly due to numerical variations of the initial positioning.

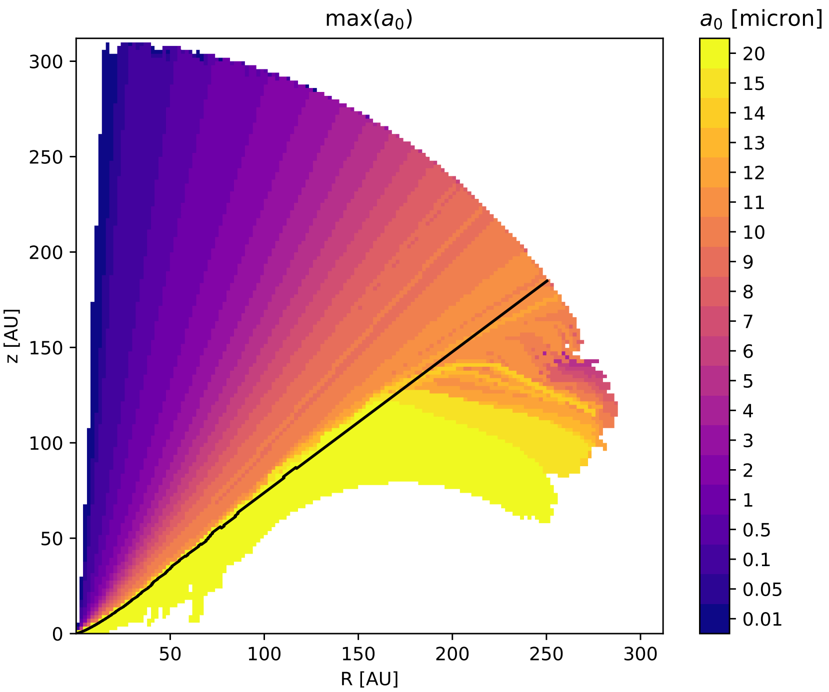

Figure 3.15: Maximum entrained grain size $\max(a_0)$ in 2D, to be compared to Fig. 3.7. As with Figs. 3.6 and 3.14, the differences caused by $\sigma(v_i)$ are minor at best.

when comparing Figs. 3.14 and 3.15 to Figs. 3.6 and 3.7, respectively. $\max(a_0)$ does vary slightly along the base of the wind; this is to be expected due to the randomised initial placement of the dust grains. Yet the position of the peak is well-preserved – just as for $\sigma(v) = 0$, we find $\max(a_0) = 11\,\mu\mathrm{m}$ at $R \simeq 20\,\mathrm{AU}$. The additional local maxima stem from the numerical unevenness of the launching area, demonstrated in Fig. 3.16.

If a grain with a velocity vector that is especially enhanced in direction of the wind motion is launched from an edge point along the base line, this may allow it to enter the wind region in contrast to another particle starting from the same location, but with a more downwards-biased velocity vector. The 2D maps

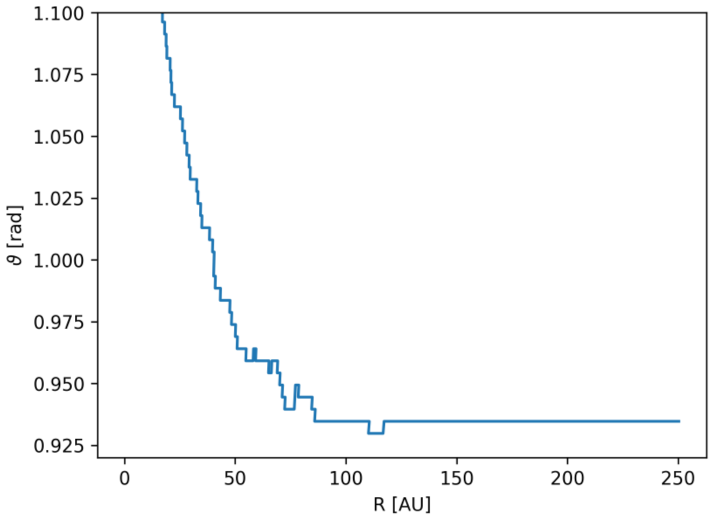

Figure 3.16: ϑ-coordinate of the base of the photoevaporative flow. Its (slightly) craggy shape is especially pronounced around $50 \lesssim R\,[\mathrm{AU}] \lesssim 90$, which leads to small numerical artifacts in our results.

for $\max(a_0)$ in Figs. 3.7 and 3.15 are almost identical, apart from few very narrow lines from individual grains of $a_0 \geq 9\,\mu$m; it stands to reason that these are caused by the randomness in the initial conditions just described.

The fits to the parameters c_1 and c_2 of Eq. (3.1), shown in Fig. 3.9, are almost entirely unaffected by the additional $\sigma(v_i)$; for brevity, suffice to state that both c_1 and c_2 deviate but in the third significant figure.

To summarize, while we must assume that there is a sensible amount of gas turbulence around the disk surface, this does not strongly affect our findings.

3.6.3 Plots and parameters for all dust grain sizes

We have modelled 20 distinct grain sizes, listed in Fig. 3.2 and Table 3.1; for clarity we have chosen to only show plots for three distinct sizes above. In the following, we present the corresponding plots for all a_0, and argue why we have chosen exactly these to represent the full sample.

An arbitrary selection of dust grain trajectories, spaced by roughly 5 AU intervals, and entering the wind-dominated region at various points along its base is shown in Fig. 3.17, the full version of Fig. 3.3. The individual trajectories are colored according to their local Stokes number St.

There are four main scenarios to be found here:

Firstly, full wind entrainment. This applies if $St \ll 1$ throughout the trajectories, that is for $a_0 \lesssim 0.1\,\mu$m. Visually, the trajectories shown for these grain sizes are mostly blue, indicating $St < 0.1$. As discussed above, these dust particles follow the gas motion very closely; this causes grains to fall back below the base of the wind along the gas streamlines, that is for $R \gtrsim 180$ AU. The most massive grains of this group have sizes $a_0 = 0.1\,\mu$m, which we have chosen for the plots in Sect. 3.3.

Secondly, slow decoupling from the gas flow. For $0.5 \lesssim a_0\,[\mu\mathrm{m}] \lesssim 5$, the grains are picked up with $St \ll 1$. Yet while the particles are blown out and hence within $r < 300$ AU, their St approaches 1. Thus the trajectories decouple from the gas; high above the disk surface, they fall below the gas streamlines, whereas close to it, they deviate upwardly, leading to a more radial outflow in all cases. Grain fallback occurs for $R \gtrsim 170\,AU$. $a_0 = 4\,\mu$m represents a grain size from this interval for which $St \to 1$ is readily apparent.

Thirdly, quick decoupling. For $6 \lesssim a_0\,[\mu\mathrm{m}] \leq 11$, the interval during which the dust grains follow the gas stream is shorter, and the grains reach higher St while being blown out. For $R \gtrsim 160\,AU$, we observe particles falling back below the base of the flow because the wind cannot provide enough momentum. The almost-largest grain size in this group is $a_0 = 10\,\mu$m ($11\,\mu$m grains are more sparse in the wind region).

Fourthly, no wind pick-up. For $a_0 > 11\,\mu$m, the grains are too heavy to be lifted up by the wind; even if they reach the disk surface, they fall back below it and successively follow the gas streams in the disk

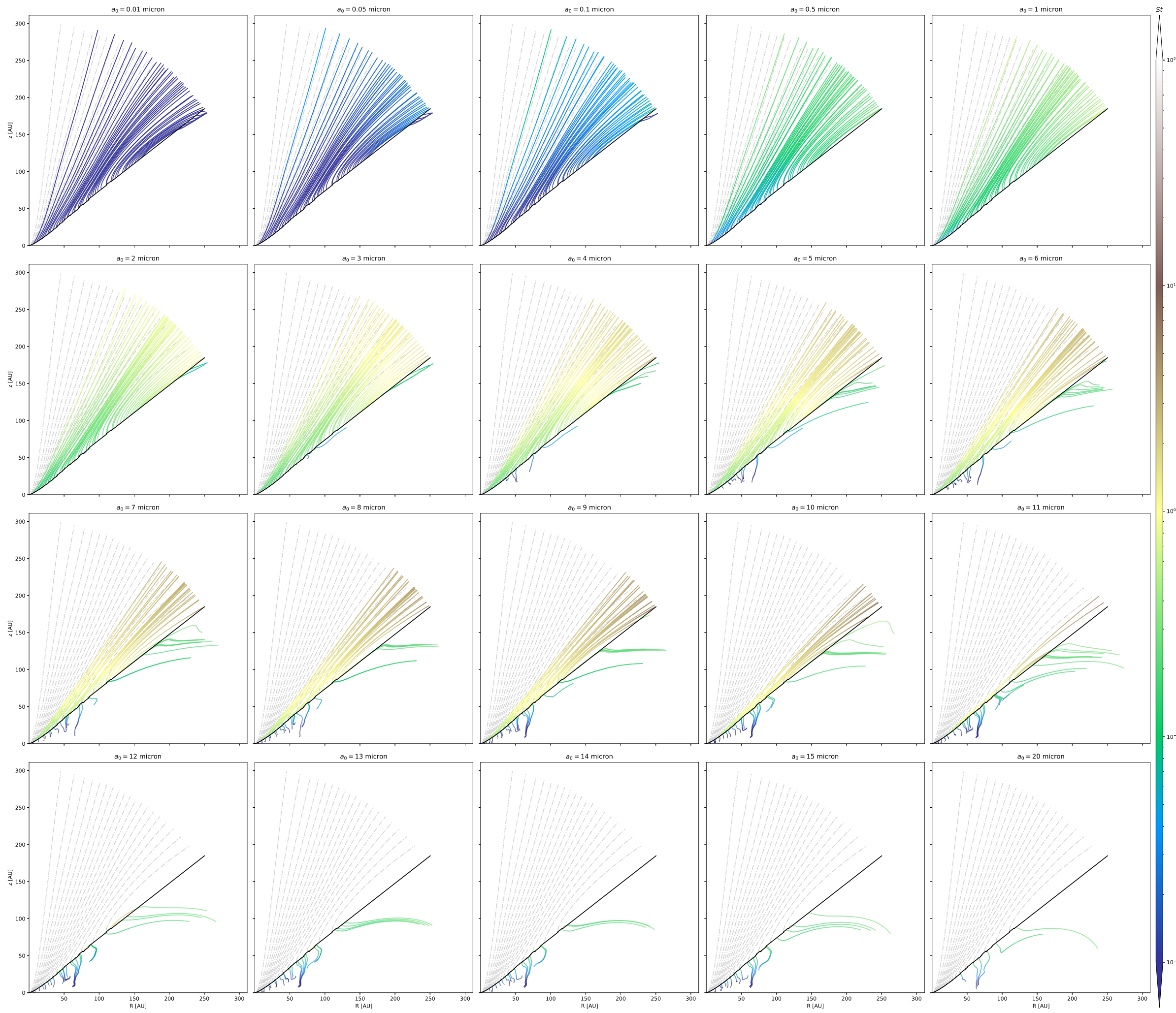

Figure 3.17: Full version of Fig. 3.3: Arbitrary selection of dust grain trajectories for all 20 a_0, colored by their local St. Wind base in black, gas streamlines in 5% steps of $\dot{M}_{\rm wind}$ in dash-dotted grey.

because of the comparably high densities there. Since we find no entrainment for these grains, we have omitted this group from the plots in Sect. 3.3.

Expanding on Fig. 3.5, Fig. 3.18 shows the times it takes the dust grains to reach $r \gtrsim 300\,\mathrm{AU}$ after wind pick-up – labelled $\Delta t_{\rm bnd}$ (data points in cyan, mean in blue) – and the (much lower) times for acceleration to the escape velocity $v_{r,\rm esc}$ – labelled $\Delta t_{\rm esc}$ (data points in orange, mean in red).[(1)]

Choosing the same size categories as above, with the panels for $a_0 > 11\,\mu\mathrm{m}$ omitted since such grains are not entrained by the photoevaporative flow, we find the following:

Firstly, very small dust grains. These are accelerated very strongly when entering the wind close to the star, resulting in low $\Delta t_{\rm bnd}$ and even lower $\Delta t_{\rm esc}$; at higher r, the timescales increase. At $R \approx 80\,\mathrm{AU}$, $\Delta t_{\rm bnd}$ peaks and starts falling off again because grains launching from further out have less distance to cover to the computational boundary at $r \simeq 300\,\mathrm{AU}$. Entrainment occurs for $R \lesssim 140...160\,\mathrm{AU}$, depending on a_0; the according time frames span $70 \lesssim \Delta t_{\rm bnd}\,[\mathrm{yr}] \lesssim 170$ and $5 \lesssim \Delta t_{\rm esc}\,[\mathrm{yr}] \lesssim 50$. The timescale of the particle motion in the wind is smaller than the Keplerian orbital timescale for grains launched from $R \gtrsim 20\,\mathrm{AU}$ ($\Delta t_{\rm bnd}$) or $R \gtrsim 1\,\mathrm{AU}$ ($\Delta t_{\rm esc}$), meaning that the motion in the wind dominates the dynamic evolution.

Secondly, small grains. They show a monotonic increase of $\Delta t_{\rm bnd}$ and $\Delta t_{\rm esc}$ with R; the peak we have seen for smaller a_0 disappears. Hence, the farther out a dust grain is picked up by the XEUV wind, the longer it takes to be blown out of the computational domain and to be accelerated to $v_{r,\rm esc}$; while this

[(1)] As outlined in Sect. 3.3, discrete output times and binning along R lead to a rasterization of the individual data points for $\Delta t_{\rm bnd}$ and $\Delta t_{\rm esc}$; hence most plotted points represent much more than one data point.

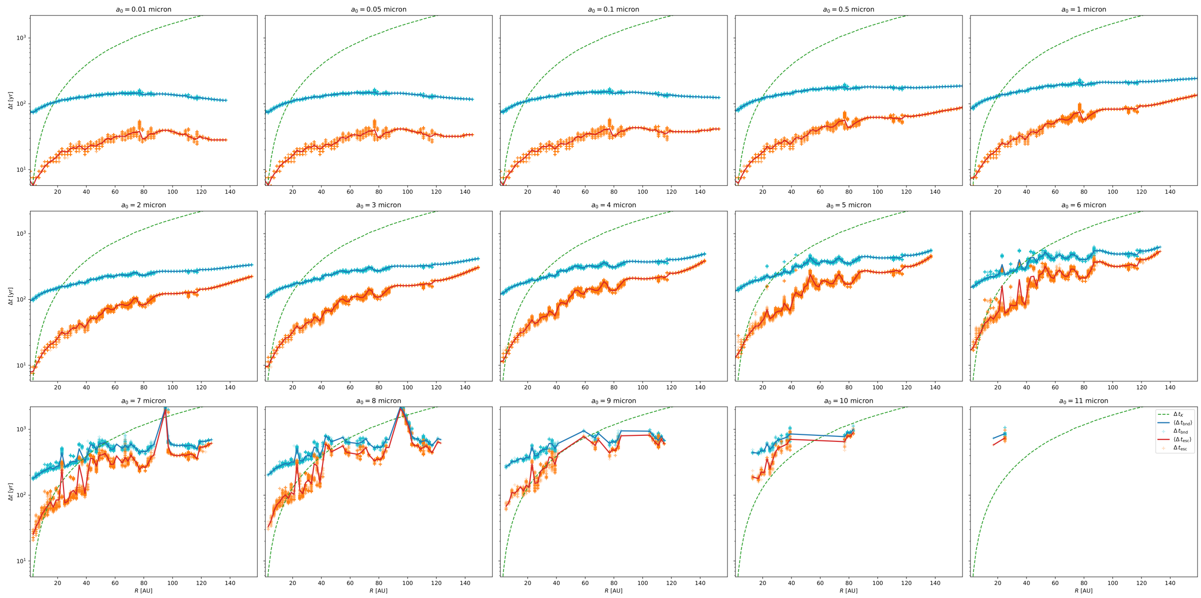

Figure 3.18: Times needed to fully blow out dust particles from their starting position along the base of the wind to the domain boundary (i.e. $\Delta t_{\rm bnd}$) and to accelerate them to $v_{r,\rm esc}$ (i.e. $\Delta t_{\rm esc}$). Individual data points in cyan and orange and mean values in blue and red, respectively. The rasterization of the former points results from a time-discrete particle tracking and a binning in R-direction; a raster point may therefore represent multiple data points. Keplerian orbital times at the base of the wind are included as dashed green lines.

may appear counter-intuitive at first, it merely illustrates that the gas flow is much stronger closer to the star. The grain transport happens on a timescale of a few yr to a few 10^2 yr; the Keplerian motion dominates the dynamic timescale for $R \gtrsim 30\,\rm AU$ ($\Delta t_{\rm bnd}$) or $R \gtrsim 5\,\rm AU$ ($\Delta t_{\rm esc}$).

Thirdly, medium-sized grains. As for the small grains, we see a mostly monotonic relation between R and $\Delta t_{\rm bnd}$. However, the graph exhibits very distinct peaks for $a_0\,[\mu\rm m] \in \{8; 9\}$, which we have not commented on in Sects. 3.2 and 3.4 because they are numerical artifacts caused by the craggy launching area (see Sects. 3.3 and 3.6.2), and interestingly disappear in the setup including an initial velocity spread.[(1)] Apart from that, we find $t_{\rm dyn} < \Delta t_{\rm bnd}$ for $R \lesssim 60\,\rm AU$ and an almost identical value for $\Delta t_{\rm esc}$, indicating that speed-up is slower for heavier grains, as would be expected.

For $R \to 0$, we find $\Delta t_{\rm esc} \to 10\,\rm yr$ for $a_0 \lesssim 9\,\mu\rm m$. This is another indicator that the photoevaporative flow is strongest close to the star, where it is most effective at accelerating the dust grains.

Last, Fig. 3.19 shows the areas occupied by the dust grains, and the according fits for $\max(z)|_R$. The fit parameters are also listed in Table 3.3, with c_1 and c_2 as defined in Eq. (3.1).

Firstly, as claimed in Sect. 3.3, these plots illustrate that all $a_0 < \max(a_0)$ populate the regions occupied by the $\max(a_0)$ shown in Fig. 3.7. Secondly, the unpopulated regions found in Fig. 3.19 are once again caused by the slight bumpiness of the base of the flow; additional test runs with a much increased spatial resolution (i.e. 1000 particles per 1 AU along the launching plane) were used to confirm this – the plots for them look very similar (and have therefore not been included here).

[(1)]Note that the $\Delta t_{\rm bnd}$ data points here have been retrieved for fully entrained grains which have left the computational domain within the computational time frame $\Delta t_{\rm sim}$. Thus, the data points almost reaching our $\Delta t_{\rm sim}$ do not indicate that the latter is too short to capture their full trajectory.

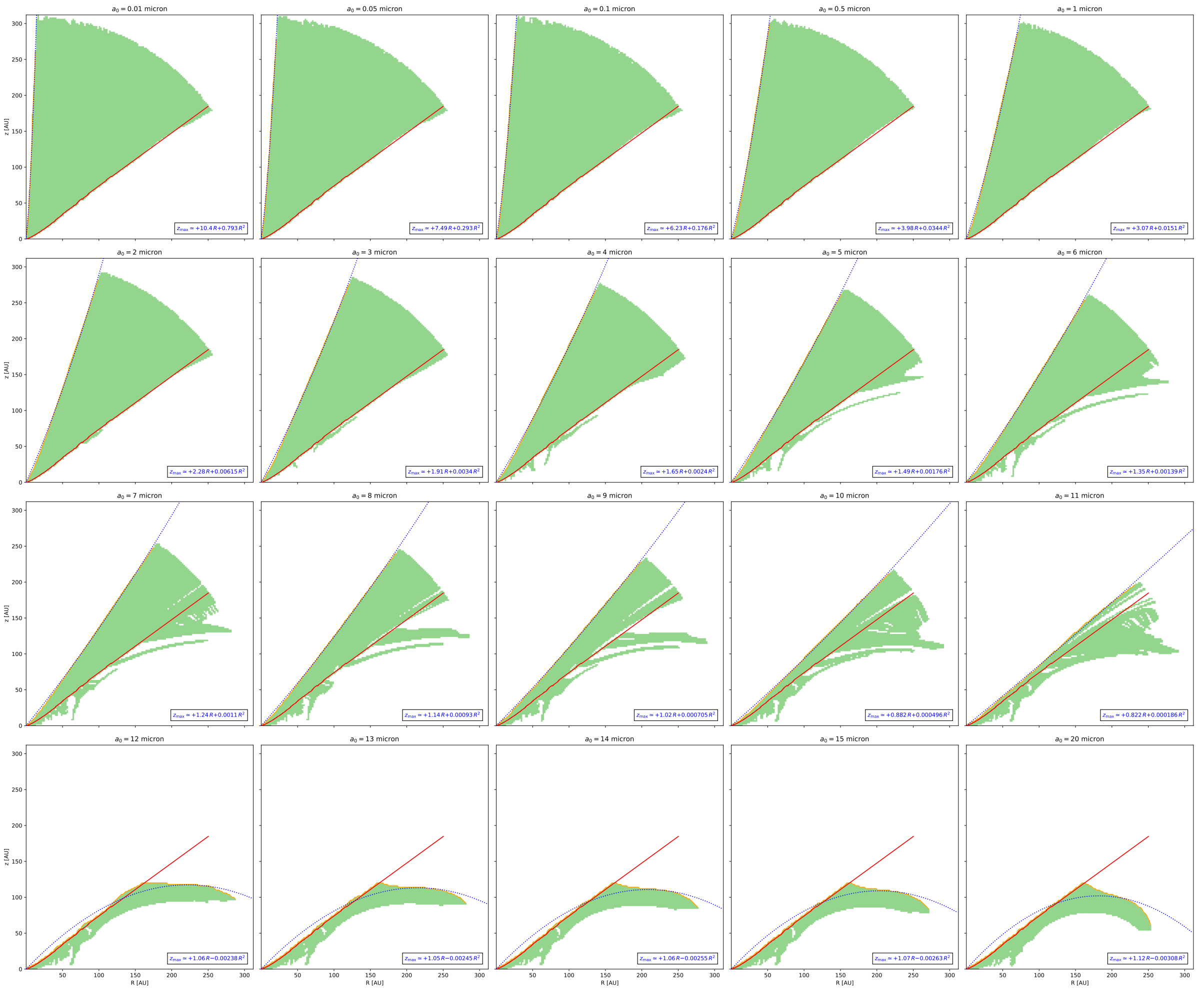

Figure 3.19: Full version of Fig. 3.8: Dust population in the wind for all a_0. We see a clear correlation between R and $\max(z)$ in the individual plots, fitted with dashed blue lines. The parameters given in the plots also listed in Table 3.3. Base of the wind in red, non-fitted population boundaries in orange.

Table 3.3: Fit parameters and standard errors for $\max(z)|_R$ for entrained grains, retrieved as shown in Fig. 3.8, for the fit provided in Eq. (3.1).

$a_0[\mu\mathrm{m}]$	c_1	$\sigma(c_1)$	c_2	$\sigma(c_2)$
0.01	10.4	1.80	$7.93 \cdot 10^{-1}$	$1.67 \cdot 10^{-1}$
0.05	7.49	$5.96 \cdot 10^{-1}$	$2.93 \cdot 10^{-1}$	$3.51 \cdot 10^{-2}$
0.1	6.23	$3.40 \cdot 10^{-1}$	$1.76 \cdot 10^{-1}$	$1.57 \cdot 10^{-2}$
0.5	3.98	$1.10 \cdot 10^{-1}$	$3.44 \cdot 10^{-2}$	$2.63 \cdot 10^{-3}$
1	3.07	$5.94 \cdot 10^{-2}$	$1.51 \cdot 10^{-2}$	$1.07 \cdot 10^{-3}$
2	2.28	$3.08 \cdot 10^{-2}$	$6.15 \cdot 10^{-3}$	$3.97 \cdot 10^{-4}$
3	1.91	$2.01 \cdot 10^{-2}$	$3.40 \cdot 10^{-3}$	$2.13 \cdot 10^{-4}$
4	1.65	$1.51 \cdot 10^{-2}$	$2.40 \cdot 10^{-3}$	$1.41 \cdot 10^{-4}$
5	1.49	$1.14 \cdot 10^{-2}$	$1.76 \cdot 10^{-3}$	$9.65 \cdot 10^{-5}$
6	1.35	$9.47 \cdot 10^{-3}$	$1.39 \cdot 10^{-3}$	$7.45 \cdot 10^{-5}$
7	1.24	$8.82 \cdot 10^{-3}$	$1.10 \cdot 10^{-3}$	$6.47 \cdot 10^{-5}$
8	1.14	$7.20 \cdot 10^{-3}$	$9.30 \cdot 10^{-4}$	$5.00 \cdot 10^{-5}$
9	1.02	$5.43 \cdot 10^{-3}$	$7.05 \cdot 10^{-4}$	$3.50 \cdot 10^{-5}$
10	0.882	$6.19 \cdot 10^{-3}$	$4.96 \cdot 10^{-4}$	$3.66 \cdot 10^{-5}$
11	0.822	$5.65 \cdot 10^{-3}$	$1.86 \cdot 10^{-4}$	$3.15 \cdot 10^{-5}$
12	1.06	$1.39 \cdot 10^{-2}$	$-2.38 \cdot 10^{-3}$	$6.21 \cdot 10^{-5}$
13	1.05	$1.42 \cdot 10^{-2}$	$-2.45 \cdot 10^{-3}$	$6.52 \cdot 10^{-5}$
14	1.06	$1.55 \cdot 10^{-2}$	$-2.55 \cdot 10^{-3}$	$7.18 \cdot 10^{-5}$
15	1.07	$1.67 \cdot 10^{-2}$	$-2.63 \cdot 10^{-3}$	$7.92 \cdot 10^{-5}$
20	1.12	$2.34 \cdot 10^{-2}$	$-3.08 \cdot 10^{-3}$	$1.19 \cdot 10^{-4}$

Chapter 4

From dust trajectories to densities and synthetic images

The contents of this chapter, with the exception of Sect. 4.6, have been published as Franz et al. (2022a).[1] Credit: Franz et al., Astronomy & Astrophysics, Volume 657, Article A69, 2022, reproduced with permission © ESO.

Chapter abstract

Context: X-ray- and extreme-ultraviolet- (together: XEUV-) driven photoevaporative winds acting on protoplanetary disks around young T-Tauri stars may crucially impact disk evolution, affecting both gas and dust distributions.

Aims: We constrain the dust densities in a typical XEUV-driven outflow, and determine whether these winds can be observed at μm-wavelengths.

Methods: We used dust trajectories modelled atop a 2D hydrodynamical gas model of a protoplanetary disk irradiated by a central T-Tauri star. With these and two different prescriptions for the dust distribution in the underlying disk, we constructed wind density maps for individual grain sizes. We used the dust density distributions obtained to synthesise observations in scattered and polarised light.

Results: For an XEUV-driven outflow around a $M_* = 0.7\,\mathrm{M}_\odot$ T-Tauri star with $L_\mathrm{X} = 2 \cdot 10^{30}$ erg/s, we find a dust mass-loss rate $\dot{M}_\mathrm{dust} \lesssim 4.1 \cdot 10^{-11}\,\mathrm{M}_\odot/\mathrm{yr}$ for an optimistic estimate of dust densities in the wind (compared to $\dot{M}_\mathrm{gas} \approx 3.7 \cdot 10^{-8}\,\mathrm{M}_\odot/\mathrm{yr}$). The synthesised scattered-light images suggest a distinct chimney structure emerging at intensities $I/I_\mathrm{max} < 10^{-4.5}$ ($10^{-3.5}$) at $\lambda_\mathrm{obs} = 1.6$ (0.4) μm, while the features in the polarised-light images are even fainter. Observations synthesised from our model do not exhibit clear features for SPHERE IRDIS, but show a faint wind signature for JWST NIRCam under optimal conditions.

Conclusions: Unambiguous detections of photoevaporative XEUV winds launched from primordial disks are at least challenging with current instrumentation; this provides a possible explanation as to why disk winds are not routinely detected in scattered or polarised light. Our calculations show that disk scale heights retrieved from scattered-light observations should be only marginally affected by the presence of an XEUV wind.

[1] This work resulted from a collaboration with the coauthors listed in the corresponding bibliography entry, that is B. Ercolano (BE), S. Casassus (SC), G. Picogna (GP), T. Birnstiel (TB), S. Pérez (SP), Ch. Rab (CHR), and A. Sharma (AS). In particular, SC provided the noise estimates for SPHERE IRDIS and corresponding routines alongside their description in the manuscript, TB provided the `disklab` and `dsharp_opac` packages as well as guidance on how to use them, SP provided the image of the re-evaluation of the MY Lupi data, CHR helped to sanity-check the opacity model, and AS provided guidance on a feature of `dsharp_opac`. BE, SC, GP, TB, SP, and CHR helped with the interpretation and discussion of the results. The author (RF) coded the computation of the density maps, computed the dust base densities (via `disklab`), the dust opacities (via `dsharp_opac`), the radiative transfer images (via `RadMC-3D`), and the synthetic images for JWST NIRCam (via `Mirage`), and drafted the manuscript.

4.1 Introduction

Planet formation needs large amounts of material and is thus expected to happen in and close to the midplane of protoplanetary disks around young stars (see e.g. Armitage, 2010). Its outcome may be affected by disk winds, which remove material from the disk, and may thus change the final masses and locations of planets by altering the dust-to-gas ratio and halting inward migration (see e.g. Alexander & Pascucci, 2012; Ercolano & Rosotti, 2015; Ercolano et al., 2017b; Carrera et al., 2017; Jennings et al., 2018; Monsch et al., 2019, 2021b).

While current literature agrees on two major scenarios that can drive disk winds – that is magnetics- and photoevaporation-driven outflows (see e.g. Owen et al., 2010; Gressel et al., 2015; Bai et al., 2016; Wang et al., 2019; Picogna et al., 2019; Wölfer et al., 2019; Rodenkirch et al., 2020) – it remains unclear which mechanism dominates during which evolutionary stages (see e.g. Ercolano & Pascucci, 2017; Coutens et al., 2019; Gressel et al., 2020). Consequently, many efforts have been focussed on determining which varieties of winds can be encountered in protoplanetary disks. One approach is to look for and model wind signatures in gas tracers (e.g. Pascucci et al., 2020; Gangi et al., 2020; Weber et al., 2020, for some recent works). However, gas tracers identified so far are difficult to interpret and cannot be unambigously inverted to obtain mass-loss rates from the winds (e.g. Ercolano & Owen, 2016); hence, forays to quantify dust entrainment in winds have recently gained traction (Hutchison et al., 2016a; Jaros et al., 2020; Vinković & Čemeljić, 2021) despite their high computational cost (see e.g. Tamfal et al., 2018).

Miyake et al. (2016) have shown that magneto-rotational turbulences can support an outflow of dust grains of several tens of μm from the inner disk region. Observationally, dust grains above the midplane of protoplanetary disks have been suggested mainly for regions close to the star, where high densities may lead to a significant shadowing of the stellar luminosity (Dodin et al., 2019; Petrov et al., 2019).(1)

Dust entrainment in photoevaporative extreme-ultraviolet- (EUV-) driven winds has first been investigated by Owen et al. (2011a), later by Hutchison et al. (2016a,b), and very recently by Hutchison & Clarke (2021) and Booth & Clarke (2021), building on the semi-analytical modelling of Clarke & Alexander (2016) (which has recently been generalised by Sellek et al., 2021). All studies found an entrainment of dust grains of several μm in size. In an earlier work (Franz et al., 2020, henceforth Paper I), we studied dust motion in X-ray-driven winds based on a new generation of X-ray and EUV (together: XEUV) gas models developed by Picogna et al. (2019), and found dust particles up to about 10 μm to be entrained, moving on a much faster timescale than in the disk midplane (see Misener et al., 2019).

Despite the evident interest in the subject, the question of whether dust outflows driven by photoevaporation are currently observable has remained unanswered to date. At the time of writing, no firm detection of such a dusty wind component exists in the literature, but this might be due to the sample selection. Thus, in this work, we aim to provide a theoretical prediction of the observability of this wind component, which may guide future observational campaigns and help interpret the datasets that are currently available.

This chapter is organised as follows: The calculations to obtain the dust densities and synthetic observations are outlined in Sect. 4.2. In Sect. 4.3, the resulting density maps and observational concurrences are shown. We discuss our findings in Sect. 4.4 and summarise them in Sect. 4.5.

4.2 Methods

Picogna et al. (2019) have provided models of protoplanetary gas disks with a photoevaporative XEUV wind, computed using `Mocassin` (Ercolano et al., 2003, 2005, 2008a) for the radiative transfer computations,(2) and `Pluto` (Mignone et al., 2007) for the successive hydrodynamical (HD) evolution.(3) In Paper I, we have used such a gas disk to simulate a collection of dust grain trajectories in its wind region, and we refer to that work for details about the modelling set-up. We now proceed to use these individual trajectories for the creation of dust density maps and successively, synthetic observations.

(1) Gárate et al. (2019) have presented an additional theoretical model to explain these observations.
(2) `Mocassin`: `https://mocassin.nebulousresearch.org/`.
(3) `Pluto`: `http://plutocode.ph.unito.it/`. Version 4.2 was used for this work.

4.2.1 Dust densities in the XEUV wind

The gas disk employed in Paper I models a $M_{\rm disk} \simeq 0.01\,M_*$ primordial disk around a young $M_* = 0.7\,{\rm M}_\odot$ T-Tauri star with an X-ray luminosity of $L_{\rm X} = 2 \cdot 10^{30}$ erg/s (Preibisch et al., 2005),[(1)] driving a gas mass-loss rate of $\dot{M}_{\rm gas} \simeq 3.7 \cdot 10^{-8}\,{\rm M}_\odot/{\rm yr}$ (Picogna et al., 2019). The $\dot{M}_{\rm gas}$ encountered in this one gas disk snapshot is somewhat higher than the $2.6 \cdot 10^{-8}\,{\rm M}_\odot/{\rm yr}$ given in Picogna et al. (2019) because in the latter work, a time-averaged value was used.

The dust grain motion was modelled on top of this gas snapshot using the Lagrangian-particle approach of Picogna et al. (2018); this yielded a collection of individual grain trajectories for a variety of grain sizes (i.e. radii) a_0 in the XEUV-driven wind region of the disk.

4.2.1.1 Dust grains: From trajectories to distributions

As detailed in Paper I, these dust grains were launched from the disk surface into a 2D gas disk with 3D velocity information. They are accelerated by the gravity of the central star and the gas drag, and may experience turbulent kicks while within the disk; disk gravity was shown to be negligible in Paper I.

As expected, small dust grains were found to be mostly entrained in the gas flow, whereas larger ones decoupled from it; the largest grains entrained by the wind (for an internal grain density of $\varrho_{\rm grain} = 1\,{\rm g/cm^3}$) had a size $a_0 = 11\,\mu$m and a Stokes number $St < 0.4$ when initially lifted up. So in order to sensibly model dust densities, we chose to create density maps for a discrete sample of a_0, that is $a_0 \in \{0.01, 0.1, 0.5, 1, 2, 4, 8, 10\}\,\mu$m; this limitation to eight discrete values is due to the high computational cost for simulating the trajectories. From a physical point of view, the listed sizes cover all major cases between full entrainment, slow decoupling and fast decoupling (for which $a_0 \in \{0.1, 4, 10\}\,\mu$m were showcased in Paper I).

As listed in Table 4.1, we have modelled at least 200 000 dust grain trajectories for each of the a_0 investigated in order to provide reasonably high spatial resolution. The grains were initially positioned along the disk surface, using a uniform distribution within $0.33 < r\,[{\rm AU}] < 200$, with $r = \sqrt{x^2 + y^2 + z^2}$, yielding more than 1000 grains per radial AU of disk surface for each a_0.[(2)] The varying amounts of particles modelled are due to the fixed simulation time of $\Delta t \simeq 3.8$ kyr (corresponding to one orbit at 200 AU).[(3)] For all a_0, the concurrent amount of particles in the simulation is 200 000; when a particle exits the computational domain ($0.33 \le r\,[{\rm AU}] \le 300$ and $0.001 \le \vartheta\,[{\rm rad}] \le \pi/2$), it is re-inserted at a random position along the disk surface, starting an additional trajectory. Thus, we obtained more trajectories for smaller grains which move faster.

The high entrainment fractions of Table 4.1 match the results of Hutchison & Clarke (2021), who have performed a semi-analytical modelling of dust trajectories below and in an EUV-driven wind, and find entrainment for almost all the grains that could be delivered to the ionisation front. The fractions for the largest entrainable grains seem to drop, yet these do not necessarily reach the surface area in the first place (see Hutchison et al., 2016b; Booth & Clarke, 2021, Paper I, and below).

The dust density maps were obtained by mapping the dust trajectories to a grid via the particle-in-cell method, applied independently for each a_0. We employed an underlying (r, ϑ)-grid with cell sizes $\Delta r = 1$ AU ($\Delta r = 0.1$ AU for $r \le 2$ AU) and $\Delta\vartheta = 0.5°$.[(4)] Dust trajectories were grouped together according to their initial coordinates, and then used to retrieve one dust map per initial (r, ϑ)-bin, yielding a grid with particle counts per cell. These counts were obtained from the recorded grain positions and velocities, based on a simplified equation of motion:

$$\vec{r}(t_2) = \vec{r}(t_1) + \frac{1}{2}\,\left(\vec{v}(t_2) + \vec{v}(t_1)\right)(t_2 - t_1)\,. \tag{4.1}$$

The overall contribution of one particle per each (constant) simulation time step to the entire map was normalised to one. The resulting particle counts (i.e. dust masses) were successively converted to densities by dividing by the 3D cell volumes of the bins, assuming full azimuthal symmetry for the 2D grid. Subsequently, the base cells were used to normalise the dust flow originating from them. In a last step, they were weighted by the actual fraction of the disk surface within them.

(1) When using the term primordial disk in this work, we mean a primordial Class-II disk (i.e. without a cavity).

(2) For a more comprehensive take on the disk surface, see Paper I; in short, it is defined as the location of the largest drop in gas temperature.

(3) Doubling Δt results in very sparse, relative local errors $< 25\%$ (mostly $\lll 10\%$) for the dust densities. This error is negligible compared to the uncertainties in the base density estimation of Sect. 4.2.1.2.

(4) As $a_0 \lll \Delta r$ and $a_0 \lll r\,\Delta\vartheta$, no smoothing kernel was applied when mapping the particles onto this grid.

4.2.1.2 Base densities

While it is widely assumed that grains of mm-size quickly settle towards the midplane, the vertical mixing of μm-sized particles is less well-constrained. For instance, Pinte et al. (2008) have found a non-negligible signal from $1.6\,\mu$m grains from the surface of the inner disk of IM Lup, yet it is important to note that the signal is significantly weaker already for $\gtrsim 3\,\mu$m. More recently, the general presence of vertical settling has been verified by a series of ALMA observations (ALMA Partnership et al., 2015; Pinte et al., 2016; Villenave et al., 2020, and many others). Additionally, as pointed out by Avenhaus et al. (2018) based on a sample of T-Tauri disks observed with SPHERE, protoplanetary disks are in all likelihood rather diverse; vertical mixing may hence vary between individual objects. This has been corroborated by Villenave et al. (2019). Thus, theoretical estimates range from a globally constant dust-to-gas ratio for μm-sized grains (e.g. Takeuchi et al., 2005, and references therein) to a strong dependence of the vertical dust scale height on a_0 even for small grains (e.g. Dullemond & Dominik, 2004; Fromang & Nelson, 2009; Birnstiel et al., 2010, 2016; Hutchison et al., 2016a, 2018).

Because the base densities have a considerable impact on the resulting dust density maps in our model, we decided to investigate two different setups. Firstly, we assumed a fixed dust-to-gas ratio throughout the disk; we refer to this model as 'fixed' below.

For the second case, hereafter denoted as 'variable', we used a dust scale height prescription providing a rather strong fall-off of the dust densities with a_0 over z; this was done via the `disklab` scripts collection (Dullemond & Birnstiel, in prep.). In this approach, we used the gas disk data and the same dust-to-gas ratio. The gas disk was then rendered into hydrostatic equilibrium (see e.g. Armitage, 2010) such that

$$\frac{\partial}{\partial z}\left(c_s^2 \cdot \varrho_{\rm gas}\right) = -\varrho_{\rm gas} \cdot \frac{G\,M_*\,z}{r^3}\ , \tag{4.2}$$

with $\sqrt{P_{\rm gas}/\varrho_{\rm gas}} = c_s = \sqrt{(k_{\rm B}\,T)/(\mu\,m_{\rm H})}$ the speed of sound and $\mu = 1.37125$ the mean atomic mass in proton masses $m_{\rm H}$ (same value as in Picogna et al., 2019, and Paper I). The dust densities were then computed for a vertical settling-mixing equilibrium (Fromang & Nelson, 2009) such that

$$\frac{\partial}{\partial z}\left(\frac{\varrho_{\rm dust}}{\varrho_{\rm gas}}\right) = -\frac{\Omega_K^2\,t_{\rm stop}}{D} \cdot z\ , \tag{4.3}$$

with $\Omega_K = \sqrt{G\,M_*/r^3}$, $t_{\rm stop}$ the dust grain stopping time, and D the diffusion coefficient (see Fromang & Nelson, 2009, and sources within).

For both the 'fixed' and 'variable' cases, we employed a MRN distribution (Mathis et al., 1977) with $n(a) \propto a^{-3.5}\,{\rm d}a$, using a logarithmically-spaced grid with 400 bins for $1\,{\rm nm} = a_{\rm min} \leq a \leq a_{\rm max} = 1\,{\rm mm}$ to quantify the relative abundances of dust grain sizes. The underlying total dust-to-gas (mass) ratio was

Table 4.1: Statistics for the dust trajectories used to create the density maps: grain size, number of all trajectories modelled, number of fully entrained trajectories thereof.

a_0 [μm]	$N_{\rm all}$	$N_{\rm entrained}$
0.01	5 495 998	4 497 540
0.1	5 492 527	5 012 884
0.5	4 555 823	4 329 718
1	3 968 894	3 730 741
2	3 138 379	2 834 014
4	1 537 412	1 274 661
8	508 545	217 772
10	337 515	33 294

The differing numbers stem from a constant sample size of 200 000 grains processed simultaneously over similar simulation time spans, with grains being reinserted at a random position along the disk surface once they exit the computational domain. ($N_{\rm entrained}$ is smaller for $0.01\,\mu$m than for $0.1\,\mu$m because the former grains are even more coupled to the gas stream which points slightly back towards the disk surface at larger R, see Paper I.)

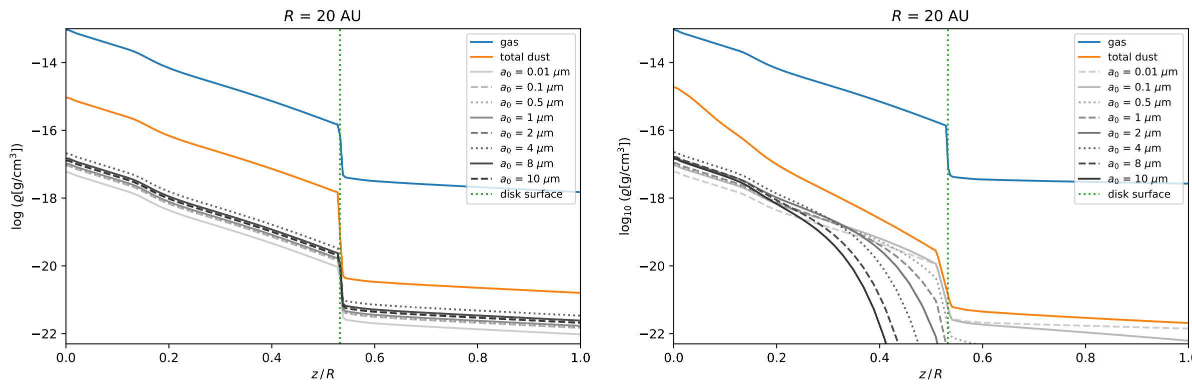

Figure 4.1: Base density profiles for a vertical slice at $R \approx 20\,\mathrm{AU}$: gas in blue (identical values in both plots), total dust (for $a_{\mathrm{max}} = 1\,\mathrm{mm}$) in orange and individual dust species used for modelling the wind in grey, according to Sect. 4.2.1.2. *Left:* Results for a globally 'fixed' dust-to-gas ratio of 0.01, and *right:* for the 'variable' dust scale height dependent on a_0. The disk-wind interface (green dotted line) is characterised by a sharp drop-off of both gas and dust densities. This drop-off is particularly pronounced for the 'fixed' total dust density at the disk surface, since we have no grains $> 11.5\,\mu$m in the wind.

set to the usually assumed value of 0.01;(1) this yields a dust mass fraction of $\approx 10^{-3}$ for grains $\lesssim 10\,\mu$m in relation to the gas. A maximum grain size of 1 mm for the total dust content of the disk is a lower limit (see e.g. Hutchison & Clarke, 2021), but corresponds to the largest grains proven to exist by ALMA (e.g. ALMA Partnership et al., 2015); hence it serves our intention of providing a maximum estimate, as higher a_{max} would entail a lower dust content for the wind.

These 400 bins of the MRN distribution were combined into eight bins for the eight grain sizes included in our model. This was done by fully attributing the contribution of a bin to the (linearly) closest grain size. Contributions from grains $> 11.5\,\mu$m were discarded since these cannot be entrained (see Paper I) and hence cannot populate the wind region.(2)

The resulting base densities for the 'fixed' and 'variable' setups are shown in Fig. 4.1 for $R = 20\,\mathrm{AU}$ (with $R = \sqrt{x^2 + y^2}$), the approximate value from which the largest grains are entrained (see Paper I). For the same underlying gas density profile, we see a clear difference in dust scale heights between the 'fixed' and 'variable' models, especially for the larger a_0. Furthermore, as the density profiles of the eight a_0 happen to be comparable in magnitude for the 'fixed' setup, its mass contributions of the grain size bins are similar.

4.2.1.3 Dust densities in the wind

For the dust densities within the disk, we directly used those computed in Sect. 4.2.1.2; for the wind region, we combined the densities at the disk surface with the dust maps from Sect. 4.2.1.1. For clarity, the whole process is sketched in Fig. 4.2.

Since the dust grids were computed for the wind region, the base densities need to be extracted from the position of the disk surface which is already affected by the wind; this corresponds to the minimum value along the density drop at the disk surface seen in Fig. 4.1. This approach also mostly reproduces the results of Booth & Clarke (2021), who find the rate of dust flux to gas flux across the ionisation front to be $\lesssim 1$ for a setup similar to ours.

The dust densities in the wind region were slightly smoothed with a Gaussian filter ($\sigma = 2\,\mathrm{AU}$) in order to smear out numerical artefacts in the form of very narrow, overdense outflow channels next to sparsely populated areas, caused by employing Lagrangian particles on top of a Eulerian grid. This affected neither the total dust masses in the wind, nor the results of the radiative-transfer computations.

The 'fixed' setup represents the highest (maximum) base densities possible, and the 'variable' one produces a more realistic estimate. In order to provide a minimum case as well – and to allow for a better

(1) Larger values of the dust-to-gas ratio are possible (see e.g. Miotello et al., 2017; Soon et al., 2019), and would lead to a higher dust content in the wind.

(2) The large grains cannot be in the wind region; they could be in the disk region, where they might marginally increase brightness. So disregarding them will either not affect or slightly enhance wind visibility.

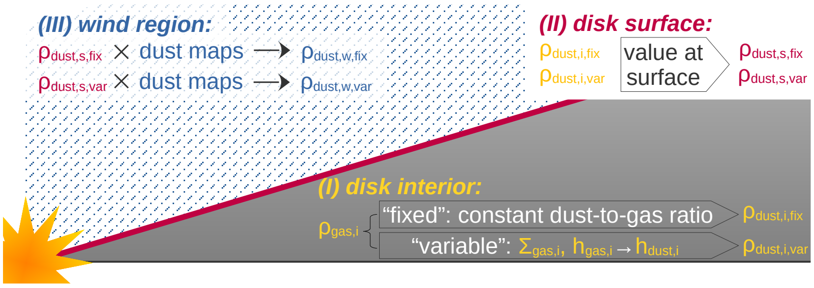

Figure 4.2: Schematics for determining ϱ_{dust} in the wind region: The dust densities in the disk are computed from ϱ_{gas} (see Sect. 4.2.1.2). ϱ_{dust} at the disk surface is directly taken from these; it is then combined with the density maps from Sect. 4.2.1.1 to obtain ϱ_{dust} in the wind (see Sect. 4.2.1.3).

estimation of the visibility of XEUV winds – we further added models with a fully dust-free wind region ('no wind') for both setups.

4.2.1.4 Dust mass-loss rates

From the individual dust trajectories, we also know the velocities at which the dust travels when leaving the computational domain at $r \simeq 300\,\mathrm{AU}$.[(1)] In addition, we found a very clear correlation between the launching point of a grain along the disk surface and its final velocity; having a mean velocity per radially outermost (r, ϑ)-bin and knowing its volume (assuming azimuthal symmetry), this allows for the computation of the wind mass-loss rates for each a_0. Simple numerical integration was then employed to obtain a total dust mass-loss rate.

4.2.2 Synthetic observations

In order to get a handle on the observability of the dust outflows of our XEUV wind model, we produced synthetic images for inclinations of $i \in \{0; 30; 60; 75; 90\}^{\circ}$, using `RadMC-3D` (Dullemond et al., 2012).[(2)] These were further converted into simulated instrument responses for the James Webb Space Telescope (JWST) Near Infrared Camera (NIRCam) scattered-light imaging (Rieke et al., 2003, 2005) using `Mirage` (Hilbert et al., 2019),[(3)] and the JWST pipeline,[(4)] and polarised-light imaging with the Spectro-Polarimetric High-contrast Exoplanet REsearch (SPHERE) + InfraRed Dual-band Imager and Spectrograph (IRDIS) instrument of the Very Large Telescope (VLT) (Beuzit et al., 2019).[(5)]

4.2.2.1 Dust opacities

We employed the `dsharp_opac` package (Birnstiel et al., 2018) to compute two sets of opacities:[(6)] Firstly, Disk Substructures at High Angular Resolution Project (DSHARP) opacities, employing optical constants from Warren & Brandt (2008, for water ice), Draine (2003b, for silicates), and Henning & Stognienko (1996, for troilite and organics). The overall material density for this mix was combined with a porosity of $\simeq 0.4$ to maintain the internal grain density of $\varrho_{\mathrm{grain}} = 1.0\,\mathrm{g/cm^3}$ from Paper I. Secondly, astrosilicate opacities, also using `dsharp_opac` with $\varrho_{\mathrm{grain}} = 1.0\,\mathrm{g/cm^3}$.

The `RadMC-3D` runs revealed dust temperatures $T_{\mathrm{dust}} < 115\,\mathrm{K}$ for $r > 35\,\mathrm{AU}$ in the wind region; so the wind may be too hot to contain (water) ice. Additionally, the stellar radiation field may further photo-desorb any ices. Thus we used the DSHARP opacities for the disk region and pure astrosilicate opacities for the wind region of the dust density maps; this will slightly enhance the visibility of dust grains in the wind, which serves our intention of providing a best-case scenario for their observability.

(1) The dust grains reach escape velocity before leaving the domain, see Paper I.
(2) `RadMC-3D`: `http://www.ita.uni-heidelberg.de/~dullemond/software/radmc-3d/`. Version 2.0 was used for this work.
(3) `Mirage`: `https://mirage-data-simulator.readthedocs.io/`. Version 2.1.0 was used for this work.
(4) `jwst`: `https://jwst-pipeline.readthedocs.io/`.
(5) Overview of the available filters: `https://jwst-docs.stsci.edu/near-infrared-camera/nircam-instrumentation/nircam-filters` for JWST NIRCam, `https://www.eso.org/sci/facilities/paranal/instruments/sphere/inst/filters.html` for SPHERE.
(6) `dsharp_opac`: `https://github.com/birnstiel/dsharp_opac/`.

4.2.2.2 Radiative transfer

The dust density maps were expanded to full 3D models by assuming midplane and azimuthal symmetry. Our grids were illuminated by the star detailed in Sect. 4.2.1, modelled as a simple black body with $R_* = 2.5\,R_\odot$ and $T_* = 5000\,\mathrm{K}$,(1) and the radiative transfer was performed with 400 logarithmically spaced wavelength points in the interval $10^{-1} \leq \lambda\,[\mu\mathrm{m}] \leq 10^4$. Using the full anisotropic scattering of `RadMC-3D`, we created SEDs, and also I, Q, and U images at a resolution of 800×800 pixels (i.e. > 1 pixel per AU).

As wavelengths λ_obs for the simulated images, we chose $0.7\,\mu$m (for JWST NIRCam's F070W filter), $1.2\,\mu$m (for JWST NIRCam's F115W filter, and SPHERE IRDIS's J-band), $1.6\,\mu$m (for JWST NIRCam's F150W, F150W2+F162M and F150W2+F164N filters, and SPHERE IRDIS's H-band), and $1.8\,\mu$m (for JWST NIRCam's F182M filter in combination with the MASRK210R coronagraph). Additionally, we investigated $\lambda_\mathrm{obs} \in \{0.4, 3.2\}\,\mu$m.

For the results shown in this work, we used $N_\mathrm{phot}^\mathrm{therm} = 10^8$ photon packets for the Monte-Carlo computation of the dust temperature maps, and $N_\mathrm{phot}^\mathrm{scat} = 10^6$ photon packets for the imaging. We furthermore checked that for the results with the most prominent wind signature, these do not significantly change (a) for $N_\mathrm{phot}^\mathrm{scat} = 10^7$, and (b) when re-mapping the dust densities to a grid logarithmic in r (and thus providing better resolution close to the star).(2)

4.2.2.3 Scattered-light instrument response for JWST NIRCam

JWST NIRCam will provide both high sensitivity and high angular resolution for upcoming observations. If this instrument is able to pick up an outflow signature from a dusty XEUV wind, then observational probes into the existence of XEUV winds (as modelled here) would become possible.

Using `Mirage`, we synthesised a scattered-light instrument response for the wavelengths and filters listed in Sect. 4.2.2.2. As we find in Sect. 4.3 that the dust in the wind should be more visible at shorter wavelengths, we forwent the integration of an additional long-channel filter.

The protoplanetary disk was assumed to be located at a distance of 100 pc; this resulted in a rather bright (probably overexposed) region around the star for lower i. We ran synthetic imaging for the `SUB320` subarray of module B1, using ten integrations with ten groups each for various readout patterns (RAPID, MEDIUM8, DEEP8, etc).(3) The resulting uncalibrated images were post-processed using the `jwst` pipeline.

As shown by Beichman et al. (2010, their Fig. 6), the JWST NIRCam coronagraphs provide a contrast $\gtrsim 10^{-4}$ for separations $\lesssim 0\farcs3$ (i.e. 30 AU at 100 pc), and are available for filters corresponding to $\lambda_\mathrm{obs} \gtrsim 1.8\,\mu$m. `Mirage` does not yet support full coronagraphic imaging simulations, so we only mimicked the effect of a coronagraph by applying an intensity reduction to the RadMC results, according to the instrument transmission, before processing them with `Mirage`.(4),(5)

4.2.2.4 Polarised-light instrument response for SPHERE IRDIS

The Stokes images $Q(\vec{r})$ and $U(\vec{r})$ emergent from `RadMC-3D`, in native resolution, can be used to predict the instrumental response in a polarisation observation with SPHERE IRDIS. As in Sect. 4.2.2.3, a distance of 100 pc to the hypothetical object was assumed for this.

A convolution with a Gaussian kernel, b_diff, whose dispersion σ_diff is set at the diffraction limit, $\sigma_\mathrm{diff} = \frac{1.2}{2\sqrt{2\,\ln(2)}}\frac{\lambda}{D}$, represents an ideal adaptive-optics correction for a telescope of diameter D. The IRDIS coronagraph is taken as a pill-box with diameter $0\farcs25$, $T(\vec{r})$, and the diffracted Stokes images are thus approximated as $Q_s = (b_\mathrm{diff} \cdot Q) \times (b_\mathrm{diff} \cdot T)$ and $U_s = (b_\mathrm{diff} \cdot U) \times (b_\mathrm{diff} \cdot T)$.

An estimate of the polarised intensity $P = \sqrt{Q^2 + U^2}$, alleviated from the positive-definite bias, can be obtained with a linear combination of Q_s and U_s in the so-called radial-Stokes formalism (Schmid et al., 2006). The idea, adapted to axially symmetric sources, is to assume that the polarisation direction

(1) We checked that our results are not affected by changing T_* to 4000K.

(2) For an analysis of the amount of photon packets needed for viable results in `RadMC-3D`, see Kataoka et al. (2015).

(3) The Astronomer's Proposal Tool (`APT`, `https://www.stsci.edu/scientific-community/software/astronomers-proposal-tool-apt/`) gives science durations between 107 s (RAPID) and 2010 s (DEEP8) for these parameters.

(4) The transmission data have been retrieved from `https://jwst-docs.stsci.edu/near-infrared-camera/nircam-instrumentation/nircam-coronagraphic-occulting-masks-and-lyot-stops`: `https://jwst-docs.stsci.edu/files/97978137/97978146/1/1596073154569/transmissions.tar`

(5) The science duration for coronagraphic imaging is higher, ranging from 2095 s (RAPID) to 39350 s (DEEP8).

is azimuthal, as in the case of single scattering (Schmid et al., 2006; Avenhaus et al., 2014; Garufi et al., 2014; Canovas et al., 2015; Avenhaus et al., 2017, 2018; Monnier et al., 2019). Here we follow the same convention as in Avenhaus et al. (2018), with

$$Q_\phi = Q_s \cos(2\,\phi) + U_s \sin(2\,\phi), \tag{4.4}$$

$$U_\phi = -Q_s \sin(2\,\phi) + U_s \cos(2\,\phi), \tag{4.5}$$

where $\phi = \arctan(-\Delta\alpha/\Delta\delta)$ is the position angle and $\Delta\alpha$, $\Delta\delta$ are offsets along right-ascension and declination. Another application of these radial Stokes parameters can be found in Casassus et al. (2018).

The $Q_\phi(\vec{r})$ image approximates the polarised intensity field in the case of perfectly azimuthal polarisation, that is when $U_\phi(\vec{r}) \equiv 0$. However, as discussed by Canovas et al. (2015), the emergent radiation from an intrinsically axially symmetric object such as a protoplanetary disk, when seen at even moderate inclinations, undergoes multiple scattering events that produce a radial polarisation component, with a non-vanishing U_ϕ and negatives in Q_ϕ. The radial Stokes parameters are nonetheless widely used in the field, as they convey the same information as Q and U, and we therefore estimate instrumental responses using this formalism.

In adaptive-optics-assisted imaging, it is often the case that an unresolved and very strong central signal, due for example to an inner disk or to net stellar polarisation, is spread out by the PSF wings to large stellocentric separations. Since we use a Gaussian PSF to estimate the instrumental response, this effect should be negligible in the bulk of the disk in the synthetic images, but might be important near the edges of the synthetic coronagraph. For consistency with the procedure applied to actual data, we also implemented the correction for 'stellar polarisation', which refers to the subtraction of the large-scale pattern due to the convolution of the unresolved central component with the PSF. For a synthetic 'stellar polarisation' subtraction, we simply define a radius, in polar coordinates $R = \sqrt{\Delta\alpha^2 + \Delta\delta^2}$, that encloses all of the 'stellar polarisation' signal, and set $Q^\star = Q$ and $Q^\star(R > R^\star) = 0$, and similarly for $U^\star$. In practice, we chose the same radius for $R^\star$ as that of the synthetic coronagraph, or $R^\star = 0\farcs125$. We then applied the same radial Stokes formalism to $Q^\star$ and $U^\star$ to produce $Q^\star_\phi$ and $U^\star_\phi$, which were then subtracted from the predicted Q_ϕ and U_ϕ images. The stellar polarisation subtraction had but a small impact on the resulting images.

The IRDIS observations of DoAr 44 in H-band, presented in Avenhaus et al. (2018), can be compared with the RT predictions in Casassus et al. (2018) to estimate the expected instrumental response for similar targets, that is other T-Tauri stars such as considered in this work. We calibrated the observed Q_ϕ and U_ϕ images of DoAr 44 by scaling with the RT predictions, thus extracting the noise level in H-band.

The synthetic images of the emergent polarisation in this work were thus cast into the radial-Stokes formalism, and reinterpolated to match the IRDIS CCD array, with the addition of Gaussian noise. This ensures that the predicted instrumental response represents a concrete setup in realistic conditions.

4.2.3 Limitations of the model

In order to limit computational costs, we made a number of simplifying assumptions. Firstly, we neglected dust sublimation. The inner boundary of the computational domain is placed at $r = 0.33$ AU; this allows us to capture the full extent of the photoevaporative wind (Picogna et al., 2019). This inner boundary also is well beyond the sublimation radius; assuming a dust sublimation temperature $T_{\rm sub} \approx 1500$ K (Pollack et al., 1994; Muzerolle et al., 2003b; Robitaille et al., 2006; Vinković, 2009), `RadMC-3D` yields $T_{\rm dust} \ll T_{\rm sub}$ for $r > 0.2$ AU in the wind regions of our models.

Secondly, radiation pressure for grain acceleration was not included in our model (see Paper I). Recently, Owen & Kollmeier (2019) have argued that radiation pressure may drive the bulk of the dust mass loss if grains are fragmented to small enough sizes ($a_0 \lesssim 0.6\,\mu$m for our setup, see Paper I); and Vinković & Čemeljić (2021) have shown that radiation pressure may severely affect dust trajectories in a magneto-hydrodynamic (MHD) wind region within $r \lesssim 30\,R_*$. However, almost all of our smaller grains are entrained from the disk surface anyways (see Table 4.1), implying that additional radiation pressure should be negligible for our setup (the fraction of entrained grains could not be much higher anyways). Furthermore, radiation pressure could lead to a small speed-up of the grains in the wind region; this would then lead to slightly reduced densities there as the grains would be blown out faster. Yet Booth & Clarke (2021) have argued that radiation pressure should not strongly affect grain entrainment by (X)EUV winds at least for an advection-dominated scenario.

4.3 Results

4.3.1 Dust distribution in the wind

4.3.1.1 Dust densities

The dust density maps in (R, z) for the eight a_0 modelled are shown in Figs. 4.3 ('fixed') and 4.4 ('variable'). The 'fixed' setup entails relatively high dust densities in the wind region for all a_0, albeit with bigger grains reaching lower maximum z in the wind for a given R (as expected from Paper I). The disk surface, that is the transition region from the very smooth-looking disk regions to the outflow-dominated wind regions, is clearly visible for all a_0. It marks a density decrease of about two orders of magnitude, as expected from Fig. 4.1.

For the 'variable' setup, the high-density regions for larger a_0 are compressed towards the disk midplane, and the dust content of the upper disk layers is strongly reduced. This leads to a wind region much less populated by dust grains of μm size; the very light green regions in Fig. 4.4 indicate $\varrho_{\mathrm{dust}} < 10^{-28}\,\mathrm{g/cm^3}$.

As expected, especially small dust grains are well-coupled to the gas. Fig. 4.5 shows the deviation between the dust-to-gas ratio computed according to Sect. 4.2.1.2 and the ratio yielded by our 'fixed' model for small grains ($a_0 = 0.1\,\mu$m). Simply put, this illustrates the deviation of the dust densities we computed, from a model assuming a constant dust-to-gas ratio for the wind region as well. The gas streamlines are included as dotted grey lines; the directions of the gas flow and the dust outflow channels match well, as would be expected (see Paper I). This, in turn, validates our approach of using the dust densities at the wind-dominated side of the disk surface (see Sect. 4.2.1.3).

For wind-driven outflows originating from $R \lesssim 10\,$AU, we notice a slight decrease of the relative dust content. This matches the results of Hutchison et al. (2016a); Hutchison & Clarke (2021), who find a decrease of the dust-to-gas ratio in the wind region in their models. Conversely, we see enhanced densities close to the disk surface far from the star ($R \gtrsim 100\,$AU). These are caused by grains being picked up by the wind at large R, and then travelling only slightly above the disk surface at a comparably low speed. This density enhancement occurs for all grain sizes investigated. Conversely, in the 'variable' model, the relative dust-to-gas ratios in the wind are smaller than for the 'fixed' setup, and < 1 for $a_0 \geq 0.5\,\mu$m.

Interestingly, in Fig. 4.5, the uppermost outflow channel with slightly enhanced dust densities starts from $R \approx 20\,$AU (also somewhat visible in Figs. 4.3 and 4.4), which coincides with the R-value from which we found the largest grains to be entrained in Paper I. This shows a correlation between general wind strength, material outflow and maximum entrained grain size.

4.3.1.2 Dust mass-loss rates

The XEUV-induced gas mass-loss rate is $\dot{M}_{\mathrm{gas}} \simeq 3.7 \cdot 10^{-8}\,\mathrm{M_\odot/yr}$ (see Sect. 4.2.1). The dust mass-loss rates $\dot{M}_{\mathrm{dust}}$ per a_0 for the 'fixed' and 'variable' cases are shown in Fig. 4.6; the corresponding (cumulative) values are listed in Table 4.2.

Table 4.2: Total $\dot{M}_{\mathrm{dust}}$ per grain size per model and cumulative values.

	$\dot{M}_{\mathrm{dust}}$ [$\mathrm{M_\odot/yr}$]	
a_0	'fix'	'var'
0.01	5.5e-12	5.8e-12
0.1	8.1e-12	4.6e-12
0.5	6.8e-12	9.9e-13
1	6.0e-12	1.1e-13
2	7.3e-12	7.1e-15
4	6.6e-12	3.6e-17
8	1.0e-12	3.6e-22
10	1.9e-13	9.5e-30
(sum)	4.1e-11	1.2e-11

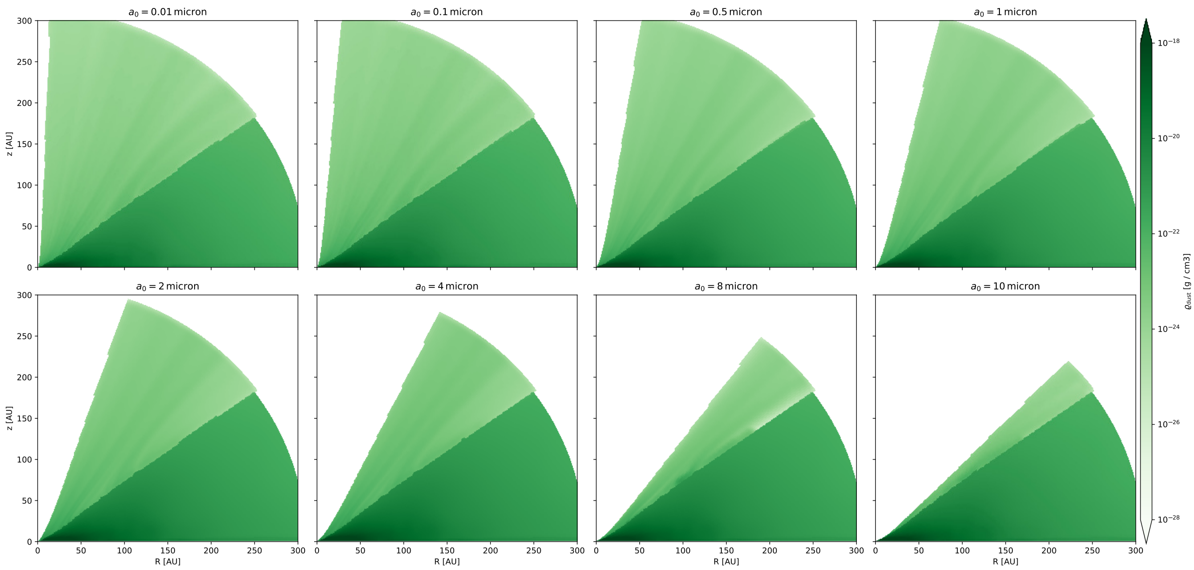

Figure 4.3: Dust densities for the XEUV-irradiated primordial disk in (R, z) for a 'fixed' dust-to-gas ratio throughout the disk. Enough material of all grain sizes is present at the base of the XEUV-driven outflow, resulting in high dust densities in the wind. Due to the model setup, the disk-wind interface is clearly discernible.

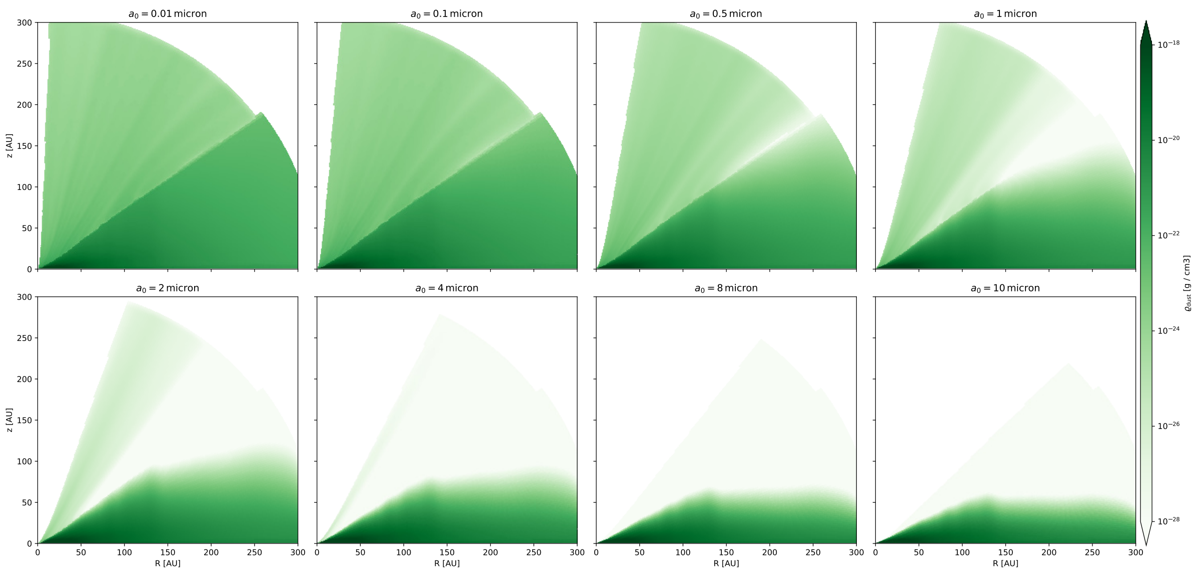

Figure 4.4: As Fig. 4.3, but for a 'variable' dust-to-gas ratio in the disk; same grain sizes and colour bar. The (lower) 'variable' dust scale height results in much lower dust densities in the wind than in the 'fixed' model, even for very small grains. The slightly wiggly appearance of the in-disk densities at $R \simeq 150\,\mathrm{AU}$ is caused by the underlying gas disk; it can be ignored as most dust entrainment occurs for smaller R (in respect to both total mass and radius).

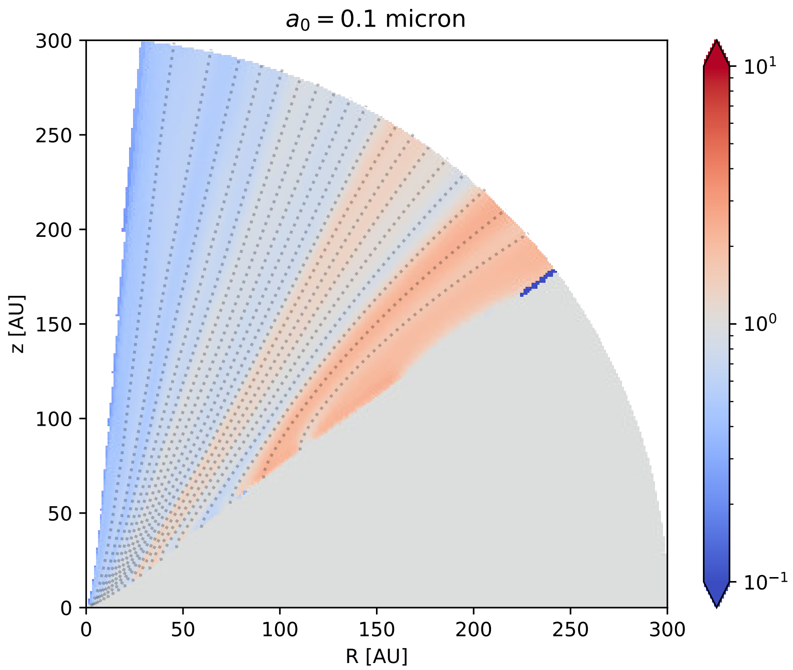

Figure 4.5: Ratio between gas density and dust density for $a_0 = 0.1\,\mu$m for the 'fixed' model, normalised to the value in the disk for clarity. The density of this small, and hence well-coupled grain species closely follows the gas density. For comparison with the density variations in the dust, the gas streamlines (one per 5% $\dot{M}_{\rm gas}$) are added as dotted grey lines.

For the 'fixed' setup, the dust mass-loss rate is fuelled by grains of all sizes, with only the contribution from $a_0 \gtrsim 8\,\mu$m falling off; this is expected since it represents the underlying mass distribution (see Sect. 4.2.1.2) and entrainment rates (see Table 4.1). For all a_0, $\dot{M}_{\rm dust}$ peaks closer to the disk surface than to the jet region. The cumulative mass-loss rate is $\dot{M}_{\rm dust} \simeq 4.1 \cdot 10^{-11}\,{\rm M}_\odot/{\rm yr} \simeq 1.1 \cdot 10^{-3}\,\dot{M}_{\rm gas}$. Coincidentally, the sum of the mass contributions from the MRN distribution for $a_0 < 11.5\,\mu$m is $\approx 11\%$; so accounting for the underlying dust-to-gas ratio of 0.01, this matches with the setup. Of course, not all large grains are entrained; considering that the eight size bins we employed have approximately similar mass contributions in the disk, this hints at a possible over-estimate for the dust masses in the wind (which suits our purposes), most probably due to the convolution of base densities and dust maps described in Sect. 4.2.1.3.

The 'variable' setup entails a lower $\dot{M}_{\rm dust}$, yielding a cumulative value of $\dot{M}_{\rm dust} \simeq 1.2 \cdot 10^{-11}\,{\rm M}_\odot/{\rm yr} \simeq 3.2 \cdot 10^{-4}\,\dot{M}_{\rm gas}$, about one third of the values for the 'fixed' scenario. Here, the bulk of the dust mass-loss is due to the grains $< 1\,\mu$m. The contribution from the smallest a_0 is even slightly higher than in the 'fixed' case; this is most likely due to the vertical settling-mixing equilibrium employed favouring higher vertical scale heights for small grains.

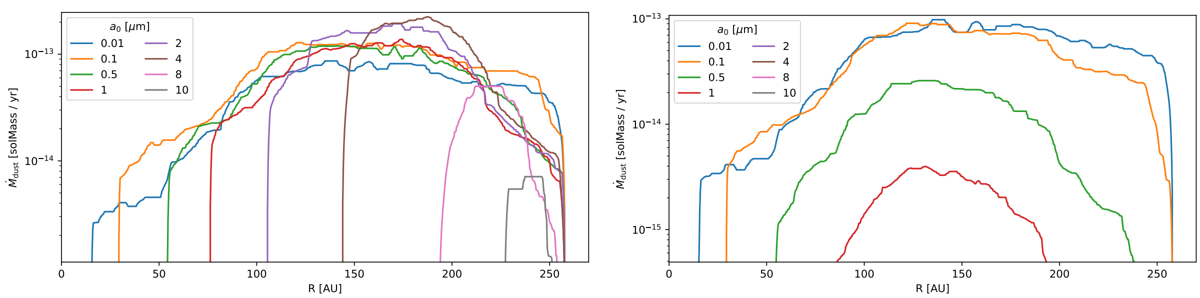

Figure 4.6: Median-filtered (for clarity) $\dot{M}_{\rm dust}$ over R for the 'fixed' (*right*) and 'variable' (*left*) scenarios, accounting for an assumed midplane symmetry. For no grain size do we find high $\dot{M}_{\rm dust}$ in the jet region.

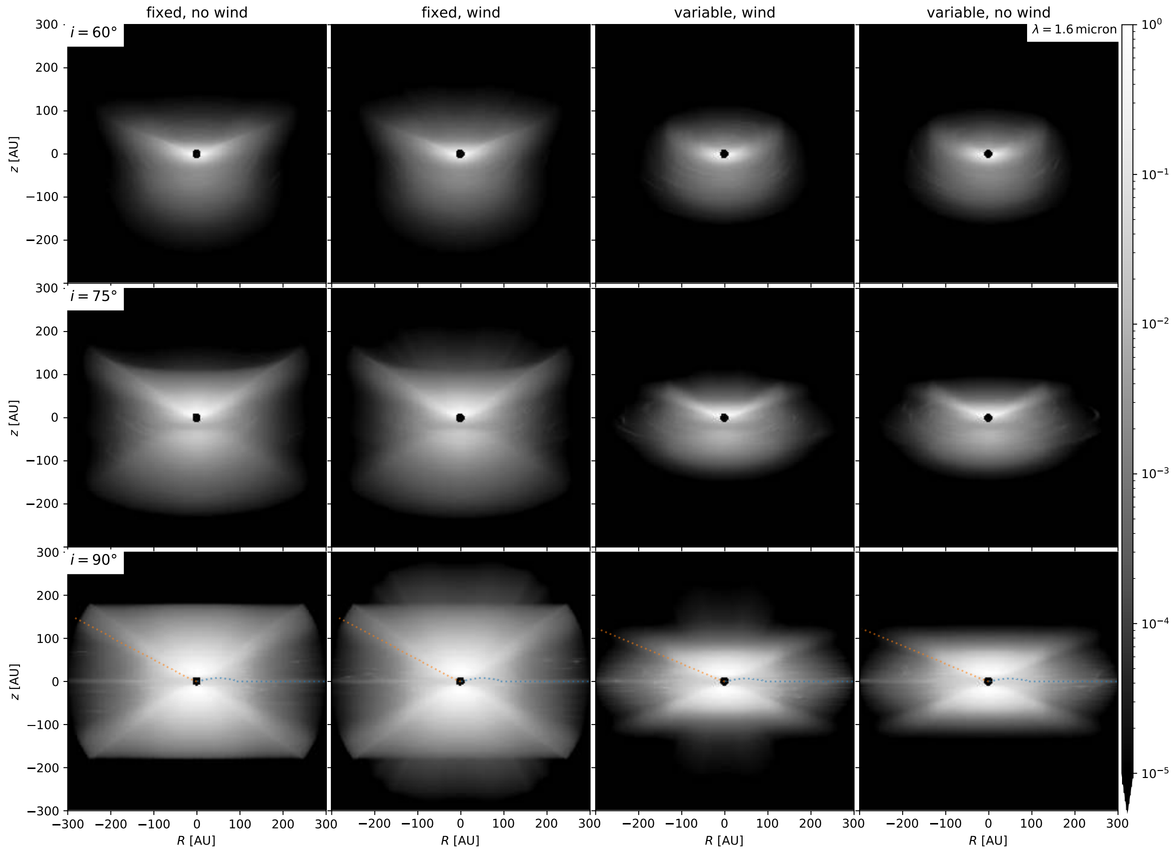

Figure 4.7: Radiative-transfer intensities for $\lambda_{\rm obs} = 1.6\,\mu$m. The max($I$) for the logarithmic colour scale is taken for each plot individually, after application of an artificial coronagraph of radius 10 AU. The ($\tau = 1$)-surfaces from $r = 0$ and $z = \infty$ are indicated by dotted orange and blue lines, respectively. *Rows:* inclinations $i \in \{60; 75; 90\}°$, *columns:* results without (first and fourth) and with (second and third) dusty wind outflow; 'fixed' model on the *left*, 'variable' one on the *right*. The wind signature is most noticeable at high inclinations, revealing a chimney-like structure with a distinctly narrower opening angle than the disk surface; it remains clearly less bright than said disk surface. The 'variable' dust scale height yields a much fainter outflow signal.

4.3.2 Synthetic observations

The scattered-light intensities simulated from the dust densities of Figs. 4.3 and 4.4 for $\lambda_{\rm obs} = 1.6\,\mu$m are shown in Fig. 4.7. The 'wind' images (inner columns) are accompanied by corresponding 'no wind' images (outer columns) for direct comparability. To provide better visibility of fainter features, an artificial coronagraph of $r = 10$ AU was introduced at the location of the star.

The differences between the 'fixed' and 'variable' models are much more pronounced than between their respective 'wind' and 'no wind' cases. In all cases, the wind appears featureless at low inclinations i ($i \lesssim 45°$) and for hence more face-on disks, even despite using logarithmic stretch.

For the 'fixed' setup (left columns of Fig. 4.7), cone- or chimney-like features start to envelop the z-axis for more edge-on objects ($i \gtrsim 60°$); however, they are distinctly less bright than the disk component. The relative intensity of the wind features is $I/I_{\rm max} \lesssim 10^{-4.5}$, $I_{\rm max} \equiv \max(I)$, at $i = 90°$ (best case), rendering these wind features at least challenging to observationally detect.

For the 'variable' model, the dusty outflow is less bright, and is noticeable at $i \gtrsim 75°$; it is qualitatively similar to the 'fixed' results. Furthermore, due to the reduced dust scale heights, the disk appears flatter, which is also illustrated by the ($\tau = 1$)-lines indicating where the optical depth reaches one starting from $r = 0$ (orange lines in Fig. 4.7). In addition, the disk appears smaller at $i < 90°$, caused by the decreased delivery of grains $\gtrsim 1\,\mu$m to the disk surface (see Fig. 4.4).

The low dust densities in the outflow do not lead to a notable enhancement in apparent dust scale heights; again, this can be seen from the ($\tau = 1$)-surfaces for an observer at $z = \infty$ (blue lines in Fig. 4.7). These surfaces do not visibly differ between the respective 'wind' and 'no wind' models.

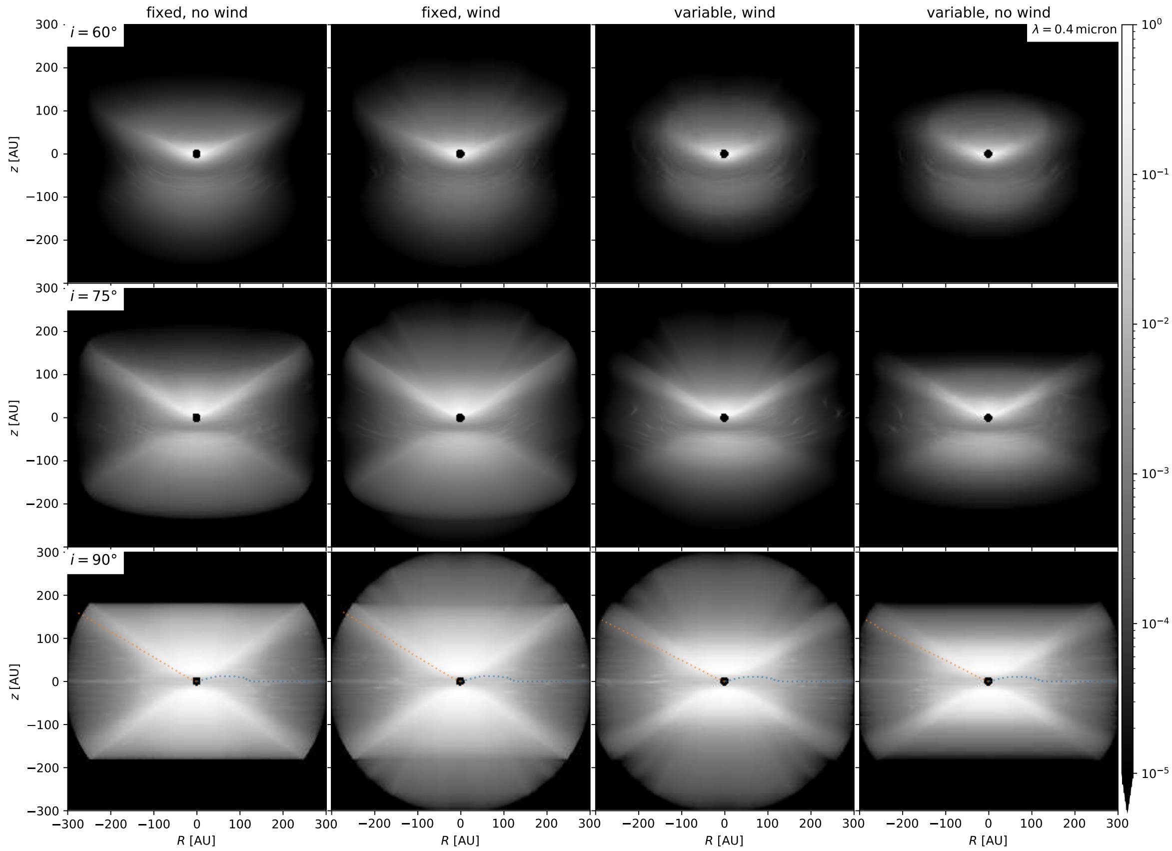

Figure 4.8: Radiative-transfer intensities for $\lambda_{\rm obs} = 0.4\,\mu$m, all else equal to Fig. 4.7. Both the 'fixed' and 'variable' models produce a noticeable wind signature (in logarithmic stretch), and the disks look quite similar.

The scattered-light images for $\lambda_{\rm obs} = 0.4\,\mu\text{m} = 400\,\text{nm}$ are shown in Fig. 4.8. For smaller a_0, the density maps for the 'fixed' and 'variable' models are more similar (see Figs. 4.3 and 4.4); this results in more similar images at $\lambda_{\rm obs} = 0.4\,\mu$m compared to $1.6\,\mu$m. Thus, the scattered-light intensities for the 'no wind' cases are almost model-independent at $i = 90°$; at $i < 90°$, the 'variable' disk still appears smaller. Yet it looks considerably more puffed up than at $\lambda_{\rm obs} = 1.6\,\mu$m, as would be expected from a size-dependent vertical-settling prescription.

The XEUV-driven dust outflow signature is quite comparable for the 'wind' models, and reaches relative intensities of $I/I_{\rm max} \lesssim 10^{-3.5}$ at $i = 90°$. The ($\tau = 1$)-surfaces are still almost identical within the 'fixed' and 'variable' models, meaning that the apparent dust scale height is still not significantly impacted. Furthermore, the opening angle of the emerging cone feature(s) does not really change in comparison to $\lambda_{\rm obs} = 1.6\,\mu$m, indicating that it is unrelated to the maximum outflow heights parametrised in Paper I.

When comparing the SEDs from disks without and with a dusty wind, we found no features that clearly stood out above the Monte-Carlo-induced noise. This indicates that the emission at the wavelength range investigated is dominated by the bound disk.

4.3.2.1 Scattered-light images

Due to the comparatively very bright inner area around the star, sporting radiative-transfer intensities of up to $\approx 2 \cdot 10^8\,\text{nJy/arcsec}^2 \simeq 2 \cdot 10^5\,\text{nJy/pix}$, JWST NIRCam images synthesised without accounting for a coronagraph are clearly over-exposed even using the RAPID readout pattern; this leads to an overexposure pattern which bleeds far into the disk. The relative brightness of the dusty XEUV outflow is thus too low to be picked up, or contaminated by overflow from the inner region. This means that we cannot use the F070W filter for our purposes.

Instead, we switched to $\lambda_{\rm obs} = 1.8\,\mu$m with the F182M filter in combination with the simplified coronagraph implementation as described in Sect. 4.2.2.3; the resulting synthesised images are shown in

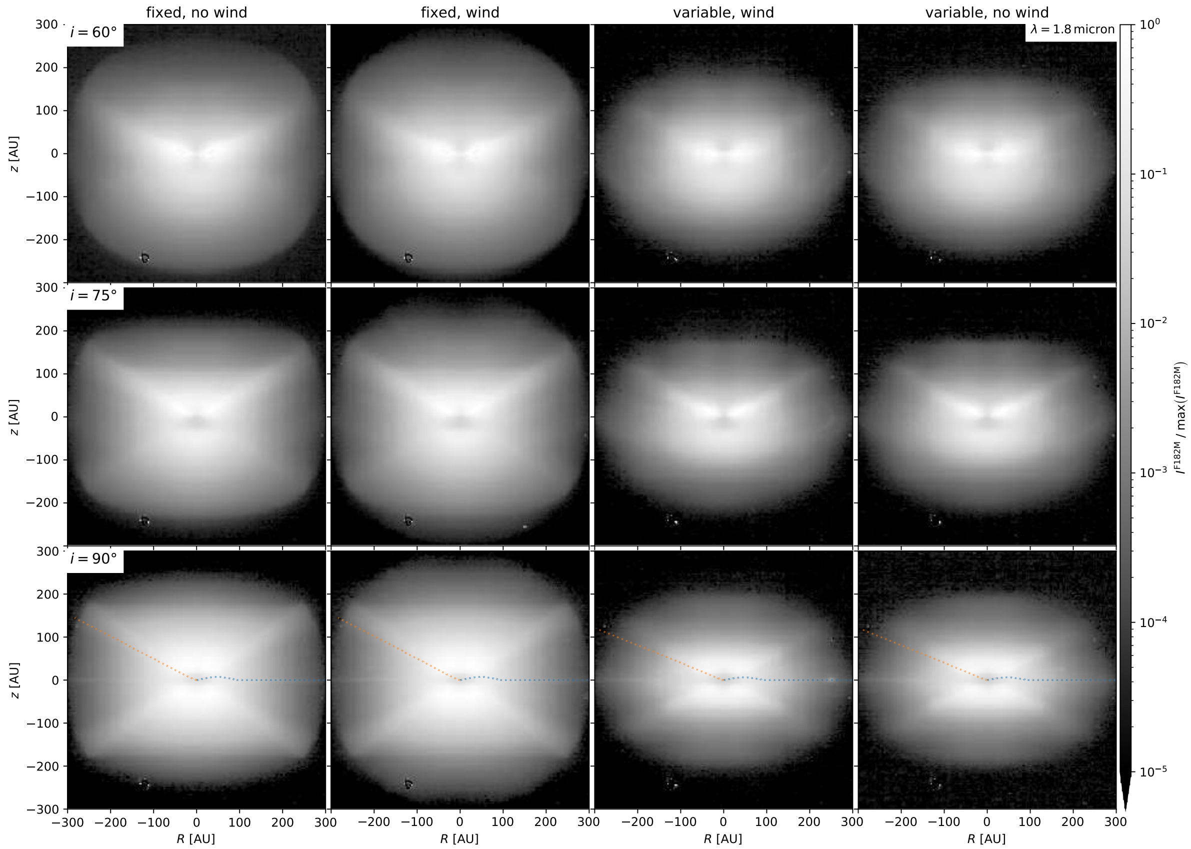

Figure 4.9: Synthesised intensities for JWST NIRCam's F182M filter with a simulated MASK210R coronagraph (MEDIUM8 readout pattern, 10 groups for 10 integrations). The orange and blue lines indicate the ($\tau = 1$)-surfaces from $r = 0$ and $z = \infty$. We find a slight difference in the vertical extent of the 'no wind' and 'wind' 'fixed' models. At $i \gtrsim 75°$, a faint cone-like pattern emerges, in agreement with the direct radiative-transfer results of Fig. 4.7.

Fig. 4.9. For these, the MEDIUM8 readout pattern was employed, providing the best middle ground between an overexposed central region (DEEP8) and noisy outer regions (RAPID). Varying the number of groups and integrations yielded very similar results.

For the 'fixed' setup, we find a slightly enhanced vertical extent for $i \gtrsim 75°$, reminiscent of the cone-shaped feature of the radiative-transfer results (see Fig. 4.7). However, the cone itself does not stand out as clearly, and the corresponding difference between the 'wind' and 'no wind' images may be too small to be used as a definite outflow indicator without detailed modelling of the source. The 'wind' and 'no wind' images of the 'variable' model do not differ in any noticeable way.

4.3.2.2 Polarised-light images

Fig. 4.10 displays the Q_ϕ signal synthesised for SPHERE IRDIS's H-band for the inclinations of interest. There is no feature differentiating the dusty XEUV 'wind' models from their 'no wind' counterparts; this holds if we look at the data in logarithmic instead of linear stretch. While differential imaging reveals a faint enhancement of the 'variable' 'wind' model compared to its 'no wind' counterpart at $i = 90°$, the difference is too small to be useful for distinguishing between them. This implies that, at least for the setup investigated here, XEUV-driven outflows may be too faint to be picked up by current instruments. As can be seen from Avenhaus et al. (2018, their Fig. 3), SPHERE IRDIS can detect a signal down to a relative intensity of $\gtrsim 10^{-5}$ under optimal conditions; however, we do not find significant wind features when looking at Fig. 4.10 in logarithmic stretch, mainly because any possible signal disappears in the instrument noise. Higher mass-loss rates, as for instance provided by a centrally concentrated MHD wind model, might provide a more distinct signal; this should be explored in future calculations.

Synthesised J-band images ($\lambda_{\rm obs} = 1.2\,\mu$m) do not exhibit any notable 'wind' features either, and neither do images for P. When looking at Q_ϕ maps for $\lambda_{\rm obs} = 0.4\,\mu$m without a synthesised instrument

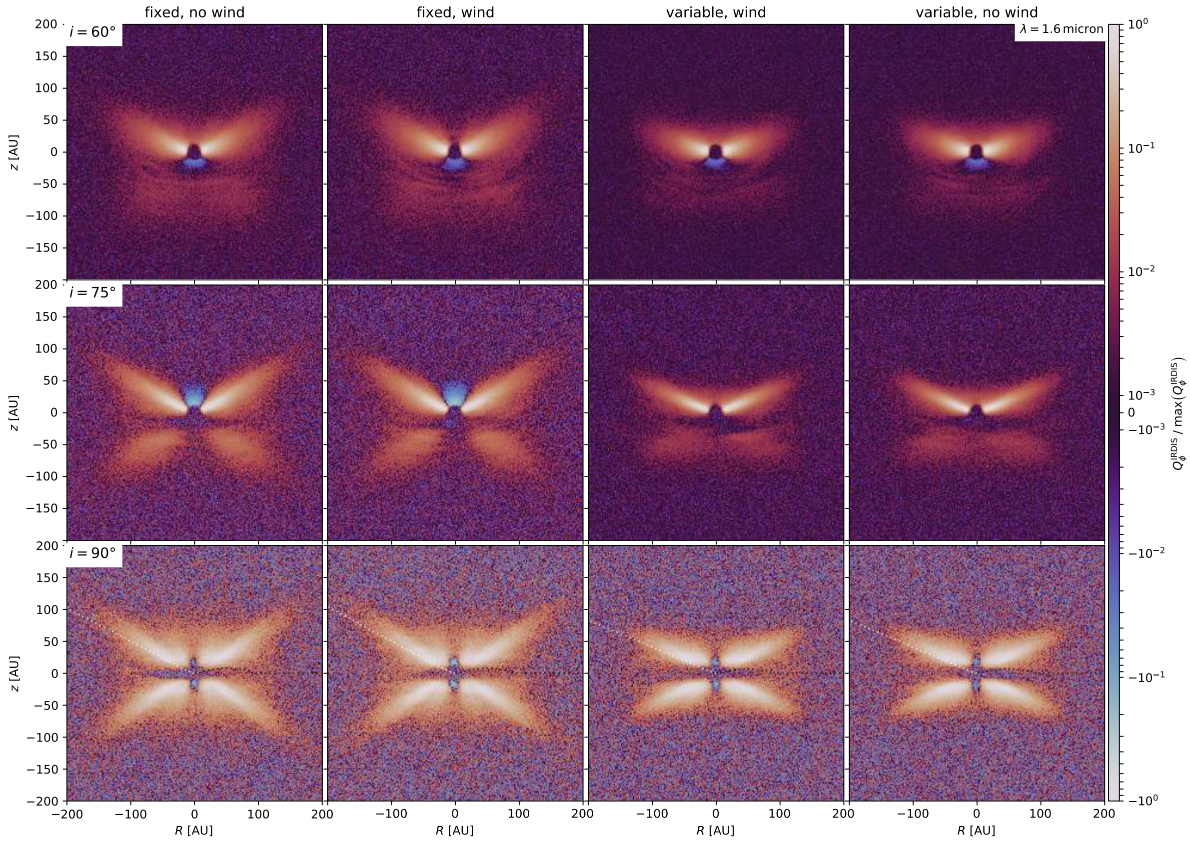

Figure 4.10: Q_ϕ maps (logarithmic stretch for the inner inner 200 AU × 200 AU) synthesised for SPHERE IRDIS's H-band ($\lambda_{\text{obs}} = 1.6\,\mu$m); ($\tau = 1$)-surfaces from $r = 0$ and from $z = \infty$ added as dotted white and black lines, respectively. No distinct difference emerges between the disks without (first and fourth columns) and with (second and third columns) a dusty wind; the difference between the 'fixed' and 'variable' dust scale heights has a much larger impact on the synthesised instrument response.

response, a wind signature starts to emerge for $Q_\phi/\max(Q_\phi) \lesssim 10^{-3}$ ($i = 90°$) in the same chimney-shaped region we have seen in Fig. 4.8. This contrast is comparable to the one needed to see a wind signature in said image.

4.4 Discussion

Theoretical models of photoevaporative winds agree that qualitatively, a certain amount of dust is entrained in the outflow above the protoplanetary disk (e.g. Clarke et al., 2001; Owen et al., 2011a, 2012; Ercolano & Pascucci, 2017). However, to our knowledge, there has not yet been an estimate of the actual dust content of this outflow, and hence its observability.

4.4.1 Dust distribution

4.4.1.1 Dust densities

The 'hovering' (or at least slow-moving) dust grains seen for the 'fixed' case in Fig. 4.5 at larger R might potentially cause a diffuse signal in scattered- and polarised-light images at high inclinations; the polarised-light images provided by SPHERE IRDIS for RY Lup (Langlois et al., 2018), 2MASS J16083070-3828268 (Villenave et al., 2019), and MY Lup (Avenhaus et al., 2018) could be examples of this. As pointed out by Booth & Clarke (2021), the vertical transport mechanisms at play will heavily influence the vertical disk height, and thus the size of these grains. The disk scale height itself would need to be better constrained via observational data sets for our models to be more refined.[(1)] Nonetheless, our results seem to match the findings of Pinte et al. (2008); Villenave et al. (2020) and others, who find μm-sized dust grains well above the disk midplane; in addition, the presence of μm-sized dust grains at the disk surface (and probably above) is well-documented by early SED data (Dullemond & Dominik, 2005, 'small-grains problem') and scattered-light images of edge-on disks. Furthermore, the absence of big grains in the wind matches the results of Hutchison & Clarke (2021); Booth & Clarke (2021), who find that the majority of grains in the wind has sizes well below the theoretically possible value; we also match their result that almost all grains delivered to the base of the outflow will be entrained (within a given Stokes number range).

4.4.1.2 Mass-loss rates

Due to $\dot{M}_{\rm dust}/\dot{M}_{\rm gas}$ being smaller than the assumed dust-to-gas ratio, the dust-to-gas ratio in the disk will increase as a result of photoevaporation, particularly in the regions where the latter is most efficient (i.e. around the gravitational radius). Not accounting for probably varying rates and various other effects, the gas and dust masses in our model would be equal about 0.15 Myr after XEUV photoevaporation starts.

This could potentially explain high dust-to-gas ratios as found for instance by Miotello et al. (2017). It is also expected to favour planetesimal formation by the streaming instability; however, recent studies which assume a dust-free photoevaporative wind, disagree on the efficiency of this process (Carrera et al., 2017; Ercolano et al., 2017b). Moreover, as found for instance by Kunitomo et al. (2020), photoevaporative winds are supposed to dominate over MHD outflows in the later stages of the disk lifetime, at least in terms of $\dot{M}_{\rm gas}$. And indeed, dust entrainment may be significantly enhanced once the transition disk phase begins, that is when the midplane dust at the outer gap edge would automatically be located at the disk-wind interface without the need for efficient vertical transport mechanisms.

4.4.2 Observability of XEUV winds

We find a chimney-like outflow signature in Figs. 4.7 and 4.8; however, MHD winds may well dominate in terms of dust entrainment in the immediate vicinity and the jet region of a star (see e.g. Miyake et al., 2016). These MHD winds could even be prominent all the way down to the disk surface (Rodenkirch et al., 2020).

Villenave et al. (2020, and sources therein) have presented a collection of images of highly inclined disks in scattered light at μm-wavelengths ($0.4 \lesssim \lambda_{\rm obs}\,[\mu{\rm m}] \lesssim 2.2$). Most of these objects (e.g. HH 30, 2MASS J04202144+2813491, HV Tau C) do not exhibit well-defined cone-like features as those shown in Figs. 4.7 and 4.8. Nonetheless, a diffuse emission above the disk surface is visible in some objects, and may be due to 'hovering' dust grains. Some other objects (e.g. IRAS 04158+2805, see Villenave et al., 2020) exhibit a distinct region of enhanced outflow above the disk midplane; yet this feature appears to extend to large scale heights above the disk midplane and involves the entire jet region. Thus, it is quite difficult to trace the origin of this emission without a tailored modelling of the source.

The 'variable' dust scale height entails a darkening of the outer disk regions ($R \gtrsim 140\,$AU). This is probably caused by shadowing from the inner 140 AU of the disk, after which the density especially of large grains around the disk surface drops due to vertical settling (see Fig. 4.4). In principle, this is comparable to the model 'B' of Dullemond (2002), which shows a puffed-up inner rim to produce a shadow. It is not an effect caused by photoevaporative winds because the 'wind' and 'no wind' models are both affected.

4.4.2.1 Predictions in scattered light

Hubble Space Telescope (HST) images of disks have not yet shown any evidence for disk winds driven by internal photoevaporation; this may be because the signal is too faint,[(2)] or the jet contaminates fainter features (Wolff et al., 2017). JWST NIRCam will provide notably higher contrast. In theory, this means that as we have seen from Fig. 4.9, the XEUV-driven dusty outflow modelled here may actually produce an observable signature, at least for the highly inclined disks of the 'fixed' model. Since the cone shape of the wind-driven dusty outflow does not stand out strongly, and provides only a slight increment in vertical height for the 'wind' images over their 'no wind' counterparts, it is debatable whether an isolated image

[(1)] Constraining the dust delivery at the base of the wind would require modelling the evolution of disk material, and self-consistently accounting for dust growth together with gas and dust hydrodynamics; this complex task is well beyond the scope of this work, where we take the approach of showing limiting cases.

[(2)] External photoevaporation may have already been imaged, see O'Dell & Wen (1994); Miotello et al. (2012).

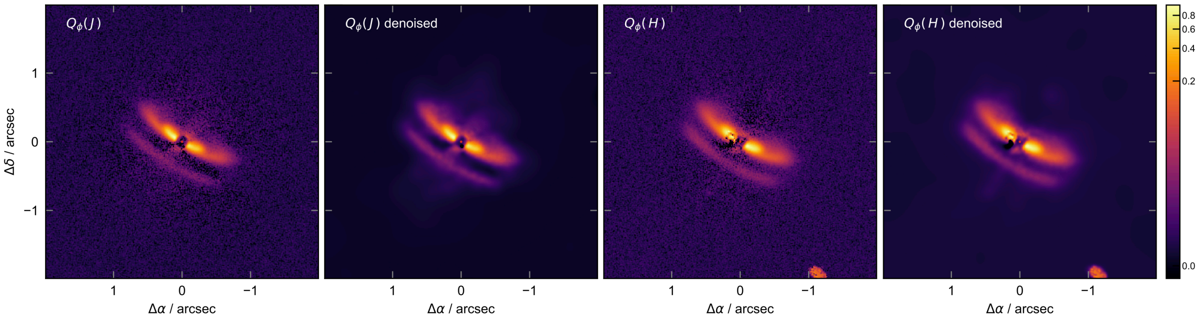

Figure 4.11: Q_ϕ images of MY Lup in J- and H-band, based on a new reduction of the data presented in Avenhaus et al. (2018). For both bands, the images are shown without and with smoothing by a denoising algorithm (Price, 2007). There is a faint signal from the minor axis of the disk, which hints at a dusty outflow.

of a primordial disk would suffice to determine the presence or absence of a wind. Reducing (extending) the cutoff radius (here: $r \simeq 300\,\mathrm{AU}$) of the model would likely enhance (degrade) the visibility of the outflow.

The 'variable' setup does not exhibit any outflow pattern, despite the synthesised images showing faint traces of overexposure in their centre (which should enhance the visibility of far-out features). On a different note, a higher underlying dust-to-gas ratio (see Sect. 4.2.1.2) may lead to a more distinct wind pattern for the setup presented here (see also Dahlbüdding et al., in prep.).

The synthetic observations shown in this work have been computed from and for a primordial disk. We conclude that intriguingly, with JWST NIRCam the observation of wind signatures is entering the realm of possibilities.

4.4.2.2 Comparison to observations in polarised light

The differential-polarised imaging data presented in Avenhaus et al. (2018) and Garufi et al. (2020) target 29 nearby T-Tauri stars, with stellar masses in the range $0.5 \leq M_* \,[\mathrm{M}_\odot] \leq 1.0$ (Garufi et al., 2020, hereafter DARTTS-S sample), and correspond to the domain considered by our model predictions. The DARTTS-S sample includes high-inclination sources, with a favourable view of material away from the disk midplanes. In general, none of these T-Tauri stars display any evidence for nebulosity along the disk minor axis that might correspond to an XEUV wind; for instance, one can look at the Q_ϕ image of DoAr 25 in H-band presented by Garufi et al. (2020, their Fig. 1). The absence of conspicuous wind features is consistent with our predictions, and does not indicate the absence of XEUV-driven photoevaporative winds.

By contrast, MY Lup is the one object in the DARTTS-S sample with diffuse emission along the disk minor axis. Some extended negatives along the disk minor axis in the data originally presented by Avenhaus et al. (2018) prompted us to reduce the images using the IRDAP pipeline (van Holstein et al., 2020), with special attention to stellar polarisation subtraction; for this, the IRDIS images have been processed using an adaptive kernel smoothing technique called `denoise` (part of the `splash` suite, Price, 2007).(1) The resulting data are presented in Fig. 4.11; they show some diffuse signal indicating a dusty outflow. Furthermore, the signal is more conspicuous in J-band ($\lambda_{\mathrm{obs}} \approx 1.2\,\mu\mathrm{m}$) than in H-band, which is consistent with Rayleigh-scattering if the entrained dust is smaller than $\sim 1\,\mu\mathrm{m}$. New polarisation observations at shorter wavelengths, for instance with SPHERE ZIMPOL in the V-band broad-band filter, could confirm this tentative detection.

As found by Alcalá et al. (2019), MY Lup likely does not have a dust cavity, which would allow for an almost direct comparison to our primordial disk model. Alternatively, they allow for the possibility that the high CO depletion found by Miotello et al. (2017) could explain the high mass-accretion rates and enhanced winds (Wölfer et al., 2019). Furthermore, the presence of a dusty wind could explicate the anomalous extinction law towards the central star, which may have led to an overestimate of the age of the system ($\approx 17\,\mathrm{Myr}$, see Alcalá et al., 2017, 2019).

As seen in Fig. 4.10, we do not find a distinct signal enhancement along the disk minor axis for the Q_ϕ images synthesised for SPHERE IRDIS from our 'wind' models; we checked that this also holds for

(1) `denoise`: `https://github.com/danieljprice/denoise/`.

$\lambda_{\rm obs} = 1.2\,\mu$m. Thus, while we would argue that the outflow seen in Fig. 4.11 is indeed driven by a wind, we cannot say whether said wind is an MHD wind, or possibly a CO-depleted, thus enhanced, XEUV one. In any case, however, its corresponding $\dot{M}_{\rm dust}$ supposedly must be at least an order of magnitude higher than the values we have reported for our models ($\dot{M}_{\rm dust} \lesssim 4.1 \cdot 10^{-11}\,{\rm M}_\odot$/yr, see Sect. 4.3.1.2), which would indicate a rapid depletion of dust at and around the disk surface. This, in turn, would raise the question whether such a strong outflow could be stable for prolonged periods of time, or whether it may be a periodical or short-lived phenomenon.

So the possible detection of a dusty wind in MY Lup, while it is absent in the other DARTTS-S sources, suggests that our model is missing some of the diversity of real physical systems; more custom-tailored models for this source are needed in order to answer this question. In addition, our findings lead us to expect dusty XEUV winds from primordial disks to be detectable at $0.4\,\mu$m (in logarithmic stretch), which is only a factor of ~ 3 in wavelength from the possible detection in MY Lup.

4.5 Summary

Based on the trajectories of dust grains in the XEUV-driven wind region of a protoplanetary disk around a T-Tauri star, we have computed the dust density in said wind region. Our main findings are as follows:

- Photoevaporative winds can entrain μm-sized dust grains.
- The dust densities at the base of the disk wind heavily impact the dust content of the wind.
- The dust mass-loss rate due to XEUV winds is significantly lower than expected from the corresponding gas mass-loss rates. This may lead to an enhancement of the dust-to-gas ratio in the disk.

In addition, we have used these dust densities to synthesise observations in scattered light (for JWST NIRCam) and polarised light (for SPHERE IRDIS). The results have led us to the following conclusions:

- Observations of dusty disk winds are challenging with current instrumentation – which is limited to comparably large wavelengths –, even if the base of the wind is rich in μm-size grains. It is thus not surprising that current observational campaigns in scattered light have yet to find a definite wind signature. This does not necessarily imply the absence of a photoevaporative wind.
- Dusty winds launched from primordial disks should, in the majority of cases, not lead to a strong vertical puff-up of the disks.
- There is a tentative detection of a disk wind in MY Lup. This could be confirmed by tailored modelling of deeper observations, and observations at shorter wavelengths.

However, the models presented here are only applicable to primordial disks. In a next step, we intend to investigate disk models with an inner cavity, which may produce more distinct signatures of XEUV-driven disk winds.

Acknowledgements: We would like to thank A. Garufi, C. Dullemond, P. Rodenkirch, M. Hutchison, and T. Grassi for helpful discussions, and the (anonymous) referee for a constructive report which improved the manuscript.
Furthermore, we thank C. Dullemond for providing the soon-to-be-open-sourced `disklab` package together with T.B.
This research was funded by the Deutsche Forschungsgemeinschaft (DFG, German Research Foundation), grant 325594231 (FOR 2634/1 and FOR 2634/2), and the Munich Institute for Astro- and Particle Physics (MIAPP) of the DFG cluster of excellence *Origin and Structure of the Universe*. B.E. and T.B. acknowledge funding by the Deutsche Forschungsgemeinschaft under Germany's Excellence Strategy – EXC-2094-390783311. S.C. and S.P. acknowledge support from Agencia Nacional de Investigación y Desarrollo de Chile (ANID) through FONDECYT Regular grants 1211496 and 1191934. T.B. acknowledges funding from the European Research Council (ERC) under the European Union's Horizon 2020 research and innovation programme under grant agreement No 714769. The simulations have mostly been carried out on the computing facilities of the Computational Center for Particle- and Astrophysics (C2PAP).

4.6 Additional material

4.6.1 Outflow speed

To expand on the outflow velocities shown in Fig. 3.4 (also in the light of the results of Rodenkirch & Dullemond, 2022), and to provide an illustration for the correlation between grain launching position (along the disk surface) and final velocity claimed in Sect. 4.2.1.4, we show the latter in Fig. 4.12. There, the terminal radial outflow speeds ($v_{r,\mathrm{out}}$, when reaching the computational domain boundary) of the dust grains are plotted in relation to their starting position R_0. The small grains reach outflow velocities comparable to the gas (see also Sect. 3.3.2), while the larger, but still entrainable grains move more slowly.

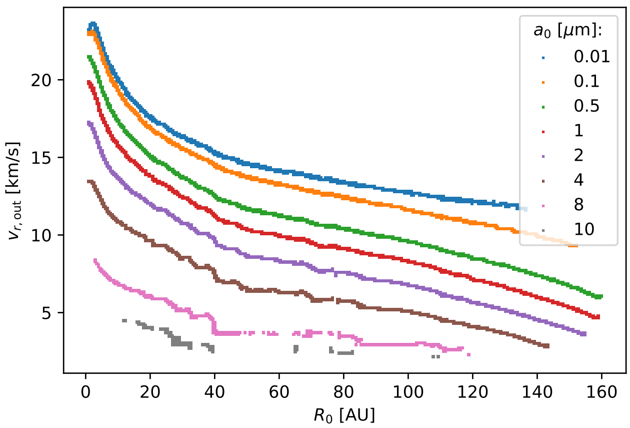

Figure 4.12: Final radial velocities v_r for fully entrained dust grains of various sizes launched from the disk surface at R_0. There is a very clear correlation between R_0 and v_r, and also a_0 and v_r.

4.6.2 Images

In order to provide a complete suite of theoretical and observational predictions, additional plots are included here. Figs. 4.13 and 4.14 show the radiative-transfer results for the scattered-light intensity I at $\lambda_{\mathrm{obs}} = 0.7\,\mu$m and $1.2\,\mu$m, respectively. The relative intensities of the wind features lie between those of Fig. 4.8 ($0.4\,\mu$m) and Fig. 4.7 ($1.6\,\mu$m); the cone feature is already significantly darker at $0.7\,\mu$m than at $0.4\,mu$m. This underlines the importance of observations (and, on a long term note, development of instruments) with both high contrast and high resolution.

For brevity, we excluded the radiative-transfer results for polarised-light Q_ϕ from Sect. 4.3; the images for $\lambda_{\mathrm{obs}} = \{0.7, 1.2, 1.6\}\mu$m are shown in Figs. 4.15, 4.16, and 4.17. in contrast to the synthesised instrument responses of SPHERE IRDIS, there is a difference in signal between the 'wind' and 'no wind' cases, which is more prominent for the 'fixed' than for the 'variable' case. The colour of the wind region (i.e. $Q_\phi < 0$ or $Q_\phi > 0$) varies with λ_{obs}; it may also depend on the opacity prescription used (see Sect. 5.6.1).

The Q_ϕ signal seen in Figs. 4.15 to 4.17 is however too faint to be detectable with SPHERE IRDIS; this is the case for both H-band (as shown in Fig. 4.10) and J-band (see Fig. 4.18).

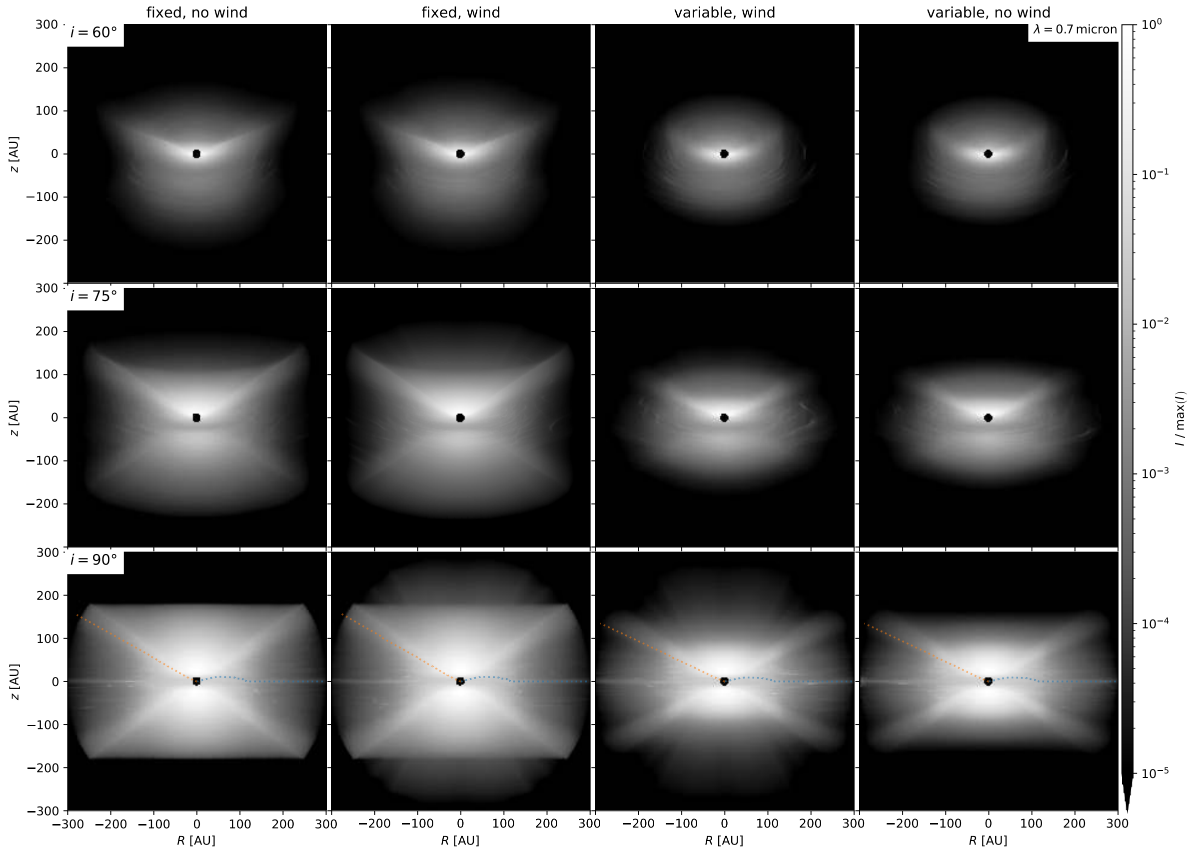

Figure 4.13: Radiative-transfer results for the scattered-light intensities I for $\lambda_{\mathrm{obs}} = 0.7\,\mu$m, all else equal to Fig. 4.7.

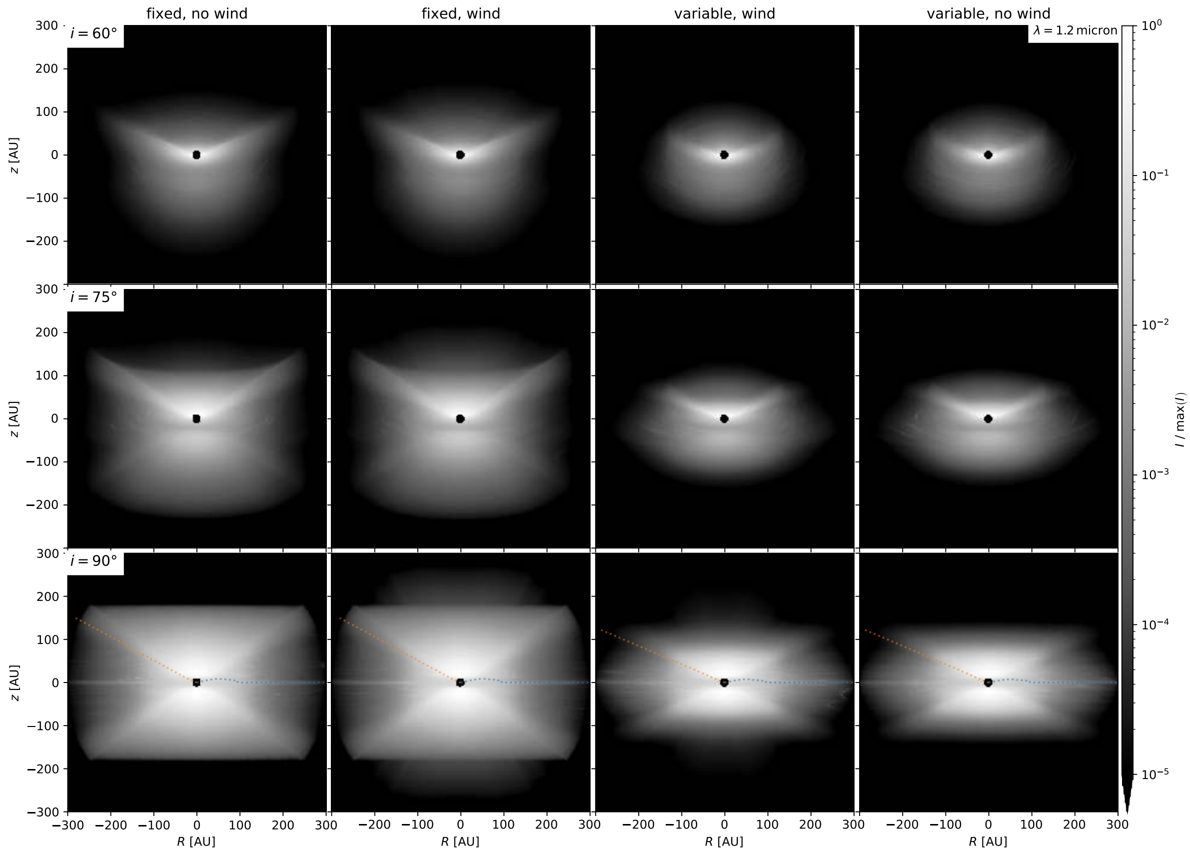

Figure 4.14: Radiative-transfer results for the scattered-light intensities I for $\lambda_{\mathrm{obs}} = 1.2\,\mu$m, all else equal to Fig. 4.7.

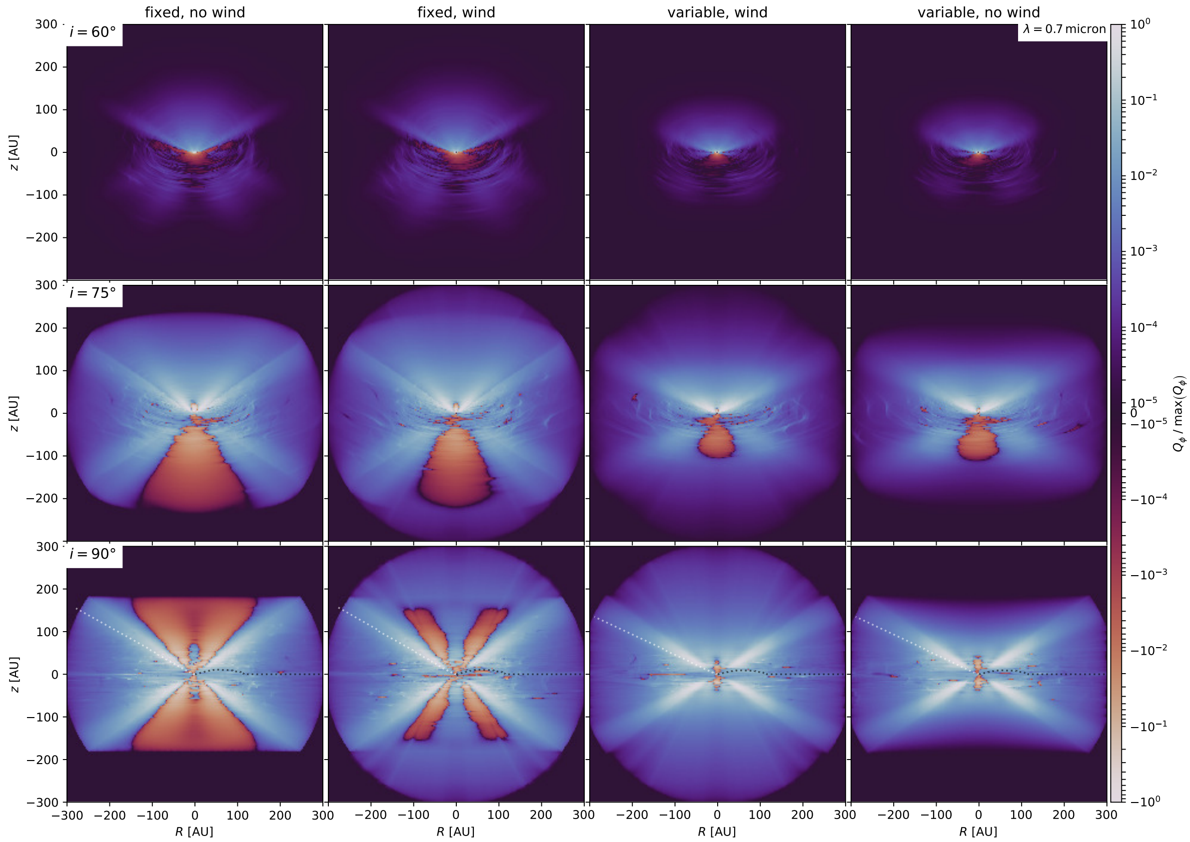

Figure 4.15: Radiative-transfer results for the polarized-light intensities Q_ϕ for $\lambda_{\rm obs} = 0.7\,\mu$m, all else equal to Fig. 4.10.

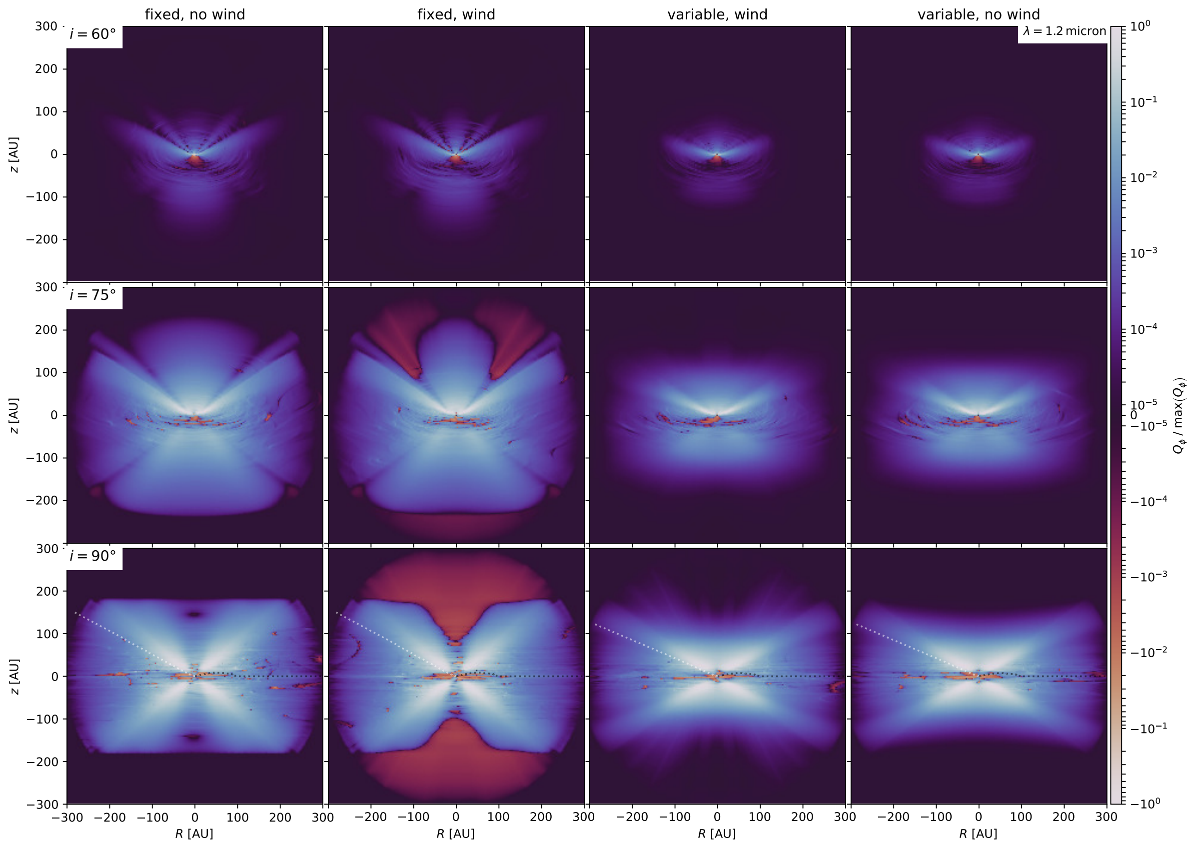

Figure 4.16: Radiative-transfer results for the polarized-light intensities Q_ϕ for $\lambda_{\rm obs} = 1.2\,\mu$m, all else equal to Fig. 4.10.

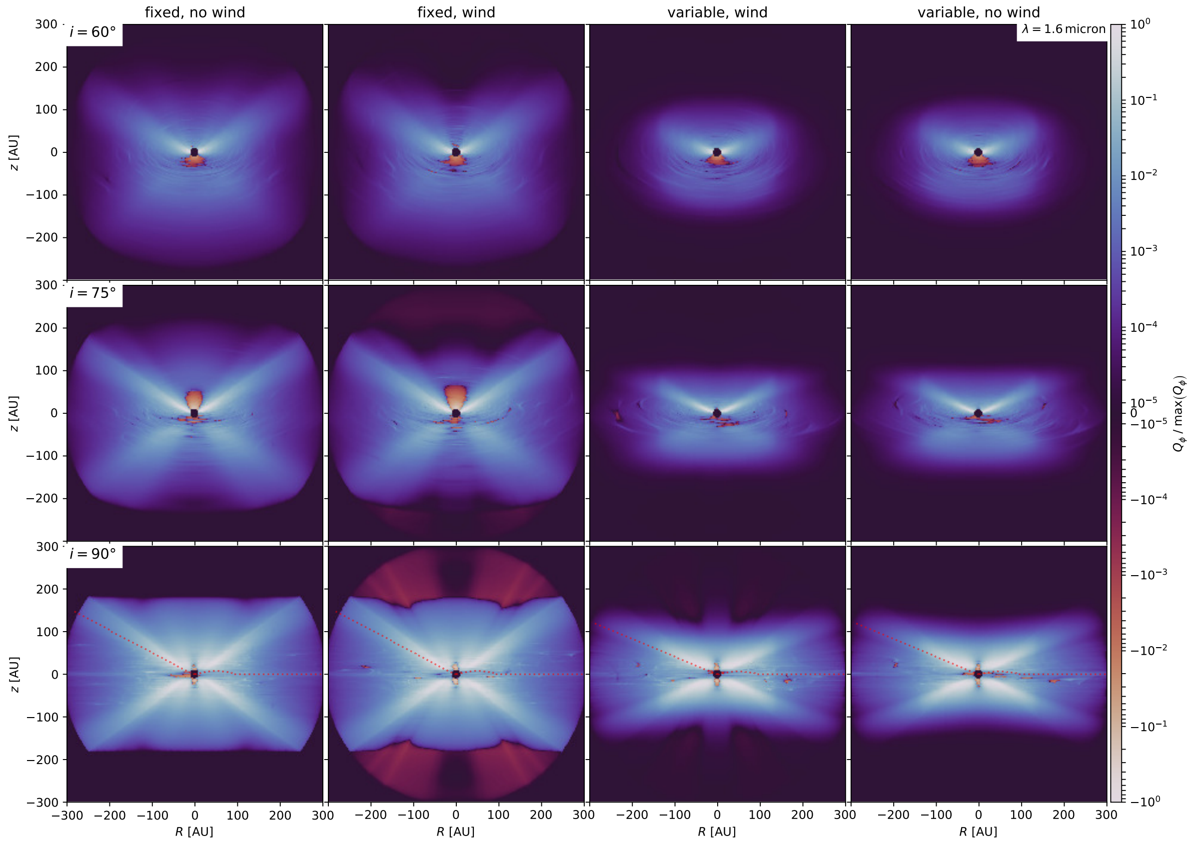

Figure 4.17: Radiative-transfer results for the polarized-light intensities Q_ϕ for $\lambda_{\rm obs} = 1.6\,\mu$m, all else equal to Fig. 4.10.

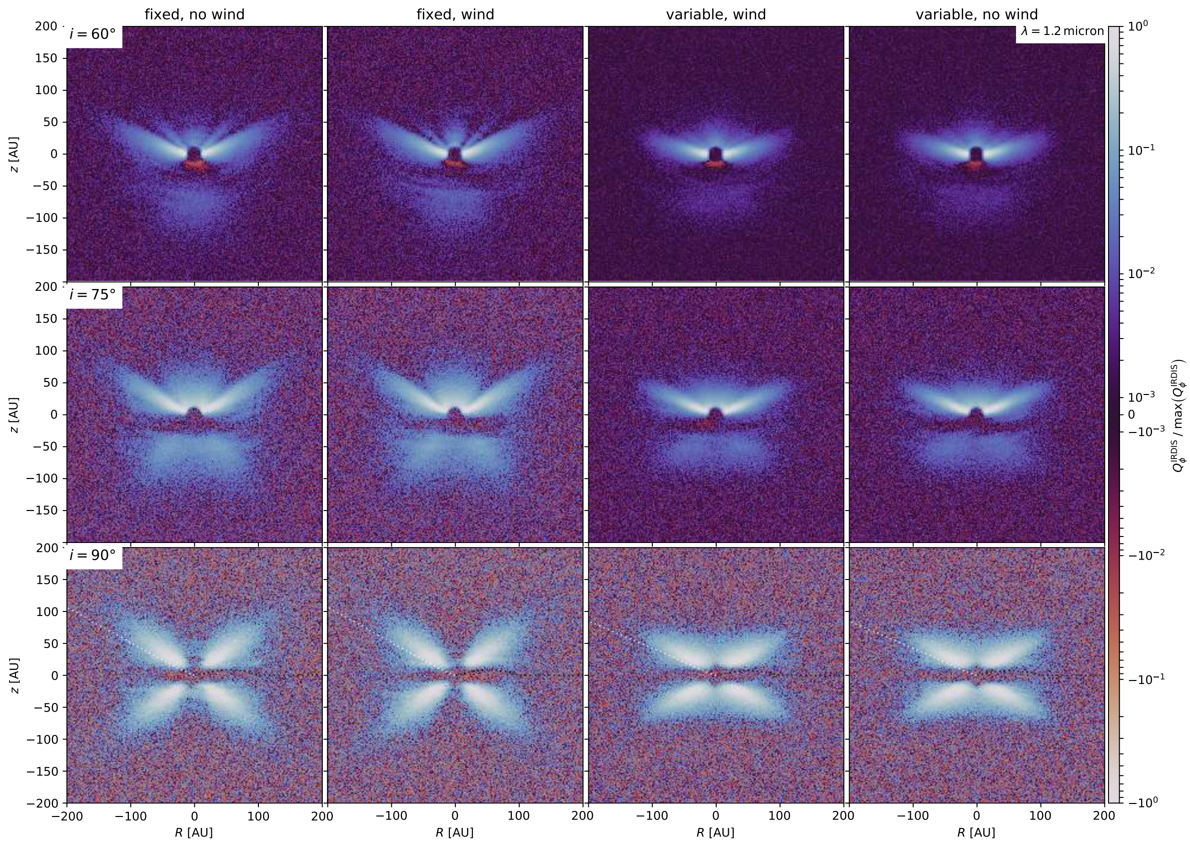

Figure 4.18: Q_ϕ maps synthesised for SPHERE+IRDIS's J-band ($\lambda_{\rm obs} = 1.2\,\mu$m), all else equal to Fig. 4.10.

Chapter 5

Synthetic observations of transition disks

The contents of this chapter have been published as Franz et al. (2022b).[(1)]
Credit: Franz et al., Astronomy & Astrophysics, Volume 659, Article A90, 2022, reproduced with permission © ESO.

Chapter abstract

Context: X-ray- and extreme-ultraviolet- (XEUV-) driven photoevaporative winds acting on protoplanetary disks around young T-Tauri stars may strongly impact disk evolution, affecting both gas and dust distributions. Small dust grains in the disk are entrained in the outflow and may produce a detectable signal. In this work, we investigate the possibility of detecting dusty outflows from transition disks with an inner cavity.

Aims: We compute dust densities for the wind regions of XEUV-irradiated transition disks and determine whether they can be observed at wavelengths $0.7 \lesssim \lambda_{\mathrm{obs}}\,[\mu\mathrm{m}] \lesssim 1.8$ with current instrumentation.

Methods: We simulated dust trajectories on top of 2D hydrodynamical gas models of two transition disks with inner holes of 20 and 30 AU, irradiated by both X-ray and EUV spectra from a central T-Tauri star. The trajectories and two different settling prescriptions for the dust distribution in the underlying disk were used to calculate wind density maps for individual grain sizes. Finally, the resulting dust densities were converted to synthetic observations in scattered and polarised light.

Results: For an XEUV-driven outflow around a $M_* = 0.7\,\mathrm{M}_\odot$ T-Tauri star with $L_\mathrm{X} = 2 \cdot 10^{30}$ erg/s, we find dust mass-loss rates $\dot{M}_{\mathrm{dust}} \lesssim 2.0 \cdot 10^{-3}\,\dot{M}_{\mathrm{gas}}$, and if we invoke vertical settling, the outflow is quite collimated. The synthesised images exhibit a distinct chimney-like structure. The relative intensity of the chimneys is low, but their detection may still be feasible with current instrumentation under optimal conditions.

Conclusions: Our results motivate observational campaigns aimed at the detection of dusty photoevaporative winds in transition disks using JWST NIRCam and SPHERE IRDIS.

[(1)]This work resulted from a collaboration with the coauthors listed in the corresponding bibliography entry, that is G. Picogna (GP), B. Ercolano (BE), S. Casassus (SC), T. Birnstiel (TB), Ch. Rab (CHR), and S. Pérez (SP). In particular, GP provided the steady-state gas models of the transition disks and the foundation for the code for the dust motion, see Chap. 3, SC provided the noise estimate for SPHERE IRDIS (as for Chap. 4) as well as the code to retrieve the spectral indices and their differences, and TB provided guidance on the `disklab` package with respect to transition disks and proposed the investigation of different opacity models. GP, BE, SC, TB, CHR, and SP helped with the interpretation and discussion of the results. The author (RF) adapted the code base of Chaps. 3 and 4 to work with transition disk models, computed the dust trajectories, converted them to dust density maps, retrieved the dust base densities from `disklab` and the dust opacities from `dsharp_opac`, produced the radiative-transfer images (via `RadMC-3D`) as well as the JWST NIRCam predictions (via `Mirage`), and drafted the manuscript.

5.1 Introduction

Planets form from the reservoir of gas and dust within the protoplanetary disk initially surrounding the host star (see e.g. Armitage, 2018); once this material has been dispersed, planet formation necessarily comes to a halt. Photoevaporative winds, driven by highly energetic radiation from the central star, are one of the mechanisms proposed to clear out disk material (e.g. Clarke et al., 2001); especially X-ray and extreme-ultraviolet (together: XEUV) winds are thought to be very efficient at driving outflows that eventually disperse the disk from the inside out, via the formation of a transition disk (Ercolano et al., 2009; Owen et al., 2010, 2012). Transition disks, that is disks with an inner cavity, may also be formed by other processes, such as dynamical interactions with giant planets or magneto-hydrodynamical (MHD) winds (see e.g. Kunitomo et al., 2020; Pascucci et al., 2020). The detection of photoevaporative winds is important in order to assess their role in disk evolution; so determining possible observational tracers is key to refine our understanding of this important mechanism.

The presence of disk winds can be inferred in a variety of ways; for instance, Monsch et al. (2019, 2021a,b) predicted orbital distributions of hot Jupiters in XEUV-irradiated disks, and Ercolano & Owen (2010), Ercolano & Owen (2016), and Weber et al. (2020) modelled line profiles for disks impacted by photoevaporation. Furthermore, Owen et al. (2011a), Hutchison et al. (2016a,b), Booth & Clarke (2021), and Hutchison & Clarke (2021) have worked to model and analytically formulate dust entrainment in photoevaporative winds. In Franz et al. (2020, henceforth Paper I) and Franz et al. (2022a, henceforth Paper II), we numerically simulated the dust content and observability of dusty XEUV-driven outflows around a primordial protoplanetary disk based on the hydrodynamical (HD) models of Picogna et al. (2019) (which have since been refined by Ercolano et al., 2021; Picogna et al., 2021). The results of Papers I and II have shown that a dusty outflow signature is indeed expected at μm-wavelengths for the primordial disk model investigated there (hereafter 'PD'), but its detection and interpretation would be challenging with current instrumentation.

In this work, we set out to investigate possible signatures of dust entrained in photoevaporative winds launched from transition disks, that is disks where an inner cavity has already formed. In these objects, the stellar radiation reaches the disk midplane at the gap edge, allowing more material to be entrained from this location where gas and dust densities are much higher than at the disk-wind interface; the latter is several scale heights above the midplane (see e.g. Ercolano & Pascucci, 2017).

This chapter is organised as follows: The calculations to obtain the dust densities and synthetic observations are outlined in Sect. 5.2. In Sect. 5.3, the resulting density maps and observational concurrences are presented. We discuss our findings in Sect. 5.4 and summarise them in Sect. 5.5.

5.2 Methods

Our goal is to investigate the observability of photoevaporative winds in transition disks as traced by the entrained dust grains. To this end, we have followed the approach of Paper I to first simulate dust grain trajectories, and of Paper II to then obtain dust density maps and synthetic observations. The general methods employed will be briefly summarised in the next subsections, but we refer to Papers I and II for a more detailed description.

5.2.1 Gas models

We consider two model disks with cavities of $r_{\text{gap}} \approx \{20, 30\}$ AU, which we refer to as 'TD20' and 'TD30' below, respectively. Significantly larger gap sizes lead to instabilities with the employed setup (see Wölfer et al., 2019). Much smaller gap sizes would be difficult to observationally distinguish from primordial disks with current instruments; in addition, we wanted to investigate radii close to which the XEUV wind reaches its full potential for this model (see Paper I). This corresponds to the overall goal of Paper II to present a best-case scenario for the observability of a photoevaporative wind launched from the disk model. As in Papers I and II, the gas models for the disks – in this case, slightly modified versions of the transition disks presented by Picogna et al. (2019) – were computed using a modified version of the `Pluto` code (Mignone et al., 2007) for the hydrodynamical evolution.[1] This modified version includes a temperature prescription obtained via `Mocassin` (Ercolano et al., 2003, 2005, 2008a). In these simulations, azimuthal and midplane symmetries were assumed as well as an α-viscosity (Shakura & Sunyaev, 1973) of $1 \cdot 10^{-3}$ (to match the new setup of Picogna et al., 2021) and a mean atomic mass of 1.37125. The

[1] `Pluto`: `http://plutocode.ph.unito.it/`. Version 4.2 was used for this work.

initial density distributions of Picogna et al. (2019) were obtained from a steady-state primordial disk profile, adding an exponential cut-off function at the location of the gap. The steady-state profile of the transition disks used in this work are the result of the interaction of the viscous spreading of the initial density profile, and the increased mass-loss rate due to the photoevaporative wind at the inner disk edge.

The system consists of a $M_* = 0.7\,\mathrm{M}_\odot$ T-Tauri star with an X-ray luminosity of $L_\mathrm{X} = 2 \cdot 10^{30}\,\mathrm{erg/s}$ (which represents the median of the stars in Orion, see Preibisch et al., 2005). The mass of the primordial disks, prior to gap opening, was $M_\mathrm{disk} \simeq 0.01\,M_*$, of which about 60% (TD20) or 45% (TD30) remain in the transition disk models. The corresponding photoevaporation-driven gas mass-loss rates are $\dot{M}_\mathrm{gas}^\mathrm{TD20} \simeq 3.0 \cdot 10^{-8}\,\mathrm{M}_\odot/\mathrm{yr}$ and $\dot{M}_\mathrm{gas}^\mathrm{TD30} \simeq 2.9 \cdot 10^{-8}\,\mathrm{M}_\odot/\mathrm{yr}$.(1)

The region between the star and r_gap has been completely cleared in our models. We do not consider transition disks with an inner disk (see e.g. Francis & van der Marel, 2020); in the case of an inner disk blocking the stellar radiation, one can assume that these objects behave similar to primordial disks, unless a strong difference in gas scale heights between the inner and outer disks exists.

5.2.2 Dust in the wind

To summarise the methodology of Paper II, the gas distribution in the disk (taken from Picogna et al., 2019, see above) was used to compute the dust distribution up to the disk-wind interface (the 'base' of the wind or disk surface, determined as the location of the largest drop in gas temperature, see Paper I). There, the gas and dust densities (ϱ_gas and ϱ_dust) are thus directly linked. Then, a collection of dust grain trajectories was simulated using the prescriptions of Picogna et al. (2018); they were launched directly from the base in order to focus on the dust motion in the wind. We did not use a physical density prescription for their initial placement. This allowed us to derive normalised wind density maps from the trajectories via a particle-in-cell approach; these were combined with the base densities to obtain ϱ_dust in the wind.

5.2.2.1 Trajectories

We employed a grid extending to $r \lesssim 300\,\mathrm{AU}$, with $r = \sqrt{x^2 + y^2 + z^2}$ to model trajectories for eight distinct grain sizes a_0, in this case $a_0 \in \{0.01, 0.1, 0.5, 1, 2, 4, 8, 12\}\,\mu\mathrm{m}$, with an internal grain density of $\varrho_\mathrm{grain} = 1.0\,\mathrm{g/cm}^3$ (as in Papers I and II). The grains were initially placed along the disk surface within $r_\mathrm{gap} \lesssim r \lesssim 200\,\mathrm{AU}$. To fully cover the strong vertical slope close to the outer gap edge,(2) we placed the particles along the (r, ϑ)-coordinates of the disk surface using a uniform random distribution.

The simulations were evolved for about 3.8 kyr; a constant amount of 200 000 particles was kept in the simulations at all times, with blown-out particles being replaced by ones newly spawned along the disk surface. The resulting dust grain counts are summarised in Table 5.1.(3)

The resulting trajectories were then used to create dust maps, using the method described in Paper II and employing a grid with $\Delta r = 0.5\,\mathrm{AU}$ for $r < 50\,\mathrm{AU}$ and $\Delta r = 1\,\mathrm{AU}$ from there on out, and $\Delta\vartheta = 0.5°$. The dust grains reach escape velocity within $10^2 ... 10^3$ yr just like for the PD (see Paper I), which signifies a much smaller timeframe than the $10^5 ... 10^6$ yr on which the overall dispersal of the gas happens (see e.g. Mamajek, 2009). Thus, dust entrainment can still be regarded as a separate process, and using a steady-state gas snapshot should not affect our results.

5.2.2.2 Densities

In order to retrieve our dust density estimates for the wind, the dust maps need to be combined with sensible estimates for the dust densities at the wind launching region. As a basis, we selected 400 grain species, spaced logarithmically in size for $1\,\mathrm{nm} \leq a_0 \leq 1\,\mathrm{mm}$, and drawn from a MRN distribution with $n(a) \propto a^{-3.5}$ (Mathis et al., 1977). We then constructed two different setups: Firstly, we assumed a globally fixed dust-to-gas ratio of 0.01, labelled 'fixed'.(4) Secondly, in a setup referred to as 'variable' below, we used `disklab` (Dullemond & Birnstiel, in prep.) to compute densities accounting for hydrostatic equilibrium in the gas (see e.g. Armitage, 2010), and vertical settling-mixing equilibrium in the dust

(1) Picogna et al. (2019) found $\dot{M}_\mathrm{gas}$ to be higher for transitional than for primordial disks. Our values of $\dot{M}_\mathrm{gas}$ are lower than for the PD of Paper II solely due to differences in the model setup. As laid out in Sect. 5.3.3, this does not detrimentally affect our results.

(2) With 'outer gap edge', we refer to the outer edge of the (inner) cavity.

(3) Since the entrainment rates for small grains are already very high, radiation pressure (see e.g. Owen & Kollmeier, 2019; Vinković & Čemeljić, 2021) should not strongly affect our results. If anything, it would increase the outflow velocity of the dust grains, thus enhancing $\dot{M}_\mathrm{dust}$ by a factor < 10.

(4) As already pointed out in Paper II, real dust-to-gas ratios may be higher (see e.g. Miotello et al., 2017).

Table 5.1: Statistics for the dust trajectories used to create the density maps: grain size, number of all trajectories modelled, number of fully entrained trajectories thereof, for both transition disk models.

	TD20		TD30	
a_0 [μm]	$N_{\rm all}$	$N_{\rm entrained}$	$N_{\rm all}$	$N_{\rm entrained}$
0.01	3 897 202	3 366 326	2 708 677	2 466 946
0.1	3 782 149	3 405 947	2 630 424	2 427 226
0.5	3 324 900	3 044 384	2 352 484	2 147 716
1	2 870 286	2 620 235	1 997 824	1 793 465
2	2 381 287	2 125 436	1 677 729	1 474 215
4	1 760 818	1 446 631	1 252 860	1 038 191
8	512 372	144 423	604 993	140 355
12	236 155	8 640	206 440	2 055

The differing numbers stem from a constant sample size of 200 000 grains processed simultaneously over similar simulation time spans, with grains being reinserted at a random position along the disk surface once they exit the computational domain.

according to Fromang & Nelson (2009). The underlying dust-to-gas ratio at the midplane was assumed to be 0.01 like in the 'fixed' case.

Preliminary investigations showed that grains $\gtrsim 12.5\,\mu$m were not entrained in the wind; so we discarded all size bins $a_0 > 12.5\,\mu$m from the original 400 species. The remaining grain species, equalling about 11% of the total dust mass, were then re-binned into eight bins matching the eight a_0 investigated.

In a last step, the dust densities at the disk surface of the 'fixed' and 'variable' models were used to populate the wind regions via the dust maps created from the trajectories; this yields a total of four setups: 'fixed' TD20 (fixTD20), 'variable' TD20 (varTD20), 'fixed' TD30 (fixTD30), and 'variable' TD30 (varTD30). Each of these 'wind' models is complemented by a counterpart with a wind region entirely devoid of dust ('no wind'), to provide a simple means of assessing the effect of the dusty outflow on the observations. In order to smooth out artefacts resulting from the discrete trajectories and the rather fine grid spacing, we applied a Gaussian filter ($\sigma = 2\,$AU) to the densities in the wind region.

5.2.2.3 Mass-loss rates

From the HD simulations, we extracted the dust outflow velocities at the domain boundary (i.e. $r \simeq 300\,$AU). In combination with $\varrho_{\rm dust}$, these were then used to compute the dust outflow rate $\dot{M}_{\rm dust}$.

5.2.3 Radiative transfer

`RadMC-3D` was employed for the radiative-transfer computations.[(1)] In a setup identical to the one used in Paper II, we used a stellar temperature of $T_* = 5000\,$K, a logarithmically-spaced wavelength grid with $10^{-1} \leq \lambda\,[\mu\text{m}] \leq 10^4$, and a photon count of $N_{\rm phot} = 10^6$ to create 800×800 pixel images in scattered and polarised light. We produced simulated images for $\lambda_{\rm obs} \in \{0.4, 0.7, 1.2, 1.6, 1.8\}\,\mu$m. In order to obtain the full Stokes parameters in full anisotropic scattering, we computed the scattering matrix coefficients using `dsharp_opac` (Birnstiel et al., 2018).[(2)]

For the disk region, we used the opacities from the Disk Substructures at High Angular Resolution Project (DSHARP), composed from the results of Henning & Stognienko (1996), Draine (2003b), and Warren & Brandt (2008); for the wind region, we employed pure astrosilicate opacities (Draine, 2003b). This distinction was made because we cannot be sure the wind is cold enough to host ice everywhere. Furthermore, astrosilicates have a higher albedo, thus slightly enhancing their observability; this matches our intent to investigate best-case scenarios for the observability of the winds. The impact of choosing this opacity prescription is investigated in Sect. 5.6.1.

(1) `RadMC-3D`: `http://www.ita.uni-heidelberg.de/~dullemond/software/radmc-3d/`. Version 2.0 was used for this work.
(2) `dsharp_opac`: `https://github.com/birnstiel/dsharp_opac/`.

5.2.3.1 Scattered light

The Near Infrared Camera (NIRCam, Rieke et al., 2003, 2005) of the *James Webb* Space Telescope (JWST) will allow for state-of-the-art scattered-light imaging in the (sub-)μm wavelength range. In Paper II, we have seen that smaller wavelengths should be most favourable for the detection of a wind signature; so we are mainly interested in the F070W filter ($\lambda_{\rm obs} = 0.7\,\mu$m). Alternatively, in order to use the smallest coronagraph (MASK210R, with a half-transmission radius of $0\farcs4$), $\lambda_{\rm obs} \gtrsim 1.8\,\mu$m is needed; for our purposes, this means the F182M filter.

`Mirage` was employed to synthesise the instrument response for JWST NIRCam,[(1)] and the resulting data sets were then post-processed with the `jwst` pipeline just as an actual observational data set would be.[(2)] The coronagraph was simulated by simply applying a transmission mask to the input intensities;[(3)] this should allow for a first-order estimate, although it disregards the peculiarities of the instrument.

5.2.3.2 Polarised light

We used the same procedure as described in Paper II to synthesise an instrument response for the Spectro-Polarimetric High-contrast Exoplanet REsearch (SPHERE, Beuzit et al., 2019) InfraRed Dual-band Imager and Spectrograph (IRDIS) of the Very Large Telescope (VLT). In particular, we focussed on the J- and H-bands ($\lambda_{\rm obs} \simeq 1.2$ and $1.6\,\mu$m, respectively) in $Q_\phi = Q\cos(2\,\phi) + U\cos(2\,\phi)$, with $\phi = \arctan(x/y)$, and in $P = \sqrt{Q^2 + U^2}$. The noise level was extracted from the comparison between an H-band observation of DoAr 44 (Avenhaus et al., 2018) and a radiative transfer modelling of that object (Casassus et al., 2018).

Furthermore, we used the predictions for the instrument response to compute the spectral index $\alpha \equiv \alpha_{J,H}$ between J- and H-bands, both for the ‘wind’ and ‘no wind’ cases ($\alpha_{\rm w}$ and $\alpha_{\rm nw}$, respectively). For each model, the difference $\Delta\alpha = \alpha_{\rm w} - \alpha_{\rm nw}$ was then investigated to check for a possible colour excess caused by the dusty wind.

5.3 Results

5.3.1 Trajectories

Following the trajectories of grains entrained in the wind, we see that the small grains in our simulation tend to have low Stokes numbers St, and thus are well-coupled to the gas phase, resulting in trajectories that hardly differ from the gas streamlines. Larger grains with higher St decouple much earlier from the gas, and their trajectories depart from the gas streamlines shortly after launch. Just like for PD, no grains are entrained from $R \gtrsim 140\,$AU, with $R = \sqrt{x^2 + y^2}$. Some randomly selected trajectories are presented in Figs. 5.1 (TD20) and 5.2 (TD30); for each model, we show three grain species to illustrate slow, intermediate and fast decoupling.

The XEUV-driven outflow launching from the outer gap edge is more vigorous than what we have seen for PD, thus grains up to $a_0 \lesssim 12\mu$m can be entrained; this however only holds for the strongly curved disk surface region close to the holes. Their (almost) vertical launch into the wind even from there, and for all grain sizes, corroborates the assumption of a vertical launch from a non-angled surface made by Clarke & Alexander (2016) for a semi-analytical EUV-only gas model. These have since been refined to include dust by Hutchison & Clarke (2021), and extended to allow for various launching angles by Sellek et al. (2021). The qualitative agreement between our numerical results and the semi-analytical work above would suggest that in theory costly hydrodynamical simulations as presented in this work could be replaced by semi-analytical formulations. In practice however, as Booth & Clarke (2021) have shown, differing assumptions as to the vertical delivery of the dust to the wind launching region will lead to significantly different density estimates for the wind region.

5.3.2 Dust densities

The dust densities computed for our various models are shown in Figs. 5.3 (fixTD20), 5.4 (varTD20), 5.5 (fixTD30) and 5.6 (varTD30). The choice of dust settling prescription has a larger impact on the morphology of the dusty wind than the $\approx 10\,$AU difference in hole size between TD20 and TD30.

(1) `Mirage`: `https://mirage-data-simulator.readthedocs.io/`. Version 2.1.0 was used for this work.
(2) `jwst`: `https://jwst-pipeline.readthedocs.io/`. Version 1.2.3 was used for this work.
(3) The transmission curves are available from `https://jwst-docs.stsci.edu/near-infrared-camera/nircam-instrumentation/nircam-coronagraphic-occulting-masks-and-lyot-stops`.

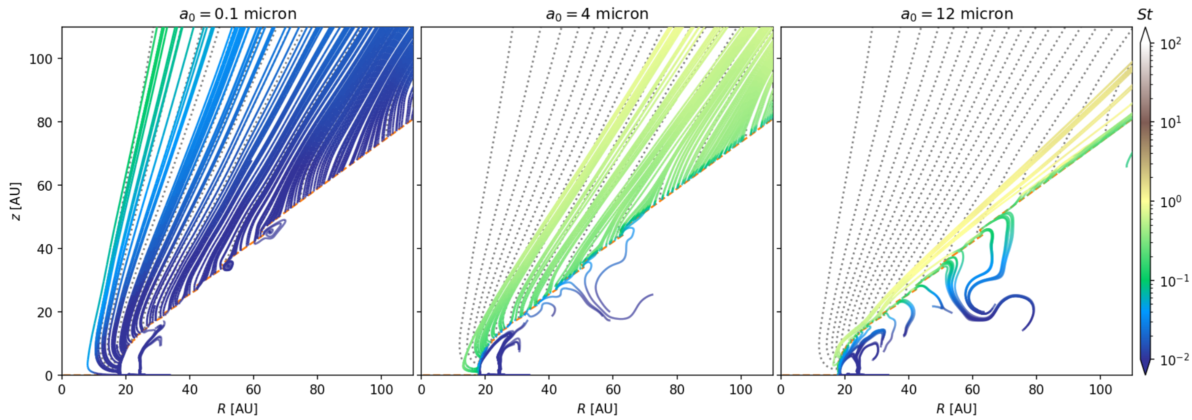

Figure 5.1: Random selection of dust trajectories in TD20, for three a_0; the image has been zoomed in to the inner 110 AU × 110 AU to give a better view of the region around the outer gap. The grains are launched from the disk surface (orange dashed line) and if picked up by the wind, they then follow the gas streamlines (grey dotted lines) more or less closely, depending on their local Stokes number St (colourbar). A few of the grains are not entrained, and proceed to move into the disk, following the gas flows there.

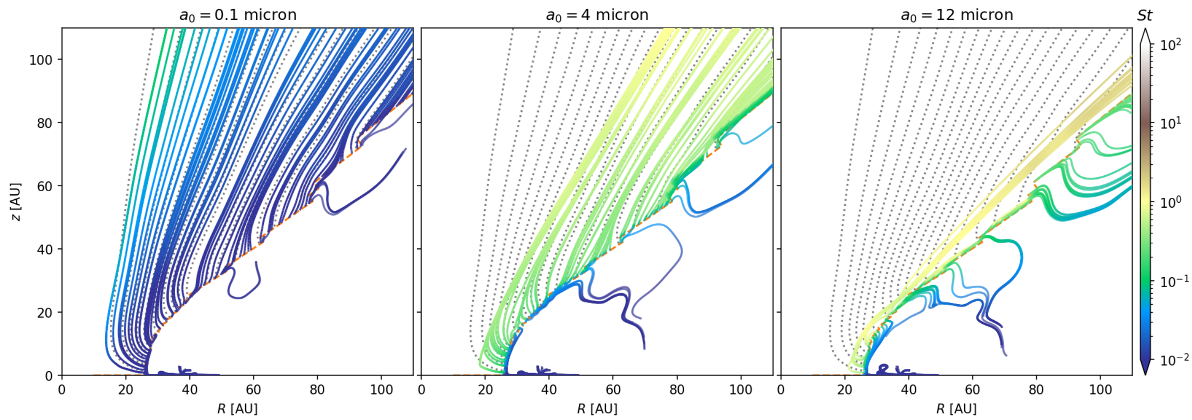

Figure 5.2: Dust trajectories for various a_0 for TD30, all else equal to Fig. 5.1. There are no systematic differences in the dust outflow patterns between TD20 and TD30.

For the 'fixed' setups (Figs. 5.3 and 5.5), the wind region is continuously populated by dust grains between the disk surface and a maximum reachable scale height (see Paper I), even though there are some outflow channels with slightly enhanced densities. This stands in stark contrast to the 'variable' models (Figs. 5.4 and 5.6). In the latter, dust with $a_0 > 0.1\,\mu$m only populates the wind regions in significant quantities if it has been launched from close to the edge of the hole, that is from low z; this leads to quite distinct outflow channels, which become narrower for larger a_0, and are close to the maximum scale height $\max(z)|_R$ the dust reaches in the wind (taken individually for each a_0, compare Paper I). For $a_0 \lesssim 4\,\mu$m, the densities in the dominant outflow channels of the 'variable' models are very similar to those found in these regions in the 'fixed' models.

This concentrated outflow pattern stands in clear contrast to the much smoother dust density maps we have seen for PD. The smallest grains ($a_0 = 0.01\,\mu$m), which are (almost) fully hydrodynamically coupled with the gas, still occupy as much of the wind region as in the 'fixed' cases, which serves as a sanity check. Contrary to PD, even the largest grains show clear non-zero wind densities.

Several recent works have investigated the maximum entrainable a_0 for MHD (Miyake et al., 2016; Giacalone et al., 2019), EUV (Hutchison et al., 2016a,b; Hutchison & Clarke, 2021), and XEUV winds (Booth & Clarke, 2021, and Paper I). However, as we can see from our 'variable' models (Figs. 5.4 and 5.6), the gas densities cannot simply be converted into dust densities via a global ratio when invoking vertical settling. So as laid out in Paper II (and also stated by many other authors, e.g. de Boer et al., 2017; Villenave et al., 2020), observational constraints on the strength of the vertical settling in protoplanetary

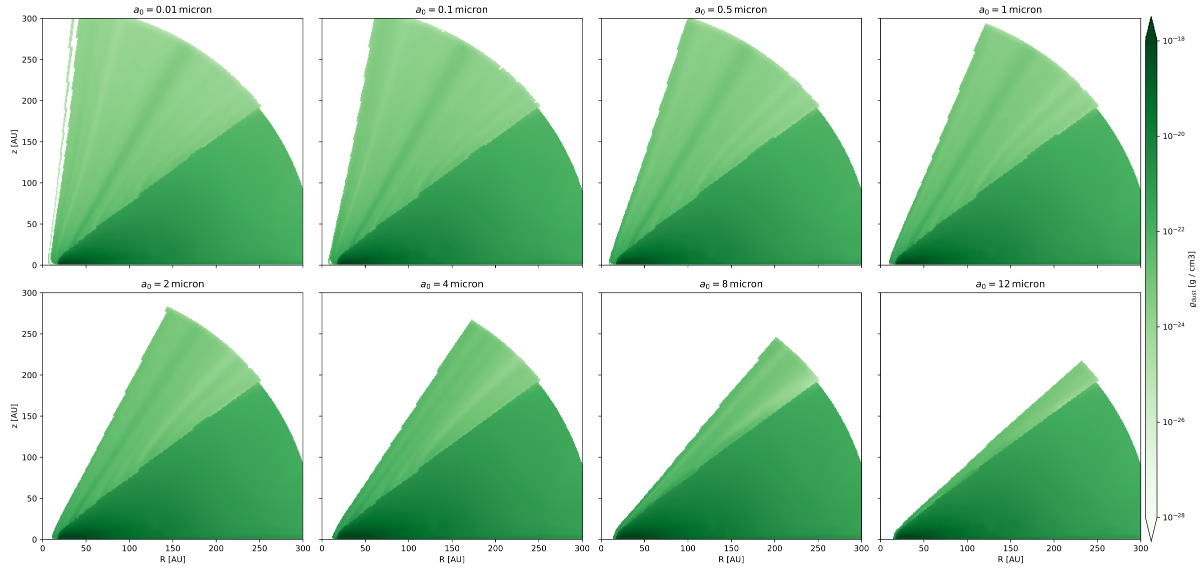

Figure 5.3: Dust densities for the XEUV-irradiated fixTD20 disk in (R, z). The presence of small dust grains everywhere along the disk surface leads to a mostly smooth distribution of dust densities in the wind.

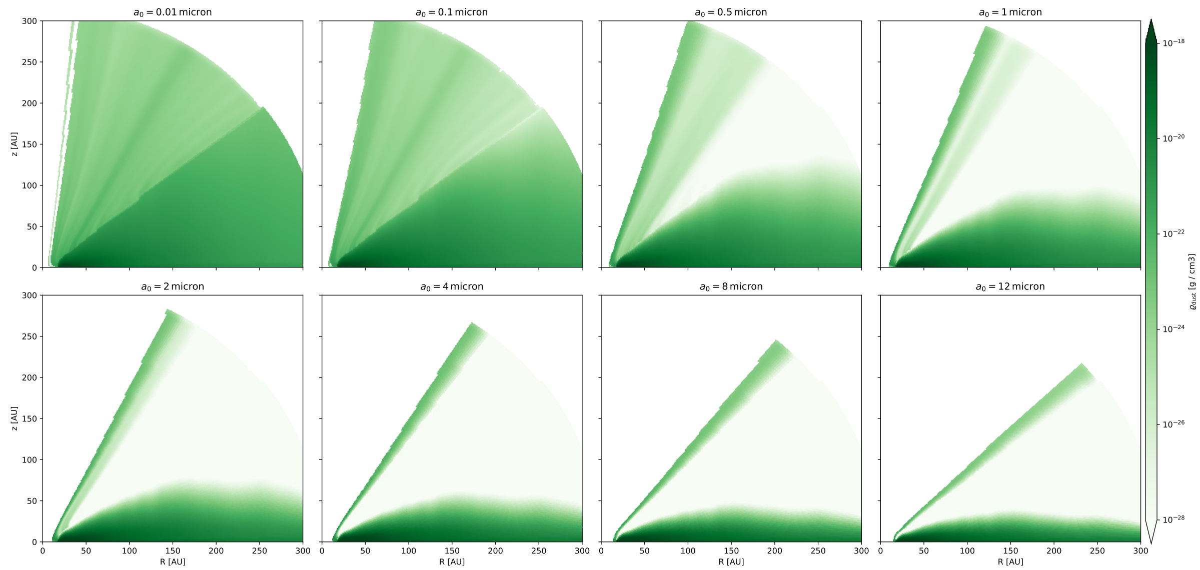

Figure 5.4: varTD20 counterpart of Fig. 5.3, using an identical colourbar. Dust settling leads to an outflow which, for $a_0 \gtrsim 0.5\,\mu$m, is mainly fueled from the outer gap edge where the wind interacts with the disk at low z.

disks are needed for more accurate modelling.

5.3.3 Mass-loss rates

For PD, we calculated $\dot{M}_{\rm dust}/\dot{M}_{\rm gas} \lesssim 1.1{\cdot}10^{-3}$ and $3.2{\cdot}10^{-4}$ for the 'fixed' and 'variable' cases, respectively (Paper II). The upper limit corresponds to the dust-to-gas ratio assumed (0.01) multiplied by the mass fraction of the entrainable grains in relation to the total dust population ($\approx 11\%$).

The XEUV-driven mass-loss rates for the transition disks modelled here are listed in Table 5.2. Within the 'fixed' and 'variable' setups, $\dot{M}_{\rm dust}/\dot{M}_{\rm gas}$ has increased for the disks with an inner hole. This stands to reason because the inner hole allows the photoevaporative wind to directly penetrate to, and thus entrain material from, regions close to the disk midplane.

While $\dot{M}_{\rm gas}$ decreases only slightly from TD20 to TD30, there is a clear decline in $\dot{M}_{\rm dust}$ between the

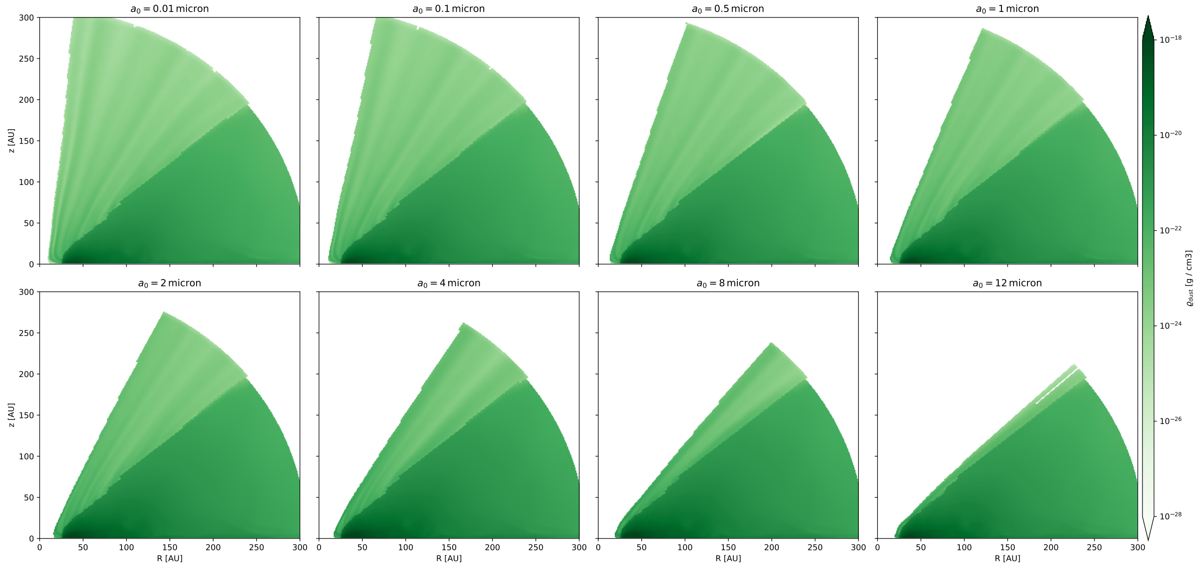

Figure 5.5: Dust densities for fixTD30, all else equal to Fig. 5.3. Apart from the larger inner hole, the differences to the other 'fixed' model (Fig. 5.3) are minor.

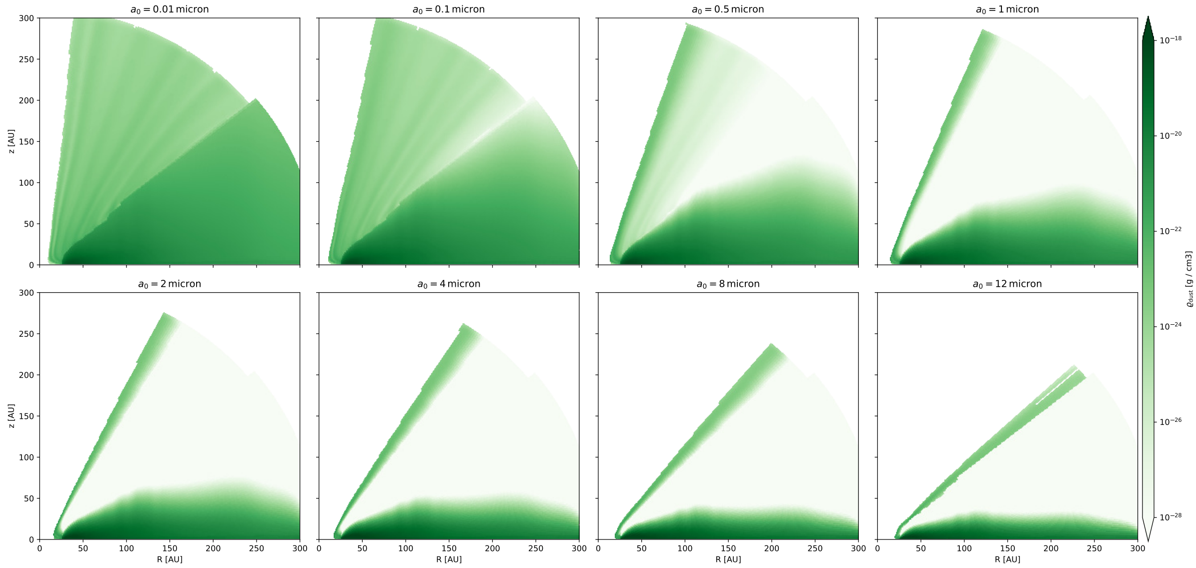

Figure 5.6: Dust densities for varTD30, all else equal to Fig. 5.5. As for the 'fixed' models, the differences between the varTD20 (Fig. 5.4) and varTD30 disks in terms of dust content in the wind are minor.

models. This is most likely due to the gas surface mass-loss rate $\dot{\Sigma}_{\rm gas}$ being higher at the gap edge for TD20, leading to an overall stronger dusty outflow.

All of the recorded cumulative values for $\dot{M}_{\rm dust}$ are above their counterparts for PD, which were $\dot{M}_{\rm dust}^{\rm `fix'} \simeq 4.1 \cdot 10^{-11}\,{\rm M}_\odot/{\rm yr}$ and $\dot{M}_{\rm dust}^{\rm `var'} \simeq 1.2 \cdot 10^{-11}\,{\rm M}_\odot/{\rm yr}$ alongside $\dot{M}_{\rm gas} \simeq 3.7 \cdot 10^{-8}\,{\rm M}_\odot/{\rm yr}$. With respect to the dust, this matches the general consensus that photoevaporative mass loss is enhanced in transition disks compared to primordial objects (see e.g. Clarke et al., 2001; Ercolano & Pascucci, 2017); it additionally coincides with a very rough time estimate for when the gas and dust mass of the disk become similar: If we assume $M_{\rm disk}^{\rm (dust)} = 0.01\,M_{\rm disk}^{\rm (gas)}$, and $\dot{M}_{\rm dust}$ to be constant, we find $M_{\rm disk}^{\rm (dust)} \gtrsim M_{\rm disk}^{\rm (gas)}$ for $t \gtrsim 0.13\,{\rm Myr}$ (TD20) or $0.11\,{\rm Myr}$ (TD30); for PD, this value was $t \gtrsim 0.15\,{\rm Myr}$. Considering that our values for $\dot{M}_{\rm dust}$ may be overestimates as laid out above, these values may be not entirely accurate, but do show that an enhancement of the XEUV-driven mass loss is quite likely once our model has reached its transitional phase.

Table 5.2: Gas and dust mass-loss rates $\dot{M}_{\rm gas}$ and $\dot{M}_{\rm dust}$ for the models, in units of [$M_\odot$/yr].

	$\dot{M}_{\rm dust}$ [$M_\odot$/yr]			
a_0 [μm]	fixTD20	varTD20	fixTD30	varTD30
0.01	$7.6 \cdot 10^{-12}$	$6.6 \cdot 10^{-12}$	$6.4 \cdot 10^{-12}$	$5.0 \cdot 10^{-12}$
0.1	$1.1 \cdot 10^{-11}$	$3.1 \cdot 10^{-12}$	$9.1 \cdot 10^{-12}$	$2.2 \cdot 10^{-12}$
0.5	$9.8 \cdot 10^{-12}$	$1.8 \cdot 10^{-12}$	$7.2 \cdot 10^{-12}$	$9.9 \cdot 10^{-13}$
1	$9.8 \cdot 10^{-12}$	$1.7 \cdot 10^{-12}$	$6.9 \cdot 10^{-12}$	$1.0 \cdot 10^{-12}$
2	$1.0 \cdot 10^{-11}$	$1.7 \cdot 10^{-12}$	$7.2 \cdot 10^{-12}$	$9.1 \cdot 10^{-13}$
4	$9.3 \cdot 10^{-12}$	$1.4 \cdot 10^{-12}$	$6.1 \cdot 10^{-12}$	$6.1 \cdot 10^{-13}$
8	$3.2 \cdot 10^{-12}$	$3.9 \cdot 10^{-13}$	$2.1 \cdot 10^{-12}$	$2.4 \cdot 10^{-13}$
12	$2.1 \cdot 10^{-13}$	$2.3 \cdot 10^{-14}$	$8.9 \cdot 10^{-14}$	$2.8 \cdot 10^{-14}$
(sum)	$6.2 \cdot 10^{-11}$	$1.7 \cdot 10^{-11}$	$4.5 \cdot 10^{-11}$	$1.1 \cdot 10^{-11}$
$\dot{M}_{\rm dust}/\dot{M}_{\rm gas}$	$2.0 \cdot 10^{-3}$	$5.5 \cdot 10^{-4}$	$1.6 \cdot 10^{-3}$	$3.8 \cdot 10^{-4}$

5.3.4 Scattered-light imaging

5.3.4.1 Radiative transfer

We performed radiative transfer calculations with `RadMC-3D`.(1) The resulting images at $\lambda_{\rm obs} = 0.7\,\mu$m, which is the shortest wavelength accessible with JWST, are shown in Figs. 5.7 (TD20) and 5.8 (TD30). To avoid saturating the central region and to enhance the visibility of the fainter outer disk and wind, we applied an artificial coronagraph of $r = 1$ AU to the images in post-processing to block out the direct stellar signal. This gives a contrast boost of $\lesssim \{3.6, 3.2, 2.6, 0.8, 0.0\}$ dex (TD20) or $\lesssim \{4.0, 3.6, 2.9, 1.9, 0.0\}$ dex (TD30) at $i = \{0, 30, 60, 75, 90\}°$.

At low inclinations ($i \leq 30°$ for the cases investigated here), the 'wind' and 'no wind' models distinctly differ in the diameter of their inner holes. For TD20 (TD30) and at $i = 0°$, the scattered light from the dust in the wind extends inwards to $r \gtrsim 7$ AU (11 AU), in contrast to the $r \gtrsim 18$ AU (26 AU) of the 'no wind' models; this corresponds to the regions which are populated by dust grains because the dust entrained from the outer gap edge moves inwards before being blown out of the domain (see Sect. 5.3.1). The apparent difference in hole size is even more pronounced at $i = 30°$, with the diffuse radiation from the dust in the wind covering the full inner hole. At $i \gtrsim 60°$, the effect disappears because a non-negligible amount of dust is located along the line of sight. Instead, we find a more distinct wind signature. As in Paper II, when comparing the 'wind' and 'no wind' images for $i \geq 60°$, we find an outflow pattern that appears like a cone (or chimney) around the polar (z-) axis of the disk. It is quite faint at $i = 60°$ and rather pronounced at $i = 90°$.

For the 'fixed' model, the wind cone is comparably wide and evenly illuminated. By contrast, the chimney of the 'variable' model is much more condensed towards $\max(z)|_R$; this corresponds to the underlying dust distributions (see Sect. 5.3.2). While the amount of dust around $\max(z)|_R$ is similar between the 'fixed' and 'variable' models, there is little dust elsewhere in the wind region for the latter setup; this leads to a more collimated appearance of the cone. Furthermore, due to the lower vertical extent of the dusty disk in the 'variable' models, the dust quantities in the wind exceed those of the disk at lower z and thus r; hence the outflowing material is illuminated more strongly by the star. The resulting steep chimney feature could potentially be used to identify a scenario in which the dust is entrained primarily from the inner gap edge.

Despite the rather small $\lambda_{\rm obs}$ and accordingly large fractions of similarly-sized dust grains entrained in the wind (see Table 5.1), the wind region is optically thin. Looking at the optical depth τ, the ($\tau = 1$)-surfaces for the corresponding 'wind' and 'no wind' models are almost identical for an observer placed both at $r = 0$ and $z = \infty$; this was already the case for PD (Paper II).

With respect to PD, the relative brightness of the wind features in transition disks is distinctly higher. At $\lambda_{\rm obs} = 0.4\,\mu$m, we found wind intensities $I/I_{\rm max} \lesssim 10^{-3.5}$, $I_{\rm max} \equiv \max(I)$, for PD; the cones of the transition disks emerge already at $I/I_{\rm max} \lesssim 10^{-2}$ (TD20) and $I/I_{\rm max} \lesssim 10^{-3}$ (TD30). At $\lambda_{\rm obs} = 0.7\,\mu$m,

(1) In order to keep the manuscript concise, we did not include the results for all $\lambda_{\rm obs}$ here. Additional plots are however provided in Sect. 5.6.2.

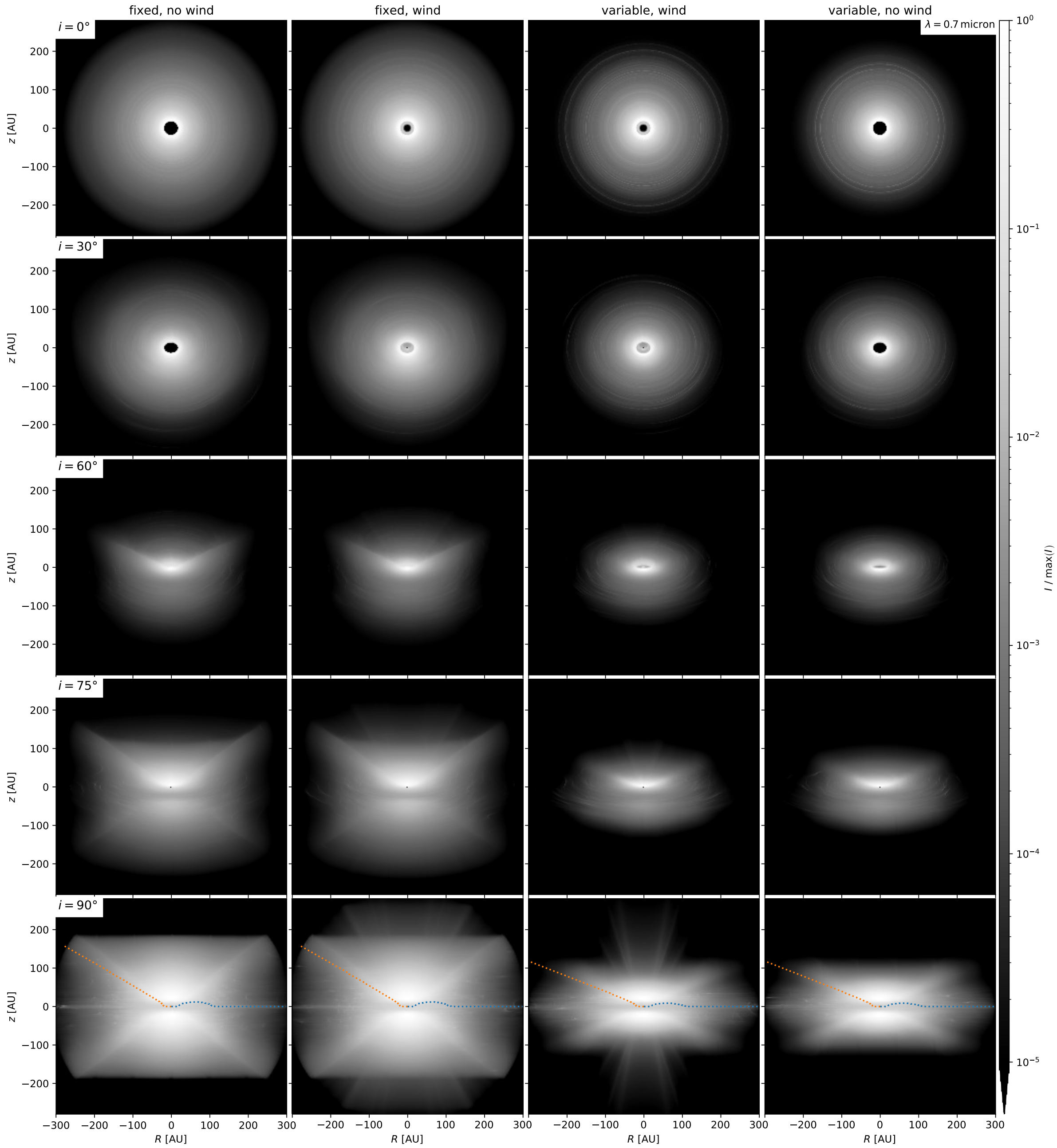

Figure 5.7: Scattered-light intensities for $\lambda_{\text{obs}} = 0.7\,\mu$m for TD20; different models in different *columns*, and different inclinations in different *rows*. An artificial coronagraph of $r = 1\,$AU is used to mask out the direct stellar signal. The $\max(I)$ for the scaling of the colourbar is taken for each image individually (after application of the coronagraphic mask). The orange and blue lines in the $(i = 90°)$-row represent the $(\tau = 1)$-surfaces for an observer at $r = 0$ and $z = \infty$, respectively. At low i, the dusty wind obscures the cavity; at higher i, it produces a cone-like feature around the z-axis.

the values are $I/I_{\max} \lesssim 10^{-3.5}$ (TD20) and $I/I_{\max} \lesssim 10^{-4.5}$ (TD30) for the most luminous features of the 'variable' disks, underlining the importance of observations at short λ_{obs}.

Figs. 5.9 and 5.10 show the `RadMC-3D` scattered-light intensities for $\lambda_{\text{obs}} = 1.6\,\mu$m. Here, the artificial coronagraph grants a contrast boost of $\lesssim \{3.5, 3.1, 2.7, 1.8, 0.0\}$ dex (TD20) or $\lesssim \{4.0, 3.5, 3.0, 2.4, 0.0\}$ dex (TD30). The main difference compared to $\lambda_{\text{obs}} = 0.7\,\mu$m is that the wind cone disappears for the 'fixed' setup. By contrast, it persists for the 'variable' setup which, due to the vertical settling of the dust grains, has a much lower dust disk scale height, making the chimney more distinct at similar z. The relative intensities are $I/I_{\max} \lesssim 10^{-3.5}$ (TD20) and $I/I_{\max} \lesssim 10^{-4}$ (TD30), versus $I/I_{\max} \lesssim 10^{-4.5}$ for PD.

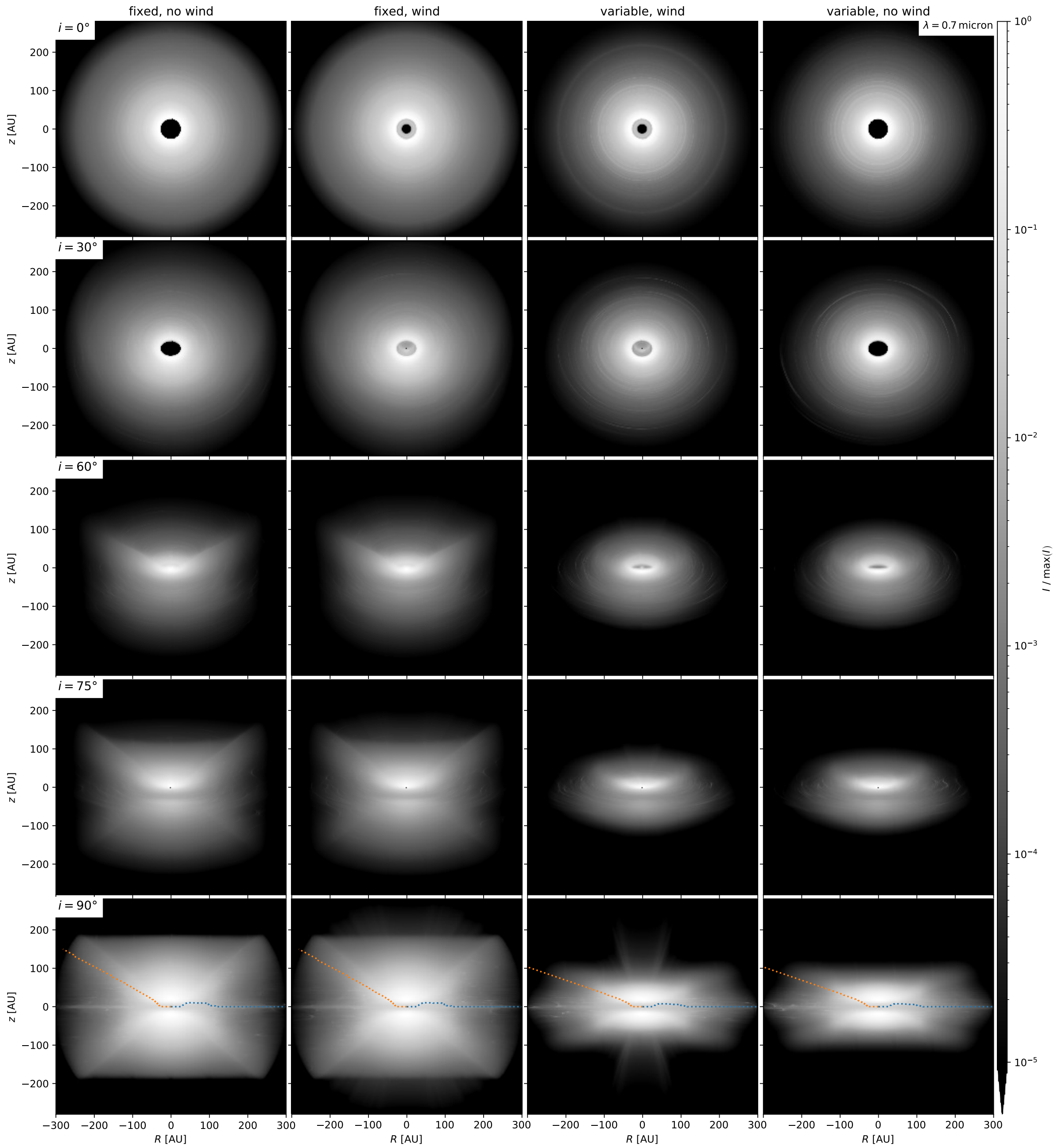

Figure 5.8: Scattered-light intensities for $\lambda_{\rm obs} = 0.7\,\mu$m for TD30, all else equal to Fig. 5.7. The wind features are similar to those of TD20, but less distinct at high i.

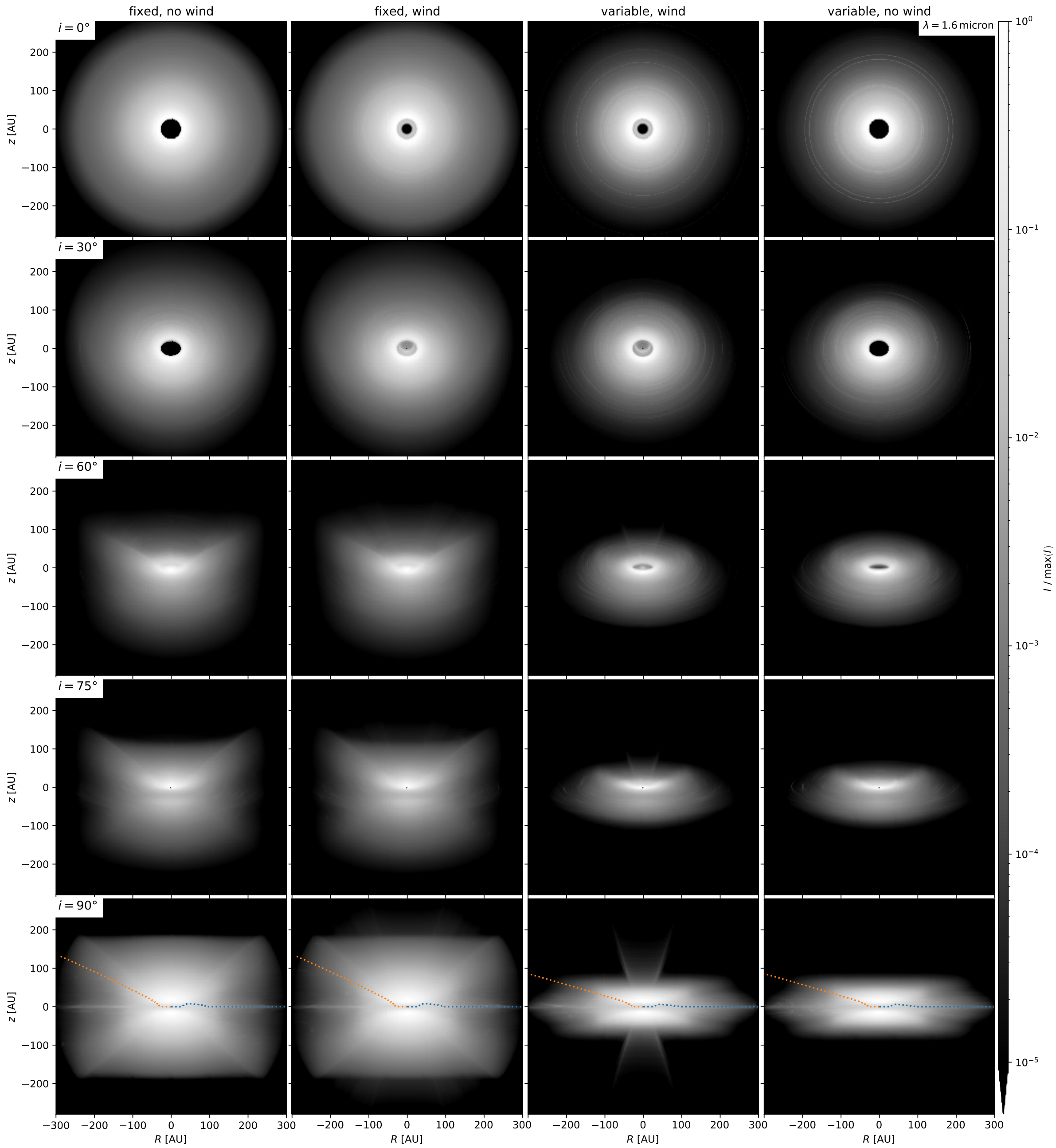

Figure 5.9: Scattered-light intensities for $\lambda_{\mathrm{obs}} = 1.6\,\mu$m for TD20, all else equal to Fig. 5.7. Vertical settling of the dust in the disk enhances the relative strength of the cone-like outflow signature.

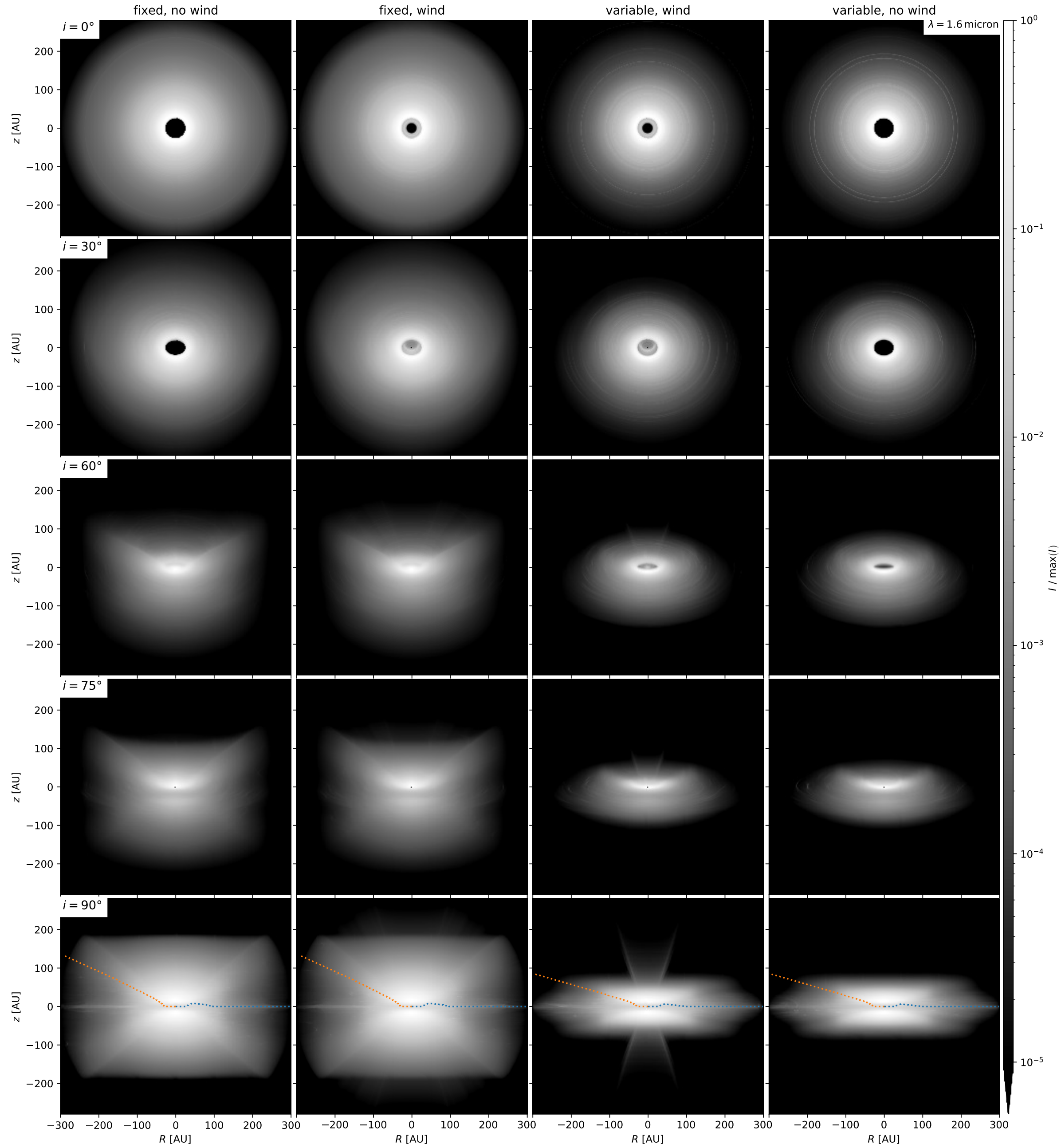

Figure 5.10: Scattered-light intensities for $\lambda_{\mathrm{obs}} = 1.6\,\mu$m for TD30, all else equal to Fig. 5.7. At this wavelength, the differences to TD20 (Fig. 5.9) are minor.

5.3.4.2 Synthetic observations for JWST NIRCam

As in Paper II, we encountered clear overexposure issues when synthesising the instrument response for JWST NIRCam via `Mirage`, polluting the image quite far out. Again, these can be circumvented by employing the MASK210R coronagraph, but that means that the smallest-wavelength filter usable is F182M, not F070W.

The synthesised coronagraphic images are shown in Figs. 5.11 (TD20) and 5.12 (TD30). For these images, the MEDIUM2 readout pattern was used; shorter science durations result in more noise obscuring potential features, while longer times lead to a more pronounced overexposure of the central regions, which may bleed out into high-r areas. Despite the transmission mask, the innermost region still exhibits high brightness; this is due to the point-spread function of the instrument.(1) The coronagraph diameter of

(1)For illustrations of the instrument PSF, see `https://jwst-docs.stsci.edu/jwst-near-infrared-camera/nircam-predicted-performance/nircam-point-spread-functions`.

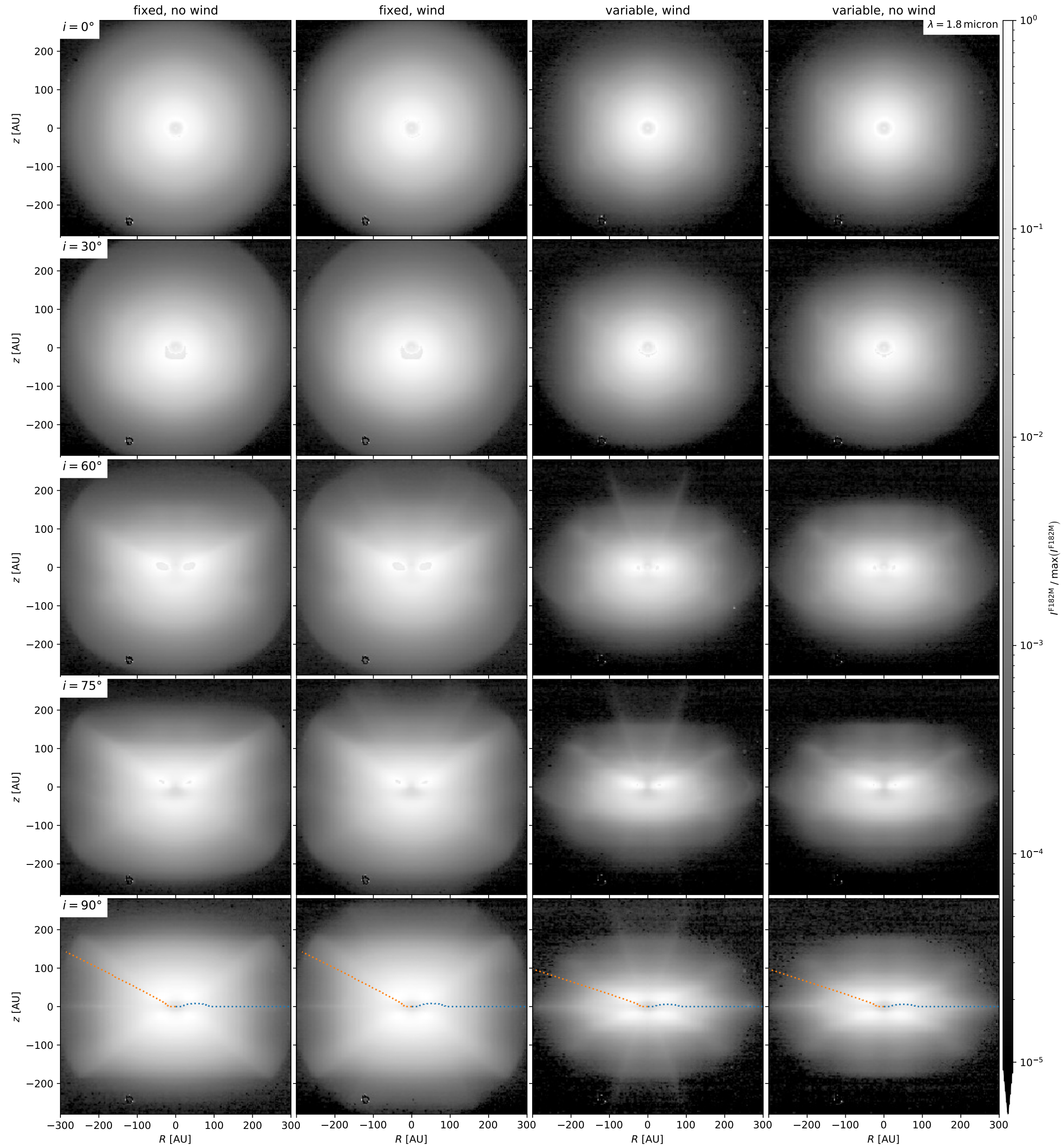

Figure 5.11: Synthesised observations of TD20 with JWST NIRCam's F182M filter, assuming the MASK210R coronagraph and MEDIUM2 readout pattern. The coloured lines indicate the ($\tau = 1$)-surfaces as in Figs. 5.7–5.10. At higher i, the cone-shaped outflow feature is visible for both the 'fixed' and 'variable' models.

$0\farcs8$ ($\simeq$ 80 AU at the assumed distance of 100 pc) renders a differentiation of the 'wind' and 'no wind' models by their inner hole sizes unfeasible.

As in the direct `RadMC-3D` results, the TD20 models show a more prominent wind signature than the TD30 ones. The 'fixed' setup produces a somewhat fuzzy wind signature at higher inclinations, that is $i \gtrsim 60°$ for fixTD20 and $i \gtrsim 75°$ for fixTD30. Depending on the actual outer radius of the dusty disk (here assumed to be $r \simeq 300$ AU), the chimney structure caused by the wind may be more or less visible in reality; looking at the fully edge-on disks, it is furthermore questionable whether a clear distinction between a 'wind' case and a slightly puffed-up disk could be made from a single observational image.

The flatter disk structure of the 'variable' models allows their dusty XEUV outflow pattern to emerge more clearly and already at lower inclinations than for their 'fixed' counterparts. A faint, non-distinct vertical bump already appears at $i = 30°$ for varTD20, and a more pronounced cone feature at $i \gtrsim 60°$

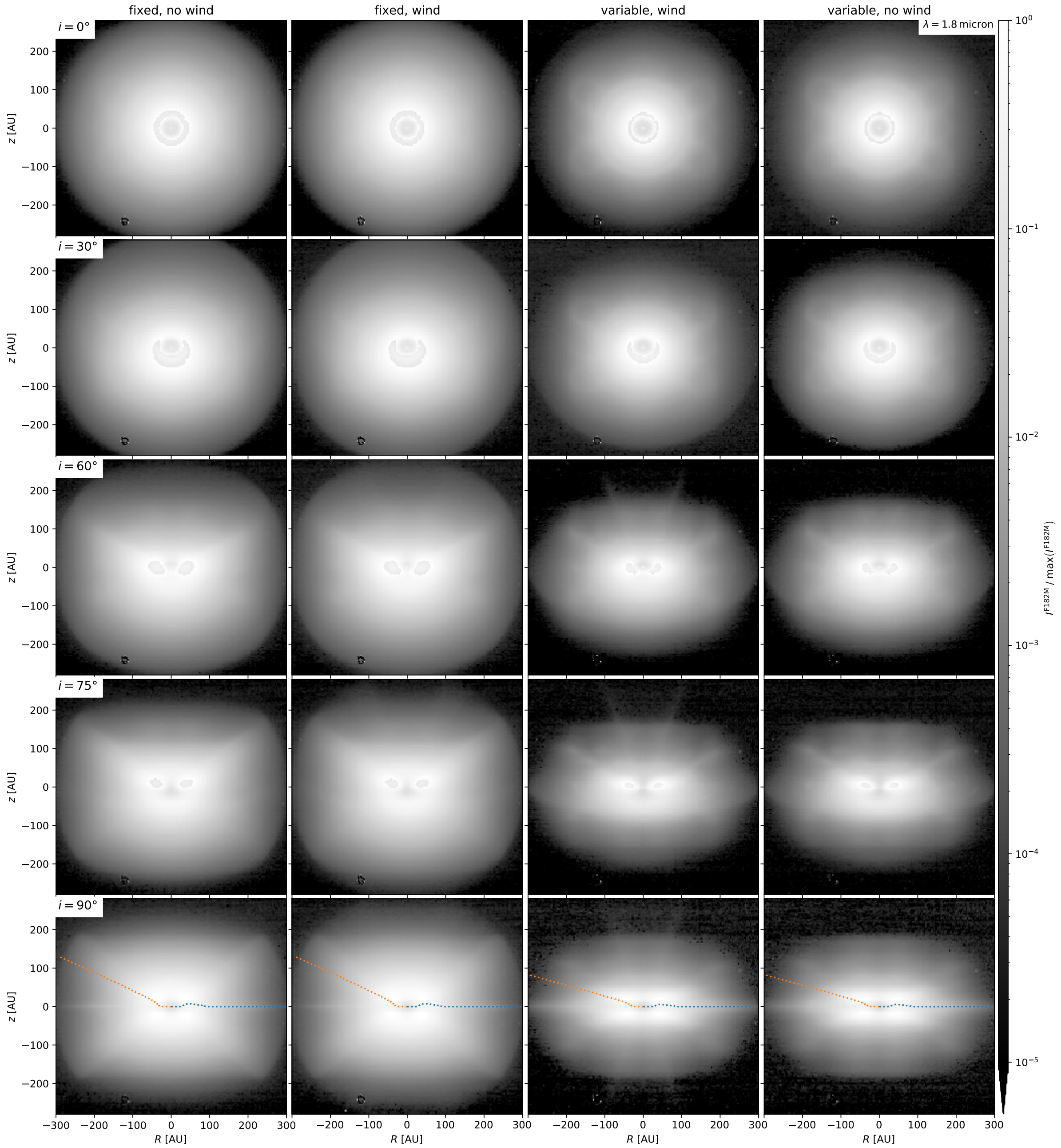

Figure 5.12: Synthesised observations of TD30 with JWST NIRCam's F182M filter, assuming the MASK210R coronagraph and MEDIUM2 redout pattern; all else equal to Fig. 5.11. The relative intensity of the wind signature is slightly smaller than for TD20.

for both varTD20 and varTD30.

5.3.5 Polarised-light images

SPHERE IRDIS's J-band corresponds to $\lambda_{\mathrm{obs}} \simeq 1.2\,\mu\mathrm{m}$, thus we chose to present our results for this wavelength here. As smaller dust grains are more likely to be entrained in the XEUV outflow, H-band observations (i.e. $\lambda_{\mathrm{obs}} \simeq 1.6\,\mu\mathrm{m}$) exhibit less distinct wind features (see Sect. 5.6.2).

5.3.5.1 Radiative transfer

The `RadMC-3D` results for Q_ϕ in polarised light at $\lambda_{\mathrm{obs}} = 1.2\,\mu\mathrm{m}$ are shown in Figs. 5.13 (TD20) and 5.14 (TD30); no artificial coronagraph has been applied to these images. Just like for the scattered-light

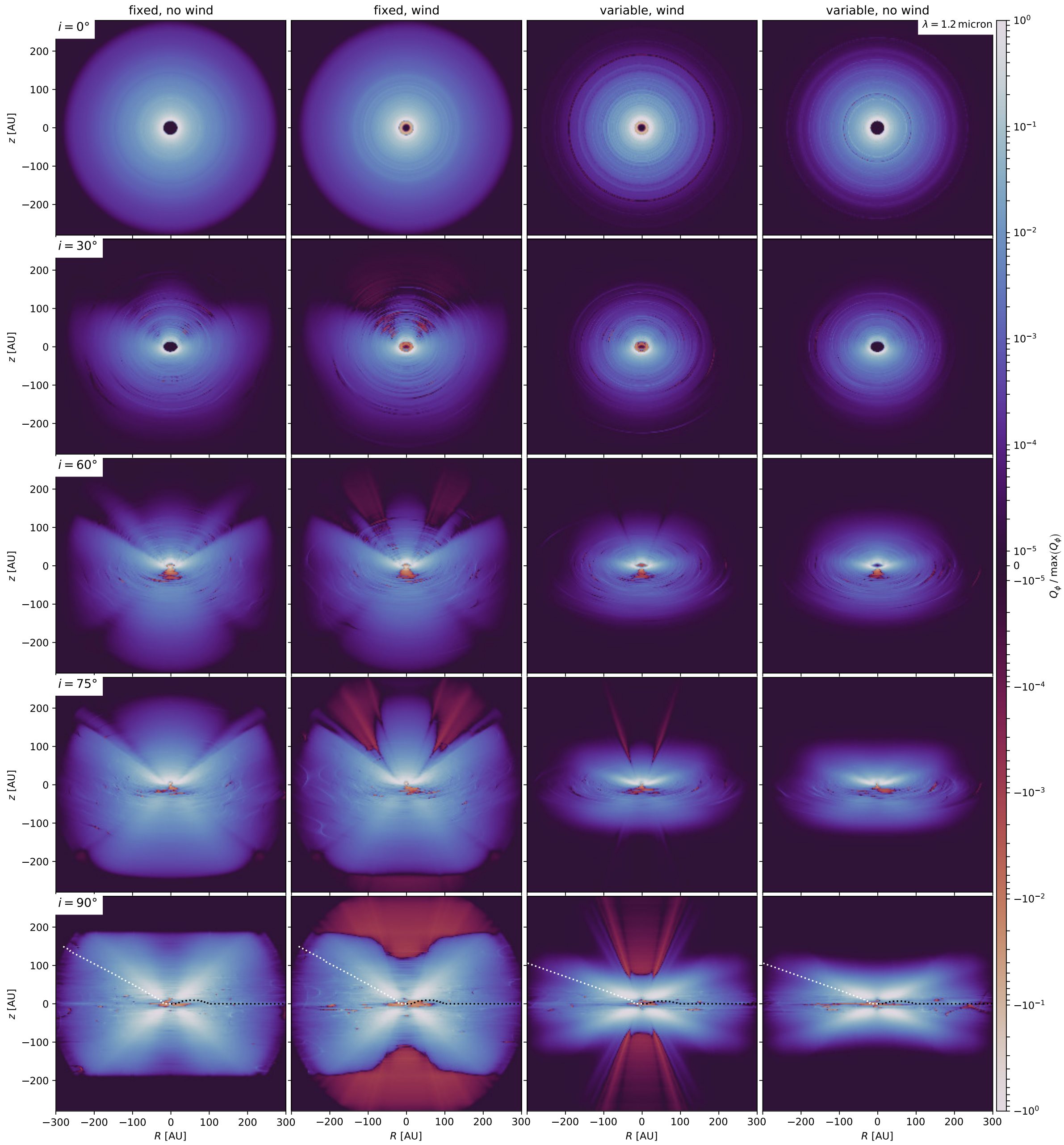

Figure 5.13: Polarised-light Q_ϕ for $\lambda_{\mathrm{obs}} = 1.2\,\mu$m for TD20. While the layout of the *rows* (inclinations) and *columns* (models) is the same as for the scattered-light images, no artificial coronagraph is applied. The dotted white (black) line indicates the ($\tau = 1$)-surface as seen from $r = 0$ ($z = \infty$). The wind produces a distinct signature especially around the jet region.

intensities, we see that the inner hole of the transition disks appears much smaller in the presence of a photoevaporative wind.

Furthermore, the wind causes an area of $Q_\phi < 0$ above (and below) the bulk of the disk, which even cuts somewhat into the high-z, low-R regions that otherwise exhibit $Q_\phi > 0$. This feature is rather broad in the 'fixed' models, and more spatially confined in the 'variable' ones; it resembles the overall cone shape of the wind signature of the scattered-light images (see Figs. 5.7–5.10). In the 'fixed' setups, it can already be seen at $i = 30°$; apart from the inner hole radius, this is the only outflow feature occurring at $i \lesssim 30°$.

The maximum relative intensities of the wind signal (i.e. the cone feature) are $Q_\phi/\max(Q_\phi) \lesssim 10^{-2}$ for $\lambda_{\mathrm{obs}} \in \{0.4, 0.7, 1.2, 1.6\}\,\mu$m.[1] This stands in contrast to the strong fall-off of the relative brightness

[1] These values were retrieved for varTD20 at $i = 90°$, which gives the strongest cone feature. About one to two orders

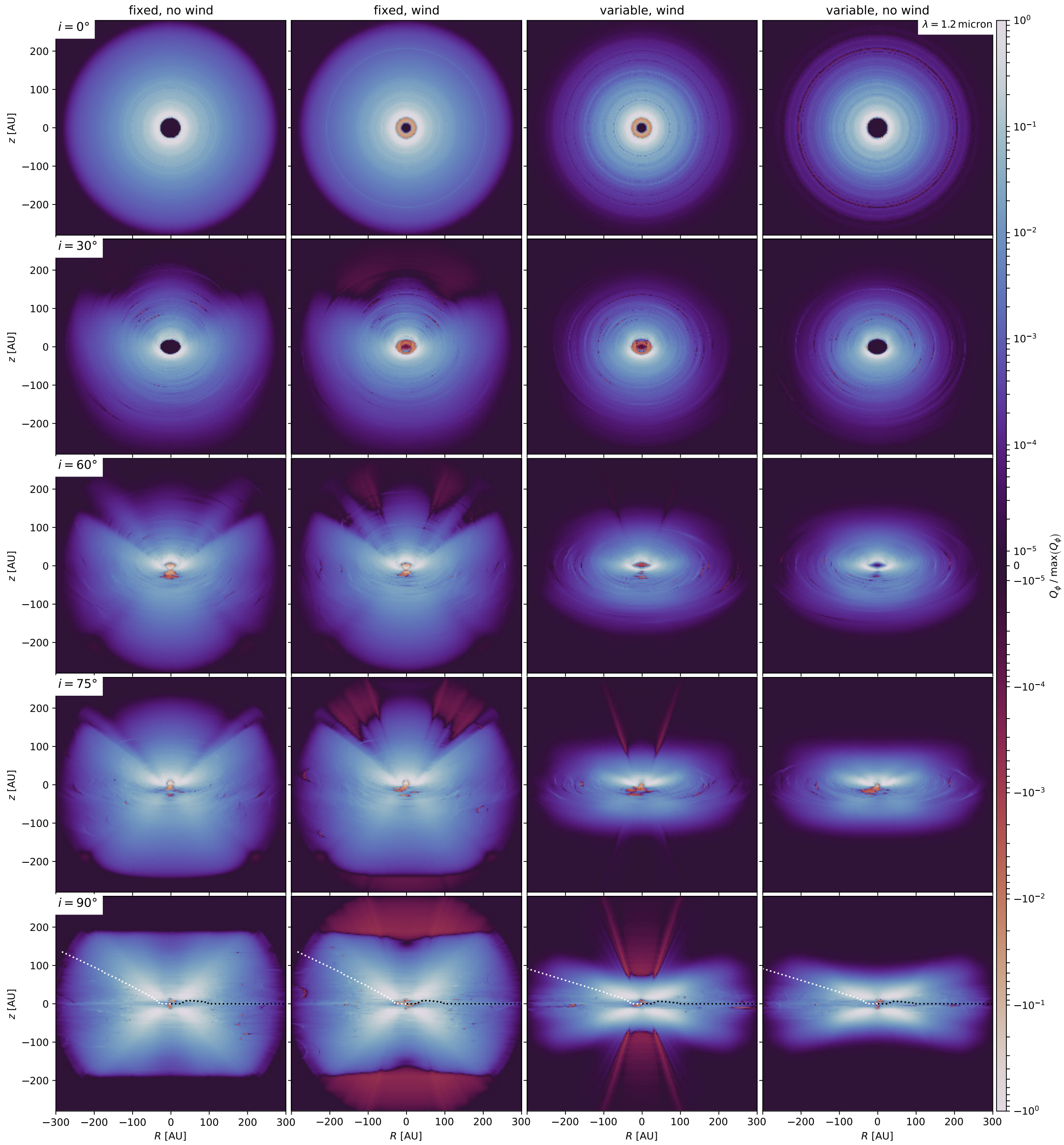

Figure 5.14: Polarised-light Q_ϕ for $\lambda_{\rm obs} = 1.2\,\mu$m for TD30, all else equal to Fig. 5.13, the characteristics of the wind signature included.

of the features with $\lambda_{\rm obs}$ seen in scattered light.

5.3.5.2 Synthetic observations for SPHERE IRDIS

The synthesised instrument responses for SPHERE IRDIS's J-band are shown in Figs. 5.15 (TD20) and 5.16 (TD30). The wind features seen in Figs. 5.13 and 5.14 are drained in instrument noise; this is also the case for H-band, so we do not include the corresponding plots.

While the coronagraph of SPHERE IRDIS obscures most of the difference in inner hole sizes found in Sect. 5.3.5.1, an inner ring of $Q_\phi < 0$ remains at $i \lesssim 30°$; probably due to the larger gap size, it is more prominent for TD30 than TD20. The cone-like features seen in the clear Q_ϕ images (Figs. 5.13 and 5.14) are much less pronounced in the synthetic observations. They arguably still appear at intermediate inclinations (especially $30° \lesssim i \lesssim 60°$), and are more pronounced for the 'fixed' models. Further post-

of magnitude need to be added if looking at different models and/or lower i.

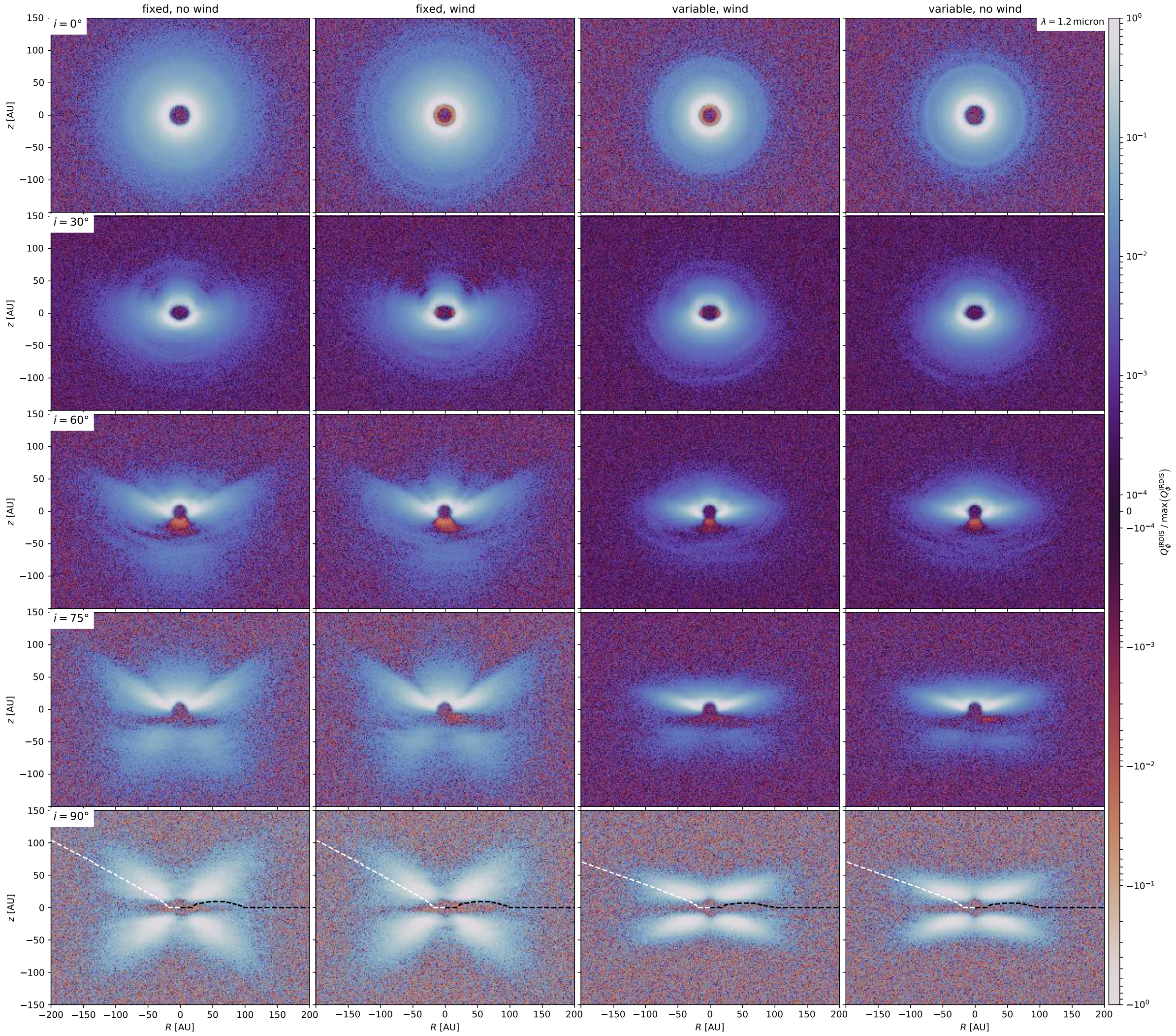

Figure 5.15: Synthesised Q_ϕ observations of TD20 in SPHERE IRDIS's J-band. The dotted white and black lines portray the same ($\tau = 1$)-surfaces as in Fig. 5.13. The instrument noise overshadows the wind features seen there.

processing with a dedicated noise removal tool such as `denoise` (Price, 2007) did not enhance the wind signatures.[(1)]

By contrast, the difference in spectral indices $\Delta\alpha$ (see Sect. 5.2.3.2) extracted from the SPHERE IRDIS P predictions is clearly non-zero. In the plots of Fig. 5.17, we see a distinct blue excess above the location of the star. It occurs for $35° \lesssim i \lesssim 75°$; for clarity and to avoid high noise levels, regions with a weak predicted signal ($P < 0.04 \cdot \max(P)$) were masked out before computing α. This indicates that above the star, $\alpha_{J,H}$ is greater in the 'wind' than in the 'no wind' cases, and thus that an XEUV wind enhances the difference in P between J- and H-bands.

5.4 Discussion

5.4.1 Scattered light

The vertical settling of the dust has a significant impact on the observability of a dusty outflow; if the disk is assumed to be large and the settling to be minimal (the 'fixed' case), large dust densities at high z are required for a noticeable signal. For a smaller disk or stronger vertical settling, less dust is needed for a current instrument to be able to pick up the signature; this is due to the radial trajectories on which

[(1)] `denoise`: `https://github.com/danieljprice/denoise/`.

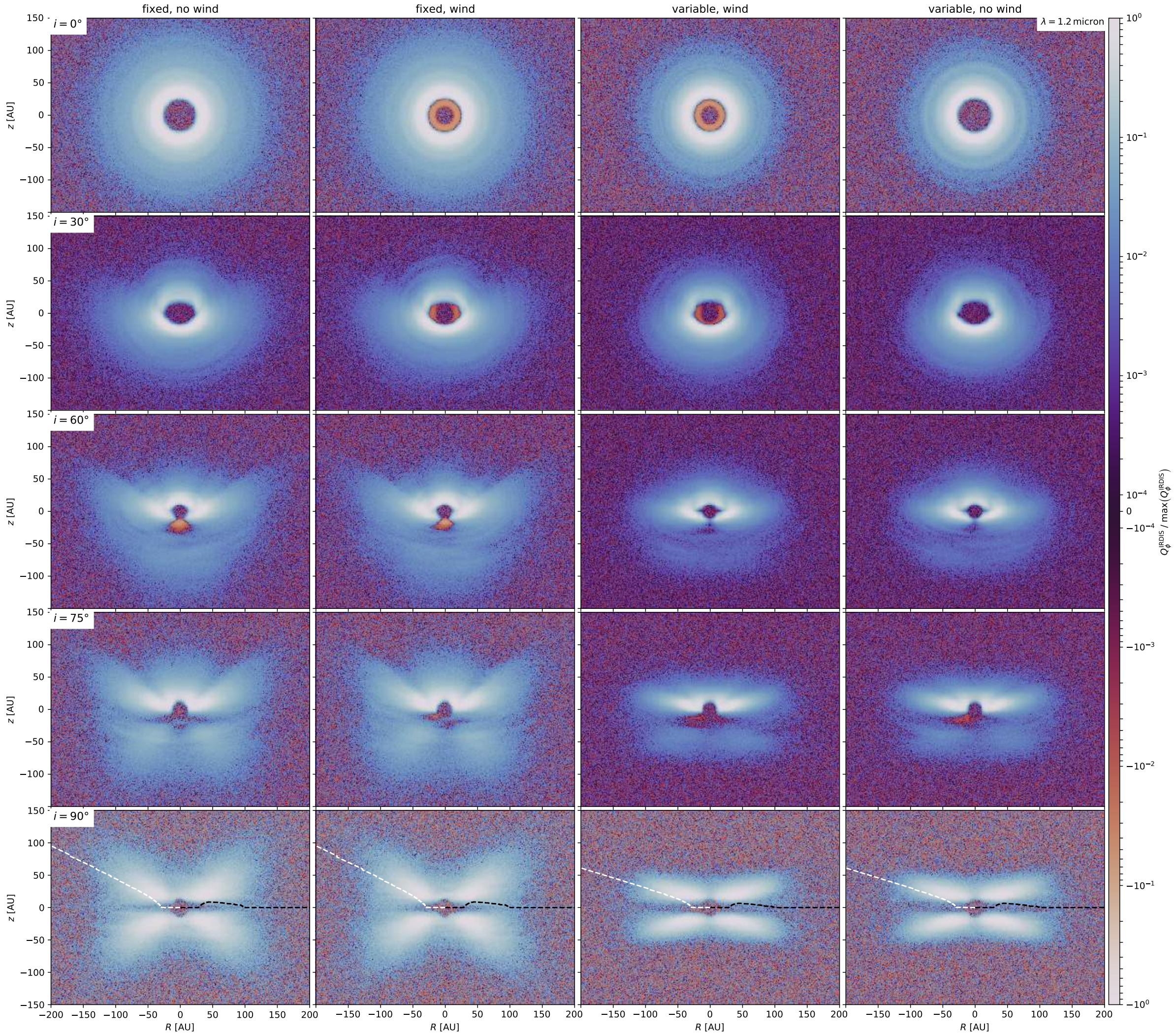

Figure 5.16: Synthesised Q_ϕ observations of TD30 in SPHERE IRDIS's J-band, all else equal to Fig. 5.15.

even the larger entrainable grains eventually leave the stellar gravity well, and which mean that the dust densities decline with r.

In Paper I, we suggested that $\max(z)|_R$ may be usable as a tracer for an XEUV wind, and thus allow one to distinguish it from a scenario dominated by an MHD wind. This did not work in Paper II, and also does not work here. Comparing the radiative-transfer results for $\lambda_{\mathrm{obs}} = 0.7\,\mu$m and $1.6\,\mu$m (see Figs. 5.7–5.10) does not show a big difference between the opening angles of the wind-induced cone features; this is despite the 'variable' models having a strong concentration of entrained dust towards $\max(z)|_R$ (see Figs. 5.3–5.6) for almost all a_0.

While we are not aware of any clear observations to date which show an outflow signature as suggested by these `RadMC-3D` results, the synthesised coronagraphic images for JWST NIRCam imply that imaging dusty winds will soon be a realistic possibility. Even if we have set up our models in Paper II and here to present best-case scenarios, the wind signatures seen in the synthesised observations (Figs. 5.11 and 5.12) are prominent especially for the 'variable' model. In addition, while trying to maximise the signal, we kept the dust-to-gas ratio at 0.01; while this value is generally used (see e.g. Andrews et al., 2009, 2010), it may underestimate the actual dust content of the disk as noted in Sect. 5.2.2.2.

For more face-on transition disks, the intensity profile of the inner hole may allow a tentative distinction between disks with and without dusty winds, as long as an estimate of the gap size can be retrieved by other means and there are no other dusty outflows (e.g. magnetically-driven jets). Planetesimals and planets (which are likely present once the disk enters its transition stage) may also strongly impact the radial brightness profile; the differences between planet-carved and photoevaporative gap intensity profiles will be investigated in a future work (Schäfer et al., in prep.).

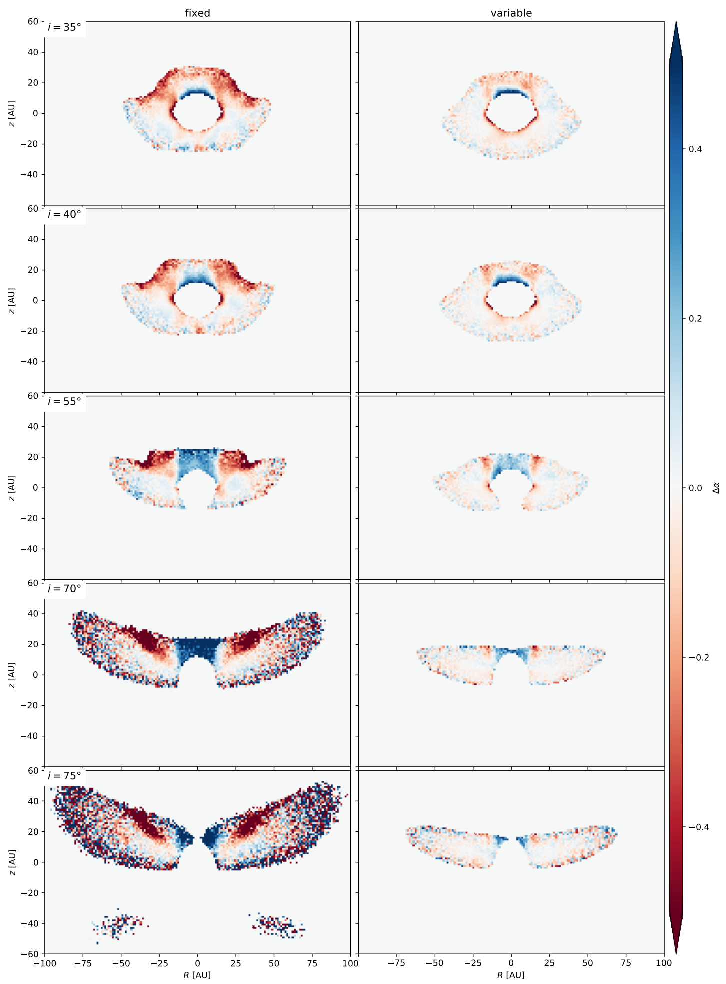

Figure 5.17: Difference $\Delta\alpha$ between the spectral indices $\alpha_{J,H}$ of the 'wind' and 'no wind' models for fixTD20 (*left*) and varTD20 (*right*); plots for the individual α values are provided in Sect. 5.6.2. For intermediate inclinations ($35° \lesssim i \lesssim 75°$), the dusty wind causes a clear colour excess, which appears particularly blue above the star.

5.4.2 Polarised light

While the clean Q_ϕ images (Figs. 5.13 and 5.14) show a clear wind signature, the noise in the synthesised observations for SPHERE IRDIS (Figs. 5.15 and 5.16) mostly obfuscates it. As is shown in Sect. 5.6.2, a reduction in instrument noise by a factor $\lesssim 10$ would allow for the detection of an observational signature, in particular at intermediate i. The narrow spatial extent of the high-intensity ($Q_\phi < 0$)-regions seen in Figs. 5.13 and 5.14 (especially for the 'variable' model) may render their detection unfeasible, considering that the contrast achievable with SPHERE IRDIS drops off at small angles (see e.g. Boccaletti et al., 2008, their Fig. 5). In that case, it may be worth looking into which coronagraphic pupil delivers the best contrast at small angles.[(1)]

Furthermore, analyses of Q_ϕ data are often performed in linear stretch in the literature. Due to the low relative intensities of the material in the wind, switching to logarithmic stretch may reveal interesting additional features (see e.g. Avenhaus et al., 2018, and Paper II). In the case of very strong dust entrainment in specific systems, signatures like the ones showcased here may be present. Speculatively, this could also be the case for MY Lup (see Paper II, Fig. 11); but whereas the analyses of Alcalá et al. (2017, using X-shooter on the VLT) suggest low accretion rates and thus a cleared inner hole similar to the models shown here (but maybe with a smaller $r_{\rm gap}$), later data retrieved by Alcalá et al. (2019, using HST) seem more in line with an intact inner disk.

The polarised signal may be more prominent when observing at smaller wavelengths. The Zurich Imaging Polarimeter (ZIMPOL) of SPHERE would be able to do exactly that, however we do not yet

[(1)]Due to the many other uncertainties of the model, we decided to not explore this avenue further in this work.

have a noise profile for this instrument. Furthermore, analyses as performed for instance by Thalmann et al. (2015) and de Boer et al. (2017) do not find clear outflow signatures. This may in part be due to most current investigations using data from SPHERE ZIMPOL to investigate systems at lower inclinations with regards to planet(esimal)s or companions (e.g. de Boer et al., 2016; Stolker et al., 2016; Avenhaus et al., 2017; Bertrang et al., 2018; Cugno et al., 2019; Willson et al., 2019).

Once a set of disks with and without confirmed dusty winds has been created from SPHERE ZIMPOL observations and (deep) SPHERE IRDIS data, the retrieved colours could then be employed to establish a baseline for the expected signal strength and morphology in polarised light. The colour excesses shown in Fig. 5.17 could then be used to determine whether a wind is present in other sources.

5.4.3 Caveats and outlook

As noted above, this work aims to present a numerically simplified, best-case scenario for the observability of XEUV winds, in order to investigate whether they could be detected via μm dust observations with modern instruments at all. The ‘fixed’ model represents the simplest setup possible, and is illustrative as it allows to decouple the effect of the wind from the complex dust evolution processes that happen in the disk. Studying the differences between the ‘fixed’ and ‘variable’ models provides insights as to what wind features may become more prominent when different physical processes drive the dust distribution at the launch region; an example is the clear enhancement of the narrow outflow channels in the case of dust settling. Nonetheless, our results may well overestimate the dust content of the photoevaporation-driven outflow.

The presence of a gas pressure bump at the outer gap edge may invalidate the assumption of a direct relation between $\varrho_{\rm gas}$ and $\varrho_{\rm dust}$, which could reduce the dust densities in the wind, but could also enhance the local dust-to-gas ratio (see e.g. Gárate et al., 2021). Further studies with a more realistic treatment of the outer gap edge will be needed to more accurately assess this aspect.

In addition, the dust evolution in the disk has been assumed to be fully decoupled from the wind model. The fast evolution of $\dot{M}_{\rm dust}/\dot{M}_{\rm gas}$, which would exceed unity in $\approx 0.1\,$Myr assuming a steady-state case, is a direct consequence of this, and as such should be treated with care; thus, dust densities in the wind may be lower than predicted here, or may vary over time. Both of these options would reduce the observability of the features presented.

The outflowing dust must be replenished at the disk surface; for the low-z environment of the outer gap edge, which accounts for the main portion of $\dot{M}_{\rm dust}$, the dominant process for this is radial drift. A quick estimate of the required drift velocities via $v_r = \dot{M}_{\rm dust}/(2\,\pi\,R\,\Sigma_{\rm dust})$ yields $v_r \approx 10...0.1\,$m/s ($2\cdot10^{-3}...2\cdot10^{-5}\,$AU/yr) for $a_0 = 0.01...12\,\mu$m; here, R has been chosen at $\max(\Sigma_{\rm gas})$, that is $R \simeq 26\,$AU for TD20 and $R \simeq 40\,$AU for TD30. Kanagawa et al. (2017) have reported drift speeds of up to $5.5\cdot10^{-3}\,$AU/yr for $\alpha = 10^{-3}$ and a dust-to-gas ratio of 0.01; but these values were found for $St \approx 1$, whereas μm-sized grains have $St \ll 1$ in the midplane. Another question would be the amount of dust already present at the gap edge, which may function as a buffer if material inflow from farther out is rather low. So in conclusion, it is questionable whether the $\dot{M}_{\rm dust}$ of Table 5.2 can be sustained over prolonged periods of time, or the outflow is for instance somewhat periodic; this will need to be investigated in a follow-up study.

5.5 Summary

In this work, we have modelled the XEUV-driven dusty outflow for two transition disks with inner hole radii of about 20 and 30 AU, and produced synthetic observations to predict their observability in scattered light with JWST NIRCam and in polarised light with SPHERE IRDIS. Throughout the modelling process, we made assumptions as to provide a best-case scenario for the visibility of the wind. Our findings can be summarised as follows:

- For a uniform dust-to-gas ratio, the dust mass outflow is still uniform as for a primordial disk. If dust settling is accounted for, preferred outflow channels emerge especially for the largest entrainable grains.

- These preferred outflow channels produce a distinct wind signature, consisting of a cone-shaped feature around the polar axis of the disk, in both scattered and polarised light. The feature is brighter at higher inclinations.

- JWST NIRCam should be able to detect a dusty photoevaporative outflow if the underlying disk is similar to the models presented here (i.e. $M_* \approx 0.7\,\mathrm{M}_\odot$, $L_\mathrm{X} \approx 2 \cdot 10^{30}\,\mathrm{erg/s}$, $M_\mathrm{disk} \approx 5 \cdot 10^{-3}\,M_*$, dust-to-gas ratio of 0.01, gap size of 20...30 AU; see Sect. 5.2.2) and the observational set-up is appropriately chosen. This also applies if no wind signature has been detected with SPHERE IRDIS.
- Compared to wind-less disks, dusty winds cause a colour excess in polarised light.

For more realistic modelling, further studies are required to better constrain the dust densities at the outer gap edge of transition disks; depending on the dust reservoir, steady or intermittent dusty wind signatures may be possible. In addition, deep observations with current instruments can be employed to try and identify objects with an XEUV-driven dusty outflow.

Acknowledgements: We would like to thank P. Rodenkirch, P.-G. Valegård, M. Gárate, and P. Weber for helpful discussions, and the (anonymous) referee for a constructive report that improved the manuscript.
Furthermore, we thank C. Dullemond for providing a pre-release version of the `disklab` package together with T.B.
This research was funded by the Deutsche Forschungsgemeinschaft (DFG, German Research Foundation), grant 325594231 (FOR 2634/1 and FOR 2634/2), and the Munich Institute for Astro- and Particle Physics (MIAPP) of the DFG cluster of excellence *Origin and Structure of the Universe*. B.E. and T.B. acknowledge funding by the DFG under Germany's Excellence Strategy – EXC-2094-390783311. S.C. and S.P. acknowledge support from Agencia Nacional de Investigación y Desarrollo de Chile (ANID) through FONDECYT Regular grants 1211496 and 1191934. T.B. acknowledges funding from the European Research Council (ERC) under the European Union's Horizon 2020 research and innovation programme under grant agreement No 714769, as well as funding by the DFG under grant 361140270. Ch.R. is grateful for support from the Max Planck Society. The simulations have mostly been carried out on the computing facilities of the Computational Center for Particle- and Astrophysics (C2PAP).

5.6 Appendix

5.6.1 The impact of the opacity

For this work as well as Paper II, we used an opacity prescription assuming DSHARP values for the disk and pure astrosilicates for the wind (see Sect. 5.2.3). To test the impact of the opacity prescription, we performed additional radiative transfer simulations for the 'wind' models of TD20 at $\lambda_\mathrm{obs} = 1.2\,\mu\mathrm{m}$ and $i = 90°$, using different opacities. In these simulations, both the disk and wind regions of the model employ the same opacity prescription. The opacities tested were, firstly, pure astrosilicates (Draine, 2003b), secondly, DSHARP values (Birnstiel et al., 2018, and references therein), and thirdly, Ricci opacities (Ricci et al., 2010a, and references therein).(1) The results are shown in Figs. 5.18 (fixTD20) and 5.19 (varTD20).

Expectedly, assuming a silicate-only material composition yields the highest intensities for both the disk and wind regions; switching to DSHARP opacities for only the disk (as done in the main part of this work) slightly reduces the signal from the dusty outflow. Conversely, using DSHARP-only or Ricci-only opacities strongly reduces the signal caused by the XEUV wind; the latter results appear quite similar, despite the difference in absorption opacities between the prescriptions.(2) All in all, the opacity prescription used in this work (and Paper II) fits its purpose of providing a best-case scenario.

In addition, comparing (highly detailed) observational data in polarised light to models with various opacities may help to identify the most realistic model for the dust composition and settling. This can be seen from the varying signs of Q_ϕ in Figs. 5.20 and 5.21, where the only parameter varied between the individual subplots is their opacity model.

5.6.2 Additional images

For clarity, we have not included all our radiative-transfer results in Sect. 5.3; however, some of them may still be of interest for future observational campaigns. Figs. 5.22 and 5.23 show the scattered-light

(1) The Ricci opacities are computed for $\varrho_\mathrm{grain} = 1.2\,\mathrm{g/cm^3}$; while this differs from our usual value of $\varrho_\mathrm{grain} = 1\,\mathrm{g/cm^3}$, the difference should be small enough to not significantly impact the overall results.

(2) At least for smooth disks, Ricci opacities might be more realistic than DSHARP ones, see Zormpas et al. (2022).

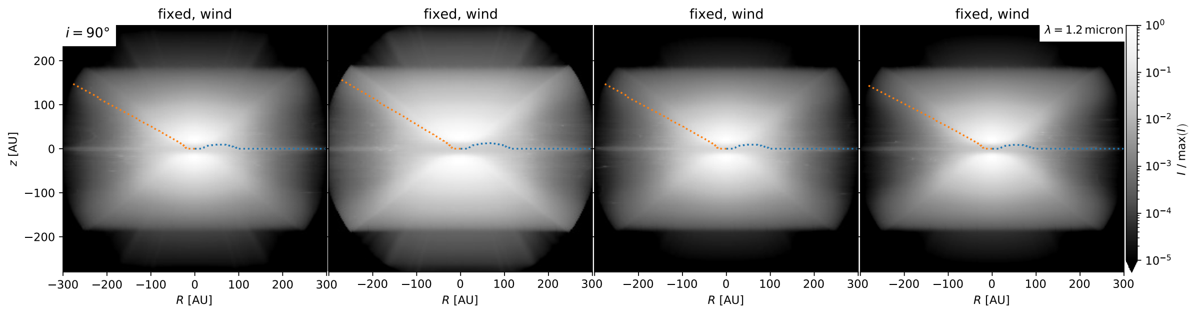

Figure 5.18: Scattered-light intensities for fixTD20, $\lambda_{\rm obs} = 1.2\,\mu$m, $i = 90°$. The panels show, from left to right, the results for our opacity mix, pure astrosilicates, DSHARP opacities (Birnstiel et al., 2018), and Ricci et al. (2010a) opacities. The coloured lines indicate the ($\tau = 1$)-surfaces as in Fig. 5.7.

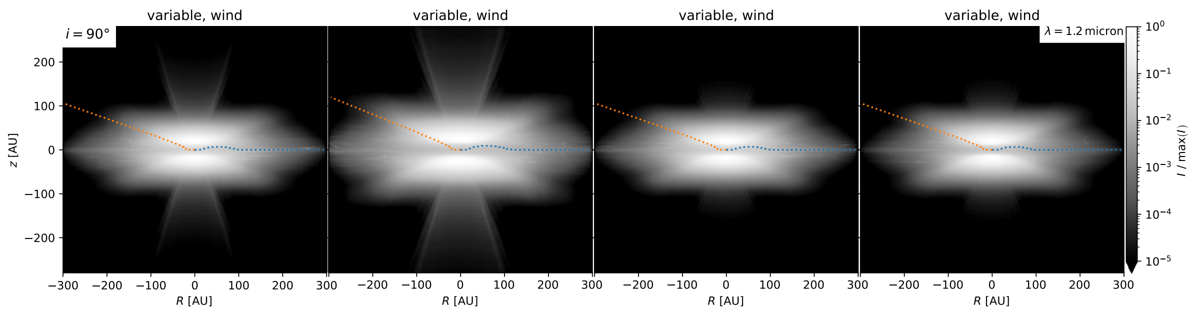

Figure 5.19: Scattered-light intensities for varTD20, $\lambda_{\rm obs} = 1.2\,\mu$m, $i = 90°$; all else equal to Fig. 5.18.

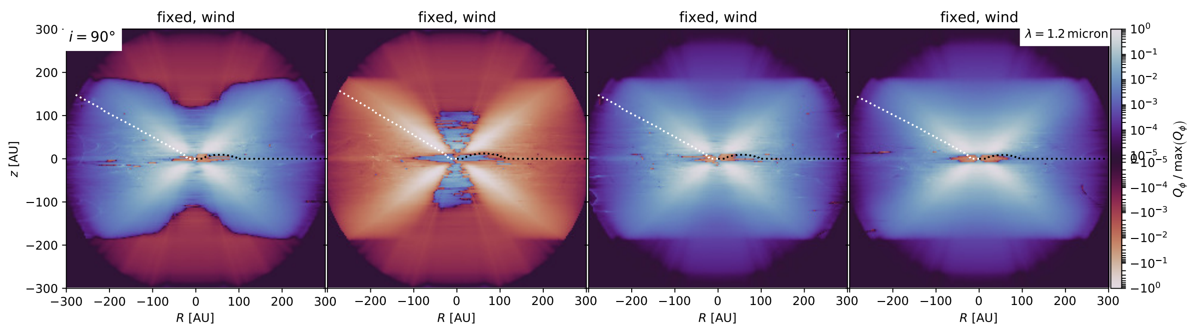

Figure 5.20: Polarised-light Q_ϕ for fixTD20, $\lambda_{\rm obs} = 1.2\,\mu$m, $i = 90°$. The panels show, from left to right, the results for our opacity mix, pure astrosilicates, DSHARP opacities (Birnstiel et al., 2018), and Ricci et al. (2010a) opacities. The coloured lines indicate the ($\tau = 1$)-surfaces as in Fig. 5.24.

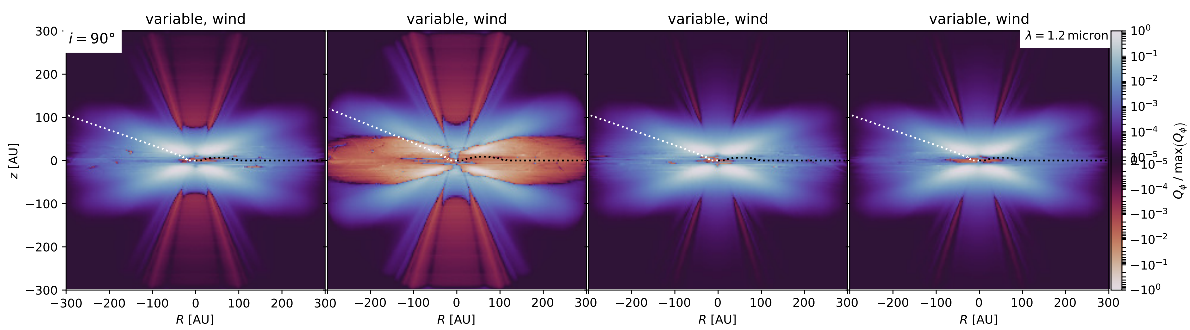

Figure 5.21: Polarised-light Q_ϕ for varTD20, $\lambda_{\rm obs} = 1.2\,\mu$m, $i = 90°$; all else equal to Fig. 5.20.

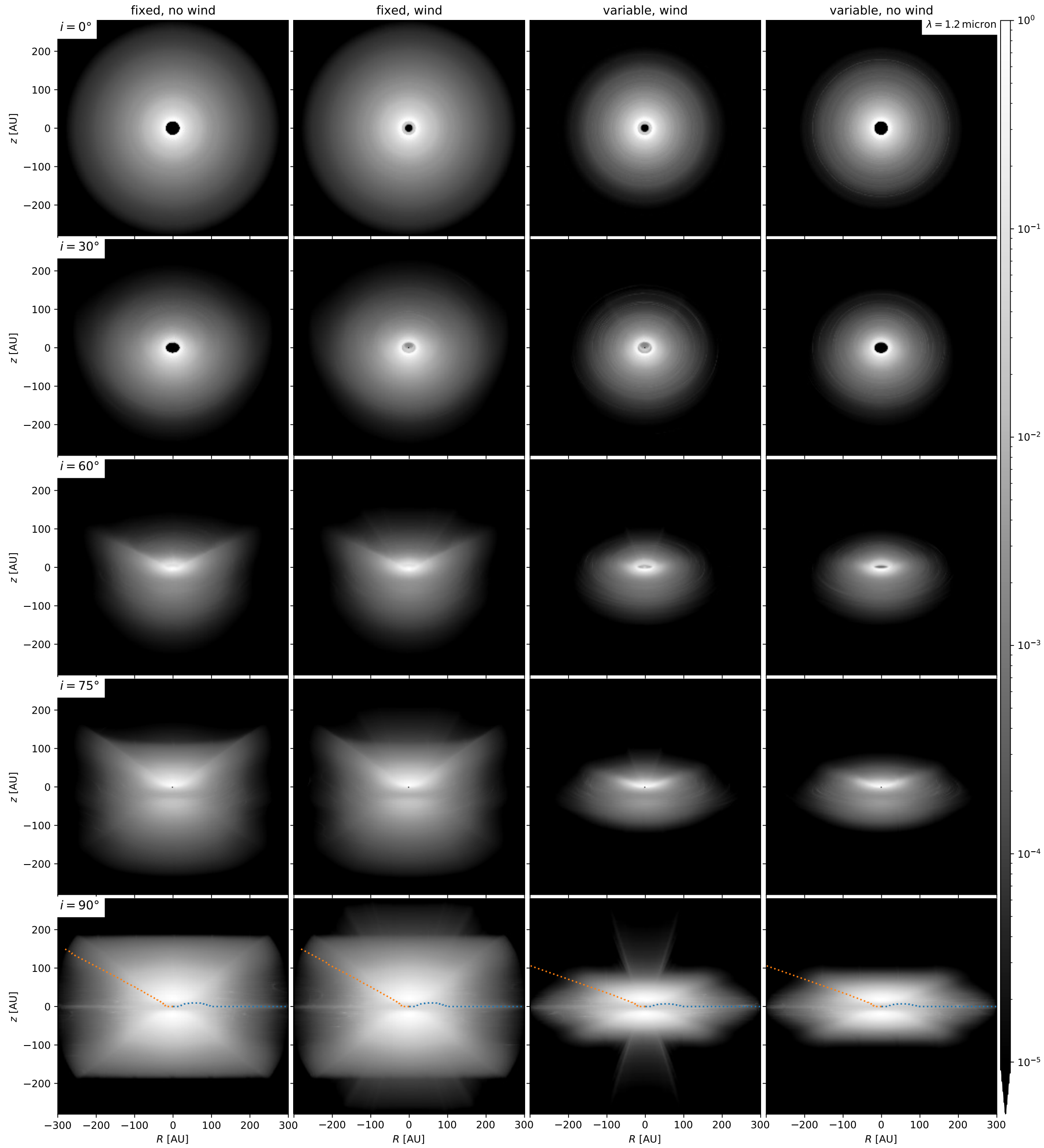

Figure 5.22: Scattered-light intensities for $\lambda_{\rm obs} = 1.2\,\mu$m for TD20, all else equal to Fig. 5.7.

intensities for $\lambda_{\rm obs} = 1.2\,\mu$m. As can be seen from a comparison between these images and Figs. 5.7–5.10, smaller $\lambda_{\rm obs}$ do not necessarily lead to stronger wind features; this is the case especially for the 'variable' model, probably due to the disk being more vertically settled for larger a_0. At $\lambda = 1.2\,\mu$m and $i = 30°$, varTD20 already exhibits a wind-driven cone feature.

The Q_ϕ images for $\lambda_{\rm obs} = 0.7\,\mu$m, which may be interesting also for SPHERE ZIMPOL, can be seen in Figs. 5.24 (TD20) and 5.25 (TD30); their counterparts for $\lambda_{\rm obs} = 1.6\,\mu$m are shown in Figs. 5.26 (TD20) and 5.27 (TD30). When including $\lambda_{\rm obs} = 1.2\,\mu$m (Figs. 5.13 and 5.14) for comparison, we see that the sign of the Q_ϕ signal of the XEUV-driven outflow changes between the plots for $0.7\,\mu$m and $1.2\,\mu$m. In all cases, we do however retain the cone-shaped feature above the disk midplane.

As noted in Sect. 5.4.2, reducing the instrument noise by a factor of 10 would result in a possible distinction between a 'wind' and 'no wind' disk with SPHERE IRDIS. For reference, the corresponding synthesised image for TD20 (to be compared to Fig. 5.15) is shown in Fig. 5.28.

Furthermore, in Sect. 5.3.5.2, we investigated the difference $\Delta\alpha$ between the spectral indices $\alpha \equiv \alpha_{J,H}$ of the P-values of the 'wind' and 'no wind' models of TD20. For reference, the individual spectral indices

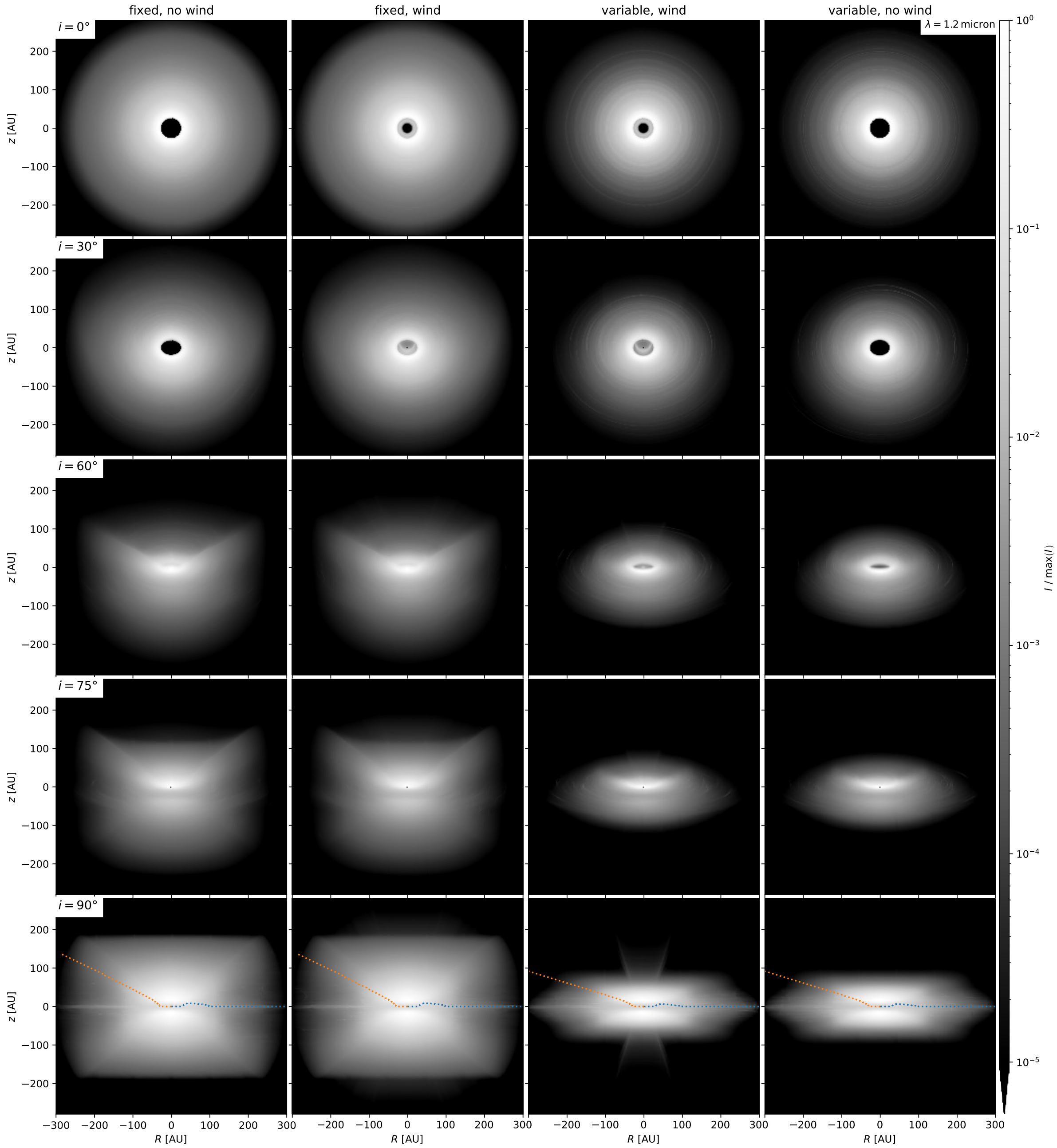

Figure 5.23: Scattered-light intensities for $\lambda_{\mathrm{obs}} = 1.2\,\mu$m for TD30, all else equal to Fig. 5.7.

are included in Fig. 5.29; the noise masking of Fig. 5.17 has not been applied.

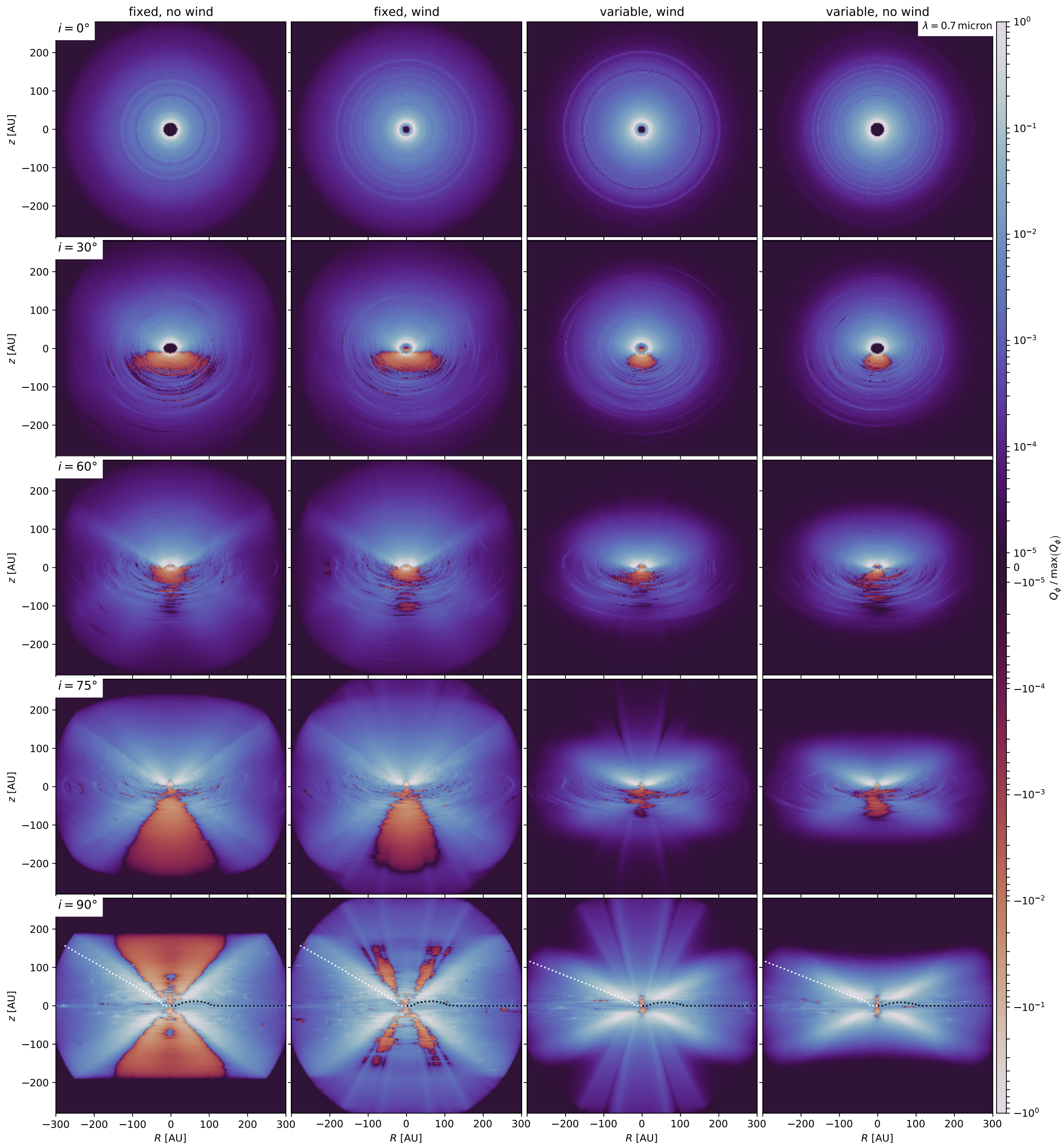

Figure 5.24: Polarised-light Q_ϕ for $\lambda_{\rm obs} = 0.7\,\mu$m for TD20, all else equal to Fig. 5.13.

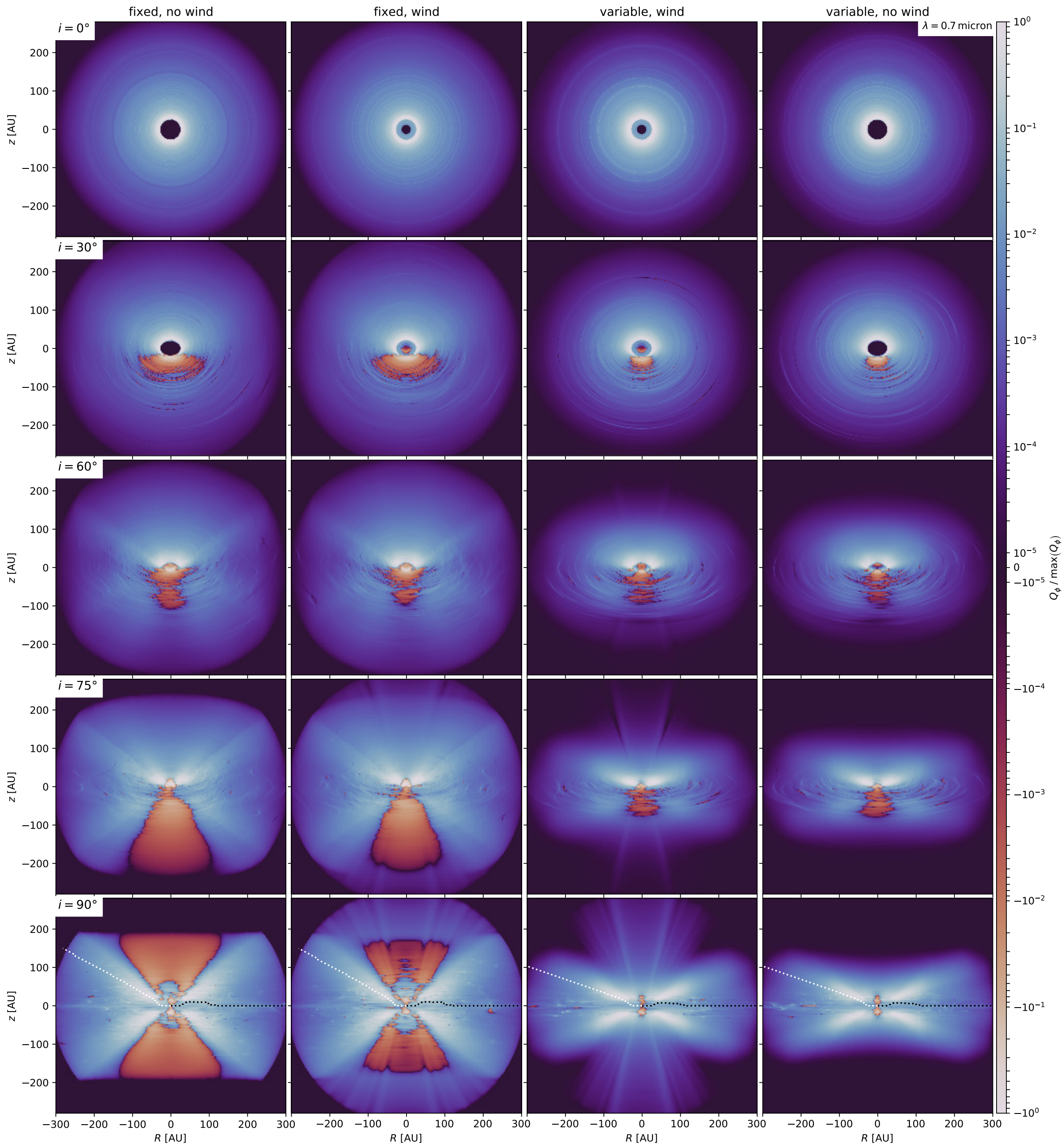

Figure 5.25: Polarised-light Q_ϕ for $\lambda_{\mathrm{obs}} = 0.7\,\mu$m for TD30, all else equal to Fig. 5.13.

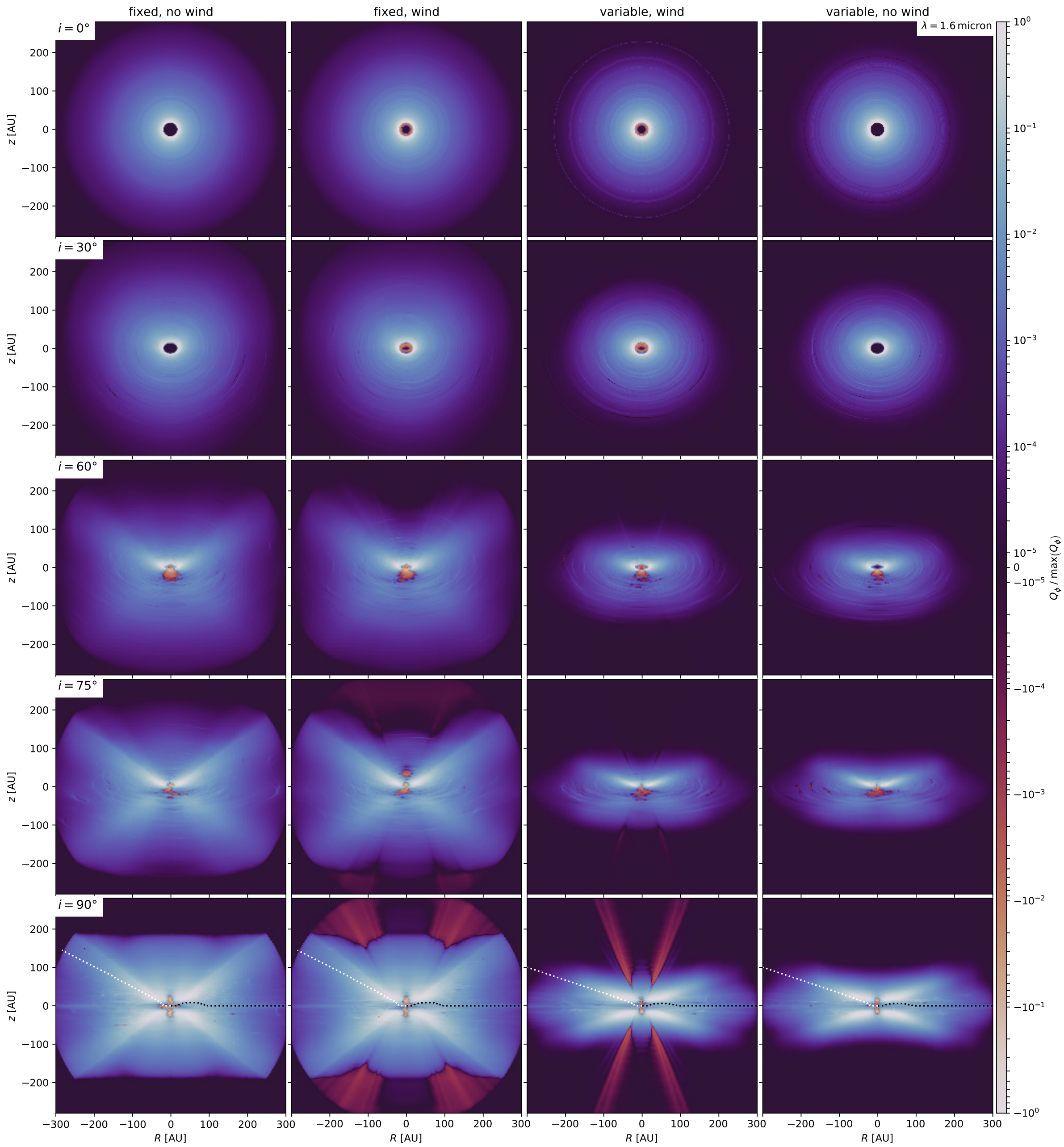

Figure 5.26: Polarised-light Q_ϕ for $\lambda_{\rm obs} = 1.6\,\mu$m for TD20, all else equal to Fig. 5.13.

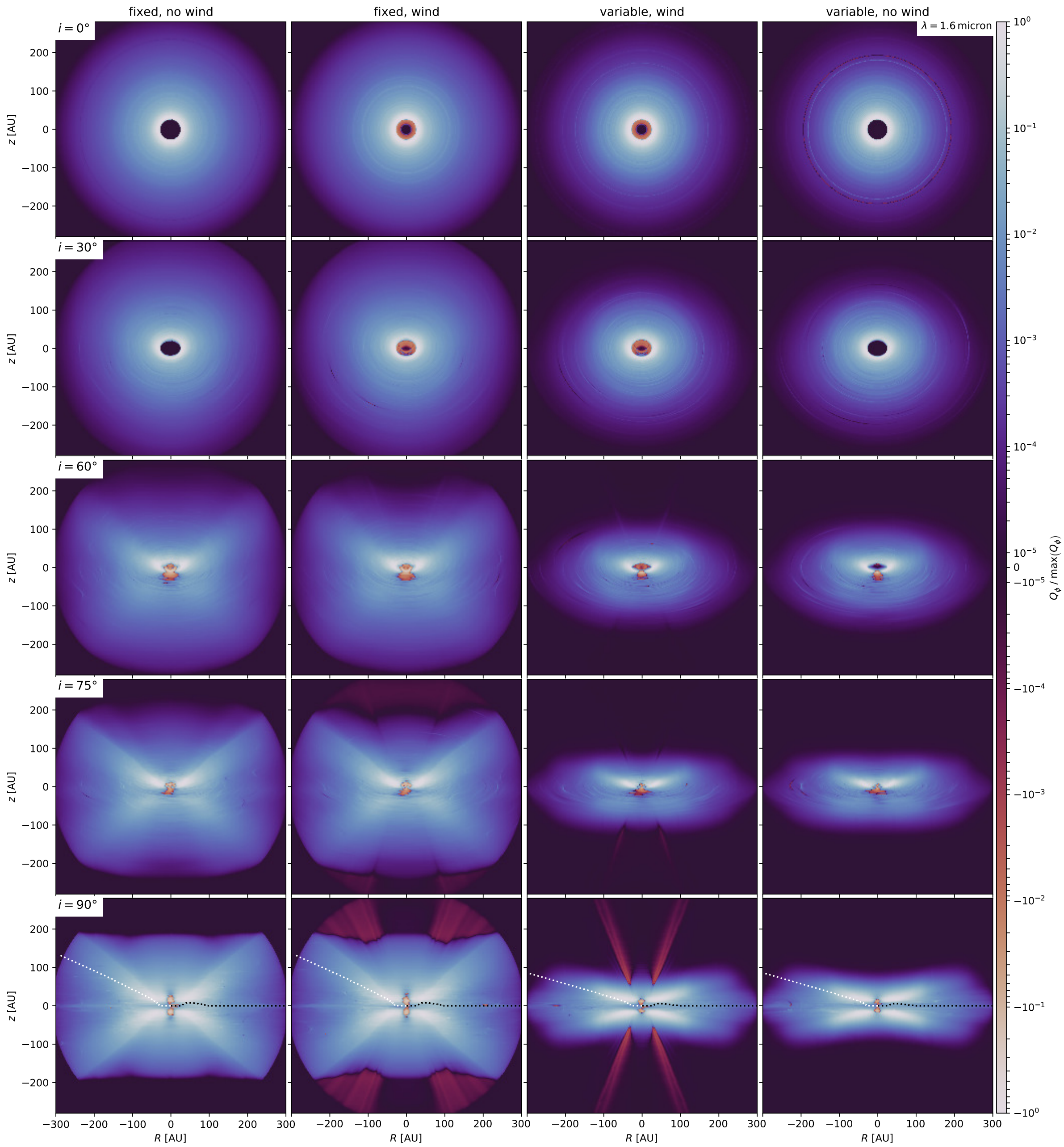

Figure 5.27: Polarised-light Q_ϕ for $\lambda_{\rm obs} = 1.6\,\mu$m for TD30, all else equal to Fig. 5.13.

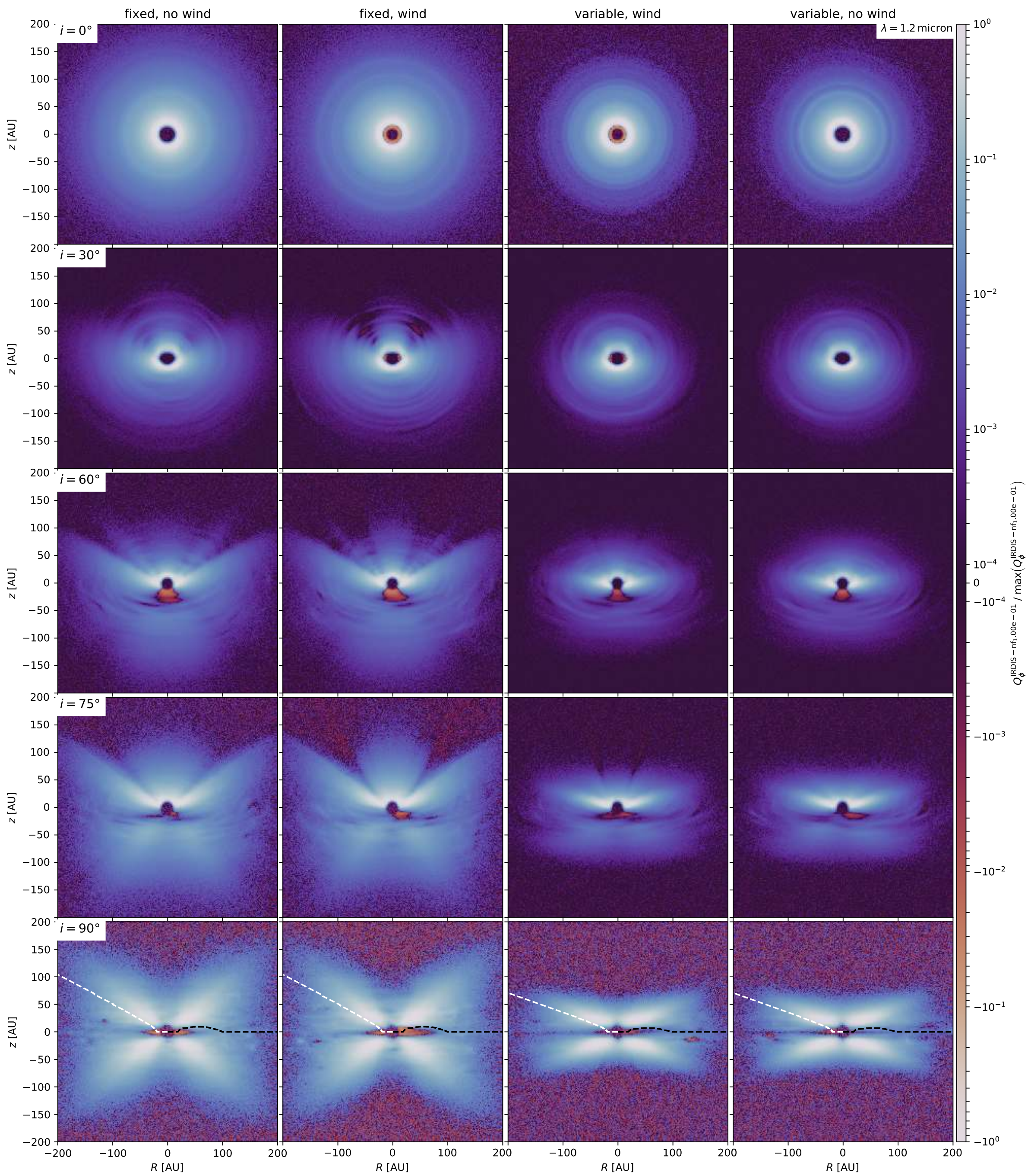

Figure 5.28: Synthesised instrument response for TD20 for SPHERE IRDIS in J-band, assuming a reduction of the instrument noise by a factor of 10; all else equal to Fig. 5.15. In contrast to said Fig. 5.15, there are visible differences between the 'wind' and 'no wind' models, for both fixTD20 and varTD20.

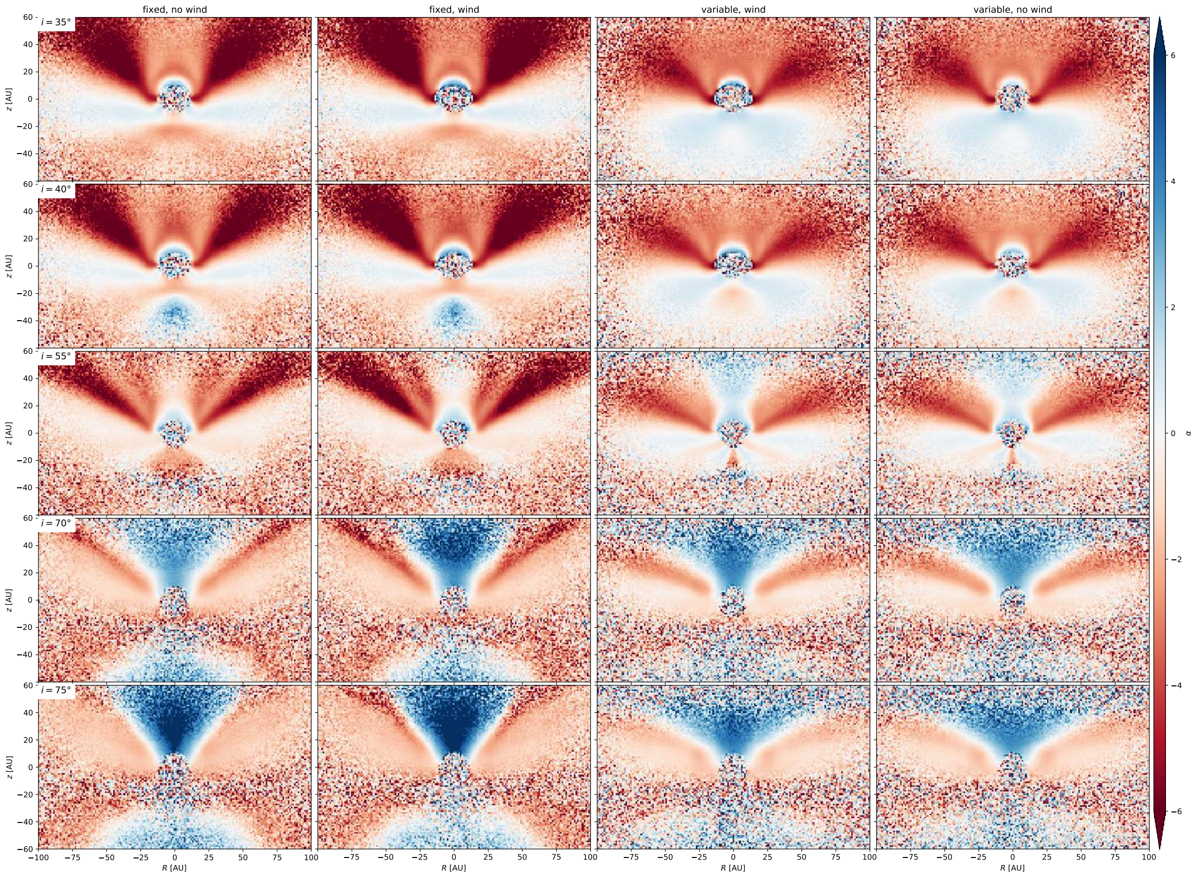

Figure 5.29: Spectral indices $\alpha \equiv \alpha_{J,H}$ for the individual models of TD20, at the inclinations shown in Fig. 5.17.

Chapter 6

Conclusion

6.1 Summary

As laid out in Sect. 1.1, the purpose of this thesis has been to achieve a better understanding of one of the many processes involved in the evolution of protoplanetary disks (outlined in Chap. 2), that is a photoevaporative wind driven by X-rays and EUV photons from the central star; in particular, we focused on dust entrainment in such an outflow.

Owen et al. (2011a) modelled the dust component of an EUV-only wind; however, their simulations were performed for a comparatively high-mass ($M_* = 2.5\,\mathrm{M}_\odot$) Herbig Ae/Be star, the wind was launched from the disk midplane (hence also disregarding vertical transport of material to the disk-wind interface), the computation of the dust trajectories was simplified, and only results for edge-on disks ($i = 90°$) were shown. The lack of a dedicated disk component for the retrieved radiative-transfer images rendered a direct comparison to observational data somewhat complicated, and the rise of X-ray and FUV-enhanced models in the following years – explicitly disregarded by Owen et al. (2011a) due to their increased computational cost – invited an update.

In Chap. 3 (published as Franz et al., 2020), we used an adapted version of the particle code of Picogna et al. (2018) to model dust trajectories for a variety of grain sizes $a \equiv a_0$ in the wind region of a protoplanetary disk; they were launched directly from the disk-wind interface because modelling their motion also in the disk and up to its surface would have multiplied computing times. The gas model was supplied by Picogna et al. (2019), simulating an XEUV-driven outflow from a circumstellar disk around a T-Tauri star of $M_* = 0.7\,\mathrm{M}_\odot$ and $L_\mathrm{X} = 2 \cdot 10^{30}\,\mathrm{erg/s}$. The dust particle motion accounted for stellar gravity, gas drag, and – below the disk surface – kicks induced by the vertical shear instability. As would have been expected from theoretical considerations, we found small ($a \lesssim 0.1\,\mu\mathrm{m}$) grains to follow the gas motion very closely, particles with $0.5 \lesssim a\,[\mu\mathrm{m}] \lesssim 5$ to decouple during the outflow, and those with $6 \lesssim a\,[\mu\mathrm{m}] \lesssim 11$ to decouple from the gas flow rather soon after being picked up by the wind; when the pick-up occurs, $St \ll 1$ however. Grains larger than $a \approx 11\,\mu\mathrm{m}$ are not entrained, and particles with $a \approx 11\,\mu\mathrm{m}$ only from a radial range of $15 \lesssim R\,[\mathrm{AU}] < 30$. All grains picked up by the outflow are sped up to escape velocity within a time frame of $t < 10^3\,\mathrm{yr}$ and within $r < 300\,\mathrm{AU}$, and exhibit an almost radial outwards motion. Said motion matches the (EUV) results of Owen et al. (2011a); furthermore, our maximum entrainable particle size of $a \lesssim 11\,\mu\mathrm{m}$ is (roughly) of the same order of magnitude as their $a \lesssim 2.2\,\mu\mathrm{m}$, and the $a \lesssim 4\,\mu\mathrm{m}$ of Hutchison et al. (2016b).

Qualitatively, the grain size distribution in the wind looks similar to that of Owen et al. (2011a) down to the region occupied by the largest grains; in our simulations, the area below is quite simply populated by the disk, indicating the importance of including the latter. A cross-check with the simplified dust motion prescriptions employed by Giacalone et al. (2019, in their model only for small a) illustrated the importance of numerical simulations for our use case. A comparison to the MHD modelling of Miyake et al. (2016) suggested that at least with respect to grain size, dusty outflows are mainly magnetically driven at small R, and are primarily caused by photoevaporation at larger R.

In Chap. 4 (published as Franz et al., 2022a), we employed the trajectories of Chap. 3 to compute the dust densities in the wind region of the same primordial disk. Since the initial setup lacked a self-consistent density prescription for the dust densities at the base of the outflow, we compiled two different models for the dust population within the disk. Firstly, ϱ_dust was assumed to be directly proportional to ϱ_gas; secondly, it was retrieved from the vertical settling-mixing prescriptions of Fromang & Nelson (2009) after invoking vertical hydrostatic equilibrium, hence lowering the amount of bigger grains at high altitude. This yields a dust population in the wind that is limited to a maximum z depending on R (as expected from Chap. 3), and considerably less massive than its gas counterpart (since only small grains are picked up by the outflow). Vertical settling proved to further reduce the population of the larger still entrainable grains in the wind, as had already been predicted by Hutchison et al. (2016a,b) as well as Booth & Clarke (2021) and Hutchison & Clarke (2021), highlighting the importance of an efficient upwards transport mechanism for the dust.

In a next step, the retrieved ϱ_{dust} were used for radiative-transfer modelling at wavelengths $0.4 \leq \lambda\,[\mu\text{m}] \leq 1.8$. The resulting images were additionally post-processed to produce synthetic observations in scattered and polarised light (for JWST NIRCam and VLT SPHERE IRDIS, respectively); we decided to focus on imaging predictions to complement other observational tracers of photoevaporative winds, in order to allow for a better estimation of the importance of the latter in the grand scheme of protoplanetary disk evolution.(1) Especially at smaller wavelengths, for which the corresponding grains are more populous in the wind, the clean images show a faint cone-like signature for the dusty outflow in scattered light, as well as wavelength-dependent polarisation above the disk. However, the synthesised data did not reproduce these features, indicating that they would be drained out by instrument noise.

In Chap. 5 (published as Franz et al., 2022b), we modelled wind trajectories and densities for dust grains in two transition disk models akin to those of Picogna et al. (2019), because photoevaporative winds are thought to increase in strength once an inner cavity has opened; the hole sizes of 20 and 30 AU were chosen such that they match the radial range from which the strongest mass loss is expected, and from which the largest grains had been found to be entrained in Chap. 3. As for the primordial disk, the dust grains are launched almost vertically into the wind, and then decouple from it more or less quickly depending on their size. The largest entrainable grains, at $a \lesssim 12\,\mu$m slightly bigger than for the primordial disk, are indeed entrained mainly from the outer edge of the inner cavity. Especially with vertical settling, we encountered rather collimated outflows for dust particles with $a \gtrsim 0.5\,\mu$m from the low-altitude environment of the cavity edge; by contrast, without vertical settling, the dust densities in the wind are about as smooth as for the primordial disk for all a.

For the transition disks, the synthesised images show tentatively detectable outflow signatures in both scattered and polarised light; again, these take the form of a cone structure around the vertical axis. This dusty wind tracer is more pronounced in the case of vertical settling, as the latter compacts the disk more along the z-axis; this enhances the relative brightness of the dust in the wind, whose densities are in all cases still significantly lower than within the disk. The location of the optical surfaces furthermore illustrates this; for all disks modelled, they lie within the disk, not within the wind region.

The synthesised images of Chaps. 4 and 5 were set up as best-case scenarios, as this work was aimed at establishing a framework for computing the dust densities in the wind, and at giving a first impression of whether dust entrained in an XEUV-driven photoevaporative outflow can serve as an observational tracer at all. While Sect. 6.2 elaborates on how to render the model more realistic, the overall result – that picking up strong photoevaporation-driven dusty outflows in targeted observations is not entirely unrealistic –, therefore holds value on its own.

In comparison to the work of Owen et al. (2011a), our cone-shaped patterns qualitatively resemble their wingnut morphology; in particular, their simulations for $\Phi_* \leq 10^{42}$/s exhibit a similar, more distinct pattern around the highest-$|z|$ edges of the outflow. Yet the angles of their and our cones differ, probably due to their assumption of a thin disk. Nonetheless, also other current models corroborate (their and) our results. Rodenkirch & Dullemond (2022) used the gas models of Picogna et al. (2019) to simulate dusty outflows driven by photoevaporative as well as magneto-thermal winds, from a disk with an inner gap of 2 AU (hence providing an intermediate scenario between our primordial and transitional disks). For their XEUV case, they report an outflow pattern similar to ours, and estimate comparable grain sizes of $a \lesssim 4\,\mu$m to be picked up by the wind.(2) In addition, a dusty outflow signature matching our predictions might have been detected in polarised light in RY Tauri, using VLT SPHERE ZIMPOL's I'-band ($0.79\,\mu$m; Garufi et al., 2019);(3) a simplistic, phenomenological modelling of the suspected wind by Valegård et al. (in prep.) has yielded a cone-like signature resembling ours (Valegård, priv. comm.). Thus even if our simulations are just a first step, they match other recent studies, which may be interpreted as a first affirmation.

(1) Comparisons of synthetic SEDs for disks with and without winds did not yield any robust features.

(2) Since their full simulations only included $a \in \{0.1, 1, 10\}\,\mu$m, their size estimate stems from a streamline computation from a single point (at $R = 8$ AU) along the disk-wind interface. Our Fig. 3.6 yields $a_0 \lesssim 9\,\mu$m for this R, yet Tables 4.1 5.1 indicate that not all of our large grains are entrained.

(3) RY Tauri has a stellar mass of $M_* \simeq 1.9\,\mathrm{M}_\odot$, however (see Garufi et al., 2019, and references therein), rendering it somewhat too massive for a direct comparison.

6.2 Outlook

6.2.1 Observational benchmarking

In the spirit of Chap. 1, a series of high-resolution, high-sensitivity observational campaigns could and should now be used to test our predictions, and hence to indicate how well the models developed and presented in this work represent reality.

In scattered light, HST data cover the right wavelengths, but seem to lack especially the contrast our synthetic imaging requires, see for instance the images of Pinte et al. (2008, IM Lupi), Wolff et al. (2017, 2MASS J11111083-7641574), Wolff et al. (2021, 2MASS J16313124-2426281), or Madlener et al. (2012, HH 30).[(1)] Optimally, a careful re-reduction of the data would yield refined results, but even tentative detections of dusty winds with HST are very rare; and the example reported by Miotello et al. (2012) was ascribed to external, not internal photoevaporation. Similarly, *Keck* (Wizinowich et al., 2000) observations with its NIRC2 and Vortex coronagraph (Serabyn et al., 2017) have not yet yielded definite results, although imaging of PDS 144N (a Herbig Ae/Be star part of a binary system; Perrin et al., 2006) provides a tentative verification of the wingnut morphology predicted by Owen et al. (2011a, as argued therein). Multi-band observations of HK Tauri B (McCabe et al., 2011) are inconclusive, as are various other results (see e.g. Currie et al., 2012; Mawet et al., 2017).

So now that JWST has been launched successfully, its NIRCam is the best tool to try and find dusty outflows at μm wavelengths in scattered light; due to the required coronagraphic imaging, the observation times necessary are however significant, which is likely going to constrain the amount of dedicated, targeted campaigns. Careful target selection is therefore paramount, accounting for factors such as the evolutionary stage of the system (class II or III), (high) inclination, and (sufficient) distance from external (FUV) radiation sources. To give just one example, HH 30 may be a promising target as Louvet et al. (2018) have reported a gaseous outflow which they note could be caused by a disk wind.

In polarised light, VLT SPHERE's IRDIS may be able to pick up a wind signature under optimal conditions (see Sect. 5.6.2); however, here as well, careful (re)processing of the (existing) data and logarithmic plotting are paramount, as our synthetic images do not show wind features in linear or r^2-scaled stretch.[(2)] In Sect. 4.4.2.2, we have presented a potential outflow signature in MY Lupi; either targeted modelling of the source, or a high-contrast follow-up observation could provide a valuable reference point for our simulations. Whereas synthetic observations in scattered light benefitted from smaller observational wavelengths, this is not the case for polarised light (see Sect. 5.3.5.1); VLT SPHERE ZIMPOL may still be able to provide additional data points, even though the noise levels will probably be similar (see e.g. de Boer et al., 2016, RX J1615.3-3255).

In the medium to long term, the quest for new instruments is always ongoing. Telescopes like the next-generation Very Large Array (ngVLA; Selina et al., 2018), Twinkle (Wells, 2016), or Extremely Large Telescope (ELT; Gilmozzi & Spyromilio, 2007) will open up new avenues of research (see e.g. Pascucci et al., 2018; van der Marel et al., 2019b), and hopefully allow us to place better constraints on dust entrainment in the process.

6.2.2 Possible model refinements

Our models have pioneered more detailed simulations of dust entrainment in protostellar winds, a field which has recently been gaining traction (see Booth & Clarke, 2021; Hutchison & Clarke, 2021; Rodenkirch & Dullemond, 2022). Judging from those studies as well as the results of Chaps. 4 and 5, these are therefore quite interesting times to take a closer look at dusty disk winds. To help pave the way, and potentially inspire future research, we will conclude this thesis by listing a few of the many possible model refinements and expansions; this should also give a pointer as to what to do in case our predictions do not match the data at all.

Coronagraphic modelling: As noted in Sect. 4.2.2.3, a dedicated module for synthesising coronagraphic images with `Mirage` is still in development (Perrin, priv. comm.). Hence, the scattered-light imaging predictions presented in Chaps. 4 and 5 are still preliminary; first data releases from JWST NIRCam may convey a more accurate impression of what can (and cannot) be done with the corona-

(1) In addition, while the objects investigated by Schneider et al. (2014) are gas-depleted debris disks, their images still illustrate the problem of determining the exact morphology of potential outflows.

(2) There are different quantities representing polarised intensities; in our investigations, Q_ϕ and P did not show strong qualitative differences, but a corresponding re-analysis of observational data might still unearth some features in the data.

graph. Accordingly, a re-post-processing of the radiative-transfer results may be in order to adjust the model predictions.[(1)]

Spectral index: A comparison of the synthesised spectral indices between J- and H-bands in polarised light (P) showed a distinctive excess in case of a dusty wind launched from a transition disk (see Sect. 5.3.5.2); in principle, this is similar to the colour change posited by Owen et al. (2011a). We have not yet evaluated observational data with regard to this spectral index, but that may be rather worthwhile; depending on the results, it could enable a direct classification of the disks investigated, or (more realistically) the creation of a database to be relied on once a colour baseline for disks without and with dusty winds has been established via a set of high-contrast observations. In any case, analysis of the spectral index could significantly simplify disk classifications, which would allow for high(er)-number statistics to be performed on (dusty) photoevaporative outflows.

Dust composition: To match the simulational setup of Owen et al. (2011a), we chose an internal grain density of $1\,\mathrm{g/cm^3}$; as discussed in Chap. 3.3.4, this clearly affects our results. Varying grain composition (and porosity, see e.g. Joswiak et al., 2007) in one and the same disk could soften the size limits on entrainment (see also e.g. Boehler et al., 2013), as could non-spherical geometries, which can realistically be expected (see e.g. Rahul et al., 2020); the latter may also impact the scattering properties of the dust (see e.g. Kirchschlager & Bertrang, 2020). But even when sticking with spherical grains, a basic evaluation concerning the predominance of fluffy or compact aggregates should be possible (Kataoka et al., 2014).

A closer inspection of the dust opacity prescriptions seems worthwhile. To optimise the visibility of the dusty outflow, and to avoid issues due to potential dust sublimation at the disk-wind interface or in the hot wind, we assumed astrosilicate opacities for the wind regions.[(2)] This matches the results of Pollack et al. (1994), who found monochromatic opacities computed at mid-infrared wavelengths to correspond to those of astrosilicates,[(3)] but still over-emphasises the wind because (smaller) DSHARP (Birnstiel et al., 2018) opacities were subsumed for the disk regions. In Sect. 5.6.1, we tested different material compositions for the particles in the outflow, that is the mixes of Birnstiel et al. (2018, DSHARP) and Ricci et al. (2010a). The resulting images in polarised light (Q_ϕ) vary not only in intensity, but also in sign; so high-resolution, high-contrast imaging could hint at the predominant composition of photoevaporated and in-disk dust (the opacity of which may vary even within one and the same protostellar system, see e.g. Chacón-Tanarro et al., 2019).

Overall dust mass budget: The ratio of dust to gas masses in protoplanetary disks is commonly, and thus also in our models, taken to be $\varepsilon_{\mathrm{dtg}} = 0.01$, the value for the ISM; yet as outlined in Sect. 2.2.1.3, the validity of this assumption is questionable especially for evolved (class II & III) disks, where the dust has had time to grow and drift (see e.g. Birnstiel et al., 2010; Birnstiel & Andrews, 2014; Villenave et al., 2019). The global $\varepsilon_{\mathrm{dtg}}$ may thus vary by one or maybe two orders of magnitude (see e.g. Ansdell et al., 2016; Miotello et al., 2017; Soon et al., 2019), which would impact $\varrho_{\mathrm{dust,\,wind}}$ accordingly. To better constrain the latter especially for smaller a, more concise modelling, informed by targeted observational campaigns, would be instrumental.

In addition, constraints on the overall disk masses are rather loose (see Sect. 2.2.1.3). So while a disk mass of $M_{\mathrm{disk}} \lesssim 0.01\,M_*$ as used in our models (see Sects. 4.2.1 and 5.2.1) is certainly realistic, different mass budgets (and hence dust masses) are possible. While a first approximation could be to simply scale the photoevaporation-driven mass fluxes accordingly, secondary effect such as increased column depth and gravitational instabilities could further influence the results.

Dust settling: Due to the aforementioned growth and drift, $\varepsilon_{\mathrm{dtg}}$ likely varies with both R and z; this has also been suggested by observations (see e.g. Pinte et al., 2016). But while mm-sized grains are known to settle more strongly than μm-sized ones (see e.g. Villenave et al., 2020; Wolff et al., 2021, and Sect. 2.2.2.5), the relative dust scale heights of grains within the μm-size range are less well-constrained (see e.g. Boehler et al., 2013), even though at the disk surface, dust decoupling from the gas may start to

(1) We employed a similar transmission mask for synthesising the SPHERE IRDIS data, however in that case, observations have not revealed any systematic effects (Casassus, priv. comm.).

(2) Judging from the dust temperatures calculated in the radiative-transfer simulations, dust sublimation should be negligible at $R \gtrsim 0.2\,\mathrm{AU}$ (see Sect. 4.2.3; also checked for the transition disks).

(3) More detailed testing for instance with the framework of Grassi et al. (2017) could nonetheless produce interesting results.

become significant depending on the exact a (see e.g. Pinte et al., 2008). The current lack of data means that theoretical models such as presented by Birnstiel et al. (2010, see also Sect. 2.2.2.5) cannot be fully fine-tuned to realistic conditions.

The differences between our models with and without dust settling in Chaps. 4 and 5 have illustrated the importance of accurately determining the material densities at the base of the outflow; this had already been parametrised for the gas component by Clarke & Alexander (2016) – generalised by Sellek et al. (2021) –, and for the dust by Hutchison et al. (2016b). Recent works have corroborated that the (non-)delivery of material from within the disk to the disk-wind interface is the limiting factor for the outflow in terms of mass and grain sizes (Booth & Clarke, 2021; Hutchison & Clarke, 2021). The NIRCam filters of JWST, spanning $0.7 \lesssim \lambda\,[\mu\mathrm{m}] \lesssim 4.8$, applied to highly-inclined disks, could hence provide a treasure trove of high-resolution data, and thus complement ALMA data ($0.3 \lesssim \lambda\,[\mathrm{mm}] \lesssim 8.5$). This should allow for various model refinements (see e.g. Duchêne et al., 2003); but already a concise determination of the grain sizes in the wind would indicate which a are present at the disk surface in non-negligible quantities, and thus allow for more realistic, although potentially targeted, modelling.

The amount of dust at the disk-wind interface is also impacted by the general location of the latter; while simulations suggest $|z| \simeq 4.5\,H_{\mathrm{gas}}$ (see e.g. Gressel et al., 2015; Bai, 2017; Picogna et al., 2019), this is hard to verify observationally. Potentially, the inclination of the disk surface can be traced via dusty winds by investigating their outflow angles and adjusting the modelling accordingly; yet a lot of different factors can change these angles (see Rodenkirch & Dullemond, 2022). Nonetheless, better constraints on the location of the ionisation front could help to inform models of vertical settling, too.

Dust growth: In our investigations, we have assumed the dust grains to be of constant size $a \equiv a_0 \equiv a(t=0)$. This is probably a valid assumption for the wind region, in which the outflow is fast and laminar (see Chap. 3), and where ϱ_{dust} is significantly lower than in the disk (see Chaps. 4 and 5). However, while dust growth is certainly most important in and around the disk midplane (see Sect. 2.2.2.6), it may still affect the respective densities of $\lesssim \mu$m-sized species at higher altitudes; this depends on the nature of the vertical transport processes, and the timescale on which particles close to the disk surface are picked up by the wind; for example, the 'floating grains' of Miyake et al. (2016) could entail a shift in the dust size distribution available for entrainment. While we would expect this to be of rather negligible consequence, it may still be worth verifying.

Processes at the gap edge: The dusty wind signatures of the transition disk models of Chap. 5 are in large parts fuelled by material from the edge of the cavity; yet, as noted in Sect. 5.4.3, this work is not accurately accounting for the expected difference between the gas and dust distributions caused by the pressure bump (compare e.g. Birnstiel et al., 2016; Drążkowska et al., 2019). A more detailed prescription, using for instance the (1D) setup of Gárate et al. (2021), should be used to check ϱ_{dust} in the midplane; then, either the existing vertical prescriptions could be used, or a 2D (R, z)-model for dust transport along a photoevaporatively heated gap edge could be developed, in order to refine the densities at the base of the outflow.

Furthermore, disk gravity could safely be ignored for the primordial setup (see Sect. 3.6.1); but it may matter very close to the midplane in the case of transition disks. While we verified that regions $z \gtrsim 1\,\mathrm{AU}$ are mostly unaffected even when accounting for the full M_{disk} for vertical acceleration, regions at $z \ll 1\,\mathrm{AU}$ may be affected to some degree, in particular if there is a dust mass build-up due to the gas pressure bump.[(1)]

Planet(s): More intricate simulations of dust distributions around pressure bumps could also be used to investigate the influence of planets of various masses on the structure of a disk wind. For example, Weber et al. (in prep.) have simulated gas distributions for a photoevaporating disk with a planet-carved gap, in which the latter significantly changes the flow structure of the outflow; their gas maps could be used as an input to the pipeline established in the course of this work.

Far-ultraviolet radiation: So far, the underlying disk model has been computed for only X-ray and EUV irradiation, simply due to the additional computational cost accurate FUV (and microphysical) modelling would incur.[(2)] Nonetheless, the dust densities retrieved could be used as a first input for

[(1)]As the outflow signature retrieved by Rodenkirch & Dullemond (2022) is qualitatively similar to ours (see Sect. 6.1), we do not expect our results to be entirely invalidated.

[(2)]Efforts to reduce the cost of astrochemical modelling are underway, see for instance Grassi et al. (2020, 2021).

opacity estimates. As laid out in Sect. 2.3.3.5, the exact impact of additional FUV photons is unclear. For one thing, they might enhance dust mass-loss rates only at large R, or already further in. But for the smaller species ($a \lesssim 4\,\mu$m), most dust grains are entrained anyways (see Tables 4.1 and 5.1); so in particular when accounting for vertical settling, the direct impact of FUV photoevaporation on mass loss should be minor, unless it also influences the flow structures within the disk (which is possible due to its high penetration depth, see Table 2.1). For another thing, FUV irradiation could change the morphology of the outflow, and hence the opening angle of the predicted cone. This should be kept in mind if dedicated modelling of individual sources with XEUV setups does not yield sensible matches to observations. Simulations combining X-ray, EUV, and FUV photoevaporation – and mitigating the potential shortfalls of Gorti & Hollenbach (2009), Wang & Goodman (2017b), and Nakatani et al. (2018b) – would allow to finally pinpoint the importance of the individual photon energy ranges in relation to each other.

Especially FUV irradiation from the protostellar neighbourhood can also drive a photoevaporative outflow (see Sect. 2.3.3.4). Depending on the exact circumstances like the angle of the disk to the external photon source(s) and the luminosity of the latter, the resulting winds may overshadow the internally-driven ones, or at least alter their morphology. While accurate models combining internally- and externally-driven photoevaporation would be quite intriguing, a more reasonable approach would be to focus observational data collection on objects thought to not be strongly affected by external effects (see Sect. 6.2.1).

Radiation pressure: We have neglected the impact of radiation pressure as we presumed it to be minor; the smaller grains most likely impacted by it are entrained anyway (see Sects. 3.4.1, 4.2.3, and 5.2.2.1).(1) Yet as stated by Vinković & Čemeljić (2021), radiation pressure may collimate dusty outflows; this could change the shape of the cone-like patterns predicted from purely XEUV-driven winds. Since radiation pressure acts to accelerate especially small grains radially away from the star, it might decrease $\max(z)\,|_R$ (i.e. the maximum height z of the outflow at a certain R). This would condense the density maps towards lower z, and thus increase the opening angle of the cone features.

Magneto-thermal modelling: As outlined in Sect. 2.3.4, magnetic processes are expected to affect disk evolution in the case of even relatively weak background fields; this has also been illustrated by the recent work of Rodenkirch & Dullemond (2022), who compared gas and dust flows for one protoplanetary disk model for different B_z with and without XEUV photoevporation. Their results highlight that the presence of a non-negligible magnetic field will enhance $\dot{M}_{\rm wind}$, more so for the dust than the gas, and that photoevaporative irradiation enables the (efficient) entrainment of grains with $a \gtrsim 1\,\mu$m.(2)

This suggests that unless a star-forming region is shown to have $\beta \gtrsim 10^7$ (compare Rodenkirch et al., 2020, and Sect. 2.3.4), including MHD modelling is probably unavoidable, especially when tailoring simulations to match specific sources. In combination with accurate vertical transport, FUV irradiation, microphysics, radiation pressure, and considerations as to the charge (distributions) of dust grains, such simulations will most probably be extremely computationally costly; but in order to advance the field of disk winds, they may not be avoidable, at least in the long run (see e.g. Lyra et al., 2019).(3)

Simultaneous gas and dust evolution: The dust trajectories presented and used in this work have been computed using a steady-state gas snapshot; this is a valid approximation since $\dot{M}_{\rm wind}$ stabilises rather quickly (on the order of $t_{\rm eq} \approx 10^3$ yr, see Picogna et al., 2019; Rodenkirch et al., 2020; Rodenkirch & Dullemond, 2022). However, a combined evolution of the gas and dust is computationally possible;(4) it would allow to investigate a potential periodicity of the outflow, which may be caused by insufficient re-supply of dust grains to the wind surface (see Sect. 5.4.3), the dust in the wind changing the temperature and ionisation structure of the photoevaporative outflow (see e.g. Gárate et al., 2019; Kasagi et al., 2022, and Sect. 2.3.3.2), or variability or flares in the stellar $L_{\rm X}$ (see Sect. 2.2.1.5).(5) Due to the very small timescales of the latter two aspects ($t_{\rm flare} \approx 0.1...1$ yr $\ll t_{\rm eq}$, see e.g. Rodriguez et al., 2013), treating

(1) Depending on the grain properties and geometry, as discussed above, this assumption may need to be revised.

(2) Rodenkirch & Dullemond (2022) suggest an analysis of the opening angle of the outflow to discern between their different scenarios; this would be very worthwhile, but may be complicated by the rather small – and probably also model-dependent – differences especially for the better-detectable, smaller grains.

(3) When concocting such a numerical monstrosity, the warning words of Heng (2014) should nonetheless be heeded.

(4) The code base used in this work for evaluating the dust trajectories has been only partly generalised for the case of simultaneous gas evolution.

(5) Normal stellar luminosity evolution should not affect the wind (see e.g. Kunitomo et al., 2020).

them would require either full radiative-transfer modelling for each time step, or at least updates to the temperature structure.

When evolving the gas and dust together, the back-reaction of the latter onto the former could also be incorporated into the simulations. Dipierro et al. (2018) have shown this back-reaction to be non-negligible, but the effect may be reduced depending on how much dust is present at the disk-wind interface, and its height z; this may be a subject for an additional study.

Semi-analytical solutions: The update of the photoevaporation models of Picogna et al. (2019) by Ercolano et al. (2021) as well as the additional parameter ranges introduced by Picogna et al. (2021) mean that dust entrainment could be (updated and) examined at the very least in the parameter space of $(M_*, L_\mathrm{X}, R_\mathrm{disk}, M_\mathrm{disk}, r_\mathrm{gap}, \alpha)$ with the existing set of gas models (and in terms of carbon depletion, too, see Wölfer et al., 2019). However, although the numerical calculations have been optimised and fully parallelised for this work, the computational cost of all of these models would still be enormous.(1)

One option to resolve this would be to sample the grain motion more sparsely; considering that the outflow is quite laminar (see Sects. 3.3.2 and 5.3.1), the incurred error should be low. Furthermore, the application of a Gaussian filter to the resulting dust densities (as already practiced, see Sects. 4.2.1.3 and 5.2.2.2) should smooth out inaccuracies.

A more elegant solution would be to derive semi-analytical descriptions of the dust motion in the wind, based on the gas modelling by Clarke & Alexander (2016) and Sellek et al. (2021),(2) and possibly also integrating the dust delivery prescriptions of Hutchison & Clarke (2021) and Booth & Clarke (2021).(3) Fundamentally, for instance the near-vertical launch of dust grains of all sizes into the wind region which we have seen in Sects. 3.3.2 and 5.3.1 already corresponds quite well to the aforementioned theoretical formulations of the gaseous outflow, leaving in particular the dust motion after decoupling for closer parametrisation.

In conclusion, there are many exciting possibilities to refine the work presented in this thesis, and in the process, acquire new knowledge as to the formation of planets in general, and the Earth in particular.(4)

(1) The code is written in `C`, and uses `MPI`. A re-working of the particle code of Picogna et al. (2018) and its interface with `Pluto` allowed us to have all CPU cores processing an identical number of grains.

(2) As we have seen in Sect. 3.4.2, overly simplified prescriptions for the dust motion are insufficient for our purposes.

(3) An integration of the semi-analytical modelling of MHD winds presented by Lesur (2021) may furthermore allow to produce a fully magneto-thermal wind prescription.

(4) So, if we were to think back to Socrates's 'I think I know nothing' of Chap. 1, the author would be happy to have fooled their audience into thinking that now they do know something, and that they thus have made a small contribution to the evolution of science.

Bibliography

Adams, F. C., & Shu, F. H., 1986, *Infrared Spectra of Rotating Protostars*, in Astrophysical Journal, 308, 836, ADS: 1986ApJ...308..836A

Adams, F. C., Lada, C. J., & Shu, F. H., 1987, *Spectral Evolution of Young Stellar Objects*, in Astrophysical Journal, 312, 788, ADS: 1987ApJ...312..788A

Adams, F. C., Hollenbach, D., Laughlin, G., & Gorti, U., 2004, *Photoevaporation of Circumstellar Disks Due to External Far-Ultraviolet Radiation in Stellar Aggregates*, in Astrophysical Journal, 611, 360, ADS: 2004ApJ...611..360A

Adams, F. C., Proszkow, E. M., Fatuzzo, M., & Myers, P. C., 2006, *Early Evolution of Stellar Groups and Clusters: Environmental Effects on Forming Planetary Systems*, in Astrophysical Journal, 641, 504, ADS: 2006ApJ...641..504A

Akiyama, E., Hashimoto, J., Liu, H. B., Li, J. I.-H., Bonnefoy, M., et al., 2016, *Spiral Structure and Differential Dust Size Distribution in the LKHα 330 Disk*, in Astronomical Journal, 152, 222, ADS: 2016AJ....152..222A

Alcalá, J. M., Manara, C. F., Natta, A., Frasca, A., Testi, L., et al., 2017, *X-shooter spectroscopy of young stellar objects in Lupus. Accretion properties of class II and transitional objects*, in Astronomy & Astrophysics, 600, A20, ADS: 2017A&A...600A..20A

Alcalá, J. M., Manara, C. F., France, K., Schneider, C. P., Arulanantham, N., et al., 2019, *HST spectra reveal accretion in MY Lupi*, in Astronomy & Astrophysics, 629, A108, ADS: 2019A&A...629A.108A

Alexander, R., Pascucci, I., Andrews, S., Armitage, P., & Cieza, L., 2014, *The Dispersal of Protoplanetary Disks*, in Protostars and Planets VI, edited by H. Beuther, R. S. Klessen, C. P. Dullemond, & T. Henning, 475, ADS: 2014prpl.conf..475A

Alexander, R. D., Clarke, C. J., & Pringle, J. E., 2004a, *On the origin of ionizing photons emitted by T Tauri stars*, in Monthly Notes of the Royal Astronomical Society, 348, 879, ADS: 2004MNRAS.348..879A

Alexander, R. D., Clarke, C. J., & Pringle, J. E., 2004b, *The effects of X-ray photoionization and heating on the structure of circumstellar discs*, in Monthly Notes of the Royal Astronomical Society, 354, 71, ADS: 2004MNRAS.354...71A

Alexander, R. D., Clarke, C. J., & Pringle, J. E., 2005, *Constraints on the ionizing flux emitted by T Tauri stars*, in Monthly Notes of the Royal Astronomical Society, 358, 283, ADS: 2005MNRAS.358..283A

Alexander, R. D., Clarke, C. J., & Pringle, J. E., 2006a, *Photoevaporation of protoplanetary discs - I. Hydrodynamic models*, in Monthly Notes of the Royal Astronomical Society, 369, 216, ADS: 2006MNRAS.369..216A

Alexander, R. D., Clarke, C. J., & Pringle, J. E., 2006b, *Photoevaporation of protoplanetary discs - II. Evolutionary models and observable properties*, in Monthly Notes of the Royal Astronomical Society, 369, 229, ADS: 2006MNRAS.369..229A

Alexander, R. D., 2008, *[NeII] emission-line profiles from photoevaporative disc winds*, in Monthly Notes of the Royal Astronomical Society, 391, L64, ADS: 2008MNRAS.391L..64A

Alexander, R. D., & Pascucci, I., 2012, *Deserts and pile-ups in the distribution of exoplanets due to photoevaporative disc clearing*, in Monthly Notes of the Royal Astronomical Society, 422, L82, ADS: 2012MNRAS.422L..82A

Allen, A., Li, Z.-Y., & Shu, F. H., 2003, *Collapse of Magnetized Singular Isothermal Toroids. II. Rotation and Magnetic Braking*, in Astrophysical Journal, 599, 363, ADS: 2003ApJ...599..363A

ALMA Partnership, Brogan, C. L., Pérez, L. M., Hunter, T. R., Dent, W. R. F., et al., 2015, *The 2014 ALMA Long Baseline Campaign: First Results from High Angular Resolution Observations toward the HL Tau Region*, in Astrophysical Journal, 808, L3, ADS: 2015ApJ...808L...3A

Alves, F. O., Cleeves, L. I., Girart, J. M., Zhu, Z., Franco, G. A. P., et al., 2020, *A Case of Simultaneous Star and Planet Formation*, in Astrophysical Journal, 904, L6, ADS: 2020ApJ...904L...6A

Anderson, J. M., Li, Z.-Y., Krasnopolsky, R., & Blandford, R. D., 2003, *Locating the Launching Region* *of T Tauri Winds: The Case of DG Tauri*, in Astrophysical Journal, 590, L107, ADS: 2003ApJ...590L.107A

Andre, P., Ward-Thompson, D., & Barsony, M., 1993, *Submillimeter Continuum Observations of rho Ophiuchi A: The Candidate Protostar VLA 1623 and Prestellar Clumps*, in Astrophysical Journal, 406, 122, ADS: 1993ApJ...406..122A

André, P., Di Francesco, J., Ward-Thompson, D., Inutsuka, S. I., Pudritz, R. E., et al., 2014, *From Filamentary Networks to Dense Cores in Molecular Clouds: Toward a New Paradigm for Star Formation*, in Protostars and Planets VI, edited by H. Beuther, R. S. Klessen, C. P. Dullemond, & T. Henning, 27, ADS: 2014prpl.conf...27A

Andrews, S. M., & Williams, J. P., 2005, *Circumstellar Dust Disks in Taurus-Auriga: The Submillimeter Perspective*, in Astrophysical Journal, 631, 1134, ADS: 2005ApJ...631.1134A

Andrews, S. M., & Williams, J. P., 2007a, *High-Resolution Submillimeter Constraints on Circumstellar Disk Structure*, in Astrophysical Journal, 659, 705, ADS: 2007ApJ...659..705A

Andrews, S. M., & Williams, J. P., 2007b, *A Submillimeter View of Circumstellar Dust Disks in ρ Ophiuchi*, in Astrophysical Journal, 671, 1800, ADS: 2007ApJ...671.1800A

Andrews, S. M., Wilner, D. J., Hughes, A. M., Qi, C., & Dullemond, C. P., 2009, *Protoplanetary Disk Structures in Ophiuchus*, in Astrophysical Journal, 700, 1502, ADS: 2009ApJ...700.1502A

Andrews, S. M., Wilner, D. J., Hughes, A. M., Qi, C., & Dullemond, C. P., 2010, *Protoplanetary Disk Structures in Ophiuchus. II. Extension to Fainter Sources*, in Astrophysical Journal, 723, 1241, ADS: 2010ApJ...723.1241A

Andrews, S. M., 2015, *Observations of Solids in Protoplanetary Disks*, in Publications of the Astronomical Society of the Pacific, 127, 961, ADS: 2015PASP..127..961A

Andrews, S. M., Wilner, D. J., Zhu, Z., Birnstiel, T., Carpenter, J. M., et al., 2016, *Ringed Substructure and a Gap at 1 au in the Nearest Protoplanetary Disk*, in Astrophysical Journal, 820, L40, ADS: 2016ApJ...820L..40A

Andrews, S. M., Terrell, M., Tripathi, A., Ansdell, M., Williams, J. P., et al., 2018a, *Scaling Relations Associated with Millimeter Continuum Sizes in Protoplanetary Disks*, in Astrophysical Journal, 865, 157, ADS: 2018ApJ...865..157A

Andrews, S. M., Huang, J., Pérez, L. M., Isella, A., Dullemond, C. P., et al., 2018b, *The Disk Substructures at High Angular Resolution Project (DSHARP). I. Motivation, Sample, Calibration, and Overview*, in Astrophysical Journal, 869, L41, ADS: 2018ApJ...869L..41A

Andrews, S. M., 2020, *Observations of Protoplanetary Disk Structures*, in Annual Review of Astronomy and Astrophysics, 58, 483, ADS: 2020ARA&A..58..483A

Ansdell, M., Williams, J. P., van der Marel, N., Carpenter, J. M., Guidi, G., et al., 2016, *ALMA Survey of Lupus Protoplanetary Disks. I. Dust and Gas Masses*, in Astrophysical Journal, 828, 46, ADS: 2016ApJ...828...46A

Ansdell, M., Williams, J. P., Manara, C. F., Miotello, A., Facchini, S., et al., 2017, *An ALMA Survey of Protoplanetary Disks in the σ Orionis Cluster*, in Astronomical Journal, 153, 240, ADS: 2017AJ....153..240A

Ansdell, M., Williams, J. P., Trapman, L., van Terwisga, S. E., Facchini, S., et al., 2018, *ALMA Survey of Lupus Protoplanetary Disks. II. Gas Disk Radii*, in Astrophysical Journal, 859, 21, ADS: 2018ApJ...859...21A

Appenzeller, I., Oestreicher, R., & Jankovics, I., 1984, *Forbidden-line profiles of T Tauri stars.*, in Astronomy & Astrophysics, 141, 108, ADS: 1984A&A...141..108A

Arai, T., Kobayashi, M., Ishibashi, K., Yoshida, F., Kimura, H., et al., 2018, *DESTINY+ Mission: Flyby of Geminids Parent Asteroid (3200) Phaethon and In-Situ Analyses of Dust Accreting on the Earth*, in 49th Annual Lunar and Planetary Science Conference, Lunar and Planetary Science Conference, 2570, ADS: 2018LPI....49.2570A

Armitage, P. J., & Hansen, B. M. S., 1999, *Early planet formation as a trigger for further planet formation*, in Nature, 402, 633, ADS: 1999Natur.402..633A

Armitage, P. J., & Bonnell, I. A., 2002, *The brown dwarf desert as a consequence of orbital migration*, in Monthly Notes of the Royal Astronomical Society, 330, L11, ADS: 2002MNRAS.330L..11A

Armitage, P. J., 2010, *Astrophysics of Planet Formation*, Cambridge University Press, ADS: 2010apf..book.....A

Armitage, P. J., 2011, *Dynamics of Protoplanetary Disks*, in Annual Review of Astronomy and Astrophysics, 49, 195, ADS: 2011ARA&A..49..195A

Armitage, P. J., Simon, J. B., & Martin, R. G., 2013, *Two Timescale Dispersal of Magnetized Protoplanetary Disks*, in Astrophysical Journal, 778, L14, ADS: 2013ApJ...778L..14A

Armitage, P. J., 2015, *Physical processes in protoplanetary disks*, in arXiv e-prints, arXiv: 1509.06382

Armitage, P. J., 2018, *A Brief Overview of Planet Formation*, in *Handbook of Exoplanets*, edited by H. J. Deeg & J. A. Belmonte, Springer International Publishing, 2185–2203, ADS: 2018haex.bookE.135A

Arrhenius, S., 1897, *On the Influence of Carbonic Acid in the Air upon the Temperature of the Earth*, in Publications of the Astronomical Society of the Pacific, 9, 14, ADS: 1897PASP....9...14A

Artymowicz, P., & Lubow, S. H., 1994, *Dynamics of Binary-Disk Interaction. I. Resonances and Disk Gap Sizes*, in Astrophysical Journal, 421, 651, ADS: 1994ApJ...421..651A

Asplund, M., Grevesse, N., Sauval, A. J., & Scott, P., 2009, *The Chemical Composition of the Sun*, in Annual Review of Astronomy and Astrophysics, 47, 481, ADS: 2009ARA&A..47..481A

Audard, M., Ábrahám, P., Dunham, M. M., Green, J. D., Grosso, N., et al., 2014, *Episodic Accretion in Young Stars*, in Protostars and Planets VI, edited by H. Beuther, R. S. Klessen, C. P. Dullemond, & T. Henning, 387, ADS: 2014prpl.conf..387A

Avenhaus, H., Quanz, S. P., Meyer, M. R., Brittain, S. D., Carr, J. S., et al., 2014, *HD100546 Multi-epoch Scattered Light Observations*, in Astrophysical Journal, 790, 56, ADS: 2014ApJ...790...56A

Avenhaus, H., Quanz, S. P., Schmid, H. M., Dominik, C., Stolker, T., et al., 2017, *Exploring Dust around HD 142527 down to 0.″025 (4 au) Using SPHERE/ZIMPOL*, in Astronomical Journal, 154, 33, ADS: 2017AJ....154...33A

Avenhaus, H., Quanz, S. P., Garufi, A., Perez, S., Casassus, S., et al., 2018, *Disks around T Tauri Stars with SPHERE (DARTTS-S). I. SPHERE/IRDIS Polarimetric Imaging of Eight Prominent T Tauri Disks*, in Astrophysical Journal, 863, 44, ADS: 2018ApJ...863...44A

Ayliffe, B. A., Laibe, G., Price, D. J., & Bate, M. R., 2012, *On the accumulation of planetesimals near disc gaps created by protoplanets*, in Monthly Notes of the Royal Astronomical Society, 423, 1450, ADS: 2012MNRAS.423.1450A

Bai, X.-N., & Stone, J. M., 2010, *Dynamics of Solids in the Midplane of Protoplanetary Disks: Implications for Planetesimal Formation*, in Astrophysical Journal, 722, 1437, ADS: 2010ApJ...722.1437B

Bai, X.-N., & Stone, J. M., 2011, *Effect of Ambipolar Diffusion on the Nonlinear Evolution of Magnetorotational Instability in Weakly Ionized Disks*, in Astrophysical Journal, 736, 144, ADS: 2011ApJ...736..144B

Bai, X.-N., 2011a, *Magnetorotational-instability-driven Accretion in Protoplanetary Disks*, in Astrophysical Journal, 739, 50, ADS: 2011ApJ...739...50B

Bai, X.-N., 2011b, *The Role of Tiny Grains on the Accretion Process in Protoplanetary Disks*, in Astrophysical Journal, 739, 51, ADS: 2011ApJ...739...51B

Bai, X.-N., & Stone, J. M., 2013, *Wind-driven Accretion in Protoplanetary Disks. I. Suppression of the Magnetorotational Instability and Launching of the Magnetocentrifugal Wind*, in Astrophysical Journal, 769, 76, ADS: 2013ApJ...769...76B

Bai, X.-N., Ye, J., Goodman, J., & Yuan, F., 2016, *Magneto-thermal Disk Winds from Protoplanetary Disks*, in Astrophysical Journal, 818, 152, ADS: 2016ApJ...818..152B

Bai, X.-N., 2016, *Towards a Global Evolutionary Model of Protoplanetary Disks*, in Astrophysical Journal, 821, 80, ADS: 2016ApJ...821...80B

Bai, X.-N., 2017, *Global Simulations of the Inner Regions of Protoplanetary Disks with Comprehensive Disk Microphysics*, in Astrophysical Journal, 845, 75, ADS: 2017ApJ...845...75B

Balbus, S. A., & Hawley, J. F., 1991, *A Powerful Local Shear Instability in Weakly Magnetized Disks. I. Linear Analysis*, in Astrophysical Journal, 376, 214, ADS: 1991ApJ...376..214B

Banzatti, A., Pascucci, I., Edwards, S., Fang, M., Gorti, U., et al., 2019, *Kinematic Links and the Coevolution of MHD Winds, Jets, and Inner Disks from a High-resolution Optical [O I] Survey*, in Astrophysical Journal, 870, 76, ADS: 2019ApJ...870...76B

Banzatti, A., Abernathy, K. M., Brittain, S., Bosman, A. D., Pontoppidan, K. M., et al., 2022, *Scanning disk rings and winds in CO at 0.01-10 au: a high-resolution M-band spectroscopy survey with IRTF-iSHELL*, in arXiv e-prints, arXiv: 2202.03438

Baruteau, C., Crida, A., Paardekooper, S. J., Masset, F., Guilet, J., et al., 2014, *Planet-Disk Interactions and Early Evolution of Planetary Systems*, in Protostars and Planets VI, edited by H. Beuther, R. S. Klessen, C. P. Dullemond, & T. Henning, 667, ADS: 2014prpl.conf..667B

Basri, G., & Bertout, C., 1993, *T-Tauri Stars and Their Accretion Disks*, in Protostars and Planets III, edited by E. H. Levy & J. I. Lunine, 543, ADS: 1993prpl.conf..543B

Bate, M. R., 2018, *On the diversity and statistical properties of protostellar discs*, in Monthly Notes of the Royal Astronomical Society, 475, 5618, ADS: 2018MNRAS.475.5618B

Bayo, A., Barrado, D., Huélamo, N., Morales-Calderón, M., Melo, C., et al., 2012, *Spectroscopy of very low-mass stars and brown dwarfs in the Lambda Orionis star-forming region. II. Rotation, activity and* *other properties of spectroscopically confirmed members of Collinder 69*, in Astronomy & Astrophysics, 547, A80, ADS: 2012A&A...547A..80B

Beckwith, S., Zuckerman, B., Skrutskie, M. F., & Dyck, H. M., 1984, *Discovery of solar system size halos around young stars.*, in Astrophysical Journal, 287, 793, ADS: 1984ApJ...287..793B

Beckwith, S. V. W., & Sargent, A. I., 1993, *The Occurrence and Properties of Disks around Young Stars*, in Protostars and Planets III, edited by E. H. Levy & J. I. Lunine, 521, ADS: 1993prpl.conf..521B

Beichman, C. A., Krist, J., Trauger, J. T., Greene, T., Oppenheimer, B., et al., 2010, *Imaging Young Giant Planets From Ground and Space*, in Publications of the Astronomical Society of the Pacific, 122, 162, ADS: 2010PASP..122..162B

Benisty, M., Tatulli, E., Ménard, F., & Swain, M. R., 2010, *The complex structure of the disk around HD 100546. The inner few astronomical units*, in Astronomy & Astrophysics, 511, A75, ADS: 2010A&A...511A..75B

Benisty, M., Stolker, T., Pohl, A., de Boer, J., Lesur, G., et al., 2017, *Shadows and spirals in the protoplanetary disk HD 100453*, in Astronomy & Astrophysics, 597, A42, ADS: 2017A&A...597A..42B

Benisty, M., Bae, J., Facchini, S., Keppler, M., Teague, R., et al., 2021, *A Circumplanetary Disk around PDS70c*, in Astrophysical Journal, 916, L2, ADS: 2021ApJ...916L...2B

Benz, W., Ida, S., Alibert, Y., Lin, D., & Mordasini, C., 2014, *Planet Population Synthesis*, in Protostars and Planets VI, edited by H. Beuther, R. S. Klessen, C. P. Dullemond, & T. Henning, 691, ADS: 2014prpl.conf..691B

Bergin, E. A., Cleeves, L. I., Gorti, U., Zhang, K., Blake, G. A., et al., 2013, *An old disk still capable of forming a planetary system*, in Nature, 493, 644, ADS: 2013Natur.493..644B

Bergin, E. A., & Williams, J. P., 2018, *The determination of protoplanetary disk masses*, in arXiv e-prints, arXiv: 1807.09631

Bertrang, G. H. M., Avenhaus, H., Casassus, S., Montesinos, M., Kirchschlager, F., et al., 2018, *HD 169142 in the eyes of ZIMPOL/SPHERE*, in Monthly Notes of the Royal Astronomical Society, 474, 5105, ADS: 2018MNRAS.474.5105B

Béthune, W., Lesur, G., & Ferreira, J., 2017, *Global simulations of protoplanetary disks with net magnetic flux. I. Non-ideal MHD case*, in Astronomy & Astrophysics, 600, A75, ADS: 2017A&A...600A..75B

Béthune, W., & Latter, H., 2020, *Electric heating and angular momentum transport in laminar models of protoplanetary discs*, in Monthly Notes of the Royal Astronomical Society, 494, 6103, ADS: 2020MNRAS.494.6103B

Beuzit, J. L., Vigan, A., Mouillet, D., Dohlen, K., Gratton, R., et al., 2019, *SPHERE: the exoplanet imager for the Very Large Telescope*, in Astronomy & Astrophysics, 631, A155, ADS: 2019A&A...631A.155B

Bhatt, H., Pandey, J. C., Singh, K. P., Sagar, R., & Kumar, B., 2013, *X-ray Observations of Eight Young Open Star Clusters: I. Membership and X-ray Luminosity*, in Journal of Astrophysics and Astronomy, 34, 393, ADS: 2013JApA...34..393B

Bi, J., & Fung, J., 2022, *Dust Dynamics in Transitional Disks: Clumping and Disk Recession*, in arXiv e-prints, arXiv: 2202.02328

Binkert, F., Szulágyi, J., & Birnstiel, T., 2021, *First 3D grid-based gas-dust simulations of circumstellar discs with an embedded planet*, in Monthly Notes of the Royal Astronomical Society, 506, 5969, ADS: 2021MNRAS.506.5969B

Birnstiel, T., Dullemond, C. P., & Brauer, F., 2009, *Dust retention in protoplanetary disks*, in Astronomy & Astrophysics, 503, L5, ADS: 2009A&A...503L...5B

Birnstiel, T., Dullemond, C. P., & Brauer, F., 2010, *Gas- and dust evolution in protoplanetary disks*, in Astronomy & Astrophysics, 513, A79, ADS: 2010A&A...513A..79B

Birnstiel, T., Ormel, C. W., & Dullemond, C. P., 2011, *Dust size distributions in coagulation/fragmentation equilibrium: numerical solutions and analytical fits*, in Astronomy & Astrophysics, 525, A11, ADS: 2011A&A...525A..11B

Birnstiel, T., Klahr, H., & Ercolano, B., 2012a, *A simple model for the evolution of the dust population in protoplanetary disks*, in Astronomy & Astrophysics, 539, A148, ADS: 2012A&A...539A.148B

Birnstiel, T., Andrews, S. M., & Ercolano, B., 2012b, *Can grain growth explain transition disks?*, in Astronomy & Astrophysics, 544, A79, ADS: 2012A&A...544A..79B

Birnstiel, T., & Andrews, S. M., 2014, *On the Outer Edges of Protoplanetary Dust Disks*, in Astrophysical Journal, 780, 153, ADS: 2014ApJ...780..153B

Birnstiel, T., Fang, M., & Johansen, A., 2016, *Dust Evolution and the Formation of Planetesimals*, in Space Science Reviews, 205, 41, ADS: 2016SSRv..205...41B

Birnstiel, T., Dullemond, C. P., Zhu, Z., Andrews, S. M., Bai, X.-N., et al., 2018, *The Disk Substructures* *at High Angular Resolution Project (DSHARP). V. Interpreting ALMA Maps of Protoplanetary Disks in Terms of a Dust Model*, in Astrophysical Journal, 869, L45, ADS: `2018ApJ...869L..45B`

Bitsch, B., Johansen, A., Lambrechts, M., & Morbidelli, A., 2015, *The structure of protoplanetary discs around evolving young stars*, in Astronomy & Astrophysics, 575, A28, ADS: `2015A&A...575A..28B`

Blandford, R. D., & Payne, D. G., 1982, *Hydromagnetic flows from accretion disks and the production of radio jets.*, in Monthly Notes of the Royal Astronomical Society, 199, 883, ADS: `1982MNRAS.199..883B`

Blitz, L., 1993, *Giant Molecular Clouds*, in Protostars and Planets III, edited by E. H. Levy & J. I. Lunine, 125, ADS: `1993prpl.conf..125B`

Blum, J., & Wurm, G., 2008, *The growth mechanisms of macroscopic bodies in protoplanetary disks.*, in Annual Review of Astronomy and Astrophysics, 46, 21, ADS: `2008ARA&A..46...21B`

Boccaletti, A., Abe, L., Baudrand, J., Daban, J.-B., Douet, R., et al., 2008, *Prototyping coronagraphs for exoplanet characterization with SPHERE*, in Society of Photo-Optical Instrumentation Engineers (SPIE) Conference Series, Vol. 7015, Adaptive Optics Systems, edited by N. Hubin, C. E. Max, & P. L. Wizinowich, 70151B, ADS: `2008SPIE.7015E..1BB`

Boehler, Y., Dutrey, A., Guilloteau, S., & Piétu, V., 2013, *Probing dust settling in proto-planetary discs with ALMA*, in Monthly Notes of the Royal Astronomical Society, 431, 1573, ADS: `2013MNRAS.431.1573B`

Bohlin, R. C., Savage, B. D., & Drake, J. F., 1978, *A survey of interstellar H I from Lα absorption measurements. II.*, in Astrophysical Journal, 224, 132, ADS: `1978ApJ...224..132B`

Booth, R. A., & Ilee, J. D., 2019, *Planet-forming material in a protoplanetary disc: the interplay between chemical evolution and pebble drift*, in Monthly Notes of the Royal Astronomical Society, 487, 3998, ADS: `2019MNRAS.487.3998B`

Booth, R. A., & Clarke, C. J., 2021, *Modelling the delivery of dust from discs to ionized winds*, in Monthly Notes of the Royal Astronomical Society, 502, 1569, ADS: `2021MNRAS.502.1569B`

Borucki, W. J., Koch, D., Basri, G., Batalha, N., Brown, T., et al., 2010, *Kepler Planet-Detection Mission: Introduction and First Results*, in Science, 327, 977, ADS: `2010Sci...327..977B`

Bozhinova, I., Scholz, A., Costigan, G., Lux, O., Davis, C. J., et al., 2016, *The disappearing act: a dusty wind eclipsing RW Aur*, in Monthly Notes of the Royal Astronomical Society, 463, 4459, ADS: `2016MNRAS.463.4459B`

Brauer, F., Dullemond, C. P., & Henning, T., 2008a, *Coagulation, fragmentation and radial motion of solid particles in protoplanetary disks*, in Astronomy & Astrophysics, 480, 859, ADS: `2008A&A...480..859B`

Brauer, F., Henning, T., & Dullemond, C. P., 2008b, *Planetesimal formation near the snow line in MRI-driven turbulent protoplanetary disks*, in Astronomy & Astrophysics, 487, L1, ADS: `2008A&A...487L...1B`

Bruno, G., 1584, *De l'infinito universo et Mondi*

Burrows, C. J., Stapelfeldt, K. R., Watson, A. M., Krist, J. E., Ballester, G. E., et al., 1996, *Hubble Space Telescope Observations of the Disk and Jet of HH 30*, in Astrophysical Journal, 473, 437, ADS: `1996ApJ...473..437B`

Cabrit, S., Edwards, S., Strom, S. E., & Strom, K. M., 1990, *Forbidden-Line Emission and Infrared Excesses in T Tauri Stars: Evidence for Accretion-driven Mass Loss?*, in Astrophysical Journal, 354, 687, ADS: `1990ApJ...354..687C`

Cabrit, S., 2007, *The accretion-ejection connexion in T Tauri stars: jet models vs. observations*, in Star-Disk Interaction in Young Stars, edited by J. Bouvier & I. Appenzeller, Vol. 243, 203–214, ADS: `2007IAUS..243..203C`

Callendar, G. S., 1938, *The artificial production of carbon dioxide and its influence on temperature*, in Quarterly Journal of the Royal Meteorological Society, 64, 223, ADS: `1938QJRMS..64..223C`

Calvet, N., & Gullbring, E., 1998, *The Structure and Emission of the Accretion Shock in T Tauri Stars*, in Astrophysical Journal, 509, 802, ADS: `1998ApJ...509..802C`

Calvet, N., Muzerolle, J., Briceño, C., Hernández, J., Hartmann, L., et al., 2004, *The Mass Accretion Rates of Intermediate-Mass T Tauri Stars*, in Astronomical Journal, 128, 1294, ADS: `2004AJ....128.1294C`

Campbell, B., Walker, G. A. H., & Yang, S., 1988, *A Search for Substellar Companions to Solar-type Stars*, in Astrophysical Journal, 331, 902, ADS: `1988ApJ...331..902C`

Canovas, H., Ménard, F., de Boer, J., Pinte, C., Avenhaus, H., et al., 2015, *Nonazimuthal linear polarization in protoplanetary disks*, in Astronomy & Astrophysics, 582, L7, ADS: `2015A&A...582L...7C`

Carrera, D., Gorti, U., Johansen, A., & Davies, M. B., 2017, *Planetesimal Formation by the Streaming Instability in a Photoevaporating Disk*, in Astrophysical Journal, 839, 16, ADS: `2017ApJ...839...16C`

Carroll, S. M., 2019, *Beyond Falsifiability: Normal Science in a Multiverse*, in *Why Trust a Theory? – Epistemology of Fundamental Physics*, edited by R. Dardashti, R. Dawid, & K. Thébault, Cambridge University Press, ADS: 2018arXiv180105016C

Casassus, S., van der Plas, G. M., Perez, S., Dent, W. R. F., Fomalont, E., et al., 2013, *Flows of gas through a protoplanetary gap*, in Nature, 493, 191, ADS: 2013Natur.493..191C

Casassus, S., Wright, C. M., Marino, S., Maddison, S. T., Wootten, A., et al., 2015, *A Compact Concentration of Large Grains in the HD 142527 Protoplanetary Dust Trap*, in Astrophysical Journal, 812, 126, ADS: 2015ApJ...812..126C

Casassus, S., 2016, *Resolved Observations of Transition Disks*, in Publications of the Astronomical Society of Australia, 33, e013, ADS: 2016PASA...33...13C

Casassus, S., Avenhaus, H., Pérez, S., Navarro, V., Cárcamo, M., et al., 2018, *An inner warp in the DoAr 44 T Tauri transition disc*, in Monthly Notes of the Royal Astronomical Society, 477, 5104, ADS: 2018MNRAS.477.5104C

Casassus, S., Christiaens, V., Cárcamo, M., Pérez, S., Weber, P., et al., 2021, *A dusty filament and turbulent CO spirals in HD 135344B - SAO 206462*, in Monthly Notes of the Royal Astronomical Society, 507, 3789, ADS: 2021MNRAS.507.3789C

Cassan, A., Kubas, D., Beaulieu, J. P., Dominik, M., Horne, K., et al., 2012, *One or more bound planets per Milky Way star from microlensing observations*, in Nature, 481, 167, ADS: 2012Natur.481..167C

Chacón-Tanarro, A., Pineda, J. E., Caselli, P., Bizzocchi, L., Gutermuth, R. A., et al., 2019, *Dust opacity variations in the pre-stellar core L1544*, in Astronomy & Astrophysics, 623, A118, ADS: 2019A&A...623A.118C

Charnoz, S., Fouchet, L., Aleon, J., & Moreira, M., 2011, *Three-dimensional Lagrangian Turbulent Diffusion of Dust Grains in a Protoplanetary Disk: Method and First Applications*, in Astrophysical Journal, 737, 33, ADS: 2011ApJ...737...33C

Chatterjee, S., & Tan, J. C., 2014, *Inside-out Planet Formation*, in Astrophysical Journal, 780, 53, ADS: 2014ApJ...780...53C

Chiang, E., & Murray-Clay, R., 2007, *Inside-out evacuation of transitional protoplanetary discs by the magneto-rotational instability*, in Nature Physics, 3, 604, ADS: 2007NatPh...3..604C

Cieza, L. A., Casassus, S., Tobin, J., Bos, S. P., Williams, J. P., et al., 2016, *Imaging the water snow-line during a protostellar outburst*, in Nature, 535, 258, ADS: 2016Natur.535..258C

Clarke, C. J., Gendrin, A., & Sotomayor, M., 2001, *The dispersal of circumstellar discs: the role of the ultraviolet switch*, in Monthly Notes of the Royal Astronomical Society, 328, 485, ADS: 2001MNRAS.328..485C

Clarke, C. J., & Pringle, J. E., 2006, *The $\dot{M} - M$ relationship in pre-main sequence stars*, in Monthly Notes of the Royal Astronomical Society, 370, L10, ADS: 2006MNRAS.370L..10C

Clarke, C. J., 2007, *The photoevaporation of discs around young stars in massive clusters*, in Monthly Notes of the Royal Astronomical Society, 376, 1350, ADS: 2007MNRAS.376.1350C

Clarke, C. J., & Owen, J. E., 2013, *Evolutionary constraints on the planetary hypothesis for transition discs.*, in Monthly Notes of the Royal Astronomical Society, 433, L69, ADS: 2013MNRAS.433L..69C

Clarke, C. J., & Alexander, R. D., 2016, *A self-similar solution for thermal disc winds*, in Monthly Notes of the Royal Astronomical Society, 460, 3044, ADS: 2016MNRAS.460.3044C

Cleeves, L. I., Öberg, K. I., Wilner, D. J., Huang, J., Loomis, R. A., et al., 2016, *The Coupled Physical Structure of Gas and Dust in the IM Lup Protoplanetary Disk*, in Astrophysical Journal, 832, 110, ADS: 2016ApJ...832..110C

Coutens, A., Liu, H. B., Jiménez-Serra, I., Bourke, T. L., Forbrich, J., et al., 2019, *VLA cm-wave survey of young stellar objects in the Oph A cluster: constraining extreme UV- and X-ray-driven disk photoevaporation. A pathfinder for Square Kilometre Array studies*, in Astronomy & Astrophysics, 631, A58, ADS: 2019A&A...631A..58C

Cugno, G., Quanz, S. P., Hunziker, S., Stolker, T., Schmid, H. M., et al., 2019, *A search for accreting young companions embedded in circumstellar disks. High-contrast Hα imaging with VLT/SPHERE*, in Astronomy & Astrophysics, 622, A156, ADS: 2019A&A...622A.156C

Currie, T., & Sicilia-Aguilar, A., 2011, *The Transitional Protoplanetary Disk Frequency as a Function of Age: Disk Evolution In the Coronet Cluster, Taurus, and Other 1-8 Myr Old Regions*, in Astrophysical Journal, 732, 24, ADS: 2011ApJ...732...24C

Currie, T., Rodigas, T. J., Debes, J., Plavchan, P., Kuchner, M., et al., 2012, *Keck/NIRC2 Imaging of the Warped, Asymmetric Debris Disk around HD 32297*, in Astrophysical Journal, 757, 28, ADS: 2012ApJ...757...28C

Cuzzi, J. N., Dobrovolskis, A. R., & Champney, J. M., 1993, *Particle-Gas Dynamics in the Midplane of*

a Protoplanetary Nebula, in Icarus, 106, 102, ADS: 1993Icar..106..102C
Dainotti, M. G., De Simone, B., Schiavone, T., Montani, G., Rinaldi, E., et al., 2021, *On the Hubble Constant Tension in the SNe Ia Pantheon Sample*, in Astrophysical Journal, 912, 150, ADS: 2021ApJ...912..150D
D'Alessio, P., Hartmann, L., Calvet, N., Franco-Hernández, R., Forrest, W. J., et al., 2005, *The Truncated Disk of CoKu Tau/4*, in Astrophysical Journal, 621, 461, ADS: 2005ApJ...621..461D
Dartois, E., Dutrey, A., & Guilloteau, S., 2003, *Structure of the DM Tau Outer Disk: Probing the vertical kinetic temperature gradient*, in Astronomy & Astrophysics, 399, 773, ADS: 2003A&A...399..773D
de Boer, J., Salter, G., Benisty, M., Vigan, A., Boccaletti, A., et al., 2016, *Multiple rings in the transition disk and companion candidates around RX J1615.3-3255. High contrast imaging with VLT/SPHERE*, in Astronomy & Astrophysics, 595, A114, ADS: 2016A&A...595A.114D
de Boer, J., Girard, J. H., Canovas, H., Min, M., Sitko, M., et al., 2017, *BP Piscium: its flaring disc imaged with SPHERE/ZIMPOL*★, in Monthly Notes of the Royal Astronomical Society, 466, L7, ADS: 2017MNRAS.466L...7D
Dehant, V., Debaille, V., Dobos, V., Gaillard, F., Gillmann, C., et al., 2019, *Geoscience for Understanding Habitability in the Solar System and Beyond*, in Space Science Reviews, 215, 42, ADS: 2019SSRv..215...42D
Demtröder, W., 2006, *Experimentalphysik 1*, 4th edn., Springer, ADS: 2006exp1.book.....D
Desch, S. J., 2007, *Mass Distribution and Planet Formation in the Solar Nebula*, in Astrophysical Journal, 671, 878, ADS: 2007ApJ...671..878D
Dipierro, G., & Laibe, G., 2017, *An opening criterion for dust gaps in protoplanetary discs*, in Monthly Notes of the Royal Astronomical Society, 469, 1932, ADS: 2017MNRAS.469.1932D
Dipierro, G., Laibe, G., Alexander, R., & Hutchison, M., 2018, *Gas and multispecies dust dynamics in viscous protoplanetary discs: the importance of the dust back-reaction*, in Monthly Notes of the Royal Astronomical Society, 479, 4187, ADS: 2018MNRAS.479.4187D
Disk Dynamics Collaboration, Armitage, P. J., Bae, J., Benisty, M., Bergin, E. A., et al., 2020, *Visualizing the Kinematics of Planet Formation*, in arXiv e-prints, arXiv: 2009.04345
Dodin, A., Grankin, K., Lamzin, S., Nadjip, A., Safonov, B., et al., 2019, *Analysis of colour and polarimetric variability of RW Aur A in 2010-2018*, in Monthly Notes of the Royal Astronomical Society, 482, 5524, ADS: 2019MNRAS.482.5524D
Doi, K., & Kataoka, A., 2021, *Estimate on Dust Scale Height from the ALMA Dust Continuum Image of the HD 163296 Protoplanetary Disk*, in Astrophysical Journal, 912, 164, ADS: 2021ApJ...912..164D
Dominik, C., & Dullemond, C. P., 2011, *Accretion through the inner hole of transitional disks: what happens to the dust?*, in Astronomy & Astrophysics, 531, A101, ADS: 2011A&A...531A.101D
Draine, B. T., 2003a, *Interstellar Dust Grains*, in Annual Review of Astronomy and Astrophysics, 41, 241, ADS: 2003ARA&A..41..241D
Draine, B. T., 2003b, *Scattering by Interstellar Dust Grains. II. X-Rays*, in Astrophysical Journal, 598, 1026, ADS: 2003ApJ...598.1026D
Drake, J. J., Ercolano, B., Flaccomio, E., & Micela, G., 2009, *X-ray Photoevaporation-Starved T Tauri Accretion*, in Astrophysical Journal, 699, L35, ADS: 2009ApJ...699L..35D
Drążkowska, J., & Alibert, Y., 2017, *Planetesimal formation starts at the snow line*, in Astronomy & Astrophysics, 608, A92, ADS: 2017A&A...608A..92D
Drążkowska, J., & Dullemond, C. P., 2018, *Planetesimal formation during protoplanetary disk buildup*, in Astronomy & Astrophysics, 614, A62, ADS: 2018A&A...614A..62D
Drążkowska, J., Li, S., Birnstiel, T., Stammler, S. M., & Li, H., 2019, *Including Dust Coagulation in Hydrodynamic Models of Protoplanetary Disks: Dust Evolution in the Vicinity of a Jupiter-mass Planet*, in Astrophysical Journal, 885, 91, ADS: 2019ApJ...885...91D
Drążkowska, J., Stammler, S. M., & Birnstiel, T., 2021, *How dust fragmentation may be beneficial to planetary growth by pebble accretion*, in Astronomy & Astrophysics, 647, A15, ADS: 2021A&A...647A..15D
Duchêne, G., Ménard, F., Stapelfeldt, K., & Duvert, G., 2003, *A layered edge-on circumstellar disk around HK Tau B*, in Astronomy & Astrophysics, 400, 559, ADS: 2003A&A...400..559D
Duchêne, G., & Kraus, A., 2013, *Stellar Multiplicity*, in Annual Review of Astronomy and Astrophysics, 51, 269, ADS: 2013ARA&A..51..269D
Dullemond, C. P., 2002, *The 2-D structure of dusty disks around Herbig Ae/Be stars. I. Models with grey opacities*, in Astronomy & Astrophysics, 395, 853, ADS: 2002A&A...395..853D
Dullemond, C. P., & Dominik, C., 2004, *The effect of dust settling on the appearance of protoplanetary disks*, in Astronomy & Astrophysics, 421, 1075, ADS: 2004A&A...421.1075D

Dullemond, C. P., & Dominik, C., 2005, *Dust coagulation in protoplanetary disks: A rapid depletion of small grains*, in Astronomy & Astrophysics, 434, 971, ADS: `2005A&A...434..971D`

Dullemond, C. P., Hollenbach, D., Kamp, I., & D'Alessio, P., 2007, *Models of the Structure and Evolution of Protoplanetary Disks*, in Protostars and Planets V, edited by B. Reipurth, D. Jewitt, & K. Keil, 555, ADS: `2007prpl.conf..555D`

Dullemond, C. P., Juhasz, A., Pohl, A., Sereshti, F., Shetty, R., et al., 2012, *RADMC-3D: A multi-purpose radiative transfer tool*, ADS: `2012ascl.soft02015D`

Dullemond, C. P., Birnstiel, T., Huang, J., Kurtovic, N. T., Andrews, S. M., et al., 2018, *The Disk Substructures at High Angular Resolution Project (DSHARP). VI. Dust Trapping in Thin-ringed Protoplanetary Disks*, in Astrophysical Journal, 869, L46, ADS: `2018ApJ...869L..46D`

Dullemond, C. P., & Birnstiel, T., in prep., *disklab: A protoplanetary disk modeling package in Python*

Dutrey, A., Guilloteau, S., & Ho, P., 2007, *Interferometric Spectroimaging of Molecular Gas in Protoplanetary Disks*, in Protostars and Planets V, edited by B. Reipurth, D. Jewitt, & K. Keil, 495, ADS: `2007prpl.conf..495D`

Dutrey, A., Guilloteau, S., Piétu, V., Chapillon, E., Wakelam, V., et al., 2017, *The Flying Saucer: Tomography of the thermal and density gas structure of an edge-on protoplanetary disk*, in Astronomy & Astrophysics, 607, A130, ADS: `2017A&A...607A.130D`

Edwards, S., Cabrit, S., Strom, S. E., Heyer, I., Strom, K. M., et al., 1987, *Forbidden Line and H alpha Profiles in T Tauri Star Spectra: A Probe of Anisotropic Mass Outflows and Circumstellar Disks*, in Astrophysical Journal, 321, 473, ADS: `1987ApJ...321..473E`

Emsenhuber, A., Mordasini, C., Burn, R., Alibert, Y., Benz, W., et al., 2021a, *The New Generation Planetary Population Synthesis (NGPPS). I. Bern global model of planet formation and evolution, model tests, and emerging planetary systems*, in Astronomy & Astrophysics, 656, A69, ADS: `2021A&A...656A..69E`

Emsenhuber, A., Mordasini, C., Burn, R., Alibert, Y., Benz, W., et al., 2021b, *The New Generation Planetary Population Synthesis (NGPPS). II. Planetary population of solar-like stars and overview of statistical results*, in Astronomy & Astrophysics, 656, A70, ADS: `2021A&A...656A..70E`

Epstein, P. S., 1924, *On the Resistance Experienced by Spheres in their Motion through Gases*, in Physical Review, 23, 710, ADS: `1924PhRv...23..710E`

Ercolano, B., Barlow, M. J., Storey, P. J., & Liu, X. W., 2003, *MOCASSIN: a fully three-dimensional Monte Carlo photoionization code*, in Monthly Notes of the Royal Astronomical Society, 340, 1136, ADS: `2003MNRAS.340.1136E`

Ercolano, B., Barlow, M. J., & Storey, P. J., 2005, *The dusty MOCASSIN: fully self-consistent 3D photoionization and dust radiative transfer models*, in Monthly Notes of the Royal Astronomical Society, 362, 1038, ADS: `2005MNRAS.362.1038E`

Ercolano, B., Young, P. R., Drake, J. J., & Raymond, J. C., 2008a, *X-Ray Enabled MOCASSIN: A Three-dimensional Code for Photoionized Media*, in Astrophysical Journal Supplement Series, 175, 534, ADS: `2008ApJS..175..534E`

Ercolano, B., Drake, J. J., Raymond, J. C., & Clarke, C. C., 2008b, *X-Ray-Irradiated Protoplanetary Disk Atmospheres. I. Predicted Emission-Line Spectrum and Photoevaporation*, in Astrophysical Journal, 688, 398, ADS: `2008ApJ...688..398E`

Ercolano, B., Clarke, C. J., & Drake, J. J., 2009, *X-Ray Irradiated Protoplanetary Disk Atmospheres. II. Predictions from Models in Hydrostatic Equilibrium*, in Astrophysical Journal, 699, 1639, ADS: `2009ApJ...699.1639E`

Ercolano, B., & Clarke, C. J., 2010, *Metallicity, planet formation and disc lifetimes*, in Monthly Notes of the Royal Astronomical Society, 402, 2735, ADS: `2010MNRAS.402.2735E`

Ercolano, B., & Owen, J. E., 2010, *Theoretical spectra of photoevaporating protoplanetary discs: an atlas of atomic and low-ionization emission lines*, in Monthly Notes of the Royal Astronomical Society, 406, 1553, ADS: `2010MNRAS.406.1553E`

Ercolano, B., Clarke, C. J., & Hall, A. C., 2011, *The clearing of discs around late-type T Tauri stars: constraints from the infrared two-colour plane*, in Monthly Notes of the Royal Astronomical Society, 410, 671, ADS: `2011MNRAS.410..671E`

Ercolano, B., & Glassgold, A. E., 2013, *X-ray ionization rates in protoplanetary discs*, in Monthly Notes of the Royal Astronomical Society, 436, 3446, ADS: `2013MNRAS.436.3446E`

Ercolano, B., Mayr, D., Owen, J. E., Rosotti, G., & Manara, C. F., 2014, *The dot{M}-M_* relation of pre-main-sequence stars: a consequence of X-ray driven disc evolution*, in Monthly Notes of the Royal Astronomical Society, 439, 256, ADS: `2014MNRAS.439..256E`

Ercolano, B., & Rosotti, G., 2015, *The link between disc dispersal by photoevaporation and the semimajor* *axis distribution of exoplanets*, in Monthly Notes of the Royal Astronomical Society, 450, 3008, ADS: 2015MNRAS.450.3008E

Ercolano, B., Koepferl, C., Owen, J., & Robitaille, T., 2015, *Far-infrared signatures and inner hole sizes of protoplanetary discs undergoing inside-out dust dispersal*, in Monthly Notes of the Royal Astronomical Society, 452, 3689, ADS: 2015MNRAS.452.3689E

Ercolano, B., & Owen, J. E., 2016, *Blueshifted [O I] lines from protoplanetary discs: the smoking gun of X-ray photoevaporation*, in Monthly Notes of the Royal Astronomical Society, 460, 3472, ADS: 2016MNRAS.460.3472E

Ercolano, B., Rosotti, G. P., Picogna, G., & Testi, L., 2017a, *A photoevaporative gap in the closest planet-forming disc*, in Monthly Notes of the Royal Astronomical Society, 464, L95, ADS: 2017MNRAS.464L..95E

Ercolano, B., & Pascucci, I., 2017, *The dispersal of planet-forming discs: theory confronts observations*, in Royal Society Open Science, 4, 170114, ADS: 2017RSOS....470114E

Ercolano, B., Jennings, J., Rosotti, G., & Birnstiel, T., 2017b, *X-ray photoevaporation's limited success in the formation of planetesimals by the streaming instability*, in Monthly Notes of the Royal Astronomical Society, 472, 4117, ADS: 2017MNRAS.472.4117E

Ercolano, B., Weber, M. L., & Owen, J. E., 2018, *Accreting transition discs with large cavities created by X-ray photoevaporation in C and O depleted discs*, in Monthly Notes of the Royal Astronomical Society, 473, L64, ADS: 2018MNRAS.473L..64E

Ercolano, B., Picogna, G., Monsch, K., Drake, J. J., & Preibisch, T., 2021, *The dispersal of protoplanetary discs - II: photoevaporation models with observationally derived irradiating spectra*, in Monthly Notes of the Royal Astronomical Society, 508, 1675, ADS: 2021MNRAS.508.1675E

Ercolano, B., Rab, C., Molaverdikhani, K., Edwards, B., Preibisch, T., et al., 2022, *Observations of PAHs in the atmospheres of discs and exoplanets*, in Monthly Notes of the Royal Astronomical Society, ADS: 2022MNRAS.tmp..520E

Espaillat, C., D'Alessio, P., Hernández, J., Nagel, E., Luhman, K. L., et al., 2010, *Unveiling the Structure of Pre-transitional Disks*, in Astrophysical Journal, 717, 441, ADS: 2010ApJ...717..441E

Espaillat, C., Ingleby, L., Hernández, J., Furlan, E., D'Alessio, P., et al., 2012, *On the Transitional Disk Class: Linking Observations of T Tauri Stars and Physical Disk Models*, in Astrophysical Journal, 747, 103, ADS: 2012ApJ...747..103E

Espaillat, C., Muzerolle, J., Najita, J., Andrews, S., Zhu, Z., et al., 2014, *An Observational Perspective of Transitional Disks*, in Protostars and Planets VI, edited by H. Beuther, R. S. Klessen, C. P. Dullemond, & T. Henning, 497, ADS: 2014prpl.conf..497E

Evans, Neal J., I., Dunham, M. M., Jørgensen, J. K., Enoch, M. L., Merín, B., et al., 2009a, *The Spitzer c2d Legacy Results: Star-Formation Rates and Efficiencies; Evolution and Lifetimes*, in Astrophysical Journal Supplement Series, 181, 321, ADS: 2009ApJS..181..321E

Evans, N., Calvet, N., Cieza, L., Forbrich, J., Hillenbrand, L., et al., 2009b, *The Diskionary: A Glossary of Terms Commonly Used for Disks and Related Objects, First Edition*, in arXiv e-prints, arXiv: 0901.1691

Exoplanet Team, 2022, *The Extrasolar Planets Encyclopaedia*, https://www.exoplanet.eu/, Accessed: 2022-02-14

Facchini, S., Clarke, C. J., & Bisbas, T. G., 2016, *External photoevaporation of protoplanetary discs in sparse stellar groups: the impact of dust growth*, in Monthly Notes of the Royal Astronomical Society, 457, 3593, ADS: 2016MNRAS.457.3593F

Facchini, S., Birnstiel, T., Bruderer, S., & van Dishoeck, E. F., 2017, *Different dust and gas radial extents in protoplanetary disks: consistent models of grain growth and CO emission*, in Astronomy & Astrophysics, 605, A16, ADS: 2017A&A...605A..16F

Fang, M., Pascucci, I., Edwards, S., Gorti, U., Banzatti, A., et al., 2018, *A New Look at T Tauri Star Forbidden Lines: MHD-driven Winds from the Inner Disk*, in Astrophysical Journal, 868, 28, ADS: 2018ApJ...868...28F

Feigelson, E., Townsley, L., Güdel, M., & Stassun, K., 2007, *X-Ray Properties of Young Stars and Stellar Clusters*, in Protostars and Planets V, edited by B. Reipurth, D. Jewitt, & K. Keil, 313, ADS: 2007prpl.conf..313F

Feigelson, E. D., & Montmerle, T., 1999, *High-Energy Processes in Young Stellar Objects*, in Annual Review of Astronomy and Astrophysics, 37, 363, ADS: 1999ARA&A..37..363F

Ferreira, J., Dougados, C., & Cabrit, S., 2006, *Which jet launching mechanism(s) in T Tauri stars?*, in Astronomy & Astrophysics, 453, 785, ADS: 2006A&A...453..785F

Flaccomio, E., Damiani, F., Micela, G., Sciortino, S., Harnden, F. R., J., et al., 2003, *Chandra X-Ray*

Observation of the Orion Nebula Cluster. II. Relationship between X-Ray Activity Indicators and Stellar Parameters, in Astrophysical Journal, 582, 398, ADS: 2003ApJ...582..398F

Flaherty, K., Hughes, A. M., Simon, J. B., Qi, C., Bai, X.-N., et al., 2020, *Measuring Turbulent Motion in Planet-forming Disks with ALMA: A Detection around DM Tau and Nondetections around MWC 480 and V4046 Sgr*, in Astrophysical Journal, 895, 109, ADS: 2020ApJ...895..109F

Flaherty, K. M., Hughes, A. M., Rose, S. C., Simon, J. B., Qi, C., et al., 2017, *A Three-dimensional View of Turbulence: Constraints on Turbulent Motions in the HD 163296 Protoplanetary Disk Using DCO^+*, in Astrophysical Journal, 843, 150, ADS: 2017ApJ...843..150F

Flaherty, K. M., Hughes, A. M., Teague, R., Simon, J. B., Andrews, S. M., et al., 2018, *Turbulence in the TW Hya Disk*, in Astrophysical Journal, 856, 117, ADS: 2018ApJ...856..117F

Flaischlen, S., Preibisch, T., Manara, C. F., & Ercolano, B., 2021, *Testing the models of X-ray driven photoevaporation with accreting stars in the Orion Nebula Cluster*, in Astronomy & Astrophysics, 648, A121, ADS: 2021A&A...648A.121F

Fleming, T. A., Gioia, I. M., & Maccacaro, T., 1989, *The Relation between X-Ray Emission and Rotation in Late-Type Stars from the Perspective of X-Ray Selection*, in Astrophysical Journal, 340, 1011, ADS: 1989ApJ...340.1011F

Flock, M., Nelson, R. P., Turner, N. J., Bertrang, G. H. M., Carrasco-González, C., et al., 2017, *Radiation Hydrodynamical Turbulence in Protoplanetary Disks: Numerical Models and Observational Constraints*, in Astrophysical Journal, 850, 131, ADS: 2017ApJ...850..131F

Flock, M., Turner, N. J., Nelson, R. P., Lyra, W., Manger, N., et al., 2020, *Gas and Dust Dynamics in Starlight-heated Protoplanetary Disks*, in Astrophysical Journal, 897, 155, ADS: 2020ApJ...897..155F

Flores, C., Duchêne, G., Wolff, S., Villenave, M., Stapelfeldt, K., et al., 2021, *The Anatomy of an Unusual Edge-on Protoplanetary Disk. II. Gas Temperature and a Warm Outer Region*, in Astronomical Journal, 161, 239, ADS: 2021AJ....161..239F

Font, A. S., McCarthy, I. G., Johnstone, D., & Ballantyne, D. R., 2004, *Photoevaporation of Circumstellar Disks around Young Stars*, in Astrophysical Journal, 607, 890, ADS: 2004ApJ...607..890F

Foote, E. N., 1856, *Circumstances Affecting the Heat of the Sun's Rays*, in American Journal of Science and Arts, 22, 382

Fouchet, L., Maddison, S. T., Gonzalez, J. F., & Murray, J. R., 2007, *The effect of a planet on the dust distribution in a 3D protoplanetary disk*, in Astronomy & Astrophysics, 474, 1037, ADS: 2007A&A...474.1037F

Fouchet, L., Gonzalez, J. F., & Maddison, S. T., 2010, *Planet gaps in the dust layer of 3D protoplanetary disks. I. Hydrodynamical simulations of T Tauri disks*, in Astronomy & Astrophysics, 518, A16, ADS: 2010A&A...518A..16F

Franceschi, R., Birnstiel, T., Henning, T., Pinilla, P., Semenov, D., et al., 2022, *Mass determination of protoplanetary disks from dust evolution*, in Astronomy & Astrophysics, 657, A74, ADS: 2022A&A...657A..74F

Francis, L., & van der Marel, N., 2020, *Dust-depleted Inner Disks in a Large Sample of Transition Disks through Long-baseline ALMA Observations*, in Astrophysical Journal, 892, 111, ADS: 2020ApJ...892..111F

Frank, A., Ray, T. P., Cabrit, S., Hartigan, P., Arce, H. G., et al., 2014, *Jets and Outflows from Star to Cloud: Observations Confront Theory*, in Protostars and Planets VI, edited by H. Beuther, R. S. Klessen, C. P. Dullemond, & T. Henning, 451, ADS: 2014prpl.conf..451F

Franz, R., Picogna, G., Ercolano, B., & Birnstiel, T., 2020, *Dust entrainment in photoevaporative winds: The impact of X-rays*, in Astronomy & Astrophysics, 635, A53, ADS: 2020A&A...635A..53F

Franz, R., Ercolano, B., Casassus, S., Picogna, G., Birnstiel, T., Pérez, S., Rab, C., & Sharma, A., 2022a, *Dust entrainment in photoevaporative winds: Densities and imaging*, in Astronomy & Astrophysics, 657, A69, ADS: 2022A&A...657A..69F

Franz, R., Picogna, G., Ercolano, B., Casassus, S., Birnstiel, T., Rab, C., & Pérez, S., 2022b, *Dust entrainment in photoevaporative winds: Synthetic observations of transition disks*, in Astronomy & Astrophysics, 659, A90, ADS: 2022A&A...659A..90F

Fromang, S., & Nelson, R. P., 2005, *On the accumulation of solid bodies in global turbulent protoplanetary disc models*, in Monthly Notes of the Royal Astronomical Society, 364, L81, ADS: 2005MNRAS.364L..81F

Fromang, S., & Nelson, R. P., 2009, *Global MHD simulations of stratified and turbulent protoplanetary discs. II. Dust settling*, in Astronomy & Astrophysics, 496, 597, ADS: 2009A&A...496..597F

Galli, D., Lizano, S., Shu, F. H., & Allen, A., 2006, *Gravitational Collapse of Magnetized Clouds. I. Ideal Magnetohydrodynamic Accretion Flow*, in Astrophysical Journal, 647, 374, ADS: 2006ApJ...

647..374G
Gammie, C. F., 1996, *Layered Accretion in T Tauri Disks*, in Astrophysical Journal, 457, 355, ADS: 1996ApJ...457..355G
Gammie, C. F., & Johnson, B. M., 2005, *Theoretical Studies of Gaseous Disk Evolution around Solar Mass Stars*, in Astronomical Society of the Pacific Conference Series, Vol. 341, Chondrites and the Protoplanetary Disk, edited by A. N. Krot, E. R. D. Scott, & B. Reipurth, 145, ADS: 2005ASPC..341..145G
Gangi, M., Nisini, B., Antoniucci, S., Giannini, T., Biazzo, K., et al., 2020, *GIARPS High-resolution Observations of T Tauri stars (GHOsT). II. Connecting atomic and molecular winds in protoplanetary disks*, in Astronomy & Astrophysics, 643, A32, ADS: 2020A&A...643A..32G
Gárate, M., Birnstiel, T., Stammler, S. M., & Günther, H. M., 2019, *The Dimming of RW Auriga: Is Dust Accretion Preceding an Outburst?*, in Astrophysical Journal, 871, 53, ADS: 2019ApJ...871...53G
Gárate, M., Birnstiel, T., Drążkowska, J., & Stammler, S. M., 2020, *Gas accretion damped by dust back-reaction at the snow line*, in Astronomy & Astrophysics, 635, A149, ADS: 2020A&A...635A.149G
Gárate, M., Delage, T. N., Stadler, J., Pinilla, P., Birnstiel, T., Stammler, S. M., Picogna, G., Ercolano, B., Franz, R., & Lenz, C., 2021, *Large gaps and high accretion rates in photoevaporative transition disks with a dead zone*, in Astronomy & Astrophysics, 655, A18, ADS: 2021A&A...655A..18G
Garaud, P., Barrière-Fouchet, L., & Lin, D. N. C., 2004, *Individual and Average Behavior of Particles in a Protoplanetary Nebula*, in Astrophysical Journal, 603, 292, ADS: 2004ApJ...603..292G
Garufi, A., Quanz, S. P., Schmid, H. M., Avenhaus, H., Buenzli, E., et al., 2014, *Shadows and cavities in protoplanetary disks: HD 163296, HD 141569A, and HD 150193A in polarized light*, in Astronomy & Astrophysics, 568, A40, ADS: 2014A&A...568A..40G
Garufi, A., Benisty, M., Pinilla, P., Tazzari, M., Dominik, C., et al., 2018, *Evolution of protoplanetary disks from their taxonomy in scattered light: spirals, rings, cavities, and shadows*, in Astronomy & Astrophysics, 620, A94, ADS: 2018A&A...620A..94G
Garufi, A., Podio, L., Bacciotti, F., Antoniucci, S., Boccaletti, A., et al., 2019, *SPHERE view of the jet and the envelope of RY Tauri*, in Astronomy & Astrophysics, 628, A68, ADS: 2019A&A...628A..68G
Garufi, A., Avenhaus, H., Pérez, S., Quanz, S. P., van Holstein, R. G., et al., 2020, *Disks Around T Tauri Stars with SPHERE (DARTTS-S). II. Twenty-one new polarimetric images of young stellar disks*, in Astronomy & Astrophysics, 633, A82, ADS: 2020A&A...633A..82G
Gatti, T., Natta, A., Randich, S., Testi, L., & Sacco, G., 2008, *Accretion properties of T Tauri stars in σ Orionis*, in Astronomy & Astrophysics, 481, 423, ADS: 2008A&A...481..423G
Gaudi, B. S., Meyer, M., & Christiansen, J., 2021, *The Demographics of Exoplanets*, in ExoFrontiers; Big Questions in Exoplanetary Science, edited by N. Madhusudhan, 2514-3433, IOP Publishing, 2–1, ADS: 2021exbi.book....2G
Getman, K. V., Flaccomio, E., Broos, P. S., Grosso, N., Tsujimoto, M., et al., 2005, *Chandra Orion Ultradeep Project: Observations and Source Lists*, in Astrophysical Journal Supplement Series, 160, 319, ADS: 2005ApJS..160..319G
Getman, K. V., Feigelson, E. D., Townsley, L., Broos, P., Garmire, G., et al., 2006, *Chandra Study of the Cepheus B Star-forming Region: Stellar Populations and the Initial Mass Function*, in Astrophysical Journal Supplement Series, 163, 306, ADS: 2006ApJS..163..306G
Getman, K. V., & Feigelson, E. D., 2021, *X-Ray Superflares from Pre-main-sequence Stars: Flare Energetics and Frequency*, in Astrophysical Journal, 916, 32, ADS: 2021ApJ...916...32G
Getman, K. V., Feigelson, E. D., & Garmire, G. P., 2021, *X-Ray Superflares from Pre-main-sequence Stars: Flare Modeling*, in Astrophysical Journal, 920, 154, ADS: 2021ApJ...920..154G
Getman, K. V., Feigelson, E. D., Garmire, G. P., Broos, P. S., Kuhn, M. A., et al., 2022, *Evolution of X-ray Activity in <25 Myr Old Pre-Main Sequence Stars*, in arXiv e-prints, arXiv: 2203.02047
Giacalone, S., Teitler, S., Königl, A., Krijt, S., & Ciesla, F. J., 2019, *Dust Transport and Processing in Centrifugally Driven Protoplanetary Disk Winds*, in Astrophysical Journal, 882, 33, ADS: 2019ApJ...882...33G
Gilmozzi, R., & Spyromilio, J., 2007, *The European Extremely Large Telescope (E-ELT)*, in The Messenger, 127, 11, ADS: 2007Msngr.127...11G
Gingold, R. A., & Monaghan, J. J., 1977, *Smoothed particle hydrodynamics: theory and application to non-spherical stars.*, in Monthly Notes of the Royal Astronomical Society, 181, 375, ADS: 1977MNRAS.181..375G
Glauser, A. M., Ménard, F., Pinte, C., Duchêne, G., Güdel, M., et al., 2008, *Multiwavelength studies of the gas and dust disc of IRAS 04158+2805*, in Astronomy & Astrophysics, 485, 531, ADS: 2008A&A...485..531G

Goethe, J. W., 1808, *Faust. Eine Tragödie.*, Cotta'sche Verlagsbuchhandlung Tübingen

Goethe, J. W., & Taylor, B., 1872, *Faust. A Tragedy by Johann Wolfgang von Goethe. The first Part. Translated, in the original metres, by Bayard Taylor.*, Brockhaus Leipzig

Goldreich, P., & Schubert, G., 1967, *Differential Rotation in Stars*, in Astrophysical Journal, 150, 571, ADS: `1967ApJ...150..571G`

Goldreich, P., & Ward, W. R., 1973, *The Formation of Planetesimals*, in Astrophysical Journal, 183, 1051, ADS: `1973ApJ...183.1051G`

Gorti, U., & Hollenbach, D., 2004, *Models of Chemistry, Thermal Balance, and Infrared Spectra from Intermediate-Aged Disks around G and K Stars*, in Astrophysical Journal, 613, 424, ADS: `2004ApJ...613..424G`

Gorti, U., & Hollenbach, D., 2008, *Line Emission from Gas in Optically Thick Dust Disks around Young Stars*, in Astrophysical Journal, 683, 287, ADS: `2008ApJ...683..287G`

Gorti, U., & Hollenbach, D., 2009, *Photoevaporation of Circumstellar Disks By Far-Ultraviolet, Extreme-Ultraviolet and X-Ray Radiation from the Central Star*, in Astrophysical Journal, 690, 1539, ADS: `2009ApJ...690.1539G`

Gorti, U., Dullemond, C. P., & Hollenbach, D., 2009, *Time Evolution of Viscous Circumstellar Disks due to Photoevaporation by Far-Ultraviolet, Extreme-Ultraviolet, and X-ray Radiation from the Central Star*, in Astrophysical Journal, 705, 1237, ADS: `2009ApJ...705.1237G`

Gorti, U., Hollenbach, D., & Dullemond, C. P., 2015, *The Impact of Dust Evolution and Photoevaporation on Disk Dispersal*, in Astrophysical Journal, 804, 29, ADS: `2015ApJ...804...29G`

Gorti, U., 2016, *Photoevaporation and Disk Dispersal*, in IAU Symposium, Vol. 314, Young Stars & Planets Near the Sun, edited by J. H. Kastner, B. Stelzer, & S. A. Metchev, 153–158, ADS: `2016IAUS..314..153G`

Grassi, T., Bovino, S., Haugbølle, T., & Schleicher, D. R. G., 2017, *A detailed framework to incorporate dust in hydrodynamical simulations*, in Monthly Notes of the Royal Astronomical Society, 466, 1259, ADS: `2017MNRAS.466.1259G`

Grassi, T., Ercolano, B., Szűcs, L., Jennings, J., & Picogna, G., 2020, *Modelling thermochemical processes in protoplanetary discs I: numerical methods*, in Monthly Notes of the Royal Astronomical Society, 494, 4471, ADS: `2020MNRAS.494.4471G`

Grassi, T., Nauman, F., Ramsey, J. P., Bovino, S., Picogna, G., et al., 2021, *Reducing the complexity of chemical networks via interpretable autoencoders*, in arXiv e-prints, arXiv: `2104.09516`

Greene, T. P., Wilking, B. A., Andre, P., Young, E. T., & Lada, C. J., 1994, *Further Mid-Infrared Study of the rho Ophiuchi Cloud Young Stellar Population: Luminosities and Masses of Pre–Main-Sequence Stars*, in Astrophysical Journal, 434, 614, ADS: `1994ApJ...434..614G`

Gressel, O., Turner, N. J., Nelson, R. P., & McNally, C. P., 2015, *Global Simulations of Protoplanetary Disks With Ohmic Resistivity and Ambipolar Diffusion*, in Astrophysical Journal, 801, 84, ADS: `2015ApJ...801...84G`

Gressel, O., Ramsey, J. P., Brinch, C., Nelson, R. P., Turner, N. J., et al., 2020, *Global Hydromagnetic Simulations of Protoplanetary Disks with Stellar Irradiation and Simplified Thermochemistry*, in Astrophysical Journal, 896, 126, ADS: `2020ApJ...896..126G`

Güdel, M., Skinner, S. L., Mel'Nikov, S. Y., Audard, M., Telleschi, A., et al., 2007, *X-rays from T Tauri: a test case for accreting T Tauri stars*, in Astronomy & Astrophysics, 468, 529, ADS: `2007A&A...468..529G`

Güdel, M., & Telleschi, A., 2007, *The X-ray soft excess in classical T Tauri stars*, in Astronomy & Astrophysics, 474, L25, ADS: `2007A&A...474L..25G`

Güdel, M., Dvorak, R., Erkaev, N., Kasting, J., Khodachenko, M., et al., 2014, *Astrophysical Conditions for Planetary Habitability*, in Protostars and Planets VI, edited by H. Beuther, R. S. Klessen, C. P. Dullemond, & T. Henning, 883, ADS: `2014prpl.conf..883G`

Gundlach, B., & Blum, J., 2015, *The Stickiness of Micrometer-sized Water-ice Particles*, in Astrophysical Journal, 798, 34, ADS: `2015ApJ...798...34G`

Güttler, C., Blum, J., Zsom, A., Ormel, C. W., & Dullemond, C. P., 2010, *The outcome of protoplanetary dust growth: pebbles, boulders, or planetesimals?. I. Mapping the zoo of laboratory collision experiments*, in Astronomy & Astrophysics, 513, A56, ADS: `2010A&A...513A..56G`

Guzmán, V. V., Huang, J., Andrews, S. M., Isella, A., Pérez, L. M., et al., 2018, *The Disk Substructures at High Angular Resolution Program (DSHARP). VIII. The Rich Ringed Substructures in the AS 209 Disk*, in Astrophysical Journal, 869, L48, ADS: `2018ApJ...869L..48G`

Habing, H. J., 1968, *The interstellar radiation density between 912 A and 2400 A*, in Bulletin of the Astronomical Institutes of the Netherlands, 19, 421, ADS: `1968BAN....19..421H`

Haisch, Karl E., J., Lada, E. A., & Lada, C. J., 2001, *Disk Frequencies and Lifetimes in Young Clusters*, in Astrophysical Journal, 553, L153, ADS: 2001ApJ...553L.153H

Hamann, F., 1994, *Emission-Line Studies of Young Stars. IV. The Optical Forbidden Lines*, in Astrophysical Journal Supplement Series, 93, 485, ADS: 1994ApJS...93..485H

Hartigan, P., Edwards, S., & Ghandour, L., 1995, *Disk Accretion and Mass Loss from Young Stars*, in Astrophysical Journal, 452, 736, ADS: 1995ApJ...452..736H

Hartmann, L., Calvet, N., Gullbring, E., & D'Alessio, P., 1998, *Accretion and the Evolution of T Tauri Disks*, in Astrophysical Journal, 495, 385, ADS: 1998ApJ...495..385H

Hartmann, L., Herczeg, G., & Calvet, N., 2016, *Accretion onto Pre-Main-Sequence Stars*, in Annual Review of Astronomy and Astrophysics, 54, 135, ADS: 2016ARA&A..54..135H

Hawley, J. F., & Balbus, S. A., 1991, *A Powerful Local Shear Instability in Weakly Magnetized Disks. II. Nonlinear Evolution*, in Astrophysical Journal, 376, 223, ADS: 1991ApJ...376..223H

Haworth, T. J., Clarke, C. J., & Owen, J. E., 2016a, *Rapid radiative clearing of protoplanetary discs*, in Monthly Notes of the Royal Astronomical Society, 457, 1905, ADS: 2016MNRAS.457.1905H

Haworth, T. J., Boubert, D., Facchini, S., Bisbas, T. G., & Clarke, C. J., 2016b, *Photochemical-dynamical models of externally FUV irradiated protoplanetary discs*, in Monthly Notes of the Royal Astronomical Society, 463, 3616, ADS: 2016MNRAS.463.3616H

Haworth, T. J., Clarke, C. J., Rahman, W., Winter, A. J., & Facchini, S., 2018, *The FRIED grid of mass-loss rates for externally irradiated protoplanetary discs*, in Monthly Notes of the Royal Astronomical Society, 481, 452, ADS: 2018MNRAS.481..452H

Hayashi, C., 1981, *Structure of the Solar Nebula, Growth and Decay of Magnetic Fields and Effects of Magnetic and Turbulent Viscosities on the Nebula*, in Progress of Theoretical Physics Supplement, 70, 35, ADS: 1981PThPS..70...35H

Helled, R., Bodenheimer, P., Podolak, M., Boley, A., Meru, F., et al., 2014, *Giant Planet Formation, Evolution, and Internal Structure*, in Protostars and Planets VI, edited by H. Beuther, R. S. Klessen, C. P. Dullemond, & T. Henning, 643, ADS: 2014prpl.conf..643H

Hendler, N., Pascucci, I., Pinilla, P., Tazzari, M., Carpenter, J., et al., 2020, *The Evolution of Dust Disk Sizes from a Homogeneous Analysis of 1-10 Myr old Stars*, in Astrophysical Journal, 895, 126, ADS: 2020ApJ...895..126H

Heng, K., 2014, *The Nature of Scientific Proof in the Age of Simulations*, in arXiv e-prints, arXiv: 1404.6248

Heng, K., & Marley, M. S., 2018, *Radiative Transfer for Exoplanet Atmospheres*, in Handbook of Exoplanets, edited by H. J. Deeg & J. A. Belmonte, 102, ADS: 2018haex.bookE.102H

Henney, W. J., O'Dell, C. R., Meaburn, J., Garrington, S. T., & Lopez, J. A., 2002, *Mass Loss and Jet Outflow in the Orion Nebula Proplyd LV 2*, in Astrophysical Journal, 566, 315, ADS: 2002ApJ...566..315H

Henning, T., & Stognienko, R., 1996, *Dust opacities for protoplanetary accretion disks: influence of dust aggregates.*, in Astronomy & Astrophysics, 311, 291, ADS: 1996A&A...311..291H

Herbig, G. H., 1962, *Spectral Classification of Faint Members of the Hyades and Pleiades and the Dating Problem in Galactic Clusters.*, in Astrophysical Journal, 135, 736, ADS: 1962ApJ...135..736H

Herbig, G. H., 1966, *On the interpretation of FU orionis*, in Vistas in Astronomy, 8, 109, ADS: 1966VA......8..109H

Herbig, G. H., 1977, *Eruptive phenomena in early stellar evolution.*, in Astrophysical Journal, 217, 693, ADS: 1977ApJ...217..693H

Herbig, G. H., 1989, *FU Orionis eruptions.*, in European Southern Observatory Conference and Workshop Proceedings, Vol. 33, European Southern Observatory Conference and Workshop Proceedings, 233–246, ADS: 1989ESOC...33..233H

Herczeg, G. J., Najita, J. R., Hillenbrand, L. A., & Pascucci, I., 2007, *High-Resolution Spectroscopy of [Ne II] Emission from TW Hydrae*, in Astrophysical Journal, 670, 509, ADS: 2007ApJ...670..509H

Hertzsprung, E., 1911, *Number 63. Zweiundzwanzigsten Bandes Erstes Stuck. Uber die Verwendung photographischer effecktiver Wellenlangen zur Bestimmung von Farbenaquivalenten*, in Publikationen des Astrophysikalischen Observatoriums zu Potsdam, 22, A1, ADS: 1911POPot..22A...1H

Hilbert, B., Sahlmann, J., Volk, K., Osborne, S., Dthatte, et al., 2019, *spacetelescope/mirage: First github release*, v1.1.1, Zenodo, ADS: 2019zndo...3519262H

Hill, G. W., 1878, *Researches in the Lunar Theory*, in American Journal of Mathematics, 1, 5, DOI: 10.2307/2369430

Hill, G. W., 1913, *Motion of a system of material points under the action of gravitation*, in Astronomical Journal, 27, 171, ADS: 1913AJ.....27..171H

Hinkel, N. R., Pepper, J., Stark, C. C., Burt, J. A., Ciardi, D. R., et al., 2021, *Final Report for SAG 22: A Target Star Archive for Exoplanet Science*, in arXiv e-prints, arXiv: 2112.04517

Hollenbach, D., Johnstone, D., Lizano, S., & Shu, F., 1994, *Photoevaporation of Disks around Massive Stars and Application to Ultracompact H II Regions*, in Astrophysical Journal, 428, 654, ADS: 1994ApJ...428..654H

Hollenbach, D., & Gorti, U., 2009, *Diagnostic Line Emission from Extreme Ultraviolet and X-ray-illuminated Disks and Shocks Around Low-mass Stars*, in Astrophysical Journal, 703, 1203, ADS: 2009ApJ...703.1203H

Hollenbach, D. J., & Tielens, A. G. G. M., 1997, *Dense Photodissociation Regions (PDRs)*, in Annual Review of Astronomy and Astrophysics, 35, 179, ADS: 1997ARA&A..35..179H

Hollenbach, D. J., Yorke, H. W., & Johnstone, D., 2000, *Disk Dispersal around Young Stars*, in Protostars and Planets IV, edited by V. Mannings, A. P. Boss, & S. S. Russell, 401–428, ADS: 2000prpl.conf..401H

Howard, A. W., Marcy, G. W., Bryson, S. T., Jenkins, J. M., Rowe, J. F., et al., 2012, *Planet Occurrence within 0.25 AU of Solar-type Stars from Kepler*, in Astrophysical Journal Supplement Series, 201, 15, ADS: 2012ApJS..201...15H

Hoyle, F., 1953, *On the Fragmentation of Gas Clouds Into Galaxies and Stars*, in Astrophysical Journal, 118, 513, ADS: 1953ApJ...118..513H

Huang, J., Andrews, S. M., Dullemond, C. P., Isella, A., Pérez, L. M., et al., 2018, *The Disk Substructures at High Angular Resolution Project (DSHARP). II. Characteristics of Annular Substructures*, in Astrophysical Journal, 869, L42, ADS: 2018ApJ...869L..42H

Hughes, A. M., Wilner, D. J., Qi, C., & Hogerheijde, M. R., 2008, *Gas and Dust Emission at the Outer Edge of Protoplanetary Disks*, in Astrophysical Journal, 678, 1119, ADS: 2008ApJ...678.1119H

Hutchison, M. A., & Laibe, G., 2016, *A Plane-Parallel Wind Solution for Testing Numerical Simulations of Photoevaporation*, in Publications of the Astronomical Society of Australia, 33, e014, ADS: 2016PASA...33...14H

Hutchison, M. A., Price, D. J., Laibe, G., & Maddison, S. T., 2016a, *On dust entrainment in photoevaporative winds*, in Monthly Notes of the Royal Astronomical Society, 461, 742, ADS: 2016MNRAS.461..742H

Hutchison, M. A., Laibe, G., & Maddison, S. T., 2016b, *On the maximum grain size entrained by photoevaporative winds*, in Monthly Notes of the Royal Astronomical Society, 463, 2725, ADS: 2016MNRAS.463.2725H

Hutchison, M. A., Price, D. J., & Laibe, G., 2018, *MULTIGRAIN: a smoothed particle hydrodynamic algorithm for multiple small dust grains and gas*, in Monthly Notes of the Royal Astronomical Society, 476, 2186, ADS: 2018MNRAS.476.2186H

Hutchison, M. A., & Clarke, C. J., 2021, *Dust delivery and entrainment in photoevaporative winds*, in Monthly Notes of the Royal Astronomical Society, 501, 1127, ADS: 2021MNRAS.501.1127H

Huxley, A., 1932, *Brave New World*, Chatto & Windus

IAU General Assembly, 2006, *Resolutions of the 26th General Assembly for the International Astronomical Union*, https://www.iau.org/news/pressreleases/detail/iau0603/, Accessed: 2022-01-04

Ida, S., & Lin, D. N. C., 2004, *Toward a Deterministic Model of Planetary Formation. I. A Desert in the Mass and Semimajor Axis Distributions of Extrasolar Planets*, in Astrophysical Journal, 604, 388, ADS: 2004ApJ...604..388I

Ida, S., Guillot, T., & Morbidelli, A., 2008, *Accretion and Destruction of Planetesimals in Turbulent Disks*, in Astrophysical Journal, 686, 1292, ADS: 2008ApJ...686.1292I

Igea, J., & Glassgold, A. E., 1999, *X-Ray Ionization of the Disks of Young Stellar Objects*, in Astrophysical Journal, 518, 848, ADS: 1999ApJ...518..848I

Isella, A., Benisty, M., Teague, R., Bae, J., Keppler, M., et al., 2019, *Detection of Continuum Submillimeter Emission Associated with Candidate Protoplanets*, in Astrophysical Journal, 879, L25, ADS: 2019ApJ...879L..25I

Jaros, R., Čemeljić, M., Kluźniak, W., Vinković, D., & Turski, C., 2020, *Transport of dust grain particles in the accretion disk*, in XXXIX Polish Astronomical Society Meeting, edited by K. Małek, M. Polińska, A. Majczyna, G. Stachowski, R. Poleski, Ł. Wyrzykowski, & A. Różańska, Vol. 10, 177–179, ADS: 2020past.conf..177J

Jeans, J. H., 1902, *The Stability of a Spherical Nebula*, in Philosophical Transactions of the Royal Society of London Series A, 199, 1, ADS: 1902RSPTA.199....1J

Jennings, J., Ercolano, B., & Rosotti, G. P., 2018, *The comparative effect of FUV, EUV and X-ray disc photoevaporation on gas giant separations*, in Monthly Notes of the Royal Astronomical Society, 477, 4131, ADS: 2018MNRAS.477.4131J

Jennings, J., Booth, R. A., Tazzari, M., Clarke, C. J., & Rosotti, G. P., 2022, *A super-resolution analysis of the DSHARP survey: substructure is common in the inner 30 au*, in Monthly Notes of the Royal Astronomical Society, 509, 2780, ADS: 2022MNRAS.509.2780J

Johansen, A., & Youdin, A., 2007, *Protoplanetary Disk Turbulence Driven by the Streaming Instability: Nonlinear Saturation and Particle Concentration*, in Astrophysical Journal, 662, 627, ADS: 2007ApJ...662..627J

Johansen, A., Oishi, J. S., Mac Low, M.-M., Klahr, H., Henning, T., et al., 2007, *Rapid planetesimal formation in turbulent circumstellar disks*, in Nature, 448, 1022, ADS: 2007Natur.448.1022J

Johansen, A., Youdin, A., & Klahr, H., 2009, *Zonal Flows and Long-lived Axisymmetric Pressure Bumps in Magnetorotational Turbulence*, in Astrophysical Journal, 697, 1269, ADS: 2009ApJ...697.1269J

Johansen, A., Blum, J., Tanaka, H., Ormel, C., Bizzarro, M., et al., 2014, *The Multifaceted Planetesimal Formation Process*, in Protostars and Planets VI, edited by H. Beuther, R. S. Klessen, C. P. Dullemond, & T. Henning, 547, ADS: 2014prpl.conf..547J

Johns-Krull, C. M., Valenti, J. A., & Linsky, J. L., 2000, *An IUE Atlas of Pre-Main-Sequence Stars. II. Far-Ultraviolet Accretion Diagnostics in T Tauri Stars*, in Astrophysical Journal, 539, 815, ADS: 2000ApJ...539..815J

Johnstone, D., Hollenbach, D., & Bally, J., 1998, *Photoevaporation of Disks and Clumps by Nearby Massive Stars: Application to Disk Destruction in the Orion Nebula*, in Astrophysical Journal, 499, 758, ADS: 1998ApJ...499..758J

Joswiak, D. J., Brownlee, D. E., Pepin, R. O., & Schlutter, D. J., 2007, *Densities and Mineralogy of Cometary and Asteroidal Interplanetary Dust Particles Collected in the Stratosphere*, in Dust in Planetary Systems, 643, 141, ADS: 2007ESASP.643..141J

Kanagawa, K. D., Muto, T., Tanaka, H., Tanigawa, T., Takeuchi, T., et al., 2016, *Mass constraint for a planet in a protoplanetary disk from the gap width*, in Publications of the Astronomical Society of Japan, 68, 43, ADS: 2016PASJ...68...43K

Kanagawa, K. D., Ueda, T., Muto, T., & Okuzumi, S., 2017, *Effect of Dust Radial Drift on Viscous Evolution of Gaseous Disk*, in Astrophysical Journal, 844, 142, ADS: 2017ApJ...844..142K

Kant, I., 1784, *Beantwortung der Frage: Was ist Aufklärung?*, in Berlinische Monatsschrift, 12, 481

Karttunen, H., Kroeger, P., Oja, H., Poutanen, M., & Donner, K. J., 2007, *Fundamental astronomy*, 5th edn., Springer, ADS: 2007fuas.conf.....K

Kasagi, Y., Kotani, T., Kawahara, H., Tajiri, T., Muto, T., et al., 2022, *Dippers from TESS Full-frame Images. II. Spectroscopic Characterization of Four Young Dippers*, in arXiv e-prints, arXiv: 2201.09459

Kataoka, A., Okuzumi, S., Tanaka, H., & Nomura, H., 2014, *Opacity of fluffy dust aggregates*, in Astronomy & Astrophysics, 568, A42, ADS: 2014A&A...568A..42K

Kataoka, A., Muto, T., Momose, M., Tsukagoshi, T., Fukagawa, M., et al., 2015, *Millimeter-wave Polarization of Protoplanetary Disks due to Dust Scattering*, in Astrophysical Journal, 809, 78, ADS: 2015ApJ...809...78K

Kaufman, V., & Minnhagen, L., 1972, *Accurate Ground-Term Combinations in Ne I*, in Journal of the Optical Society of America, 62, 92, DOI: 10.1364/JOSA.62.000092

Keeling, C. D., 1960, *The Concentration and Isotopic Abundances of Carbon Dioxide in the Atmosphere*, in Tellus, 12, 200, ADS: 1960Tell...12..200K

Kenyon, S. J., & Hartmann, L., 1987, *Spectral Energy Distributions of T Tauri Stars: Disk Flaring and Limits on Accretion*, in Astrophysical Journal, 323, 714, ADS: 1987ApJ...323..714K

Kenyon, S. J., & Hartmann, L., 1995, *Pre-Main-Sequence Evolution in the Taurus-Auriga Molecular Cloud*, in Astrophysical Journal Supplement Series, 101, 117, ADS: 1995ApJS..101..117K

Keppler, M., Benisty, M., Müller, A., Henning, T., van Boekel, R., et al., 2018, *Discovery of a planetary-mass companion within the gap of the transition disk around PDS 70*, in Astronomy & Astrophysics, 617, A44, ADS: 2018A&A...617A..44K

Kim, K. H., Watson, D. M., Manoj, P., Forrest, W. J., Najita, J., et al., 2013, *Transitional Disks and Their Origins: An Infrared Spectroscopic Survey of Orion A*, in Astrophysical Journal, 769, 149, ADS: 2013ApJ...769..149K

Kirchschlager, F., & Bertrang, G. H. M., 2020, *Self-scattering of non-spherical dust grains. The limitations of perfect compact spheres*, in Astronomy & Astrophysics, 638, A116, ADS: 2020A&A...638A.116K

Klahr, H. H., & Henning, T., 1997, *Particle-Trapping Eddies in Protoplanetary Accretion Disks*, in Icarus, 128, 213, ADS: 1997Icar..128..213K

Klahr, H. H., & Lin, D. N. C., 2001, *Dust Distribution in Gas Disks: A Model for the Ring around HR 4796A*, in Astrophysical Journal, 554, 1095, ADS: 2001ApJ...554.1095K

Kley, W., & Crida, A., 2008, *Migration of protoplanets in radiative discs*, in Astronomy & Astrophysics, 487, L9, ADS: 2008A&A...487L...9K

Kley, W., Bitsch, B., & Klahr, H., 2009, *Planet migration in three-dimensional radiative discs*, in Astronomy & Astrophysics, 506, 971, ADS: 2009A&A...506..971K

Kluska, J., Van Winckel, H., Coppée, Q., Oomen, G. M., Dsilva, K., et al., 2022, *A population of transition disks around evolved stars: Fingerprints of planets. Catalog of disks surrounding Galactic post-AGB binaries*, in Astronomy & Astrophysics, 658, A36, ADS: 2022A&A...658A..36K

Koch, D. G., Borucki, W. J., Basri, G., Batalha, N. M., Brown, T. M., et al., 2010, *Kepler Mission Design, Realized Photometric Performance, and Early Science*, in Astrophysical Journal, 713, L79, ADS: 2010ApJ...713L..79K

Koepferl, C. M., Ercolano, B., Dale, J., Teixeira, P. S., Ratzka, T., et al., 2013, *Disc clearing of young stellar objects: evidence for fast inside-out dispersal*, in Monthly Notes of the Royal Astronomical Society, 428, 3327, ADS: 2013MNRAS.428.3327K

Komaki, A., Nakatani, R., & Yoshida, N., 2021, *Radiation Hydrodynamics Simulations of Protoplanetary Disks: Stellar Mass Dependence of the Disk Photoevaporation Rate*, in Astrophysical Journal, 910, 51, ADS: 2021ApJ...910...51K

Königl, A., & Ruden, S. P., 1993, *Origin of Outflows and Winds*, in Protostars and Planets III, edited by E. H. Levy & J. I. Lunine, 641, ADS: 1993prpl.conf..641K

Königl, A., & Pudritz, R. E., 2000, *Disk Winds and the Accretion-Outflow Connection*, in Protostars and Planets IV, edited by V. Mannings, A. P. Boss, & S. S. Russell, 759, ADS: 2000prpl.conf..759K

Kornet, K., Stepinski, T. F., & Różyczka, M., 2001, *Diversity of planetary systems from evolution of solids in protoplanetary disks*, in Astronomy & Astrophysics, 378, 180, ADS: 2001A&A...378..180K

Krapp, L., Benítez-Llambay, P., Gressel, O., & Pessah, M. E., 2019, *Streaming Instability for Particle-size Distributions*, in Astrophysical Journal, 878, L30, ADS: 2019ApJ...878L..30K

Krijt, S., & Ciesla, F. J., 2016, *Dust Diffusion and Settling in the Presence of Collisions: Trapping (sub)micron Grains in the Midplane*, in Astrophysical Journal, 822, 111, ADS: 2016ApJ...822..111K

Kroupa, P., 2001, *On the variation of the initial mass function*, in Monthly Notes of the Royal Astronomical Society, 322, 231, ADS: 2001MNRAS.322..231K

Krumholz, M. R., Ireland, M. J., & Kratter, K. M., 2020, *Dynamics of small grains in transitional discs*, in Monthly Notes of the Royal Astronomical Society, 498, 3023, ADS: 2020MNRAS.498.3023K

Kuiper, G. P., 1956, *The Formation of the Planets, Part III*, in Journal of the Royal Astronomical Society of Canada, 50, 158, ADS: 1956JRASC..50..158K

Kunitomo, M., Suzuki, T. K., & Inutsuka, S.-i., 2020, *Dispersal of protoplanetary discs by the combination of magnetically driven and photoevaporative winds*, in Monthly Notes of the Royal Astronomical Society, 492, 3849, ADS: 2020MNRAS.492.3849K

Kwan, J., & Tademaru, E., 1988, *Jets from T Tauri Stars: Spectroscopic Evidence and Collimation Mechanism*, in Astrophysical Journal, 332, L41, ADS: 1988ApJ...332L..41K

Kwan, J., & Tademaru, E., 1995, *Disk Winds from T Tauri Stars*, in Astrophysical Journal, 454, 382, ADS: 1995ApJ...454..382K

Labdon, A., Kraus, S., Davies, C. L., Kreplin, A., Kluska, J., et al., 2019, *Dusty disk winds at the sublimation rim of the highly inclined, low mass young stellar object SU Aurigae*, in Astronomy & Astrophysics, 627, A36, ADS: 2019A&A...627A..36L

Lada, C. J., 1987, *Star formation: from OB associations to protostars.*, in Star Forming Regions, edited by M. Peimbert & J. Jugaku, Vol. 115, 1, ADS: 1987IAUS..115....1L

Lada, C. J., & Lada, E. A., 2003, *Embedded Clusters in Molecular Clouds*, in Annual Review of Astronomy and Astrophysics, 41, 57, ADS: 2003ARA&A..41...57L

Lambrechts, M., & Johansen, A., 2012, *Rapid growth of gas-giant cores by pebble accretion*, in Astronomy & Astrophysics, 544, A32, DOI: 10.1051/0004-6361/201219127

Lambrechts, M., & Johansen, A., 2014, *Forming the cores of giant planets from the radial pebble flux in protoplanetary discs*, in Astronomy & Astrophysics, 572, A107, ADS: 2014A&A...572A.107L

Landau, L. D., & Lifschitz, E. M., 2007, *Theoretische Physik. I. Mechanik*, fourteenth edn., Harri Deutsch (Frankfurt am Main)

Langlois, M., Pohl, A., Lagrange, A. M., Maire, A. L., Mesa, D., et al., 2018, *First scattered light detection of a nearly edge-on transition disk around the T Tauri star RY Lupi*, in Astronomy & Astrophysics, 614, A88, ADS: 2018A&A...614A..88L

Lankhaar, B., Vlemmings, W., & Bjerkeli, P., 2022, *Tracing the large-scale magnetic field morphology in protoplanetary disks using molecular line polarization*, in Astronomy & Astrophysics, 657, A106, ADS: 2022A&A...657A.106L

Larson, R. B., 1969, *Numerical calculations of the dynamics of collapsing proto-star*, in Monthly Notes of the Royal Astronomical Society, 145, 271, ADS: `1969MNRAS.145..271L`

Larson, R. B., 1981, *Turbulence and star formation in molecular clouds.*, in Monthly Notes of the Royal Astronomical Society, 194, 809, ADS: `1981MNRAS.194..809L`

Laughlin, G., & Lissauer, J. J., 2015, *Exoplanetary Geophysics: An Emerging Discipline*, in *Treatise on Geophysics*, 2nd edn., edited by G. Schubert, Elsevier (Oxford), 673–694, ADS: `2015trge.book..673L`

Law, C. J., Teague, R., Loomis, R. A., Bae, J., Öberg, K. I., et al., 2021, *Molecules with ALMA at Planet-forming Scales (MAPS). IV. Emission Surfaces and Vertical Distribution of Molecules*, in Astrophysical Journal Supplement Series, 257, 4, ADS: `2021ApJS..257....4L`

Lebreuilly, U., Commerçon, B., & Laibe, G., 2020, *Protostellar collapse: the conditions to form dust-rich protoplanetary disks*, in Astronomy & Astrophysics, 641, A112, ADS: `2020A&A...641A.112L`

Lee, C.-F., Li, Z.-Y., Codella, C., Ho, P. T. P., Podio, L., et al., 2018, *A 100 au Wide Bipolar Rotating Shell Emanating from the HH 212 Protostellar Disk: A Disk Wind?*, in Astrophysical Journal, 856, 14, ADS: `2018ApJ...856...14L`

Lesur, G., 2020, *Magnetohydrodynamics of protoplanetary discs*, in arXiv e-prints, arXiv: `2007.15967`

Lesur, G. R. J., 2021, *Systematic description of wind-driven protoplanetary discs*, in Astronomy & Astrophysics, 650, A35, ADS: `2021A&A...650A..35L`

Lewis, J. S., 1974, *The Temperature Gradient in the Solar Nebula*, in Science, 186, 440, ADS: `1974Sci...186..440L`

Li, A., & Greenberg, J. M., 1997, *A unified model of interstellar dust.*, in Astronomy & Astrophysics, 323, 566

Li, M., & Xiao, L., 2016, *Lifetimes and Accretion Rates of Protoplanetary Disks*, in Astrophysical Journal, 820, 36, ADS: `2016ApJ...820...36L`

Li, Z.-Y., Krasnopolsky, R., & Shang, H., 2011, *Non-ideal MHD Effects and Magnetic Braking Catastrophe in Protostellar Disk Formation*, in Astrophysical Journal, 738, 180, ADS: `2011ApJ...738..180L`

Li, Z. Y., Banerjee, R., Pudritz, R. E., Jørgensen, J. K., Shang, H., et al., 2014, *The Earliest Stages of Star and Planet Formation: Core Collapse, and the Formation of Disks and Outflows*, in Protostars and Planets VI, edited by H. Beuther, R. S. Klessen, C. P. Dullemond, & T. Henning, 173, ADS: `2014prpl.conf..173L`

Lichtenberg, T., Drążkowska, J., Schönbächler, M., Golabek, G. J., & Hands, T. O., 2021, *Bifurcation of planetary building blocks during Solar System formation*, in Science, 371, 365, ADS: `2021Sci...371..365L`

Lin, M.-K., & Papaloizou, J. C. B., 2012, *Outward migration of a giant planet with a gravitationally unstable gap edge*, in Monthly Notes of the Royal Astronomical Society, 421, 780, ADS: `2012MNRAS.421..780L`

Lodato, G., Scardoni, C. E., Manara, C. F., & Testi, L., 2017, *Protoplanetary disc 'isochrones' and the evolution of discs in the* $\dot{M}$*-*M_d *plane*, in Monthly Notes of the Royal Astronomical Society, 472, 4700, ADS: `2017MNRAS.472.4700L`

Louvet, F., Dougados, C., Cabrit, S., Mardones, D., Ménard, F., et al., 2018, *The HH30 edge-on T Tauri star. A rotating and precessing monopolar outflow scrutinized by ALMA*, in Astronomy & Astrophysics, 618, A120, ADS: `2018A&A...618A.120L`

Love, S. G., Joswiak, D. J., & Brownlee, D. E., 1994, *Densities of Stratospheric Micrometeorites*, in Icarus, 111, 227, ADS: `1994Icar..111..227L`

Lubow, S. H., & D'Angelo, G., 2006, *Gas Flow across Gaps in Protoplanetary Disks*, in Astrophysical Journal, 641, 526, ADS: `2006ApJ...641..526L`

Luhman, K. L., Allen, P. R., Espaillat, C., Hartmann, L., & Calvet, N., 2010, *The Disk Population of the Taurus Star-Forming Region*, in Astrophysical Journal Supplement Series, 186, 111, ADS: `2010ApJS..186..111L`

Lynas, M., Houlton, B. Z., & Perry, S., 2021, *Greater than 99% consensus on human caused climate change in the peer-reviewed scientific literature*, in Environmental Research Letters, 16, 114005, ADS: `2021ERL....16k4005L`

Lynden-Bell, D., & Pringle, J. E., 1974, *The evolution of viscous discs and the origin of the nebular variables.*, in Monthly Notes of the Royal Astronomical Society, 168, 603, ADS: `1974MNRAS.168..603L`

Lyra, W., Johansen, A., Klahr, H., & Piskunov, N., 2009, *Standing on the shoulders of giants. Trojan Earths and vortex trapping in low mass self-gravitating protoplanetary disks of gas and solids*, in Astronomy & Astrophysics, 493, 1125, ADS: `2009A&A...493.1125L`

Lyra, W., Haworth, T., Bitsch, B., Casassus, S., Cuello, N., et al., 2019, *Planet formation — The case for large efforts on the computational side*, in Bulletin of the American Astronomical Society, 51, 129, ADS: 2019BAAS...51c.129L

MacFarlane, B., Stamatellos, D., Johnstone, D., Herczeg, G., Baek, G., et al., 2019, *Observational signatures of outbursting protostars - II. Exploring a wide range of eruptive protostars*, in Monthly Notes of the Royal Astronomical Society, 487, 4465, ADS: 2019MNRAS.487.4465M

Madhusudhan, N., Knutson, H., Fortney, J. J., & Barman, T., 2014, *Exoplanetary Atmospheres*, in Protostars and Planets VI, edited by H. Beuther, R. S. Klessen, C. P. Dullemond, & T. Henning, 739, ADS: 2014prpl.conf..739M

Madhusudhan, N., Agúndez, M., Moses, J. I., & Hu, Y., 2016, *Exoplanetary Atmospheres—Chemistry, Formation Conditions, and Habitability*, in Space Science Reviews, 205, 285, ADS: 2016SSRv..205..285M

Madhusudhan, N., 2019, *Exoplanetary Atmospheres: Key Insights, Challenges, and Prospects*, in Annual Review of Astronomy and Astrophysics, 57, 617, ADS: 2019ARA&A..57..617M

Madhusudhan, N., 2021, *ExoFrontiers; Big questions in exoplanetary science*, IOP Publishing, ADS: 2021exbi.book.....M

Madlener, D., Wolf, S., Dutrey, A., & Guilloteau, S., 2012, *The circumstellar disk of HH 30. Searching for signs of disk evolution with multi-wavelength modeling*, in Astronomy & Astrophysics, 543, A81, ADS: 2012A&A...543A..81M

Mamajek, E. E., 2009, *Initial Conditions of Planet Formation: Lifetimes of Primordial Disks*, in American Institute of Physics Conference Series, Vol. 1158, Exoplanets and Disks: Their Formation and Diversity, edited by T. Usuda, M. Tamura, & M. Ishii, 3–10, ADS: 2009AIPC.1158....3M

Manara, C. F., Testi, L., Rigliaco, E., Alcalá, J. M., Natta, A., et al., 2013, *X-shooter spectroscopy of young stellar objects. II. Impact of chromospheric emission on accretion rate estimates*, in Astronomy & Astrophysics, 551, A107, ADS: 2013A&A...551A.107M

Manara, C. F., Testi, L., Natta, A., Rosotti, G., Benisty, M., et al., 2014, *Gas content of transitional disks: a VLT/X-Shooter study of accretion and winds*, in Astronomy & Astrophysics, 568, A18, ADS: 2014A&A...568A..18M

Manara, C. F., Rosotti, G., Testi, L., Natta, A., Alcalá, J. M., et al., 2016, *Evidence for a correlation between mass accretion rates onto young stars and the mass of their protoplanetary disks*, in Astronomy & Astrophysics, 591, L3, ADS: 2016A&A...591L...3M

Mann, R. K., & Williams, J. P., 2010, *A Submillimeter Array Survey of Protoplanetary Disks in the Orion Nebula Cluster*, in Astrophysical Journal, 725, 430, ADS: 2010ApJ...725..430M

Mann, R. K., Di Francesco, J., Johnstone, D., Andrews, S. M., Williams, J. P., et al., 2014, *ALMA Observations of the Orion Proplyds*, in Astrophysical Journal, 784, 82, ADS: 2014ApJ...784...82M

Mann, R. K., Andrews, S. M., Eisner, J. A., Williams, J. P., Meyer, M. R., et al., 2015, *Protoplanetary Disk Masses in the Young NGC 2024 Cluster*, in Astrophysical Journal, 802, 77, ADS: 2015ApJ...802...77M

Marino, S., Perez, S., & Casassus, S., 2015, *Shadows Cast by a Warp in the HD 142527 Protoplanetary Disk*, in Astrophysical Journal, 798, L44, ADS: 2015ApJ...798L..44M

Marsh, K. A., & Mahoney, M. J., 1992, *Evidence for Unseen Companions around T Tauri Stars*, in Astrophysical Journal, 395, L115, ADS: 1992ApJ...395L.115M

Mathis, J. S., Rumpl, W., & Nordsieck, K. H., 1977, *The size distribution of interstellar grains.*, in Astrophysical Journal, 217, 425, ADS: 1977ApJ...217..425M

Mathis, J. S., 1990, *Interstellar dust and extinction.*, in Annual Review of Astronomy and Astrophysics, 28, 37, ADS: 1990ARA&A..28...37M

Matsumoto, T., & Hanawa, T., 2003, *Fragmentation of a Molecular Cloud Core versus Fragmentation of the Massive Protoplanetary Disk in the Main Accretion Phase*, in Astrophysical Journal, 595, 913, ADS: 2003ApJ...595..913M

Mawet, D., Choquet, É., Absil, O., Huby, E., Bottom, M., et al., 2017, *Characterization of the Inner Disk around HD 141569 A from Keck/NIRC2 L-Band Vortex Coronagraphy*, in Astronomical Journal, 153, 44, ADS: 2017AJ....153...44M

Mayor, M., & Queloz, D., 1995, *A Jupiter-mass companion to a solar-type star*, in Nature, 378, 355, ADS: 1995Natur.378..355M

McCabe, C., Duchêne, G., Pinte, C., Stapelfeldt, K. R., Ghez, A. M., et al., 2011, *Spatially Resolving the HK Tau B Edge-on Disk from 1.2 to 4.7 μm: A Unique Scattered Light Disk*, in Astrophysical Journal, 727, 90, ADS: 2011ApJ...727...90M

McKee, C. F., & Ostriker, E. C., 2007, *Theory of Star Formation*, in Annual Review of Astronomy and Astrophysics, 45, 565, ADS: 2007ARA&A..45..565M

Ménard, F., & Duchêne, G., 2004, *On the alignment of Classical T Tauri stars with the magnetic field* *in the Taurus-Auriga molecular cloud*, in Astronomy & Astrophysics, 425, 973, ADS: 2004A&A...425..973M

Michel, A., van der Marel, N., & Matthews, B. C., 2021, *Bridging the Gap between Protoplanetary and Debris Disks: Separate Evolution of Millimeter and Micrometer-sized Dust*, in Astrophysical Journal, 921, 72, ADS: 2021ApJ...921...72M

Mignone, A., Bodo, G., Massaglia, S., Matsakos, T., Tesileanu, O., et al., 2007, *PLUTO: A Numerical Code for Computational Astrophysics*, in Astrophysical Journal Supplement Series, 170, 228, ADS: 2007ApJS..170..228M

Miniati, F., 2010, *A hybrid scheme for gas-dust systems stiffly coupled via viscous drag*, in Journal of Computational Physics, 229, 3916, ADS: 2010JCoPh.229.3916M

Miotello, A., Robberto, M., Potenza, M. A. C., & Ricci, L., 2012, *Evidence of Photoevaporation and Spatial Variation of Grain Sizes in the Orion 114-426 Protoplanetary Disk*, in Astrophysical Journal, 757, 78, ADS: 2012ApJ...757...78M

Miotello, A., van Dishoeck, E. F., Williams, J. P., Ansdell, M., Guidi, G., et al., 2017, *Lupus disks with faint CO isotopologues: low gas/dust or high carbon depletion?*, in Astronomy & Astrophysics, 599, A113, ADS: 2017A&A...599A.113M

Miret-Roig, N., Bouy, H., Raymond, S. N., Tamura, M., Bertin, E., et al., 2022, *A rich population of free-floating planets in the Upper Scorpius young stellar association*, in Nature Astronomy, 6, 89, ADS: 2022NatAs...6...89M

Misener, W., Krijt, S., & Ciesla, F. J., 2019, *Tracking Dust Grains during Transport and Growth in Protoplanetary Disks*, in Astrophysical Journal, 885, 118, ADS: 2019ApJ...885..118M

Mitchell, M., 1936, *Gone with the Wind*, Macmillan Company, New York

Miyake, T., Suzuki, T. K., & Inutsuka, S.-i., 2016, *Dust Dynamics in Protoplanetary Disk Winds Driven by Magnetorotational Turbulence: A Mechanism for Floating Dust Grains with Characteristic Sizes*, in Astrophysical Journal, 821, 3, ADS: 2016ApJ...821....3M

Mohanty, S., & Shu, F. H., 2008, *Magnetocentrifugally Driven Flows from Young Stars and Disks. VI. Accretion with a Multipole Stellar Field*, in Astrophysical Journal, 687, 1323, ADS: 2008ApJ...687.1323M

Mohanty, S., Ercolano, B., & Turner, N. J., 2013, *Dead, Undead, and Zombie Zones in Protostellar Disks as a Function of Stellar Mass*, in Astrophysical Journal, 764, 65, ADS: 2013ApJ...764...65M

Monnier, J. D., Harries, T. J., Bae, J., Setterholm, B. R., Laws, A., et al., 2019, *Multiple Spiral Arms in the Disk around Intermediate-mass Binary HD 34700A*, in Astrophysical Journal, 872, 122, ADS: 2019ApJ...872..122M

Monsch, K., Ercolano, B., Picogna, G., Preibisch, T., & Rau, M. M., 2019, *The imprint of X-ray photoevaporation of planet-forming discs on the orbital distribution of giant planets*, in Monthly Notes of the Royal Astronomical Society, 483, 3448, ADS: 2019MNRAS.483.3448M

Monsch, K., Picogna, G., Ercolano, B., & Kley, W., 2021a, *Giant planet migration during the disc dispersal phase*, in Astronomy & Astrophysics, 646, A169, ADS: 2021A&A...646A.169M

Monsch, K., Picogna, G., Ercolano, B., & Preibisch, T., 2021b, *The imprint of X-ray photoevaporation of planet-forming discs on the orbital distribution of giant planets. II. Theoretical predictions*, in Astronomy & Astrophysics, 650, A199, ADS: 2021A&A...650A.199M

Montesinos, B., Eiroa, C., Mora, A., & Merín, B., 2009, *Parameters of Herbig Ae/Be and Vega-type stars*, in Astronomy & Astrophysics, 495, 901, ADS: 2009A&A...495..901M

Morbidelli, A., & Raymond, S. N., 2016, *Challenges in planet formation*, in Journal of Geophysical Research (Planets), 121, 1962, ADS: 2016JGRE..121.1962M

Mordasini, C., Alibert, Y., & Benz, W., 2009, *Extrasolar planet population synthesis. I. Method, formation tracks, and mass-distance distribution*, in Astronomy & Astrophysics, 501, 1139, ADS: 2009A&A...501.1139M

Mori, S., Bai, X.-N., & Okuzumi, S., 2019, *Temperature Structure in the Inner Regions of Protoplanetary Disks: Inefficient Accretion Heating Controlled by Nonideal Magnetohydrodynamics*, in Astrophysical Journal, 872, 98, ADS: 2019ApJ...872...98M

Morishima, R., 2012, *Gap opening beyond dead zones by photoevaporation*, in Monthly Notes of the Royal Astronomical Society, 420, 2851, ADS: 2012MNRAS.420.2851M

Morishima, R., 2018, *Architectures of planetary systems formed by pebble accretion*, in arXiv e-prints, arXiv: 1804.05510

Muro-Arena, G. A., Ginski, C., Dominik, C., Benisty, M., Pinilla, P., et al., 2020, *Spirals inside the millimeter cavity of transition disk SR 21*, in Astronomy & Astrophysics, 636, L4, ADS: 2020A&A...636L...4M

Muto, T., Grady, C. A., Hashimoto, J., Fukagawa, M., Hornbeck, J. B., et al., 2012, *Discovery of Small-scale Spiral Structures in the Disk of SAO 206462 (HD 135344B): Implications for the Physical State of the Disk from Spiral Density Wave Theory*, in Astrophysical Journal, 748, L22, ADS: `2012ApJ...748L..22M`

Muzerolle, J., Hillenbrand, L., Calvet, N., Briceño, C., & Hartmann, L., 2003a, *Accretion in Young Stellar/Substellar Objects*, in Astrophysical Journal, 592, 266, ADS: `2003ApJ...592..266M`

Muzerolle, J., Calvet, N., Hartmann, L., & D'Alessio, P., 2003b, *Unveiling the Inner Disk Structure of T Tauri Stars*, in Astrophysical Journal, 597, L149, ADS: `2003ApJ...597L.149M`

Najita, J. R., Andrews, S. M., & Muzerolle, J., 2015, *Demographics of transition discs in Ophiuchus and Taurus*, in Monthly Notes of the Royal Astronomical Society, 450, 3559, ADS: `2015MNRAS.450.3559N`

Najita, J. R., & Bergin, E. A., 2018, *Protoplanetary Disk Sizes and Angular Momentum Transport*, in Astrophysical Journal, 864, 168, ADS: `2018ApJ...864..168N`

Nakagawa, Y., Sekiya, M., & Hayashi, C., 1986, *Settling and growth of dust particles in a laminar phase of a low-mass solar nebula*, in Icarus, 67, 375, ADS: `1986Icar...67..375N`

Nakamoto, T., & Nakagawa, Y., 1994, *Formation, Early Evolution, and Gravitational Stability of Protoplanetary Disks*, in Astrophysical Journal, 421, 640, ADS: `1994ApJ...421..640N`

Nakano, T., Nishi, R., & Umebayashi, T., 2002, *Mechanism of Magnetic Flux Loss in Molecular Clouds*, in Astrophysical Journal, 573, 199, ADS: `2002ApJ...573..199N`

Nakatani, R., Hosokawa, T., Yoshida, N., Nomura, H., & Kuiper, R., 2018a, *Radiation Hydrodynamics Simulations of Photoevaporation of Protoplanetary Disks by Ultraviolet Radiation: Metallicity Dependence*, in Astrophysical Journal, 857, 57, ADS: `2018ApJ...857...57N`

Nakatani, R., Hosokawa, T., Yoshida, N., Nomura, H., & Kuiper, R., 2018b, *Radiation Hydrodynamics Simulations of Photoevaporation of Protoplanetary Disks. II. Metallicity Dependence of UV and X-Ray Photoevaporation*, in Astrophysical Journal, 865, 75, ADS: `2018ApJ...865...75N`

Nakatani, R., Kobayashi, H., Kuiper, R., Nomura, H., & Aikawa, Y., 2021, *Photoevaporation of Grain-depleted Protoplanetary Disks around Intermediate-mass Stars: Investigating the Possibility of Gas-rich Debris Disks as Protoplanetary Remnants*, in Astrophysical Journal, 915, 90, ADS: `2021ApJ...915...90N`

Natta, A., Testi, L., & Randich, S., 2006, *Accretion in the ρ-Ophiuchi pre-main sequence stars*, in Astronomy & Astrophysics, 452, 245, ADS: `2006A&A...452..245N`

Natta, A., Testi, L., Alcalá, J. M., Rigliaco, E., Covino, E., et al., 2014, *X-shooter spectroscopy of young stellar objects. V. Slow winds in T Tauri stars*, in Astronomy & Astrophysics, 569, A5, ADS: `2014A&A...569A...5N`

Nelson, R. P., Gressel, O., & Umurhan, O. M., 2013, *Linear and non-linear evolution of the vertical shear instability in accretion discs*, in Monthly Notes of the Royal Astronomical Society, 435, 2610, DOI: `10.1093/mnras/stt1475`

Newton, I., 1687, *Philosophiae Naturalis Principia Mathematica*, ADS: `1687pnpm.book.....N`

Nisini, B., Antoniucci, S., Alcalá, J. M., Giannini, T., Manara, C. F., et al., 2018, *Connection between jets, winds and accretion in T Tauri stars. The X-shooter view*, in Astronomy & Astrophysics, 609, A87, ADS: `2018A&A...609A..87N`

Öberg, K. I., Guzmán, V. V., Walsh, C., Aikawa, Y., Bergin, E. A., et al., 2021, *Molecules with ALMA at Planet-forming Scales (MAPS). I. Program Overview and Highlights*, in Astrophysical Journal Supplement Series, 257, 1, ADS: `2021ApJS..257....1O`

O'Dell, C. R., Wen, Z., & Hu, X., 1993, *Discovery of New Objects in the Orion Nebula on HST Images: Shocks, Compact Sources, and Protoplanetary Disks*, in Astrophysical Journal, 410, 696, ADS: `1993ApJ...410..696O`

O'Dell, C. R., & Wen, Z., 1994, *Postrefurbishment Mission Hubble Space Telescope Images of the Core of the Orion Nebula: Proplyds, Herbig-Haro Objects, and Measurements of a Circumstellar Disk*, in Astrophysical Journal, 436, 194, ADS: `1994ApJ...436..194O`

Offner, S. S. R., Clark, P. C., Hennebelle, P., Bastian, N., Bate, M. R., et al., 2014, *The Origin and Universality of the Stellar Initial Mass Function*, in Protostars and Planets VI, edited by H. Beuther, R. S. Klessen, C. P. Dullemond, & T. Henning, 53, ADS: `2014prpl.conf...53O`

Okamoto, T., & Ida, S., 2022, *Monte Carlo Simulation of Dust Particles in a Protoplanetary Disk: Crystalline to Amorphous Silicate Ratio in Comets*, in arXiv e-prints, arXiv: `2201.05507`

Oreskes, N., Shrader-Frechette, K., & Belitz, K., 1994, *Verification, Validation, and Confirmation of Numerical Models in the Earth Sciences*, in Science, 263, 641, ADS: `1994Sci...263..641O`

Ormel, C. W., & Klahr, H. H., 2010, *The effect of gas drag on the growth of protoplanets. Analytical expressions for the accretion of small bodies in laminar disks*, in Astronomy & Astrophysics, 520, A43,

ADS: 2010A&A...520A..43O
Ormel, C. W., & Liu, B., 2018, *Catching drifting pebbles. II. A stochastic equation of motion for pebbles*, in Astronomy & Astrophysics, 615, A178, ADS: 2018A&A...615A.178O
Orwell, G., 1949, *Nineteen Eighty-Four*, Secker & Warburg
Owen, J. E., Ercolano, B., Clarke, C. J., & Alexander, R. D., 2010, *Radiation-hydrodynamic models of X-ray and EUV photoevaporating protoplanetary discs*, in Monthly Notes of the Royal Astronomical Society, 401, 1415, ADS: 2010MNRAS.401.1415O
Owen, J. E., Ercolano, B., & Clarke, C. J., 2011a, *The imprint of photoevaporation on edge-on discs*, in Monthly Notes of the Royal Astronomical Society, 411, 1104, ADS: 2011MNRAS.411.1104O
Owen, J. E., Ercolano, B., & Clarke, C. J., 2011b, *Protoplanetary disc evolution and dispersal: the implications of X-ray photoevaporation*, in Monthly Notes of the Royal Astronomical Society, 412, 13, ADS: 2011MNRAS.412...13O
Owen, J. E., Clarke, C. J., & Ercolano, B., 2012, *On the theory of disc photoevaporation*, in Monthly Notes of the Royal Astronomical Society, 422, 1880, ADS: 2012MNRAS.422.1880O
Owen, J. E., & Jackson, A. P., 2012, *Planetary evaporation by UV & X-ray radiation: basic hydrodynamics*, in Monthly Notes of the Royal Astronomical Society, 425, 2931, ADS: 2012MNRAS.425.2931O
Owen, J. E., & Clarke, C. J., 2012, *Two populations of transition discs?*, in Monthly Notes of the Royal Astronomical Society, 426, L96, ADS: 2012MNRAS.426L..96O
Owen, J. E., Hudoba de Badyn, M., Clarke, C. J., & Robins, L., 2013, *Characterizing thermal sweeping: a rapid disc dispersal mechanism*, in Monthly Notes of the Royal Astronomical Society, 436, 1430, ADS: 2013MNRAS.436.1430O
Owen, J. E., 2016, *The Origin and Evolution of Transition Discs: Successes, Problems, and Open Questions*, in Publications of the Astronomical Society of Australia, 33, e005, ADS: 2016PASA...33....5O
Owen, J. E., & Kollmeier, J. A., 2019, *Radiation pressure clear-out of dusty photoevaporating discs*, in Monthly Notes of the Royal Astronomical Society, 487, 3702, ADS: 2019MNRAS.487.3702O
Owen, J. E., 2020, *Snow lines can be thermally unstable*, in Monthly Notes of the Royal Astronomical Society, 495, 3160, ADS: 2020MNRAS.495.3160O
Paardekooper, S. J., & Mellema, G., 2004, *Planets opening dust gaps in gas disks*, in Astronomy & Astrophysics, 425, L9, ADS: 2004A&A...425L...9P
Paardekooper, S. J., & Mellema, G., 2006, *Dust flow in gas disks in the presence of embedded planets*, in Astronomy & Astrophysics, 453, 1129, ADS: 2006A&A...453.1129P
Panopoulou, G. V., Psaradaki, I., Skalidis, R., Tassis, K., & Andrews, J. J., 2017, *A closer look at the 'characteristic' width of molecular cloud filaments*, in Monthly Notes of the Royal Astronomical Society, 466, 2529, ADS: 2017MNRAS.466.2529P
Panopoulou, G. V., Clark, S. E., Hacar, A., Heitsch, F., Kainulainen, J., et al., 2022, *The width of Herschel filaments varies with distance*, in Astronomy & Astrophysics, 657, L13, ADS: 2022A&A...657L..13P
Parker, E. N., 1958, *Dynamics of the Interplanetary Gas and Magnetic Fields.*, in Astrophysical Journal, 128, 664, ADS: 1958ApJ...128..664P
Parker, E. N., 1965, *Dynamical Theory of the Solar Wind*, in Space Science Reviews, 4, 666, ADS: 1965SSRv....4..666P
Parker, R. J., 2020, *The birth environment of planetary systems*, in Royal Society Open Science, 7, 201271, ADS: 2020RSOS....701271P
Parker, R. J., Nicholson, R. B., & Alcock, H. L., 2021a, *Far and extreme ultraviolet radiation fields and consequent disc destruction in star-forming regions*, in Monthly Notes of the Royal Astronomical Society, 502, 2665, ADS: 2021MNRAS.502.2665P
Parker, R. J., Alcock, H. L., Nicholson, R. B., Panić, O., & Goodwin, S. P., 2021b, *External Photoevaporation of Protoplanetary Disks: Does Location Matter?*, in Astrophysical Journal, 913, 95, ADS: 2021ApJ...913...95P
Pascucci, I., Apai, D., Hardegree-Ullman, E. E., Kim, J. S., Meyer, M. R., et al., 2008, *Medium-Separation Binaries Do Not Affect the First Steps of Planet Formation*, in Astrophysical Journal, 673, 477, ADS: 2008ApJ...673..477P
Pascucci, I., & Sterzik, M., 2009, *Evidence for Disk Photoevaporation Driven by the Central Star*, in Astrophysical Journal, 702, 724, ADS: 2009ApJ...702..724P
Pascucci, I., Testi, L., Herczeg, G. J., Long, F., Manara, C. F., et al., 2016, *A Steeper than Linear Disk Mass-Stellar Mass Scaling Relation*, in Astrophysical Journal, 831, 125, ADS: 2016ApJ...831..125P
Pascucci, I., Andrews, S., Chandler, C., & Isella, A., 2018, *Disk Winds and the Evolution of Planet-Forming Disks*, in Astronomical Society of the Pacific Conference Series, Vol. 517, Science with a Next Generation Very Large Array, edited by E. Murphy, 155, ADS: 2018ASPC..517..155P

Pascucci, I., Banzatti, A., Gorti, U., Fang, M., Pontoppidan, K., et al., 2020, *The Evolution of Disk Winds from a Combined Study of Optical and Infrared Forbidden Lines*, in Astrophysical Journal, 903, 78, ADS: `2020ApJ...903...78P`

Pedbost, M. F., Pomalgu, T., Lintott, C., Eisner, N., & Nicholson, B., 2020, *Defining the Really Habitable Zone*, in arXiv e-prints, arXiv: `2003.13722`

Penston, M. V., 1969, *Dynamics of self-gravitating gaseous spheres-II. Collapses of gas spheres with cooling and the behaviour of polytropic gas spheres*, in Monthly Notes of the Royal Astronomical Society, 145, 457, ADS: `1969MNRAS.145..457P`

Pérez, L. M., Carpenter, J. M., Andrews, S. M., Ricci, L., Isella, A., et al., 2016, *Spiral density waves in a young protoplanetary disk*, in Science, 353, 1519, ADS: `2016Sci...353.1519P`

Perez, M. R., & Grady, C. A., 1997, *Observational Overview of Young Intermediate-Mass Objects: Herbig Ae/Be Stars*, in Space Science Reviews, 82, 407, ADS: `1997SSRv...82..407P`

Pérez, S., Casassus, S., Ménard, F., Roman, P., van der Plas, G., et al., 2015, *CO Gas Inside the Protoplanetary Disk Cavity in HD 142527: Disk Structure from ALMA*, in Astrophysical Journal, 798, 85, ADS: `2015ApJ...798...85P`

Perez-Becker, D., & Chiang, E., 2011, *Surface Layer Accretion in Conventional and Transitional Disks Driven by Far-ultraviolet Ionization*, in Astrophysical Journal, 735, 8, ADS: `2011ApJ...735....8P`

Perrin, M. D., Duchêne, G., Kalas, P., & Graham, J. R., 2006, *Discovery of an Optically Thick, Edge-on Disk around the Herbig Ae Star PDS 144N*, in Astrophysical Journal, 645, 1272, ADS: `2006ApJ...645.1272P`

Petrov, P. P., Grankin, K. N., Gameiro, J. F., Artemenko, S. A., Babina, E. V., et al., 2019, *Dynamics of wind and the dusty environments in the accreting T Tauri stars RY Tauri and SU Aurigae*, in Monthly Notes of the Royal Astronomical Society, 483, 132, ADS: `2019MNRAS.483..132P`

Picogna, G., Stoll, M. H. R., & Kley, W., 2018, *Particle accretion onto planets in discs with hydrodynamic turbulence*, in Astronomy & Astrophysics, 616, A116, ADS: `2018A&A...616A.116P`

Picogna, G., Ercolano, B., Owen, J. E., & Weber, M. L., 2019, *The dispersal of protoplanetary discs - I. A new generation of X-ray photoevaporation models*, in Monthly Notes of the Royal Astronomical Society, 487, 691, ADS: `2019MNRAS.487..691P`

Picogna, G., Ercolano, B., & Espaillat, C. C., 2021, *The dispersal of protoplanetary discs - III. Influence of stellar mass on disc photoevaporation*, in Monthly Notes of the Royal Astronomical Society, 508, 3611, ADS: `2021MNRAS.508.3611P`

Pinilla, P., Birnstiel, T., Ricci, L., Dullemond, C. P., Uribe, A. L., et al., 2012a, *Trapping dust particles in the outer regions of protoplanetary disks*, in Astronomy & Astrophysics, 538, A114, ADS: `2012A&A...538A.114P`

Pinilla, P., Benisty, M., & Birnstiel, T., 2012b, *Ring shaped dust accumulation in transition disks*, in Astronomy & Astrophysics, 545, A81, ADS: `2012A&A...545A..81P`

Pinilla, P., Klarmann, L., Birnstiel, T., Benisty, M., Dominik, C., et al., 2016, *A tunnel and a traffic jam: How transition disks maintain a detectable warm dust component despite the presence of a large planet-carved gap*, in Astronomy & Astrophysics, 585, A35, ADS: `2016A&A...585A..35P`

Pinilla, P., Benisty, M., Cazzoletti, P., Harsono, D., Pérez, L. M., et al., 2019, *An Inner Disk in the Large Gap of the Transition Disk SR 24S*, in Astrophysical Journal, 878, 16, ADS: `2019ApJ...878...16P`

Pinilla, P., Kurtovic, N. T., Benisty, M., Manara, C. F., Natta, A., et al., 2021, *A bright inner disk and structures in the transition disk around the very low-mass star CIDA 1*, in Astronomy & Astrophysics, 649, A122, ADS: `2021A&A...649A.122P`

Pinte, C., Padgett, D. L., Ménard, F., Stapelfeldt, K. R., Schneider, G., et al., 2008, *Probing dust grain evolution in IM Lupi's circumstellar disc. Multi-wavelength observations and modelling of the dust disc*, in Astronomy & Astrophysics, 489, 633, ADS: `2008A&A...489..633P`

Pinte, C., Dent, W. R. F., Ménard, F., Hales, A., Hill, T., et al., 2016, *Dust and Gas in the Disk of HL Tauri: Surface Density, Dust Settling, and Dust-to-gas Ratio*, in Astrophysical Journal, 816, 25, ADS: `2016ApJ...816...25P`

Pinte, C., Ménard, F., Duchêne, G., Hill, T., Dent, W. R. F., et al., 2018, *Direct mapping of the temperature and velocity gradients in discs. Imaging the vertical CO snow line around IM Lupi*, in Astronomy & Astrophysics, 609, A47, ADS: `2018A&A...609A..47P`

Planck Collaboration, Aghanim, N., Akrami, Y., Ashdown, M., Aumont, J., et al., 2020, *Planck 2018 results. VI. Cosmological parameters*, in Astronomy & Astrophysics, 641, A6, ADS: `2020A&A...641A...6P`

Podio, L., Garufi, A., Codella, C., Fedele, D., Bianchi, E., et al., 2020, *ALMA chemical survey of disk-outflow sources in Taurus (ALMA-DOT). II. Vertical stratification of CO, CS, CN, H_2CO, and CH_3OH*

in a Class I disk, in Astronomy & Astrophysics, 642, L7, ADS: 2020A&A...642L...7P

Pollack, J. B., Hollenbach, D., Beckwith, S., Simonelli, D. P., Roush, T., et al., 1994, *Composition and Radiative Properties of Grains in Molecular Clouds and Accretion Disks*, in Astrophysical Journal, 421, 615, ADS: 1994ApJ...421..615P

Pontoppidan, K. M., Blake, G. A., & Smette, A., 2011, *The Structure and Dynamics of Molecular Gas in Planet-forming Zones: A CRIRES Spectro-astrometric Survey*, in Astrophysical Journal, 733, 84, ADS: 2011ApJ...733...84P

Popper, K., 1935, *Logik der Forschung*, edited by P. Frank & M. Schlick, Springer Verlag Wien

Preibisch, T., & Feigelson, E. D., 2005, *The Evolution of X-Ray Emission in Young Stars*, in Astrophysical Journal Supplement Series, 160, 390, ADS: 2005ApJS..160..390P

Preibisch, T., Kim, Y.-C., Favata, F., Feigelson, E. D., Flaccomio, E., et al., 2005, *The Origin of T Tauri X-Ray Emission: New Insights from the Chandra Orion Ultradeep Project*, in Astrophysical Journal Supplement Series, 160, 401, ADS: 2005ApJS..160..401P

Preibisch, T., Mehlhorn, M., Townsley, L., Broos, P., & Ratzka, T., 2014, *Chandra X-ray observation of the H ii region Gum 31 in the Carina nebula complex*, in Astronomy & Astrophysics, 564, A120, ADS: 2014A&A...564A.120P

Prialnik, D., 2010, *An Introduction to the Theory of Stellar Structure and Evolution*, 2nd edn., Cambridge University Press, ADS: 2000itss.book.....P

Price, D. J., 2007, *splash: An Interactive Visualisation Tool for Smoothed Particle Hydrodynamics Simulations*, in Publications of the Astronomical Society of Australia, 24, 159, ADS: 2007PASA...24..159P

Pringle, J. E., 1981, *Accretion discs in astrophysics*, in Annual Review of Astronomy and Astrophysics, 19, 137, ADS: 1981ARA&A..19..137P

Quintana, E. V., Barclay, T., Raymond, S. N., Rowe, J. F., Bolmont, E., et al., 2014, *An Earth-Sized Planet in the Habitable Zone of a Cool Star*, in Science, 344, 277, ADS: 2014Sci...344..277Q

Rab, C., Güdel, M., Padovani, M., Kamp, I., Thi, W. F., et al., 2017, *Stellar energetic particle ionization in protoplanetary disks around T Tauri stars*, in Astronomy & Astrophysics, 603, A96, ADS: 2017A&A...603A..96R

Rab, C., Güdel, M., Woitke, P., Kamp, I., Thi, W. F., et al., 2018, *X-ray radiative transfer in protoplanetary disks. The role of dust and X-ray background fields*, in Astronomy & Astrophysics, 609, A91, ADS: 2018A&A...609A..91R

Rafikov, R. R., 2017, *Protoplanetary Disks as (Possibly) Viscous Disks*, in Astrophysical Journal, 837, 163, ADS: 2017ApJ...837..163R

Rahul, K. K., Shivakarthik, E., Meka, J. K., Das, A., Chandrasekaran, V., et al., 2020, *Residue from vacuum ultraviolet irradiation of benzene ices: Insights into the physical structure of astrophysical dust*, in Spectrochimica Acta Part A: Molecular Spectroscopy, 231, 117797, ADS: 2020AcSpA.23117797R

Ray, T., Dougados, C., Bacciotti, F., Eislöffel, J., & Chrysostomou, A., 2007, *Toward Resolving the Outflow Engine: An Observational Perspective*, in Protostars and Planets V, edited by B. Reipurth, D. Jewitt, & K. Keil, 231, ADS: 2007prpl.conf..231R

Raymond, S. N., & Morbidelli, A., 2020, *Planet formation: key mechanisms and global models*, in arXiv e-prints, arXiv: 2002.05756

Ribas, Á., Merín, B., Bouy, H., & Maud, L. T., 2014, *Disk evolution in the solar neighborhood. I. Disk frequencies from 1 to 100 Myr*, in Astronomy & Astrophysics, 561, A54, ADS: 2014A&A...561A..54R

Ricci, L., Testi, L., Natta, A., Neri, R., Cabrit, S., et al., 2010a, *Dust properties of protoplanetary disks in the Taurus-Auriga star forming region from millimeter wavelengths*, in Astronomy & Astrophysics, 512, A15, ADS: 2010A&A...512A..15R

Ricci, L., Testi, L., Natta, A., & Brooks, K. J., 2010b, *Dust grain growth in ρ-Ophiuchi protoplanetary disks*, in Astronomy & Astrophysics, 521, A66, ADS: 2010A&A...521A..66R

Ricci, L., Harter, S. K., Ercolano, B., & Weber, M., 2021, *Testing Photoevaporation and MHD Disk Wind Models through Future High-angular Resolution Radio Observations: The Case of TW Hydrae*, in Astrophysical Journal, 913, 122, ADS: 2021ApJ...913..122R

Rich, E. A., Teague, R., Monnier, J. D., Davies, C. L., Bosman, A., et al., 2021, *Investigating the Relative Gas and Small Dust Grain Surface Heights in Protoplanetary Disks*, in Astrophysical Journal, 913, 138, ADS: 2021ApJ...913..138R

Richert, A. J. W., Getman, K. V., Feigelson, E. D., Kuhn, M. A., Broos, P. S., et al., 2018, *Circumstellar disc lifetimes in numerous galactic young stellar clusters*, in Monthly Notes of the Royal Astronomical Society, 477, 5191, ADS: 2018MNRAS.477.5191R

Rieke, M. J., Baum, S. A., Beichman, C. A., Crampton, D., Doyon, R., et al., 2003, *NGST NIRCam Scientific Program and Design Concept*, in Society of Photo-Optical Instrumentation Engineers (SPIE)

Conference Series, Vol. 4850, IR Space Telescopes and Instruments, edited by J. C. Mather, 478–485, ADS: 2003SPIE.4850..478R

Rieke, M. J., Kelly, D., & Horner, S., 2005, *Overview of James Webb Space Telescope and NIRCam's Role*, in Society of Photo-Optical Instrumentation Engineers (SPIE) Conference Series, Vol. 5904, Cryogenic Optical Systems and Instruments XI, edited by J. B. Heaney & L. G. Burriesci, 1–8, ADS: 2005SPIE.5904....1R

Riess, A. G., Casertano, S., Yuan, W., Macri, L. M., & Scolnic, D., 2019, *Large Magellanic Cloud Cepheid Standards Provide a 1% Foundation for the Determination of the Hubble Constant and Stronger Evidence for Physics beyond ΛCDM*, in Astrophysical Journal, 876, 85, ADS: 2019ApJ...876...85R

Rigliaco, E., Pascucci, I., Gorti, U., Edwards, S., & Hollenbach, D., 2013, *Understanding the Origin of the [O I] Low-velocity Component from T Tauri Stars*, in Astrophysical Journal, 772, 60, ADS: 2013ApJ...772...60R

Robitaille, T. P., Whitney, B. A., Indebetouw, R., Wood, K., & Denzmore, P., 2006, *Interpreting Spectral Energy Distributions from Young Stellar Objects. I. A Grid of 200,000 YSO Model SEDs*, in Astrophysical Journal Supplement Series, 167, 256, ADS: 2006ApJS..167..256R

Rodenkirch, P. J., Klahr, H., Fendt, C., & Dullemond, C. P., 2020, *Global axisymmetric simulations of photoevaporation and magnetically driven protoplanetary disk winds*, in Astronomy & Astrophysics, 633, A21, ADS: 2020A&A...633A..21R

Rodenkirch, P. J., Rometsch, T., Dullemond, C. P., Weber, P., & Kley, W., 2021, *Modeling the nonaxisymmetric structure in the HD 163296 disk with planet-disk interaction*, in Astronomy & Astrophysics, 647, A174, ADS: 2021A&A...647A.174R

Rodenkirch, P. J., & Dullemond, C. P., 2022, *Dust entrainment in magnetically and thermally driven disk winds*, in Astronomy & Astrophysics, 659, A42, ADS: 2022A&A...659A..42R

Rodriguez, J. E., Pepper, J., Stassun, K. G., Siverd, R. J., Cargile, P., et al., 2013, *Occultation of the T Tauri Star RW Aurigae A by its Tidally Disrupted Disk*, in Astronomical Journal, 146, 112, ADS: 2013AJ....146..112R

Romanova, M. M., Ustyugova, G. V., Koldoba, A. V., & Lovelace, R. V. E., 2013, *Warps, bending and density waves excited by rotating magnetized stars: results of global 3D MHD simulations*, in Monthly Notes of the Royal Astronomical Society, 430, 699, ADS: 2013MNRAS.430..699R

Rometsch, T., Rodenkirch, P. J., Kley, W., & Dullemond, C. P., 2020, *Migration jumps of planets in transition discs*, in Astronomy & Astrophysics, 643, A87, ADS: 2020A&A...643A..87R

Rometsch, T., Ziampras, A., Kley, W., & Béthune, W., 2021, *Survival of planet-induced vortices in 2D disks*, in Astronomy & Astrophysics, 656, A130, ADS: 2021A&A...656A.130R

Ros, K., & Johansen, A., 2013, *Ice condensation as a planet formation mechanism*, in Astronomy & Astrophysics, 552, A137, ADS: 2013A&A...552A.137R

Rosenfeld, K. A., Andrews, S. M., Hughes, A. M., Wilner, D. J., & Qi, C., 2013, *A Spatially Resolved Vertical Temperature Gradient in the HD 163296 Disk*, in Astrophysical Journal, 774, 16, ADS: 2013ApJ...774...16R

Rosotti, G. P., Ercolano, B., & Owen, J. E., 2015, *The long-term evolution of photoevaporating transition discs with giant planets*, in Monthly Notes of the Royal Astronomical Society, 454, 2173, ADS: 2015MNRAS.454.2173R

Rosotti, G. P., Tazzari, M., Booth, R. A., Testi, L., Lodato, G., et al., 2019, *The time evolution of dusty protoplanetary disc radii: observed and physical radii differ*, in Monthly Notes of the Royal Astronomical Society, 486, 4829, ADS: 2019MNRAS.486.4829R

Russell, H. N., 1914a, *Relations Between the Spectra and Other Characteristics of the Stars*, in Popular Astronomy, 22, 275, ADS: 1914PA.....22..275R

Russell, H. N., 1914b, *Relations Between the Spectra and Other Characteristics of the Stars*, in Popular Astronomy, 22, 331, ADS: 1914PA.....22..331R

Safier, P. N., 1993, *Centrifugally Driven Winds from Protostellar Disks. I. Wind Model and Thermal Structure*, in Astrophysical Journal, 408, 115, ADS: 1993ApJ...408..115S

Sai, J., Ohashi, N., Saigo, K., Matsumoto, T., Aso, Y., et al., 2020, *Disk Structure around the Class I Protostar L1489 IRS Revealed by ALMA: A Warped-disk System*, in Astrophysical Journal, 893, 51, ADS: 2020ApJ...893...51S

Salpeter, E. E., 1955, *The Luminosity Function and Stellar Evolution.*, in Astrophysical Journal, 121, 161, ADS: 1955ApJ...121..161S

Sanchis, E., Testi, L., Natta, A., Facchini, S., Manara, C. F., et al., 2021, *Measuring the ratio of the gas and dust emission radii of protoplanetary disks in the Lupus star-forming region*, in Astronomy & Astrophysics, 649, A19, ADS: 2021A&A...649A..19S

Savvidou, S., Bitsch, B., & Lambrechts, M., 2020, *Influence of grain growth on the thermal structure of protoplanetary discs*, in Astronomy & Astrophysics, 640, A63, ADS: `2020A&A...640A..63S`

Scally, A., & Clarke, C., 2001, *Destruction of protoplanetary discs in the Orion Nebula Cluster*, in Monthly Notes of the Royal Astronomical Society, 325, 449, ADS: `2001MNRAS.325..449S`

Schaffer, N., Yang, C.-C., & Johansen, A., 2018, *Streaming instability of multiple particle species in protoplanetary disks*, in Astronomy & Astrophysics, 618, A75, ADS: `2018A&A...618A..75S`

Schmid, H. M., Joos, F., & Tschan, D., 2006, *Limb polarization of Uranus and Neptune. I. Imaging polarimetry and comparison with analytic models*, in Astronomy & Astrophysics, 452, 657, ADS: `2006A&A...452..657S`

Schneider, G., Grady, C. A., Hines, D. C., Stark, C. C., Debes, J. H., et al., 2014, *Probing for Exoplanets Hiding in Dusty Debris Disks: Disk Imaging, Characterization, and Exploration with HST/STIS Multi-roll Coronagraphy*, in Astronomical Journal, 148, 59, ADS: `2014AJ....148...59S`

Schneider, G., Debes, J. H., Grady, C. A., Gáspár, A., Henning, T., et al., 2018, *The HR 4796A Debris System: Discovery of Extensive Exo-ring Dust Material*, in Astronomical Journal, 155, 77, ADS: `2018AJ....155...77S`

Scholz, A., Jayawardhana, R., Muzic, K., Geers, V., Tamura, M., et al., 2012, *Substellar Objects in Nearby Young Clusters (SONYC). VI. The Planetary-mass Domain of NGC 1333*, in Astrophysical Journal, 756, 24, ADS: `2012ApJ...756...24S`

Schräpler, R., & Henning, T., 2004, *Dust Diffusion, Sedimentation, and Gravitational Instabilities in Protoplanetary Disks*, in Astrophysical Journal, 614, 960, ADS: `2004ApJ...614..960S`

Segura-Cox, D. M., Schmiedeke, A., Pineda, J. E., Stephens, I. W., Fernández-López, M., et al., 2020, *Four annular structures in a protostellar disk less than 500,000 years old*, in Nature, 586, 228, ADS: `2020Natur.586..228S`

Selina, R. J., Murphy, E. J., McKinnon, M., Beasley, A., Butler, B., et al., 2018, *The ngVLA Reference Design*, in Astronomical Society of the Pacific Conference Series, Vol. 517, Science with a Next Generation Very Large Array, edited by E. Murphy, 15, ADS: `2018ASPC..517...15S`

Sellek, A. D., Booth, R. A., & Clarke, C. J., 2020a, *The evolution of dust in discs influenced by external photoevaporation*, in Monthly Notes of the Royal Astronomical Society, 492, 1279, ADS: `2020MNRAS.492.1279S`

Sellek, A. D., Booth, R. A., & Clarke, C. J., 2020b, *A dusty origin for the correlation between protoplanetary disc accretion rates and dust masses*, in Monthly Notes of the Royal Astronomical Society, 498, 2845, ADS: `2020MNRAS.498.2845S`

Sellek, A. D., Clarke, C. J., & Booth, R. A., 2021, *The general applicability of self-similar solutions for thermal disc winds*, in Monthly Notes of the Royal Astronomical Society, 506, 1, ADS: `2021MNRAS.506....1S`

Serabyn, E., Huby, E., Matthews, K., Mawet, D., Absil, O., et al., 2017, *The W. M. Keck Observatory Infrared Vortex Coronagraph and a First Image of HIP 79124 B*, in Astronomical Journal, 153, 43, ADS: `2017AJ....153...43S`

Shadmehri, M., Khajenabi, F., & Pessah, M. E., 2018, *On the Dynamics of Pebbles in Protoplanetary Disks with Magnetically Driven Winds*, in Astrophysical Journal, 863, 33, ADS: `2018ApJ...863...33S`

Shakura, N. I., & Sunyaev, R. A., 1973, *Black holes in binary systems. Observational appearance.*, in Astronomy & Astrophysics, 500, 33, ADS: `1973A&A....24..337S`

Shang, H., Glassgold, A. E., Shu, F. H., & Lizano, S., 2002, *Heating and Ionization of X-Winds*, in Astrophysical Journal, 564, 853, ADS: `2002ApJ...564..853S`

Sheikhnezami, S., Fendt, C., Porth, O., Vaidya, B., & Ghanbari, J., 2012, *Bipolar Jets Launched from Magnetically Diffusive Accretion Disks. I. Ejection Efficiency versus Field Strength and Diffusivity*, in Astrophysical Journal, 757, 65, ADS: `2012ApJ...757...65S`

Shi, J.-M., & Chiang, E., 2014, *Gravito-turbulent Disks in Three Dimensions: Turbulent Velocities versus Depth*, in Astrophysical Journal, 789, 34, ADS: `2014ApJ...789...34S`

Shu, F. H., 1977, *Self-similar collapse of isothermal spheres and star formation.*, in Astrophysical Journal, 214, 488, ADS: `1977ApJ...214..488S`

Shu, F. H., Adams, F. C., & Lizano, S., 1987, *Star formation in molecular clouds: observation and theory.*, in Annual Review of Astronomy and Astrophysics, 25, 23, ADS: `1987ARA&A..25...23S`

Shu, F. H., Najita, J. R., Shang, H., & Li, Z. Y., 2000, *X-Winds Theory and Observations*, in Protostars and Planets IV, edited by V. Mannings, A. P. Boss, & S. S. Russell, 789–814, ADS: `2000prpl.conf..789S`

Siebenmorgen, R., & Krügel, E., 2010, *The destruction and survival of polycyclic aromatic hydrocarbons in the disks of T Tauri stars*, in Astronomy and Astrophysics, 511, A6, ADS: `2010A&A...511A...6S`

Siebenmorgen, R., & Heymann, F., 2012, *Polycyclic aromatic hydrocarbons in protoplanetary disks: emission and X-ray destruction*, in Astronomy and Astrophysics, 543, A25, ADS: 2012A&A...543A..25S

Silverberg, S. M., Wisniewski, J. P., Kuchner, M. J., Lawson, K. D., Bans, A. S., et al., 2020, *Peter Pan Disks: Long-lived Accretion Disks Around Young M Stars*, in Astrophysical Journal, 890, 106, ADS: 2020ApJ...890..106S

Simon, J. B., Bai, X.-N., Stone, J. M., Armitage, P. J., & Beckwith, K., 2013a, *Turbulence in the Outer Regions of Protoplanetary Disks. I. Weak Accretion with No Vertical Magnetic Flux*, in Astrophysical Journal, 764, 66, ADS: 2013ApJ...764...66S

Simon, J. B., Bai, X.-N., Armitage, P. J., Stone, J. M., & Beckwith, K., 2013b, *Turbulence in the Outer Regions of Protoplanetary Disks. II. Strong Accretion Driven by a Vertical Magnetic Field*, in Astrophysical Journal, 775, 73, ADS: 2013ApJ...775...73S

Simon, M. N., Pascucci, I., Edwards, S., Feng, W., Gorti, U., et al., 2016, *Tracing Slow Winds from T Tauri Stars via Low-velocity Forbidden Line Emission*, in Astrophysical Journal, 831, 169, ADS: 2016ApJ...831..169S

Skrutskie, M. F., Dutkevitch, D., Strom, S. E., Edwards, S., Strom, K. M., et al., 1990, *A Sensitive 10-Micron Search for Emission Arising from Circumstellar Dust Associated with Solar-Type Pre-Main-Sequence Stars*, in Astronomical Journal, 99, 1187, ADS: 1990AJ.....99.1187S

Smoluchowski, M. V., 1916, *Drei Vorträge über Diffusion, Brownsche Bewegung und Koagulation von Kolloidteilchen*, in Zeitschrift fur Physik, 17, 557, ADS: 1916ZPhy...17..557S

Soon, K.-L., Momose, M., Muto, T., Tsukagoshi, T., Kataoka, A., et al., 2019, *Investigating the gas-to-dust ratio in the protoplanetary disk of HD 142527*, in Publications of the Astronomical Society of Japan, 71, 124, ADS: 2019PASJ...71..124S

Stamatellos, D., & Inutsuka, S.-i., 2018, *The diverse lives of massive protoplanets in self-gravitating discs*, in Monthly Notes of the Royal Astronomical Society, 477, 3110, ADS: 2018MNRAS.477.3110S

Stammler, S., 2018, *A Closer Look on Dust Growth: The Spectral Index*, in Take a Closer Look, 109, ADS: 2018tcl..confE.109S

Stammler, S. M., Birnstiel, T., & Dullemond, C. P., 2017, *Can ice lines create rings? The influence of ice lines on dust growth in protoplanetary disks*, in Revista Mexicana de Astronomia y Astrofisica Conference Series, Vol. 49, Revista Mexicana de Astronomia y Astrofisica Conference Series, 78–78, ADS: 2017RMxAC..49...78S

Stapelfeldt, K. R., Krist, J. E., Ménard, F., Bouvier, J., Padgett, D. L., et al., 1998, *An Edge-On Circumstellar Disk in the Young Binary System HK Tauri*, in Astrophysical Journal, 502, L65, ADS: 1998ApJ...502L..65S

Stapelfeldt, K. R., Ménard, F., Watson, A. M., Krist, J. E., Dougados, C., et al., 2003, *Hubble Space Telescope WFPC2 Imaging of the Disk and Jet of HV Tauri C*, in Astrophysical Journal, 589, 410, ADS: 2003ApJ...589..410S

Stokes, G. G., 1851, *On the Effect of the Internal Friction of Fluids on the Motion of Pendulums*, in Transactions of the Cambridge Philosophical Society, 9, 8, ADS: 1851TCaPS...9....8S

Stolker, T., Dominik, C., Avenhaus, H., Min, M., de Boer, J., et al., 2016, *Shadows cast on the transition disk of HD 135344B. Multiwavelength VLT/SPHERE polarimetric differential imaging*, in Astronomy & Astrophysics, 595, A113, ADS: 2016A&A...595A.113S

Strom, K. M., Strom, S. E., Edwards, S., Cabrit, S., & Skrutskie, M. F., 1989, *Circumstellar Material Associated with Solar-Type Pre-Main-Sequence Stars: A Possible Constraint on the Timescale for Planet Building*, in Astronomical Journal, 97, 1451, ADS: 1989AJ.....97.1451S

Suzuki, D., Bennett, D. P., Sumi, T., Bond, I. A., Rogers, L. A., et al., 2016a, *The Exoplanet Mass-ratio Function from the MOA-II Survey: Discovery of a Break and Likely Peak at a Neptune Mass*, in Astrophysical Journal, 833, 145, ADS: 2016ApJ...833..145S

Suzuki, T. K., 2007, *Structured Red Giant Winds with Magnetized Hot Bubbles and the Corona/Cool Wind Dividing Line*, in Astrophysical Journal, 659, 1592, ADS: 2007ApJ...659.1592S

Suzuki, T. K., & Inutsuka, S.-i., 2009, *Disk Winds Driven by Magnetorotational Instability and Dispersal of Protoplanetary Disks*, in Astrophysical Journal, 691, L49, ADS: 2009ApJ...691L..49S

Suzuki, T. K., Ogihara, M., Morbidelli, A., Crida, A., & Guillot, T., 2016b, *Evolution of protoplanetary discs with magnetically driven disc winds*, in Astronomy & Astrophysics, 596, A74, ADS: 2016A&A...596A..74S

Tabone, B., Rosotti, G. P., Lodato, G., Armitage, P. J., Cridland, A. J., et al., 2021, *MHD disc winds can reproduce fast disc dispersal and the correlation between accretion rate and disc mass in Lupus*, in Monthly Notes of the Royal Astronomical Society, ADS: 2021MNRAS.tmpL.109T

Takeuchi, T., & Artymowicz, P., 2001, *Dust Migration and Morphology in Optically Thin Circumstellar*

Gas Disks, in Astrophysical Journal, 557, 990, ADS: 2001ApJ...557..990T
Takeuchi, T., & Lin, D. N. C., 2002, *Radial Flow of Dust Particles in Accretion Disks*, in Astrophysical Journal, 581, 1344, ADS: 2002ApJ...581.1344T
Takeuchi, T., & Lin, D. N. C., 2003, *Surface Outflow in Optically Thick Dust Disks by Radiation Pressure*, in Astrophysical Journal, 593, 524, ADS: 2003ApJ...593..524T
Takeuchi, T., & Lin, D. N. C., 2005, *Attenuation of Millimeter Emission from Circumstellar Disks Induced by the Rapid Dust Accretion*, in Astrophysical Journal, 623, 482, ADS: 2005ApJ...623..482T
Takeuchi, T., Clarke, C. J., & Lin, D. N. C., 2005, *The Differential Lifetimes of Protostellar Gas and Dust Disks*, in Astrophysical Journal, 627, 286, ADS: 2005ApJ...627..286T
Tamfal, T., Drążkowska, J., Mayer, L., & Surville, C., 2018, *A Subgrid Model for the Growth of Dust Particles in Hydrodynamical Simulations of Protoplanetary Disks*, in Astrophysical Journal, 863, 97, ADS: 2018ApJ...863...97T
Tanaka, K. E. I., Nakamoto, T., & Omukai, K., 2013, *Photoevaporation of Circumstellar Disks Revisited: The Dust-free Case*, in Astrophysical Journal, 773, 155, ADS: 2013ApJ...773..155T
Tarter, C. B., & Salpeter, E. E., 1969, *The Interaction of X-Ray Sources with Optically Thick Environments*, in Astrophysical Journal, 156, 953, ADS: 1969ApJ...156..953T
Tarter, C. B., Tucker, W. H., & Salpeter, E. E., 1969, *The Interaction of X-Ray Sources with Optically Thin Environments*, in Astrophysical Journal, 156, 943, ADS: 1969ApJ...156..943T
Tazaki, R., & Nomura, H., 2015, *Outward Motion of Porous Dust Aggregates by Stellar Radiation Pressure in Protoplanetary Disks*, in Astrophysical Journal, 799, 119, ADS: 2015ApJ...799..119T
Tazzari, M., Clarke, C. J., Testi, L., Williams, J. P., Facchini, S., et al., 2021, *Multiwavelength continuum sizes of protoplanetary discs: scaling relations and implications for grain growth and radial drift*, in Monthly Notes of the Royal Astronomical Society, 506, 2804, ADS: 2021MNRAS.506.2804T
Telleschi, A., Güdel, M., Briggs, K. R., Audard, M., & Palla, F., 2007, *X-ray emission from T Tauri stars and the role of accretion: inferences from the XMM-Newton extended survey of the Taurus molecular cloud*, in Astronomy & Astrophysics, 468, 425, ADS: 2007A&A...468..425T
Terebey, S., Shu, F. H., & Cassen, P., 1984, *The collapse of the cores of slowly rotating isothermal clouds*, in Astrophysical Journal, 286, 529, ADS: 1984ApJ...286..529T
Testi, L., Birnstiel, T., Ricci, L., Andrews, S., Blum, J., et al., 2014, *Dust Evolution in Protoplanetary Disks*, in Protostars and Planets VI, edited by H. Beuther, R. S. Klessen, C. P. Dullemond, & T. Henning, 339, ADS: 2014prpl.conf..339T
Thalmann, C., Mulders, G. D., Janson, M., Olofsson, J., Benisty, M., et al., 2015, *Optical Imaging Polarimetry of the LkCa 15 Protoplanetary Disk with SPHERE ZIMPOL*, in Astrophysical Journal, 808, L41, ADS: 2015ApJ...808L..41T
Thompson, S. E., Coughlin, J. L., Hoffman, K., Mullally, F., Christiansen, J. L., et al., 2018, *Planetary Candidates Observed by Kepler. VIII. A Fully Automated Catalog with Measured Completeness and Reliability Based on Data Release 25*, in Astrophysical Journal Supplement Series, 235, 38, ADS: 2018ApJS..235...38T
Tielens, A. G. G. M., & Hollenbach, D., 1985, *Photodissociation regions. I. Basic model.*, in Astrophysical Journal, 291, 722, ADS: 1985ApJ...291..722T
Toomre, A., 1964, *On the gravitational stability of a disk of stars.*, in Astrophysical Journal, 139, 1217, ADS: 1964ApJ...139.1217T
Trapman, L., Zhang, K., van't Hoff, M. L. R., Hogerheijde, M. R., & Bergin, E. A., 2022, *A Novel Way of Measuring the Gas Disk Mass of Protoplanetary Disks Using* N_2H^+ *and* $C^{18}O$, in Astrophysical Journal, 926, L2, ADS: 2022ApJ...926L...2T
Tripathi, A., Andrews, S. M., Birnstiel, T., & Wilner, D. J., 2017, *A millimeter Continuum Size-Luminosity Relationship for Protoplanetary Disks*, in Astrophysical Journal, 845, 44, ADS: 2017ApJ...845...44T
Turner, N. J., & Drake, J. F., 2009, *Energetic Protons, Radionuclides, and Magnetic Activity in Protostellar Disks*, in Astrophysical Journal, 703, 2152, ADS: 2009ApJ...703.2152T
Turner, N. J., Fromang, S., Gammie, C., Klahr, H., Lesur, G., et al., 2014, *Transport and Accretion in Planet-Forming Disks*, in Protostars and Planets VI, edited by H. Beuther, R. S. Klessen, C. P. Dullemond, & T. Henning, 411, ADS: 2014prpl.conf..411T
Urpin, V., & Brandenburg, A., 1998, *Magnetic and vertical shear instabilities in accretion discs*, in Monthly Notes of the Royal Astronomical Society, 294, 399, ADS: 1998MNRAS.294..399U
van der Marel, N., van Dishoeck, E. F., Bruderer, S., Pérez, L., & Isella, A., 2015, *Gas density drops inside dust cavities of transitional disks around young stars observed with ALMA*, in Astronomy & Astrophysics, 579, A106, ADS: 2015A&A...579A.106V

van der Marel, N., van Dishoeck, E. F., Bruderer, S., Andrews, S. M., Pontoppidan, K. M., et al., 2016a, *Resolved gas cavities in transitional disks inferred from CO isotopologs with ALMA*, in Astronomy & Astrophysics, 585, A58, ADS: 2016A&A...585A..58V

van der Marel, N., Verhaar, B. W., van Terwisga, S., Merín, B., Herczeg, G., et al., 2016b, *The (w)hole survey: An unbiased sample study of transition disk candidates based on Spitzer catalogs*, in Astronomy & Astrophysics, 592, A126, ADS: 2016A&A...592A.126V

van der Marel, N., Williams, J. P., Ansdell, M., Manara, C. F., Miotello, A., et al., 2018, *New Insights into the Nature of Transition Disks from a Complete Disk Survey of the Lupus Star-forming Region*, in Astrophysical Journal, 854, 177, ADS: 2018ApJ...854..177V

van der Marel, N., Dong, R., di Francesco, J., Williams, J. P., & Tobin, J., 2019a, *Protoplanetary Disk Rings and Gaps across Ages and Luminosities*, in Astrophysical Journal, 872, 112, ADS: 2019ApJ...872..112V

van der Marel, N., Dong, R., Pudritz, R., Wadsley, J., Boley, A., et al., 2019b, *Signposts of planet formation in protoplanetary disks*, in Canadian Long Range Plan for Astronony and Astrophysics White Papers, Vol. 2020, 6, ADS: 2019clrp.2020....6V

van der Marel, N., Birnstiel, T., Garufi, A., Ragusa, E., Christiaens, V., et al., 2021, *On the Diversity of Asymmetries in Gapped Protoplanetary Disks*, in Astronomical Journal, 161, 33, ADS: 2021AJ....161...33V

van der Marel, N., & Mulders, G. D., 2021, *A Stellar Mass Dependence of Structured Disks: A Possible Link with Exoplanet Demographics*, in Astronomical Journal, 162, 28, ADS: 2021AJ....162...28V

van Holstein, R. G., Girard, J. H., de Boer, J., Snik, F., Milli, J., et al., 2020, *Polarimetric imaging mode of VLT/SPHERE/IRDIS. II. Characterization and correction of instrumental polarization effects*, in Astronomy & Astrophysics, 633, A64, ADS: 2020A&A...633A..64V

van Leeuwen, F., 2007, *Validation of the new Hipparcos reduction*, in Astronomy & Astrophysics, 474, 653, ADS: 2007A&A...474..653V

van Terwisga, S. E., Hacar, A., & van Dishoeck, E. F., 2019, *Disk masses in the Orion Molecular Cloud-2: distinguishing time and environment*, in Astronomy & Astrophysics, 628, A85, ADS: 2019A&A...628A..85V

van Terwisga, S. E., van Dishoeck, E. F., Mann, R. K., Di Francesco, J., van der Marel, N., et al., 2020, *Protoplanetary disk masses in NGC 2024: Evidence for two populations*, in Astronomy & Astrophysics, 640, A27, ADS: 2020A&A...640A..27V

Veronesi, B., Lodato, G., Dipierro, G., Ragusa, E., Hall, C., et al., 2019, *Multiwavelength observations of protoplanetary discs as a proxy for the gas disc mass*, in Monthly Notes of the Royal Astronomical Society, 489, 3758, ADS: 2019MNRAS.489.3758V

Villaume, A., Brodie, J., Conroy, C., Romanowsky, A. J., & van Dokkum, P., 2017, *Initial Mass Function Variability (or Not) among Low-velocity Dispersion, Compact Stellar Systems*, in Astrophysical Journal, 850, L14, ADS: 2017ApJ...850L..14V

Villenave, M., Benisty, M., Dent, W. R. F., Ménard, F., Garufi, A., et al., 2019, *Spatial segregation of dust grains in transition disks. SPHERE observations of 2MASS J16083070-3828268 and RXJ1852.3-3700*, in Astronomy & Astrophysics, 624, A7, ADS: 2019A&A...624A...7V

Villenave, M., Ménard, F., Dent, W. R. F., Duchêne, G., Stapelfeldt, K. R., et al., 2020, *Observations of edge-on protoplanetary disks with ALMA. I. Results from continuum data*, in Astronomy & Astrophysics, 642, A164, ADS: 2020A&A...642A.164V

Vinković, D., 2009, *Radiation-pressure mixing of large dust grains in protoplanetary disks*, in Nature, 459, 227, ADS: 2009Natur.459..227V

Vinković, D., & Čemeljić, M., 2021, *Inner dusty regions of protoplanetary discs - II. Dust dynamics driven by radiation pressure and disc winds*, in Monthly Notes of the Royal Astronomical Society, 500, 506, ADS: 2021MNRAS.500..506V

Vlemmings, W. H. T., Lankhaar, B., Cazzoletti, P., Ceccobello, C., Dall'Olio, D., et al., 2019, *Stringent limits on the magnetic field strength in the disc of TW Hya. ALMA observations of CN polarisation*, in Astronomy & Astrophysics, 624, L7, ADS: 2019A&A...624L...7V

Vorobyov, E. I., Elbakyan, V. G., Omukai, K., Hosokawa, T., Matsukoba, R., et al., 2020, *Accretion bursts in low-metallicity protostellar disks*, in Astronomy & Astrophysics, 641, A72, ADS: 2020A&A...641A..72V

Wada, K., Tanaka, H., Okuzumi, S., Kobayashi, H., Suyama, T., et al., 2013, *Growth efficiency of dust aggregates through collisions with high mass ratios*, in Astronomy & Astrophysics, 559, A62, ADS: 2013A&A...559A..62W

Wallerstein, G., & Carlson, M., 1960, *Letter to the Editor: on the Ultraviolet Excess in G Dwarfs.*, in

Astrophysical Journal, 132, 276, ADS: 1960ApJ...132..276W

Wang, L., & Goodman, J. J., 2017a, *Wind-driven Accretion in Transitional Protostellar Disks*, in Astrophysical Journal, 835, 59, ADS: 2017ApJ...835...59W

Wang, L., & Goodman, J., 2017b, *Hydrodynamic Photoevaporation of Protoplanetary Disks with Consistent Thermochemistry*, in Astrophysical Journal, 847, 11, ADS: 2017ApJ...847...11W

Wang, L., Bai, X.-N., & Goodman, J., 2019, *Global Simulations of Protoplanetary Disk Outflows with Coupled Non-ideal Magnetohydrodynamics and Consistent Thermochemistry*, in Astrophysical Journal, 874, 90, ADS: 2019ApJ...874...90W

Wardle, M., & Ng, C., 1999, *The conductivity of dense molecular gas*, in Monthly Notes of the Royal Astronomical Society, 303, 239, ADS: 1999MNRAS.303..239W

Warren, S. G., & Brandt, R. E., 2008, *Optical constants of ice from the ultraviolet to the microwave: A revised compilation*, in Journal of Geophysical Research (Atmospheres), 113, D14220, ADS: 2008JGRD..11314220W

Weber, M. L., Ercolano, B., Picogna, G., Hartmann, L., & Rodenkirch, P. J., 2020, *The interpretation of protoplanetary disc wind diagnostic lines from X-ray photoevaporation and analytical MHD models*, in Monthly Notes of the Royal Astronomical Society, 496, 223, ADS: 2020MNRAS.496..223W

Weidenschilling, S. J., 1977, *Aerodynamics of solid bodies in the solar nebula.*, in Monthly Notes of the Royal Astronomical Society, 180, 57, ADS: 1977MNRAS.180...57W

Weinberger, A. J., Anglada-Escudé, G., & Boss, A. P., 2013, *Distance and Kinematics of the TW Hydrae Association from Parallaxes*, in Astrophysical Journal, 762, 118, ADS: 2013ApJ...762..118W

Weingartner, J. C., & Draine, B. T., 2001, *Dust Grain-Size Distributions and Extinction in the Milky Way, Large Magellanic Cloud, and Small Magellanic Cloud*, in Astrophysical Journal, 548, 296, ADS: 2001ApJ...548..296W

Wells, M., 2016, *The infrared spectrometer for Twinkle*, in Society of Photo-Optical Instrumentation Engineers (SPIE) Conference Series, Vol. 9904, Space Telescopes and Instrumentation 2016: Optical, Infrared, and Millimeter Wave, edited by H. A. MacEwen, G. G. Fazio, M. Lystrup, N. Batalha, N. Siegler, & E. C. Tong, 99044N, ADS: 2016SPIE.9904E..4NW

Whipple, F. L., 1964, *The History of the Solar System*, in Proceedings of the National Academy of Science, 52, 565, ADS: 1964PNAS...52..565W

Whipple, F. L., 1972, *On certain aerodynamic processes for asteroids and comets*, in From Plasma to Planet, edited by A. Elvius, 211, ADS: 1972fpp..conf..211W

Wilhelm, M. J. C., & Portegies Zwart, S., 2022, *Exploring the possibility of Peter Pan discs across stellar mass*, in Monthly Notes of the Royal Astronomical Society, 509, 44, ADS: 2022MNRAS.509...44W

Williams, J. P., & Cieza, L. A., 2011, *Protoplanetary Disks and Their Evolution*, in Annual Review of Astronomy and Astrophysics, 49, 67, ADS: 2011ARA&A..49...67W

Willson, M., Kraus, S., Kluska, J., Monnier, J. D., Cure, M., et al., 2019, *Imaging the disc rim and a moving close-in companion candidate in the pre-transitional disc of V1247 Orionis*, in Astronomy & Astrophysics, 621, A7, ADS: 2019A&A...621A...7W

Winn, J. N., & Fabrycky, D. C., 2015, *The Occurrence and Architecture of Exoplanetary Systems*, in Annual Review of Astronomy and Astrophysics, 53, 409, ADS: 2015ARA&A..53..409W

Winter, A. J., Clarke, C. J., Rosotti, G., Ih, J., Facchini, S., et al., 2018, *Protoplanetary disc truncation mechanisms in stellar clusters: comparing external photoevaporation and tidal encounters*, in Monthly Notes of the Royal Astronomical Society, 478, 2700, ADS: 2018MNRAS.478.2700W

Winter, A. J., Clarke, C. J., & Rosotti, G. P., 2019, *External photoevaporation of protoplanetary discs in Cygnus OB2: linking discs to star formation dynamical history*, in Monthly Notes of the Royal Astronomical Society, 485, 1489, ADS: 2019MNRAS.485.1489W

Winter, A. J., Ansdell, M., Haworth, T. J., & Kruijssen, J. M. D., 2020, *Testing viscous disc theory using the balance between stellar accretion and external photoevaporation of protoplanetary discs*, in Monthly Notes of the Royal Astronomical Society, 497, L40, ADS: 2020MNRAS.497L..40W

Wizinowich, P., Acton, D. S., Shelton, C., Stomski, P., Gathright, J., et al., 2000, *First Light Adaptive Optics Images from the Keck II Telescope: A New Era of High Angular Resolution Imagery*, in Publications of the Astronomical Society of the Pacific, 112, 315, ADS: 2000PASP..112..315W

Woitke, P., Min, M., Pinte, C., Thi, W. F., Kamp, I., et al., 2016, *Consistent dust and gas models for protoplanetary disks. I. Disk shape, dust settling, opacities, and PAHs*, in Astronomy & Astrophysics, 586, A103, ADS: 2016A&A...586A.103W

Wölfer, L., Picogna, G., Ercolano, B., & van Dishoeck, E. F., 2019, *Radiation-hydrodynamical models of X-ray photoevaporation in carbon-depleted circumstellar discs*, in Monthly Notes of the Royal Astronomical Society, 490, 5596, ADS: 2019MNRAS.490.5596W

Wölfer, L., Facchini, S., Kurtovic, N. T., Teague, R., van Dishoeck, E. F., et al., 2021, *A highly non-Keplerian protoplanetary disc. Spiral structure in the gas disc of CQ Tau*, in Astronomy & Astrophysics, 648, A19, ADS: 2021A&A...648A..19W

Wolff, S. G., Perrin, M. D., Stapelfeldt, K., Duchêne, G., Ménard, F., et al., 2017, *Hubble Space Telescope Scattered-light Imaging and Modeling of the Edge-on Protoplanetary Disk ESO-Hα 569*, in Astrophysical Journal, 851, 56, ADS: 2017ApJ...851...56W

Wolff, S. G., Duchêne, G., Stapelfeldt, K. R., Ménard, F., Flores, C., et al., 2021, *The Anatomy of an Unusual Edge-on Protoplanetary Disk. I. Dust Settling in a Cold Disk*, in Astronomical Journal, 161, 238, ADS: 2021AJ....161..238W

Wolszczan, A., & Frail, D. A., 1992, *A planetary system around the millisecond pulsar PSR1257 + 12*, in Nature, 355, 145, ADS: 1992Natur.355..145W

Woolfson, M. M., 1993, *The Solar System - Origin and Evolution*, in Quarterly Journal of the Royal Astronomical Society, 34, 1, ADS: 1993QJRAS..34....1W

Wu, Y., & Lithwick, Y., 2021, *The Irradiation Instability of Protoplanetary Disks*, in Astrophysical Journal, 923, 123, ADS: 2021ApJ...923..123W

Wyatt, M. C., 2008, *Evolution of debris disks.*, in Annual Review of Astronomy and Astrophysics, 46, 339, ADS: 2008ARA&A..46..339W

Xu, Z., Herczeg, G. J., Johns-Krull, C. M., & France, K., 2021, *Probing Protoplanetary Disk Winds with C II Absorption*, in Astrophysical Journal, 921, 181, ADS: 2021ApJ...921..181X

Youdin, A., & Johansen, A., 2007, *Protoplanetary Disk Turbulence Driven by the Streaming Instability: Linear Evolution and Numerical Methods*, in Astrophysical Journal, 662, 613, ADS: 2007ApJ...662..613Y

Youdin, A. N., & Goodman, J., 2005, *Streaming Instabilities in Protoplanetary Disks*, in Astrophysical Journal, 620, 459, ADS: 2005ApJ...620..459Y

Youdin, A. N., & Lithwick, Y., 2007, *Particle stirring in turbulent gas disks: Including orbital oscillations*, in Icarus, 192, 588, ADS: 2007Icar..192..588Y

Zakri, W., Megeath, S. T., Fischer, W. J., Gutermuth, R., Furlan, E., et al., 2022, *The Rate, Amplitude, and Duration of Outbursts from Class 0 Protostars in Orion*, in Astrophysical Journal, 924, L23, ADS: 2022ApJ...924L..23Z

Zhang, K., Booth, A. S., Law, C. J., Bosman, A. D., Schwarz, K. R., et al., 2021, *Molecules with ALMA at Planet-forming Scales (MAPS). V. CO Gas Distributions*, in Astrophysical Journal Supplement Series, 257, 5, ADS: 2021ApJS..257....5Z

Zhao, B., Caselli, P., Li, Z.-Y., Krasnopolsky, R., Shang, H., et al., 2016, *Protostellar disc formation enabled by removal of small dust grains*, in Monthly Notes of the Royal Astronomical Society, 460, 2050, ADS: 2016MNRAS.460.2050Z

Zhu, W., & Dong, S., 2021, *Exoplanet Statistics and Theoretical Implications*, in Annual Review of Astronomy and Astrophysics, 59, ADS: 2021ARA&A..59..291Z

Zhu, Z., Nelson, R. P., Hartmann, L., Espaillat, C., & Calvet, N., 2011, *Transitional and Pre-transitional Disks: Gap Opening by Multiple Planets?*, in Astrophysical Journal, 729, 47, ADS: 2011ApJ...729...47Z

Zhu, Z., Nelson, R. P., Dong, R., Espaillat, C., & Hartmann, L., 2012, *Dust Filtration by Planet-induced Gap Edges: Implications for Transitional Disks*, in Astrophysical Journal, 755, 6, ADS: 2012ApJ...755....6Z

Zhu, Z., Stone, J. M., Rafikov, R. R., & Bai, X.-n., 2014, *Particle Concentration at Planet-induced Gap Edges and Vortices. I. Inviscid Three-dimensional Hydro Disks*, in Astrophysical Journal, 785, 122, ADS: 2014ApJ...785..122Z

Zhu, Z., & Stone, J. M., 2018, *Global Evolution of an Accretion Disk with a Net Vertical Field: Coronal Accretion, Flux Transport, and Disk Winds*, in Astrophysical Journal, 857, 34, ADS: 2018ApJ...857...34Z

Zormpas, A., Picogna, G., Ercolano, B., & Kley, W., 2020, *Solid accretion onto planetary cores in radiative disks*, in Astronomy & Astrophysics, 638, A97, ADS: 2020A&A...638A..97Z

Zormpas, A., Birnstiel, T., Rosotti, G. P., & Andrews, S. M., 2022, *A large population study of protoplanetary disks: Explaining the millimeter size-luminosity relation with or without sub-structure*, in arXiv e-prints, arXiv: 2202.01241

Zsom, A., Ormel, C. W., Güttler, C., Blum, J., & Dullemond, C. P., 2010, *The outcome of protoplanetary dust growth: pebbles, boulders, or planetesimals? II. Introducing the bouncing barrier*, in Astronomy & Astrophysics, 513, A57, ADS: 2010A&A...513A..57Z

Appendix A

Nomenclature

A.1 Coordinate systems

Notation	Name	Conversion		
$\vec{r} = x\,\hat{x} + y\,\hat{y} + z\,\hat{z}$	Cartesian	$x = x$	$y = y$	$z = z$
$\vec{r} = R\,\hat{R} + z\,\hat{z} + \varphi\,\hat{\varphi}$	cylindrical	$x = R\,\cos(\varphi)$	$y = R\,\sin(\varphi)$	$z = z$
$\vec{r} = r\,\hat{r} + \vartheta\,\hat{\vartheta} + \varphi\,\hat{\varphi}$	spherical	$x = r\,\cos(\varphi)\,\sin(\vartheta)$	$y = r\,\sin(\varphi)\,\sin(\vartheta)$	$z = r\,\cos(\vartheta)$

$\hat{n}$ denotes the unit vector in direction $\vec{n}$; the velocity along $\hat{n}$ is v_n.

A.2 Physical constants

Symbol	Quantity	Value
k_{B}	Boltzmann constant	$1.380649 \cdot 10^{-23}$ J/K
G	gravitational constant	$6.67430 \cdot 10^{-11}$ m^3/(kg s^2)
h	Planck constant	$6.62607015 \cdot 10^{-34}$ J/Hz
c	speed of light	$2.99792458 \cdot 10^{8}$ m/s

A.3 Units

Symbol	Quantity	Value
AU	astronomical unit	$1.495978707 \cdot 10^{11}$ m
$\mathrm{M}_\oplus$	Earth mass	$5.9722 \cdot 10^{24}$ kg
$\mathrm{R}_\oplus$	Earth radius	$6.3781 \cdot 10^{6}$ m
eV	electronvolt	$1.602176634 \cdot 10^{-19}$ J
erg	erg	$1.0 \cdot 10^{-7}$ J
Jy	Jansky	$1.0 \cdot 10^{-26}$ W/(m^2 Hz)
$\mathrm{M}_{\mathrm{jup}}$	Jupiter mass	$1.89813 \cdot 10^{27}$ kg
pc	parsec	$3.0857 \cdot 10^{16}$ m
m_{H}	proton mass	$1.67262192369 \cdot 10^{-27}$ kg
$\mathrm{M}_\odot$	solar mass	$1.98847 \cdot 10^{30}$ kg
$\mathrm{R}_\odot$	solar radius	$6.957 \cdot 10^{8}$ m
yr	year	$3.1557600 \cdot 10^{7}$ s

A.4 Abbreviations and acronyms

General terms

Abbreviation	Name
CTTS	classical T-Tauri star
GMC	giant molecular cloud
HD	hydrodynamic(s)
HR	Hertzsprung-Russell [diagram]
HVC	high-velocity component (of a protostellar wind)
IMF	initial mass function
ISM	interstellar medium
LVC	low-velocity component (of a protostellar wind)
LVC-BC	broad component of the low-velocity component (of a protostellar wind)
LVC-NC	narrow component of the low-velocity component (of a protostellar wind)
MHD	magneto-hydrodynamic(s)
MMSN	minimum-mass solar nebula
MRN	Mathis-Rumpl-Nordsieck (particle size distribution)
MS	main sequence (on a HR diagram)
PAH	polycyclic aromatic hydrocarbon
PD	primordial disk
PE	photoevaporation
SED	spectral energy distribution
SN	supernova
SPH	smoothed-particle hydrodynamics
TD	transition(al) disk
WTTS	weak-lined T-Tauri star

Spectral ranges

See also Table 2.1.

Abbreviation	Name
EUV	extreme ultraviolet
FUV	far ultraviolet
IR	infrared
mm	millimeter
micron	micrometer
μm	micrometer
UV	ultraviolet (FUV and EUV)
XEUV	X-ray and EUV

Symbols

Symbol	Name
a or a_0	dust grain radius
c_s	sound speed
E_{grav}	gravitational energy

(continued on next page)

Symbol	Name
E_{kin}	kinetic energy
F_{drag}	gas drag force
h_{gas} or H_{gas}	gas disk scale height ($h_{\mathrm{gas}} = H_{\mathrm{gas}}/R$)
i	inclination (of an observed disk)
L_{acc}	accretion luminosity
ℓ_{fp}	mean free path
L_{X}	(stellar) X-ray luminosity
$\dot{M}_{\mathrm{acc}}$	mass-accretion rate (of the star)
M_{disk}	disk mass
$\dot{M}_{\mathrm{dust}}$	dust mass-loss rate (wind-driven)
$\dot{M}_{\mathrm{EUV}}$	gas mass-loss rate due to EUV photoevaporation
$\dot{M}_{\mathrm{ext}}$	gas mass-loss rate due to external photoevaporation
$\dot{M}_{\mathrm{FUV}}$	gas mass-loss rate due to (primarily) FUV-driven photoevaporation
$\dot{M}_{\mathrm{wind}}$ or $\dot{M}_{\mathrm{gas}}$	gas mass-loss rate (wind-driven)
$\dot{M}_{\mathrm{X}}$ or $\dot{M}_{\mathrm{XEUV}}$	gas mass-loss rate due to (primarily) X-ray-driven photoevaporation
M_*	stellar mass
n_{gas}	gas number density
Q_{Toomre}	Toomre parameter
R_c	characteristic (disk) radius
r_{gap}	inner-hole radius (of a transition disk)
R_{grav}	gravitational radius
R_*	stellar radius
r_{Hill}	Hill radius
St	Stokes number
t_{disk}	disk lifetime
T_{gas}	gas temperature
t_{stop}	stopping time
t_ν	viscous time
T_*	stellar temperature
Z	metallicity
α	Shakura-Sunyaev α-viscosity parameter
α	spectral index
β	plasma parameter (of the magnetic field)
$\varepsilon_{\mathrm{dtg}}$	dust-to-gas ratio
λ_{obs}	observational wavelength
μ	mean atomic mass
ν	kinematic viscosity
ξ_{ion}	ionisation parameter (due to X-rays)
ϱ_{dust}	dust density
ϱ_{gas}	gas volume density
ϱ_{grain}	internal density of the dust
Σ_{gas}	gas surface density
Φ_*	EUV-photon emission rate of the star
Ω_K	Keplerian orbital velocity

Symbols (also if not listed here) are defined when they first occur in the running text.

Institutions

Abbreviation	Name
ANID	Agencia Nacional de Investigación y Desarrollo de Chile
AUI	Associated Universities, Inc.
CfA	Center for Astrophysics | Harvard & Smithsonian
CIRAS	Center for Interdisciplinary Research in Astrophysics and Space Exploration
C2PAP	Computational Center for Particle- and Astrophysics
DFG	Deutsche Forschungsgemeinschaft
ERC	European Research Council
ESO	European Southern Observatory (European Organisation for Astronomical Research in the Southern Hemisphere)
IAU	International Astronomical Union
LMU	Ludwig-Maximilians-Universität (München)
MIAPP	Munich Institute for Astro- and Particle Physics
NAOJ	National Astronomical Observatory of Japan
NSF	National Science Foundation
NRAO	National Radio Astronomy Observatory
USM	Universitätssternwarte München der Fakultät für Physik der Ludwig-Maximilians-Universität

Instruments

Abbreviation	Name
ALMA	Atacama Large Millimeter/submillimeter Array
Chandra	Chandra X-ray Observatory (formerly: Advanced X-ray Astrophysics Facility)
ELT	Extremely Large Telescope
HST	Hubble Space Telescope
JWST	James Webb Space Telescope
JWST NIRCam	Near-Infrared Camera of JWST
Keck	W. M. Keck Observatory
Kepler	Kepler Space Telescope
ngVLA	Next Generation Very Large Array
(SPHERE) IRDIS	(SPHERE using the) Infrared Dual-band Imager and Spectrograph
(SPHERE) ZIMPOL	(SPHERE using the) Zurich Imaging Polarimeter
VLA	(Karl G. Jansky) Very Large Array
VLT	Very Large Telescope
(VLT) CRIRES	Cryogenic Infrared Echelle Spectrograph (of the VLT)
(VLT) SPHERE	Spectro-Polarimetric High-contrast Exoplanet REsearch (of the VLT)

Observational campaigns

Abbreviation	Name
COUP	Chandra Orion Ultradeep Project
DSHARP	Disk Substructures at High Angular Resolution Project
MAPS	Molecules with ALMA at Planet-forming scales

A.5 Software

Abbreviation	Weblink
APT	https://www.stsci.edu/scientific-community/software/astronomers-proposal-tool-apt/
astropy	https://www.astropy.org/
Debian	https://www.debian.org/
denoise	https://github.com/danieljprice/denoise/
disklab	[not yet publicly available]
dsharp_opac	https://github.com/birnstiel/dsharp_opac/
jupyter	https://jupyter.org/
jwst	https://jwst-pipeline.readthedocs.io/
matplotlib	https://matplotlib.org/
MiniConda	https://docs.conda.io/en/latest/miniconda.html
Mirage	https://mirage-data-simulator.readthedocs.io/
Mocassin	https://mocassin.nebulousresearch.org/
numpy	https://numpy.org/
RadMC-3D	https://www.ita.uni-heidelberg.de/~dullemond/software/radmc-3d/
scipy	https://scipy.org/
pandas	https://pandas.pydata.org/
Pluto	http://plutocode.ph.unito.it/
Python	https://www.python.org/
$\TeX$	https://www.latex-project.org/

Acknowledgements

Last, but certainly not least, I would like to thank the people who made this thesis possible.

On a general note, one might wonder what and whom exactly to include in an acknowledgement. At first glance, the answer may seem more than obvious – but really, where does one start? What can we take for granted, and who deserves a special mention? For instance, the occurrence of the Big Bang – assuming the validity of the Big Bang theory – was paramount for the feasibility of this thesis; but admittedly, by this definition, basically every butterfly (not just of chance) that has ever flapped its (or rather, her, his, or their) wings would need to be included here, which would go well beyond the scope of a simple 'Thank You' to those who have helped me with undertaking this particular, tiny research foray into a vast sea of open questions. Nonetheless, considering the university at which this thesis was written, it may seem in order to give a special mention to a particular group of people, merely so that their memory may continue to live on – namely the *White Rose*, who stood up for their ideals even in the darkest of times.

That being said, I shall limit myself to my – as already noted in Chap. 1, quite limited – personal point of view, and my immediate surroundings; this, however, necessarily means that I might forget to mention some people who probably had a non-negligible impact on this work. To mitigate this, and in the interest of personal privacy, I am not going to enumerate individual names in the following; I'd imagine that everyone reading this will still find themselves mentioned below.

So, without further ado, I would like to express my gratitude towards my parents, for enabling me to embark on this journey of exploring the cosmos – and in the process, myself, too. A journey that was instigated, rather randomly, by the year I could spend at Lund University, where I was formally introduced to the wonders of the Universe.

I would like to state my heartfelt appreciation for my friends, who throughout – and already before – this chapter of my life, made me smile, think, and see the world through a myriad of different lenses, and at times also reminded me that life also happens to happen outside of academia.

Speaking of which, it requires a lot of background work to keep a research institute running as smoothly as it is, and said work was and is performed by the secretaries and system administrators, whose efforts I would like to sincerely commend.

Now, finally, arriving at the field of academic research itself, I would like to thank my office mates – at the observatory, and also in Cambridge during my brief stint there – and colleagues (not just in Munich, but all over the world, i.e. this tiny rock in the vastness of space), for taking my mind off things when I got too stuck, and nonetheless (or thus) inspiring me time and again to keep reaching for the stars – or their dust, at least –, even when it made my arms ache; and who provided me with some quite sensible and very helpful hints and suggestions as to how to reach them more easily, or even at all.

My gratitude furthermore goes to my collaborators – with a special, yet non-exclusive mention of those in Chile –, who definitely contributed to the work presented in Chaps. 3, 4, and 5. Of course, this is the idea behind scientific research; but it is still quite noteworthy. Due to your suggestions, comparisons, and double-checks, and our discussions, the results attained have become much more solidified, presentable, and also relevant to the field than if I had just worked by myself.

In the end, this work would, quite literally, not have been possible without the ceaseless efforts of my advisor(s); who invited me on this journey, let me roam the world quite freely in pursuit of new insights, and granted me some time to come to grips with the subject at hand, and a lot of freedom in how to go about it, but also provided guidance when needed. Per questo, vorrei ringraziarvi di cuore.

Thank You!